Università degli Studi di Ferrara

DOTTORATO DI RICERCA IN
SCIENZE DELL'INGEGNERIA

CICLO XXI

COORDINATORE Prof. STEFANO TRILLO

ADVANCED NUMERICAL METHODS FOR THE DYNAMIC OPTIMISATION OF MECHANICAL COMPONENTS

Settore Scientifico Disciplinare: ING-IND/13

Dottorando
Dott. VENTURI VALERIO

Tutore
Prof. DALPIAZ GIORGIO

Anni 2006/2008

Università degli Studi di Ferrara

DOTTORATO DI RICERCA IN
SCIENZE DELL'INGEGNERIA

CICLO XXI

COORDINATORE Prof. STEFANO TRILLO

ADVANCED NUMERICAL METHODS FOR THE DYNAMIC OPTIMISATION OF MECHANICAL COMPONENTS

Settore Scientifico Disciplinare: ING-IND/13

Dottorando
Dott. VENTURI VALERIO

Tutore
Prof. DALPIAZ GIORGIO

Anni 2006/2008

Title:	Advanced numerical methods for the dynamic optimisation of mechanical components
Author:	Ing. Valerio Venturi

Department:	Engineering Department in Ferrara
University:	Università degli Studi di Ferrara
Address:	Via Saragat, 1 – 44100, Ferrara, Italy

Doctoral Program:	Engineering
Curriculum:	Industrial Engineering
Branch of Study:	Mechanics of Machines

Supervisor: Prof. Giorgio Dalpiaz
Engineering Department in Ferrara
Università degli Studi di Ferrara
Via Saragat, 1 – 44100, Ferrara, Italy

Number of pages:	321
Number of figures:	249
Number of tables:	24
Printed:	March 2009

Keywords:
Vibration, dynamic analysis, elastodynamic modelling, FE modelling, experimental validation, external gear pump, patches application, potential energy density, effective velocity.

To my family

UNA LUCE
di Valerio Venturi

Decenni su decenni,
il presente diviene passato,
il futuro lascia posto al presente,
il mondo si fa diverso,
le persone cambiano,
lentamente tutto ciò che è si perde,
ricordi parlano di tempi che furono,
vite vissute vengono dimenticate,
ombre cupe accolgono tempi passati,
luci di speranza avvolgono momenti che saranno,
l'oggi rimane pervaso da un senso di incognita,
onore e coraggio sembrano appartenere a un tempo che fu,
lentamente e inesorabilmente,
decenni su decenni,
si è sciupato il senso della vita,
smarrendo nel cammino speranza e fratellanza,
perdendo il ricordo della felicità della vita,
lasciando posto ad una piatta e fredda normalità.

Pesanti ombre incalzano,
la paura di vivere manovra i destini,
i destini di coloro che sono soli,
soli nel mondo,
soli nella vita,
soli nella morte.
Nulla sembrerebbe avere senso,
nulla darebbe importanza alla vita,
nulla darebbe un senso alla vita.
Malgrado sia forte e verosimile l'eventualità di tale vita,
presente passata e futura,
una LUCE rimane,
al cui confronto tutto il resto impallidisce,
una LUCE rimane,
prendendo con forza il suo posto nella vita,
una LUCE rimane,
riscaldando il cuore delle persone,
questa LUCE calda e accogliente rimane,
questa LUCE ospitale e confortevole rimane,
questa LUCE chiamata famiglia rimane e rimarrà per sempre.

ACKNOWLEDGEMENTS

With this thesis I tried to clearly and simply present the work that I have done in three years of PhD training. Of course, none of these pages could have been written without the help and the knowledge of other people and researchers. To this, I wish to thank all those fundamental people that helped me in the drawing of this thesis.

This thesis has been partially developed within the laboratory of research and technology transfer InterMech (Division Acoustic and Vibrations – LAV) realized through the contribution of Regione Emilia Romagna – Assessorato Attività

Produttive, Sviluppo Economico, Piano telematico, PRRIITT misura 3.4 azione A. The research activity performed in the first part of this thesis, relating to the study of external gear pumps for steering systems, has been carried out through collaboration between the Dept. of Engineering of the University of Ferrara in co-operation with TRW Automotive Italia S.p.A – Divisione Automotive Pumps (Ostellato, Ferrara, Italy). Therefore, I wish to thank TRW Automotive Italia S.p.A and its engineers for their active co-operation, all the people I have worked with during the last three years and a special thanks to my supervisor Prof. Giorgio Dalpiaz who proposed me this PhD course three years ago.

The research activity performed in the second part of this thesis, relating to the creation of a new methodology for vibration reduction by the application of damping patches in proper positions, has been made possible thanks to the EDSVS project that allowed me to continue my scientific education abroad. The work that I have done during the period of training and research at INSA institute has improved myself at human level and has allowed me to increase my knowledge level in relation to my work field. The place of work was relaxing, collaborative and absolutely positive. I could appreciate the spirit of unity and strength that get on everyone in the working group. Moreover, impossible to forget Prof. Goran Pavic and its Staff that helped and supported me in my stay abroad. I am proud to say that the time spent in Lyon has been one of the most beautiful and important of my life.

Last, but not least, a special thanks to my family who supported and helped me in all my educational training. If I came to this moment it is only thanks to them.

ABSTRACT

This PhD thesis concerns the development and assessment of innovative methodologies for simulating and improving the dynamic behaviour of mechanical components. In particular, two correlated issues are addressed herein: hybrid FE/LP gear pump modelling as a tool for foreseeing and optimising vibration behaviour in operational conditions; a new methodology for vibration reduction by applying damping patches in appropriate positions.

In the field of positive displacement pump modelling, external gear pumps were analysed with the aim of developing

advanced methodologies which accurately predict of the dynamic behaviour of these components. Indeed, the first part of this thesis (*PART A*) is about external gear pumps for steering systems; the research activity concerning gear pumps was carried out in collaboration with the Dept. of Engineering at the University of Ferrara in co-operation with TRW Automotive Italia S.p.A – Divisione Automotive Pumps (Ostellato, Ferrara, Italy). This research pertains to the creation of a hybrid model, obtained through the integration of a nonlinear elastodynamic model with lumped parameters in relation to moving bodies, and an FE pump model. The model referred to bodies in motion takes into account the most important phenomena involved in pump operations, such as time-varying oil pressure distribution on gears, time-varying meshing stiffness, tooth profile errors, the possibility of tooth contact, bush displacement and hydrodynamic journal bearing reactions. Coupling the FE with the various parts which make up the pump, as well as coupling the lumped-parameter model and the FE model required the development of specific advanced techniques; thus several problems related to the combination of the different models employed in order to form a single hybrid LP/FE model were studied and resolved. Using particular techniques based on comparisons between simulations and experimental results concerning acceleration, forces and moments, the model was experimentally validated.

Although this hybrid model is an excellent tool for improving the dynamic behaviour of gear pumps and for optimising the early stages of prototype design, some problems can still remain related to unwanted vibrations into precise frequency ranges. Thus, once the first part of the research was completed, it was decided to delve into the problem of structural optimisation. In particular, a methodology for surface damping treatment was created and applied. Indeed, the second part of the research activity (*PART B*) was about the optimisation of mechanical components and systems through the application of high damping material components known as patches; this research activity is being

carried out by the Dept. of Mechanical Engineering (laboratoire vibrations acoustique) at the INSA institute (Institute National des Sciences Appliquées) in Lyon (France) where I spent thirteen months between the second and third year of my doctoral studies. Such treatment can be applied to existing structures and provides high damping capability over wide temperature and frequency ranges. In many practical plate and machinery casing structures, it is difficult to treat the whole surface with constrained layer viscoelastic material, due to reduced areas or inaccessible parts. Furthermore, it may indeed be desirable to selectively apply one or more damping patches to control certain resonances. Patch damping design is an efficient and cost effective concept for solving noise and vibration problems. As a result of these considerations, the research was focused on finding a general methodology, based on a purely energetic approach, to reduce the unwanted amplitude vibration level in mechanical components through the application of appropriate elements characterized by high damping properties. The methodology was enforced using I-DEAS v7® software which makes it possible to address modelling in terms of energy distribution within a structure. Advanced methodologies were developed to reduce the vibration amplitude in components such as plate and bracket by applying patches. Specifically, potential energy estimations will precisely and accurately define the exact locations on the surface of the components which should be covered by the patches. As a result, these studies enable a reduction in vibration amplitude, in reference both to a single component and/or a complex system. In addition, this methodology makes it possible to improve the vibratory behaviour of a component in certain frequency ranges while reducing, at the same time, the effect of dangerous resonances, acting specifically on the location, extent and quantity of the patches to be applied on the surface of the base component.

During this thesis, different fields were contemporarily studied: definition and identification of structural modification

methods, theoretical aspects of material damping characteristics, vibrational propagation methods and applicative aspects relating to the implementation of models for the vibratory optimisation of mechanical components.

This thesis was developed within the LVA research and technology transfer laboratories at the INSA institute (Lyon, France) and InterMech (Division Acoustic and Vibrations – LAV); and was carried out with the contribution of the Emilia Romagna Region – Assessorato Attività Produttive, Sviluppo Economico, Piano telematico, PRRIITT misura 3.4 azione A.

SOMMARIO

L'attività di formazione e ricerca nel campo della Meccanica delle Vibrazioni è stata focalizzata sullo studio di metodologie avanzate ed innovative di modellazione, simulazione e validazione sperimentale dei modelli per lo studio del comportamento dinamico e vibratorio di macchine e componenti meccanici. In questo contesto, le due tematiche quantitativamente più rilevanti, direttamente correlate tra loro, sono: (i) modellazione di strutture meccaniche tramite l'ausilio di patch smorzanti, resa possibile dalla creazione di una nuova metodologia volta alla loro ottimizzazione tramite la riduzione del loro livello vibratorio; (ii)

modellazione ibrida LP/FE (parametri concentrati non lineare e FEM) di una pompa ad ingranaggi avente lo scopo di prevedere ed allo stesso tempo, ottimizzare il comportamento vibratorio in base a differenti condizioni operative.

Queste tematiche sono oggetto della presente tesi di dottorato dal titolo "Advanced numerical methods for the dynamic optimisation of mechanical components".

Nel campo della modellazione di pompe volumetriche sono state prese in considerazione le pompe ad ingranaggi esterni al fine di sviluppare metodologie numeriche avanzate per prevedere in maniera precisa ed accurata il comportamento dinamico dei suddetti componenti. A tal fine, la prima parte della tesi (*PART A*) riguarda pompe ad ingranaggi esterni utilizzate nei sistemi di guida in campo automobilistico. La suddetta attività di ricerca è stata resa possibile tramite una collaborazione allacciata tra il Dipartimento di Ingegneria dell'Università di Ferrara e TRW Automotive Italia S.p.A. – Divisione Automotive Pumps (Ostellato, Ferrara, Italy). Nello specifico, questa prima parte della tesi tratta la creazione di un modello ibrido, ottenuto tramite l'integrazione di un modello elastodinamico a parametri concentrati dei componenti in movimento, e la realizzazione di un modello FE del componente pompa. Il modello LP relativo a i componenti in movimento prende in considerazione i più importanti fenomeni coinvolti nel funzionamento della pompa, come: la variazione del tempo di ingranamento, la variazione della distribuzione di pressione sulle ruote dentate, gli errori direttamente correlati ai profili dei denti, le reazioni che vengono a generarsi a causa del contatto tra i denti delle ruote dentate, la possibilità di contatto tra i denti su entrambe le linee di azione (DLA e ILA), la rigidezza torsionale dell'albero motrice, lo spostamento delle boccole in direzione assiale e le reazioni generate dai cuscinetti. La fase di accoppiamento dei singoli modelli FE relativi ad ogni componente costituente il sistema pompa in modo da formare un unico modello FE, così come la fase che permette di unire il modello a parametri concentrati LP con il

modello FE, ha richiesto lo sviluppo di specifiche tecniche avanzate. Tutti i problemi riguardanti l'unione e la combinazione dei differenti modelli al fine di formarne uno unico, il modello ibrido LP/FE, sono stati studiati e conseguentemente risolti permettendo di generare un modello realistico di una pompa ad ingranaggi. I valori delle accelerazioni, delle forze e dei momenti calcolati ed ottenuti dal modello ibrido sono stati confrontati con quelli ottenuti sperimentalmente tramite l'ausilio di particolari tecniche. La qualità dei risultati ottenuti ha permesso di validare sperimentalmente il modello creato.

Sebbene questo modello ibrido sia un eccellente strumento per il miglioramento del comportamento dinamico di pompe ad ingranaggi, alcuni problemi possono comunque persistere; problemi che, per esempio, possono essere causati da vibrazioni indesiderate e pericolose in precisi range di frequenza. Si passa quindi dalla fase di modellazione del comportamento dinamico di sistemi meccanici (pompa ad ingranaggi studiata nella *PART A*), alla fase di ottimizzazione del comportamento strutturale di sistemi meccanici (applicazione dei patch studiata nella *PART B*). In altri termini, sebbene il modello sia in grado di prevedere gli effetti apportati da precise modifiche strutturali sui componenti costituenti il sistema meccanico, e sia in grado di simulare in maniera realistica il comportamento dinamico del sistema fisico reale, non è in grado di fornire nessuna spiegazione, nessuna informazione sulle modalità con cui alcune vibrazioni indesiderate generate dal sistema reale durante il funzionamento possano venire ridotte o shiftate in frequenza. Ad esempio, il componente centrale della pompa ad ingranaggi, quella che cioè contiene le ruote dentate, genera rumore e vibrazioni caratterizzati da ampiezze elevate. Risulta quindi importante agire su di esso al fine di ridurre le summenzionate vibrazioni indesiderate. Questo problema viene considerato e risolto nella seconda parte della tesi (*PART B*).

In particolare, in questa seconda parte della tesi, è stata ideata e creata una metodologia che permette di ottimizzare il

comportamento dinamico di componenti meccanici generici e sistemi tramite l'applicazione di specifici componenti caratterizzati da elevate proprietà smorzanti, definiti come patch. Questa seconda attività di ricerca è stata svolta durante un periodo di formazione e ricerca della durata di un anno presso il *Laboratoire Vibrations Acoustique* dell'INSA di Lione in ambito EDSVS sotto la supervisione del Prof. Goran Pavic. Questo tipo di trattamento può essere applicato a strutture esistenti offrendo elevate capacità smorzanti in ampi range di frequenze e temperature. In molti casi pratici, come in piatti e strutture meccaniche, a causa di posizioni inaccessibili o zone di piccola estensione (come ad esempio il componente centrale della pompa ad ingranaggi), risulta difficile trattare la totale superficie dei suddetti componenti con elementi caratterizzati da elevate proprietà smorzanti. Quindi, risulta indispensabile agire in maniera localizzata ed intelligente in corrispondenza di zone ristrette della superficie del componente meccanico; ciò è reso possibile dall'applicazione di patch in differenti posizioni accuratamente scelte sulla superficie del componente. Come risultato, nella seconda parte della tesi viene creata e messa a punto una metodologia avanzata, basata su uno studio indirizzato su un livello puramente energetico, che permette di ridurre l'ampiezza delle vibrazioni di componenti generici al fine di migliorare il comportamento vibratorio globale del sistema completo o della semplice struttura. Questa metodologia è stata validata per componenti meccanici generici quali "beam" e "plate", caratterizzati da differenti condizioni al contorno. In parallelo è stato realizzato lo studio, la stima e la valutazione dello smorzamento strutturale dei suddetti componenti meccanici sotto l'applicazione di determinate condizioni al contorno. Lo strumento utilizzato per raggiungere questo obiettivo è stato il software I-DEAS v7 che ha permesso di affrontare uno studio da un punto di vista energetico. Il percorso seguito ha permesso di ridurre le vibrazioni sia a livello locale che globale agendo sulla presenza, posizione, estensione e quantità dei "patch", rendendo al

contempo possibile un miglioramento del comportamento vibratorio del componente e una riduzione dell'ampiezza delle risonanze pericolose.

Durante l'attività di ricerca sono stati mantenuti a contatto l'aspetto teorico relativo all'utilizzo di materiali smorzanti correlato alla modalità di propagazione delle vibrazioni e l'aspetto più propriamente sperimentale, relativo alla realizzazione di modelli per il miglioramento del comportamento dinamico e vibratorio.

NOMENCLATURE

The symbol definitions used in this thesis are tabulated below, arranged alphabetically, by type of letter. Symbols that are used only in passing, in the course of a derivation, for the sake of brevity or clarity, are not included here. Each definition is followed by the paragraph and by the equation, table or figure number in which the symbol first appears. The meanings of subscripts are given for only a few exceptional cases.

English capitals

B	Relief groove dimension, A1.3.3, Figure A1.22.
B_{oil}	Oil bulk modulus, A2.5, eq. (A2.39).
C	Viscous damping matrix, A, eq. (A.1).

C_j Viscous damper coefficient of tooth pair j, A2.1, Figure A2.3.

C_r Radial clearance in the journal bearing, A2.4, eq. (A2.33).

$C_{squeeze}$ Damper squeeze coefficient, A2.1, eq. (A2.10).

C_T Torsional damper coefficient of the driving shaft, A2.1, Figure A2.2.

E Total mechanical energy, B1.5.1, eq. (B1.1).

E_{fp} Profile error for tooth flank p, A2.3, eq. (A2.29).

E_j Gears errors of the meshing teeth, A2.1, Figure A2.3.

E_p Potential energy, B1.5.1, eq. (B1.2).

E_k Kinetic energy, B1.5.1, eq. (B1.2).

E_Y Young's modulus, A2.2, eq. (A2.26).

F External force, A, eq. (A.1).

G Shear modulus, A1.3.1, eq. (A1.3).

$H_{x'x'}$ FRF with input in X'-direction and output in X'-direction, A4.8, eq. (A4.1).

$H_{x'y'}$ FRF with input in Y'-direction and output in X'-direction, A4.8, eq. (A4.1).

J_k Rotational inertia of gear k, A1.3.1, eq. (A1.2).

K Stiffness matrix, A, eq. (A.1).

K'_H Hertzian stiffness constant, A2.2, eq. (A2.25).

K_j Stiffness of tooth pair j in case of spur gears, A2.1, Figure A2.3.

K'_p Stiffness constant of tooth flank p (p=1,2,3,4), A2.2, eq. (A2.23).

K_T Torsional stiffness of the driving shaft, A1.3.1, eq. (A1.3).

L Mean Lagrangian energy density, B1.5.1, eq. (B1.12c).

M Mass matrix, A, eq. (A.1).

M_{pk} Pressure torque of gear k, A2.1, eq. (A2.7).

P Real input power, B1.5.1, eq. (B1.1).

P_b Base pitch, A1.3.1, eq. (A1.6).

P_{in} Total complex mechanical power supplied to structure, B1.5.1, eq. (B1.12a).

Q Volumetric flow rate, A2.5, eq. (A2.39).

$Q_{d,i}$ Volumetric flow rates between the tooth space and the drainage, A2.5, eq. (A2.40).

$Q_{f,i}, Q_{f,i+1}$ Volumetric flow rates between the gear lateral and the bushes, A2.5, eq. (A2.40).

$Q_{h,i}, Q_{h,i+1}$ Volumetric flow rates between the tooth tip and the case, A2.5, eq. (A2.40).

R_b Bearing radius, A1.3.3, Table A1.4.

R_{pk} Radius of the pitch circle of gear k, A1.3.1, eq. (A1.4).

R_s Shaft radius, A1.3.1, eq. (A1.1).

T Meshing period, A2.1.

U_r Complex modal amplitude, B1.5.1, eq. (B1.3).

V Volume of the control volume, A2.5, eq. (A2.39).

V_{eff} Effective velocity, B5.4, eq. (B5.1).

V_i Volume of the tooth space "i", A2.5, eq. (A2.45).

W Oscillating amplitude, B2.2, Figure B2.1.

$W_{x,y}$ Impedance amplitude in direction X and Y respectively, A2.4, eq. (A2.33).

Latin lower-case letters

a Centre distance of gear pair, A1.3.3, Table A2.4.

$a_{x'}$ Acceleration values in X'-direction, A4.8, eq. (A4.1).

b_k Gear thickness, A1.3.1, eq. (A1.1).

b_b Bush thickness, A1.3.3, Table A1.4.

d Damping capacity per-unite-volume, B2.3, eq. (B2.2).

dt Increment of time, A2.5, eq. (A2.39).

$\tilde{e}$ Eccentricity of the journal in the bearing, A2.4, eq. (A2.34).

$e_{k,r}$ Modal kinetic energy, B1.5.1, eq. (B1.5).

$e_{p,r}$ Modal potential energy, B1.5.1, eq. (B1.8).

e_p Potential energy density, B1.5.1, eq. (B1.10).

e_k Kinetic energy density, B1.5.1, eq. (B1.10).

f_{bxk} Force in the oil bearings in direction X of gear k, A2.1, eq. (A2.7).

f_{byk} Force in the oil bearings in direction Y of gear k, A2.1, eq. (A2.7).

$f_{el.j}$ Elastic force of tooth pair j, A2.1, eq. (A2.8).

f_{mgj} Meshing force of tooth pair j, A2.1, eq. (A2.7).

f_{pxk} Pressure force in direction X of gear k, A2.1, eq. (A2.7).

f_{pyk} Pressure force in direction Y of gear k, A2.1, eq. (A2.7).

$f_{v.j}$ Viscous damping force of tooth pair j, A2.1, eq. (A2.8).

f_r Complex modal force, B1.5.1, eq. (B1.4).

g Backlash along the line of action, A2.1, eq. (A2.9).

h Height of the meatus between teeth on the line of action, A2.1, eq. (A2.12).

h_i Radial clearance between tooth tip and case, A2.5, eq. (A2.41).

h_f Lateral clearance between bushes and the lateral flank of the tooth, A2.5, eq. (A2.43).

$h_{re,i}$ Radial clearance between the tooth tip and the case for a position defined by the angle θ_i and by the distance $\tilde{e}$, A2.5, eq. (A2.42).

h_w Radial height of the wear profile, A2.5, eq. (A2.42).

j Denotes pair of teeth ($j = a,b,c,d$), A2.1.

l_t Tooth tips thickness, A1.3.1, Table A1.1.

m_k Mass of gear k, A1.3.1, eq. (A1.1).

$\hat{m}_k$ Module of gear k, A1.3.1, Table A2.1.

n_{z_k} Gear velocity in r.p.m., A2.1.

p Pressure in the control volume, A2.5, Figure A2.9.

p_{atm} Atmospheric pressure, A2.5.

p_d Pressure in the drainage circle (equal to p_{atm}), A2.5.

p_i Pressure in the tooth space "*i*", A2.5, eq. (A2.41).

p_{in} Pressure in the inlet volume, A2.5, eq. (A2.49).

p_{out} Pressure in the outlet volume, A2.5, eq. (A2.49).

r_{bk} Base radius of gear *k*, A1.3.1, eq. (A1.6).

r_d Radius of the drainage circle, A1.3.3, Table A1.4.

r_{ext} Tip radius, A1.3.1, Table A1.1.

$r_{\inf}$ Minimum radial distance when the contact begins, A2.2, eq. (A2.24).

r_m Radius at half height of the tooth, A2.1, eq. (A2.12).

r_p Radial distance of contact point for tooth flank *p* (*p*=1,2,3,4), A2.2, eq. (A2.23).

r_{root} Root radius, A1.3.1, Table A1.1.

x_k Addendum modification coefficient of gear *k*, A2.2, eq. (A2.23).

t Periodic time $(0 \le t < T)$, A2.2, eq. (A2.24).

v_s Squeeze velocity of the journal bearing, A2.4, eq. (A2.33).

z_k Number of teeth of gear *k*, A1.3.1, eq. (A1.6).

Greek capitals

ΔQ Difference between the volumetric flow rate, coming into a control volume and coming out, A2.5, eq. (A2.39).

∇	Divergence, B1.5.1, eq. (B1.10).
I	Complex intensity vector, B1.5.1, eq. (B1.10).

Lower-case Greek letters

α	Operational pressure angle, A1.3.1, eq. (A1.7).
α_w	Pressure angle in working condition, A1.3.1, Table A1.1.
γ_m	Proportional damping factor for tooth meshing, A2.1, eq. (A2.9).
γ_T	Proportional damping factor for the driving shaft, A2.
ℓ	Lagrangian density, B1.5.1, eq. (B1.10).
δ	Gear material density, A1.3.1, eq. (A1.1).
ρ	Density, B3.2, Table B3.1.
ε	Strain, B2.3, eq. (B2.2).
ε_P	Contact ratio, A2.4, eq. (A2.34).
θ	Rotation angle, A1.3, Figure A1.16.
θ_i	Angular position of the point where the radial clearance must be calculated, A2.5, eq. (A2.42).
θ_0	Rotational coordinate of drive input, A2.1, Figure A2.2.
θ_p	Angular pitch, A2.5.
η	System damping/loss factor, B1.5.1, eq. (B1.1).
η_h	Hysteretic damping, B3.2, Table B3.1.

η_v	Viscous damping, B3.2.
Γ	Eccentricity angle for the shaft position, A2.4, eq. (A2.35).
μ_l	Lubricant dynamic viscosity, A2.1, eq. (A2.12).
σ	Stress, B2.3, eq. (B2.2).
υ	Poisson's coefficient, A2.2, eq. (A2.26).
φ_k	Angular variation around the rigid body position of gear k, A2.1, eq. (A2.13).
$\varphi_{k,vane,q}$	Angular position of the axis of the vane q for the gear k with respect to the X-axis, A2.6, eq. (A2.48).
ω	Angular velocity, A2.5, eq. (A2.39).
ω_k	Angular speed of gear k, A2.1, eq. (A2.13).
ω_{nr}	Natural frequency of r-mode, A3.2, Table A3.1.
ω_{res}	Resonant frequency, B1.5.1, eq. (B1.7).

CONTENTS

PART A

In this first part of the thesis, external gear pumps were considered with the aim of developing advanced methodologies to accurately predict the dynamic behaviour of these components. In fact, it is well known that in the automotive field, as well as in other fields, there is increasing demand for components which produce low noise and vibration levels for comfort reasons. This issue is consequently one of the main problems for automotive component suppliers, who are, thus, forced to increase their knowledge on the dynamic behaviour of their products. Noise and vibration control is not an easy task, as the final comfort result

depends on a number of factors. There are also several ways to address the problem, such as by applying soundproofing or the appropriate application of small amounts of high damping material on mechanical components (see *PART B*) or by modifying the component design. The latter not only requires high costs and time, but also good knowledge of the dynamic behaviour system of the product: to this end, mathematical models can be very useful tools for noise and vibration source identification and design improvement. In fact, a mathematical model makes it possible to study the influence of design and operational parameters as well as manufacturing and mounting defects on machine dynamic behaviour. Moreover, the use of mathematical models permits prediction regarding the effects of design modifications to be made and thus, reduces the number of tests required for design improvement. The development of these kinds of tools requires good system analysis in order to define the most important phenomena to be included in the model, as well as the formulation or modification of theories that allow each element to be described.

Due to the fact that both the above mentioned elements, i.e. money and time availability, are problematical for any company determined to address noise/vibration aspects, in order to, for instance, improve component comfort, the second part of this thesis, *PART B*, will present a new methodology aiming to overcome all the problems and restrictions in current component redesign.

Furthermore, as already discussed above, the need to increase knowledge on the dynamic behaviour of a mechanical system, leads to the formulation of a reliable physical model from which a mathematical model can be obtained. Then, the following step, then, is to integrate the motion equation, and only after such model validation, can the simulation results be used in order to study and analyse the dynamic behaviour of the system. In the flow chart shown below a generic modeling process of a system is presented.

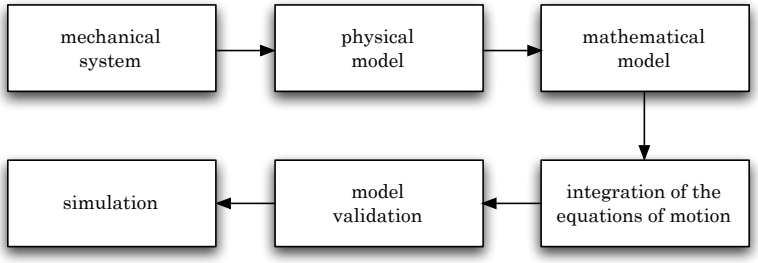

Figure A.1 - Flow chart of the modeling process.

The *physical model* (point 2 in the flow chart) represents an equivalent system to the actual mechanical system under proper hypothesis and has been chosen in order to obtain a rather simple but effective model, according to the analysis objectives. Examples of these hypotheses are:

- distributed characteristics (i.e. density, stiffness, etc) are replaced with lumped characteristics;
- the system behaviour is considered linear;
- system parameters are not time-varying;
- uncertainties are neglected;

The chosen physical model depends on the kind of analysis which has to be performed. For example, in the case of kinematic analysis, the bodies of the system are considered rigid and without mass, whilst in the kineto-static (or kineto-dynamic) analysis, the bodies are considered rigid but their inertia is taken into account; finally, in the kineto-elastodynamic analysis, the model becomes rather complex since in order to study the dynamic behaviour of the system one has to take into account:

- the inertia properties of the bodies;
- body stiffness and damping;
- the clearances between the bodies;
- variability in the parameters as a function of different system configurations.

Clearances allow separation between bodies and foresee possible impact when they join again. During body separation, the dynamic characteristics of the system change and the impact between bodies can excite natural mechanism frequencies. Moreover, clearance value will increase due to wear and therefore, in order to analyse dynamic behaviour with much more precision and foresee mechanism behaviour as a function of the wear parameters, clearances should be taken into account.

Some model parameters can change their values for different configurations, such as the meshing stiffness between teeth which is a function not only of the contact point position along the tooth surface, but also depends on the number of meshing contacts.

Taking into account all the abovementioned elements for kineto-elastodynamic modeling, the physical model becomes highly non linear.

The most frequently used methodologies for studying dynamic mechanisms are:

- the finite element method (FEM)
- the lumped parameter method
- the multibody analysis

The *finite element method* is widely used in the static and dynamic analysis of mechanical component and structures. It allows the system to be studied using a high number of degrees of freedom (DOFs). The limitations of this methodology regard the modeling of non-linear effects such as clearances, and the modelling of different system configurations which lead to an increase in the complexity of the mathematical model to be resolved. For these reasons, the finite element model is mainly used for studying bodies or stand-alone structures.

One of the limitations of the *lumped parameter method* regard the low number of DOFs taken into account; however, there are usually enough to predict the modal behaviour of a real system in the frequency range of interest. One more limitation in this method can be summed up with the following question: what is a correct number of DOFs and where are the lumped

parameters located (mass, spring, damper, etc)? These choices are very important in obtaining a reliable model. On the other hand, the simplicity of modeling the non-linearities, the reduced computational cost for simulation and the possibility of considering different mechanism configurations are the main advantages of this methodology. The dynamic analysis of the pump described in the first part of this thesis was performed by means of a hybrid lumped-parameters/FE model. The LP (lumped-parameters) part is a six degrees of freedom model which takes into account the dynamic behaviour of the moving parts of the pump, while the FE part considers the external pump case in order to calculate the acceleration on the external surfaces of the pump.

The *mathematical model* (point 3 in the flow chart) represents a differential equation in the system deduced from the physical model and describes the dynamic behaviour of the system under study. The system is defined by a set of non-homogeneous second-order differential equation systems thus:

$$[M]\ddot{x} + [C]\dot{x} + [K]x = \bar{F}(t) \tag{A.1}$$

where the matrices $[M]$, $[C]$ and $[K]$ represent the mass, the viscous damping and the stiffness of the system, and $\bar{F}(t)$ are the external forces applied to the system. If the aforementioned matrices are constant, the model is linear whilst, if the matrices C and K are not constant and moreover, the applied forces are not linear, as in our case, the model becomes a non-linear model.

Only in some simple cases can the *solution of the equations of motion* (point 4 in the flow chart) be performed via analytical calculation; on the contrary, usually, the solution is obtained numerically by means of a calculator. In this case, different algorithms (Runge-Kutta, Eulero, etc) were used for solving the equations of motion for the LP part (see *Chapter A2*), with a certain amount of precision at constant steps, as well as variable integration steps. Of course, the solution for the FE part is also

performed numerically, in this case by means of an MSC.Nastran solver [2].

The *model validation* phase (point 5 in the flow chart) aims at achieving a model which yields accurate and reliable predictions of the dynamic behaviour of the mechanical structure (point 1 in the flow chart). The following figure shows the general scheme of a model validation study.

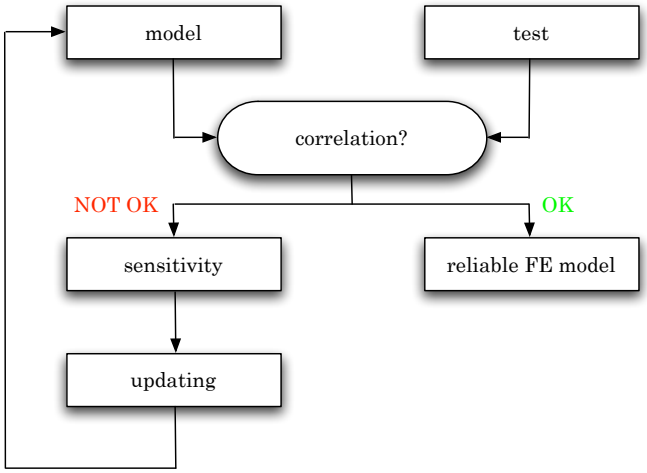

Figure A.2 – General scheme of a model validation study.

The first step is the correlation check, in which the model results are compared with the results from the tests. If correlation is good, the updating process stops here and the model is considered sufficiently reliable for further calculations and predictions. If, as is more likely, correlation is bad, the model must be correlated with an updating procedure in order to improve the correlation with experimental data. A first step in the correction of the analytical model is the selection of the updating parameters. This step, called sensitivity analysis, identifies which parameters of the model are inaccurate and have to be corrected. The selection of the updating parameters is a crucial step for the success of the updating procedure. The final step of the updating

procedure is the correction step. The correction step uses experimental data in order to find new values for the updating parameters. After the updated parameters have been introduced into the model, this model yields, in the case of a successful correction step, analytical model parameters that correlate well with the experimental model data.

In the case which has been studied, a mathematical model of the LP part has been showed (point 6 in the flow chart) in *Chapter B2*. On the other hand, as the FE part of the model is developed in an LMS Virtual.Lab environment (using MSC.Nastran as solver) it allows us to perform dynamic analysis as well as modal analysis, see *Chapter A4*. The FE model uses the results of the lumped parameter model as input in terms of dynamic forces in order to calculate the accelerations on the external surfaces of the pump. Globally, the developed hybrid kineto-elastodynamic model allows an accurate simulation of the dynamic behaviour of the system, making it possible to foresee and diagnose the dynamic effects and/or malfunctions. From a modeling point of view, the system under study is particularly complex due to its high non-linearities; in fact the system parameters, such as meshing stiffness clearances and external forces, change as the relative position of the elements changes. Moreover, the identification of some model parameters has been carried out, starting from experimental analyses like tooth profile measurements as well as modal damping evaluations and measurements of case accelerations and force reactions. These experimental data can be also used in a validation procedure in order to assess the reliability of the model and to verify if all the physical phenomena have been taken into account during the modeling phase.

Finally, an LP/FE model analysis of a gear pump is useful in order to (i) foresee the actual dynamic behaviour (real position of the gears, separations or impacts between meshing teeth, etc), (ii) estimate the trend of the forces acting on the gears and case acceleration as a function of the design parameters, (iii) analyse

the system behaviour in case of different operational conditions and design parameters (increase of the clearances, different profile error shapes, etc.), (iv) optimise the design of the mechanism as a function of its dynamics.

In order to achieve the goals listed above (analysis of the behaviour of the system, evaluation of the dynamic forces, etc.) a hybrid LP/FE model of the gear pump was developed and experimentally assessed. *Chapter A2* and *A3* are devoted to the lumped parameter model whilst in *Chapter A4*, the FE part of the model is fully described and finally the hybrid LP/FE model is validated and used for estimating case accelerations.

In *Chapter A1* the pump under study (namely GENB) is described from a practical and geometrical point of view and some details are provided about all the pump components. Moreover, how these devices function are illustrated. The GENB pump is used in steering systems for automotive applications, and for this reason in the first part of the chapter an overview of the main components of a vehicle steering system is described.

The lumped-parameter model has six degrees of freedom and includes the main important phenomena involved in the pump operation such as time-varying oil pressure distribution on gears, time-varying meshing stiffness and hydrodynamic journal bearing reactions. The model takes into account parametric excitations due to the time-varying meshing stiffness (*Section A2.2*) and tooth profile errors (*Section A2.3*); the effects of the backlash between meshing teeth, lubricant squeeze and the possibility of tooth contact on both lines of action were also included. Oil pressure distribution on gears is also time-varying (*Section A2.5*): it is instantaneously computed and the resultant force and torque are obtained (*Section A2.6*). The non-linear behaviour of the hydrodynamic journal bearings is also included, as well as the torsional stiffness and driving shaft damping (*Section A2.4*). As a consequence, the model is highly non-linear. In order to reduce integration time, the average positions of the journal axes in the bearings were previously estimated. Thus, the variable pressure

force on gears were approximately estimated from the average axis positions, before starting the numerical integration, which brought about an important reduction in integration time (see *Section A2.7*).

The assessment of the model is shown in *Chapter A3* where simulations comparisons and experimental results concerning forces and moments will be shown.

In *Chapter A4* the FE model as well the hybrid LP/FE model are set out. In particular, the FE model regards the external parts of the pump (case and end plates) while the LP model regards the interior parts (bushes and gears). Two analyses were performed using the FE model: a modal analysis with the aim of finding the natural frequencies of the pump under working conditions and a dynamic analysis for the evaluation of the acceleration levels on the external surfaces of the pump (see *Section A4.6*). In this latter analysis, the damping was estimated using data from an experimental modal analysis (EMA) (see *Section A4.7*) while the excitation forces, acting on the internal surface of the case due to bearing reactions and pressure forces, were obtained from the LP model. In this sense, the model is globally a hybrid LP/FE model. The validation of the global hybrid LP/FE model is shown in *Section A4.8*, while *Section A4.9* illustrates its application on the estimation of pump dynamic behaviour in the presence of design modifications. Evaluation of vibrations on the external surfaces is very important for companies and customers since they produce noise and they transfer vibration to the neighbouring structures (e.g. car chassis).

CHAPTER A1

Description of the gear pump

The pump universe [1] includes a wide choice of pumps as depicted in Figure A1.1; in positive displacement pumps (PD) a unit of fluid is trapped between a pumping element that physically moves (displaces) it from the inlet to the outlet. On the other hand, dynamic pumps impart a velocity into the fluid that moves the fluid from the inlet to the outlet. There are many types of PD pumps and these can be subdivided into "*rotary*" and "*reciprocating*" pumps. Rotary pumps will produce a smooth and continuous flow while reciprocating pumps will produce a pulsed flow. The pump studied in this thesis is a rotary positive displacement pump composed of two identical gears, one driven by an electrical motor, which in turn drives the other gear.

Normally three types of gears are found in gear pumps: spur, helical and herringbone. Spur gears are of the most basic design and can easily be identified by their straight teeth, which are parallel to the rotational axis. Instead of being parallel to the axis of rotation, the teeth of helical gears are cut at an angle. This angle formed by the gear teeth and the axis of rotation is called the helix angle.

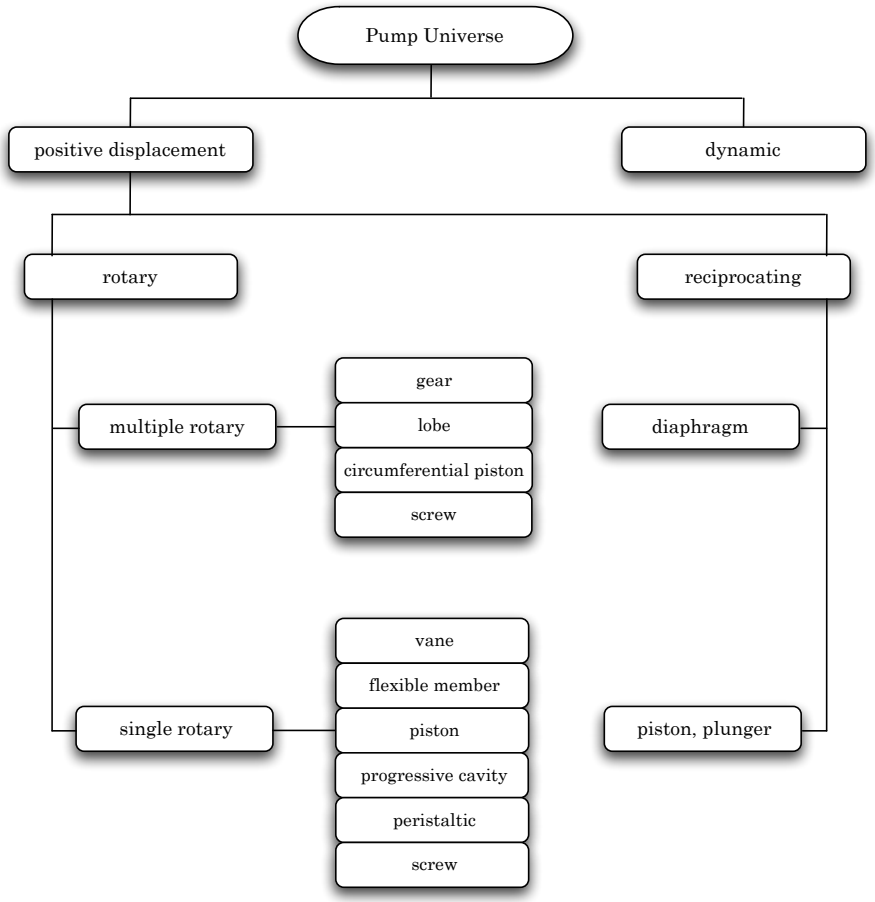

Figure A1.1 – Pump universe.

Helical gears allow the gears to run more smoothly and quietly. Herringbone gears, sometimes called double helical gears, are characterized by two sets of opposite helical teeth. Thus kind

of gears will reduce the shaft load and produce a very quiet running pump. When the pump is operating, the outlet side will be at higher pressure than the inlet side and the fluid will try and find the path of least resistance and "slip" back past the tips and sides of the gears. To prevent this occurrence, dynamic sealing takes place within the pump. This dynamic sealing allows the pumping parts to move, maintaining at the same time a distinct separation between the inlet and outlet. As is depicted by the zones A, B and C presented in Figure A1.2, a gear pump has three such dynamic sealing points. When all the parts are assembled, these dynamic seals will be maintained at any position in the rotation of the gears. However, with any dynamic seal, there must be clearances for the pumping parts to move. These clearances allow fluid to "slip" back through the pump and reduce the efficiency of the pump. The degree of internal slippage in a gear pump determines its volumetric efficiency; the slip increases with the cube of clearance (see for example eq. (A2.41) in *Chapter A2*).

Because of the relationship between slip and clearance in the moving parts, it can be seen that the design and manufacture of a pump with a very close fit is fundamental in achieving pumping efficiency. Fortunately, gears lend themselves very well to precision manufacture. The hobbing of gears is an established manufacturing technique that is used to make precision gears for a wide variety of purposes, not just gear pump. Also moulding is now used to produce precision gears in a variety of composite materials, especially for smaller gear pumps. The external case and end plates can be manufactured to close tolerance not only using standard precision machining techniques, but also employing the latest moulding technology. Whilst the component part tolerances must be minimized, each part can different slightly from a supposed identical part. Added together all of the parts in the pump and these variables combine to produce pumps that have slightly different flow rates per revolution. Consequently, two pumps run at identical speeds may not have identical outputs; however, whatever the outputs is, it will be

consistent and repeatable. This characteristic is most evident on fluid in the viscosity range of 0.1 to 100 cp (centipoise). Above this range, thicker fluids tend to seal the clearances, helping to achieve theoretical flow.

When the outlet pressure of the pump is increased, more fluid will try and slip back through the pump and this decreases the volumetric efficiency, resulting in a reduction of the flow quantity. The tighter the pump, the more efficient it will be and the decrease in flow will be less noticeable at elevated outlet pressures.

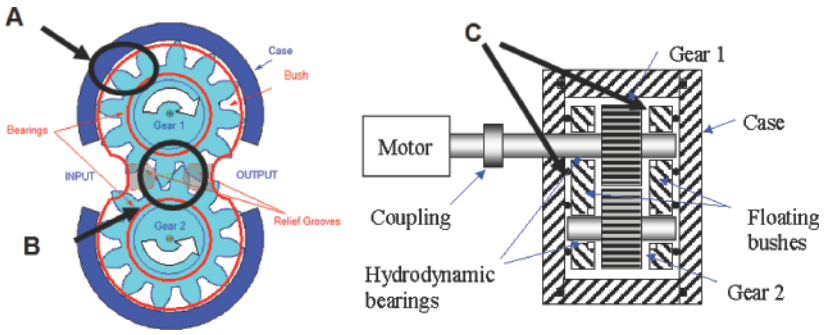

Figure A1.2 – Dynamic sealing points: Point A between the tooth tip and the case, point B in the meshing area and point C in the close mating surfaces of the gears with the bushes.

The pumped fluid can have a significant effect on pump performance. As the fluid viscosity increases, the amount of slip decreases, making the pump more efficient, with flows approaching the theoretical flow rate of the pump. Conversely, as the viscosity decreases, the amount of slip will increase and the flow rate will reduce. Newtonian fluids such as water and oil maintain viscosity under changing conditions whereas, the viscosity of non-Newtonian fluids can change under varying conditions and make the pump performance difficult to predict.

Why would you select an external gear pump versus another

pump type or technology? To help answer this question we need to review its performance characteristic and also some of its disadvantages. A gear pump will deliver a smooth and continuous flow that can be easily adjusted by altering the speed. Moreover, the relationship between pump size and its outlet flow is very good, leading to a very compact design of pump. However, the flow range of external gear pump is low, compared to many other pump types.

In conclusion from the fluid-dynamic point of view, the operation of a gear pump produces a smooth and continuous flow that can easily adjusted by altering the pump speed; the flows are normally very precise and repeatable. The combination of a smooth, variable and precise flow makes the gear pump ideal for steering systems for automotive applications, such as the gear pump studied in this first part of this thesis.

The pump under study is used in steering systems of vehicles. Different kinds of steering systems exist and in the following section their pro and con will be described focusing the attention on the EPHS steering system that uses the TRW pumps; moreover in this chapter an overview of the main components of a steering system are given. In *Sections A1.2* and *A1.3* the pump is described from a geometrical point of view giving some details about all the pump components. In particular the design parameters of the bushes, case, gears, relief grooves are described, as this is useful for the model description in the following chapters.

A1.1 The steering systems

In the last ten years, there is been an increasing demand for steering systems in Europe, Asia, but in particular Japan. Looking at the automotive reviews, it is extraordinary to find cars without the steering system already embedded. The reasons of

such a great spread have to be looked for both in the competition existing in the automotive field, aiming at increasing comfort and security, and in three more important elements that are due to expansion of steering technology towards utility passenger cars:

- the cost reduction of the steering systems;
- the increase of the performance and reliability of the steering systems;
- the reduction in power during operational condition of the system.

Furthermore, the more relevant aspects in the design of a steering system are:

- car drivability: the system must have the capacity of reducing the effort applied to the steering wheel without losing the feeling between driver and road. In fact, a regulation fixes the maximum effort (that has to be lower than 250[N]) applied to the steering wheel for describing a 24 [m] diameter circle at 10 [km/h] of speed in 4 seconds.
- security: the driver must control car stability in case of failure of the steering system also.
- reliability of the system.

Nowadays, four different steering systems exist:

- *Conventional*: the pump of the steering system is directly connected to the engine by means of a belt. This way, the velocity of the pump is constant and independent of the actual requirement; the oil flow in the pump is continuous.
- *EPHS, Electrically Powered Hydraulic Steering*: an electrical motor drives the pump; the pump velocity (rpm) and the delivered oil flow strictly depend on the kind of swerve. In fact, the electrical motor works at low speed (stand-by) if no power for swerving is needed, with a consequent energy saving. Such a system needs

500[W] for working compared to 1000[W] for the conventional one.

- *Closed centre*: a pump (or a compressor), driven by an electrical motor, raises the pressure of a reservoir to a fixed limit.
- *Electrical steering system*: In this system no pump is needed, but it is an electrical motor that directly controls the steering wheel. This system is used in some utility passenger cars.

The major energy saving, because the system works only when necessary, the simple change of the system parameters in order to obtain the best performance as a function of the typology of car (city car, family car, sport car, etc), the simplicity in the system assembly with the possibility of finding the best location in the car, the reduction of the temperature reached by the operational oil and the simple replacement of system components in case of failure, are the advantages of the EPHS system and are the reasons for which this kind of system is the most widespread steering system.

A1.1.1 The E.P.H.S. system

The TRW pumps are used in the EPHS systems; a scheme of this system is represented in Figure A1.3. The system is controlled by means of an electrical central unit (ECU) that acquires the data coming from the engine, from the steering wheel (by the steering rate sensor depicted in Figure A1.3 and Figure A1.4) and from the tachymeter also. In fact, the central unit is able to determine the correct velocity of the electrical motor that drives the pump as a function of the vehicle speed, swiftness and degree of the swerve.

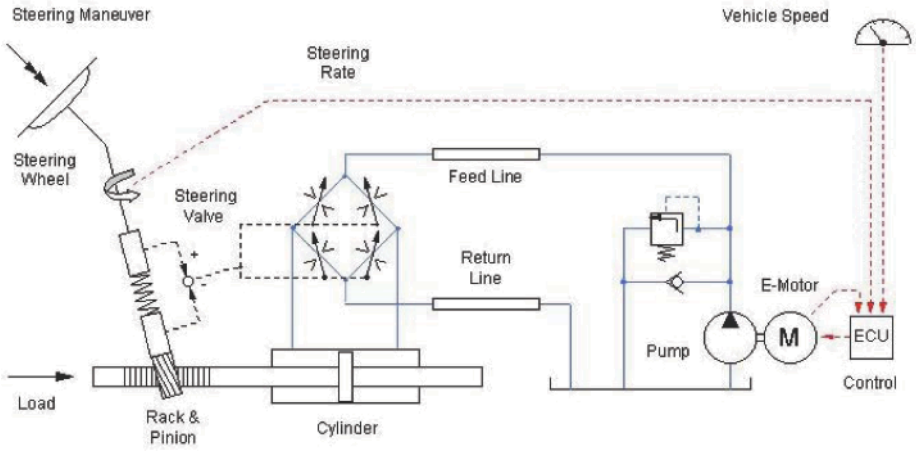

Figure A1.3 – Schematic diagram of the E.P.H.S. system.

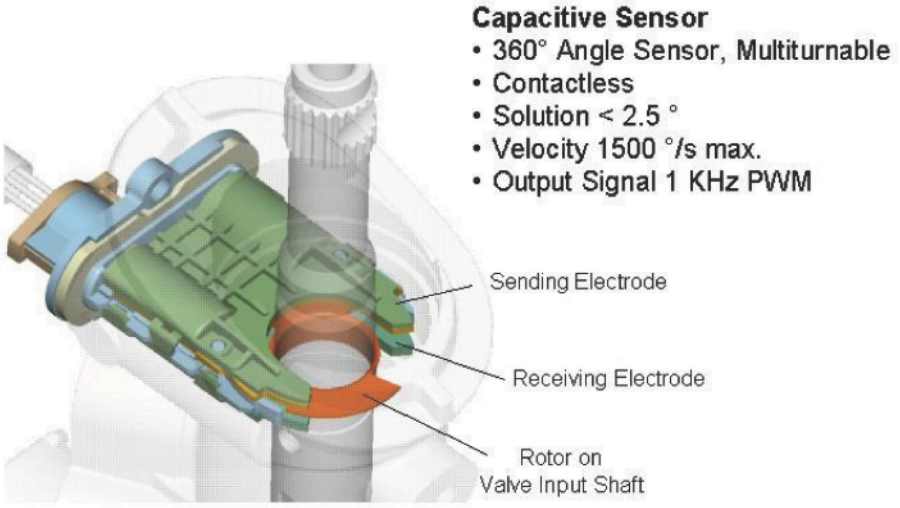

Figure A1.4 – Steering rate sensor.

The flow rate and the oil pressures are controlled by the steering valve housed in the pinion (see Figure A1.5); the valve is connected to the two chambers of an oleo-dynamic actuator

(cylinder) that is itself connected to the rack. The piston in the cylinder, moved by the oil under pressure, will help the movement of the rack in the desired direction (left or right in Figure A1.3).

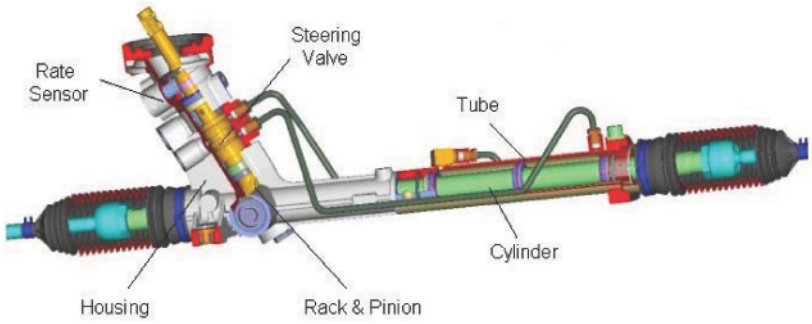

Figure A1.5 – Components of the dynamic circuit in the EPHS system.

The outlet pressure ranges from 100 bar, in case of maximum degree of swerve and zero vehicle speed, to 3.5 bar when the vehicle drives on a straight road. Figure A1.6 shows the locations of gear pump, electrical motor and steering gear when assembled in the front of the vehicle.

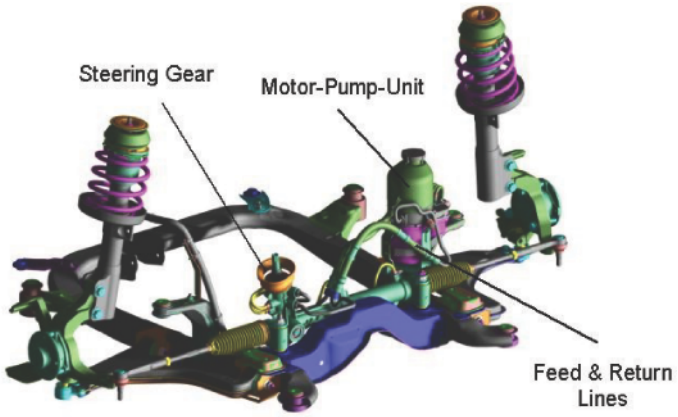

Figure A1.6 – EPHS system when assembled in the front of the vehicle.

The gear pump is driven by an electrical motor with 500 [W] power, 14 poles and working in direct current (DC). On the left side of Figure A1.7 is shown an exploded drawing of the electrical

motor.

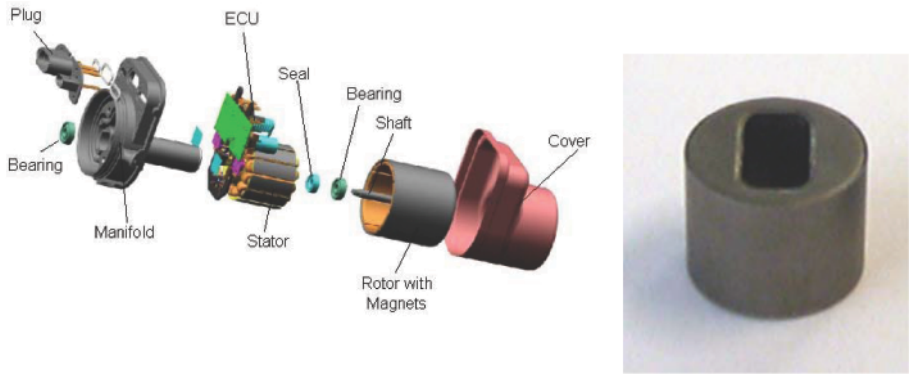

Figure A1.7 – Exploded drawing of the electrical motor that drives the gear pump and Oldham joint (right).

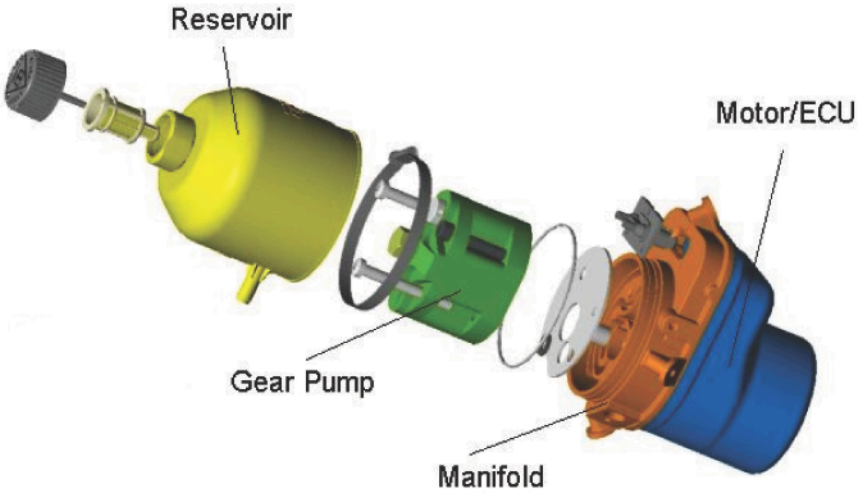

Figure A1.8 – Exploded drawing of the motor-pump unit.

The pump intakes the oil from the reservoir (Figure A1.8) by means of the manifold (see Figure A1.7 and Figure A1.8) that is embedded in the electrical motor. The complex ducts inside the manifold aims at reducing the pressure fluctuation due to the pressure variation in the inlet chamber of the pump in operational condition. As shown in Figure A1.9, in the manifold is

the oil circuit carrying the oil from the reservoir to the gears and the outlet hole carrying the oil under pressure to the hydraulic circuit and then to the cylinder (Figure A1.3). Finally, an Oldham joint (see the right side of Figure A1.7) connects the electrical motor to the pump.

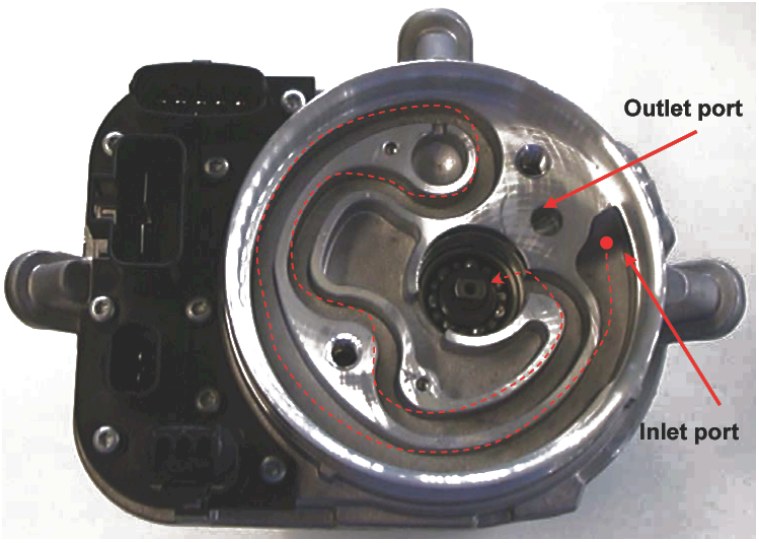

Figure A1.9 – Photo of the manifold.

A1.2 Pump description

External gear pumps are popular pumping components well suited for handling viscous fluids such as fuel and lubricating oils. They are simple and robust devices that can work in a wide range of pressures and rotational speed providing at the same time a high reliability. Their main applications can be found as lubrication pumps in machine tools, as oil pumps in engines or in fluid power transfer units. Depending on the application, several designs are available, nevertheless the most usual configuration

uses twin gears, which are assembled by a couple of lateral floating bushes acting as seals for the lateral ends. Figure A1.10.a shows an exploded drawing where the main pump components are identified. In Figure A1.10.b a scheme highlighting the clearances between the core elements of the pump is presented.

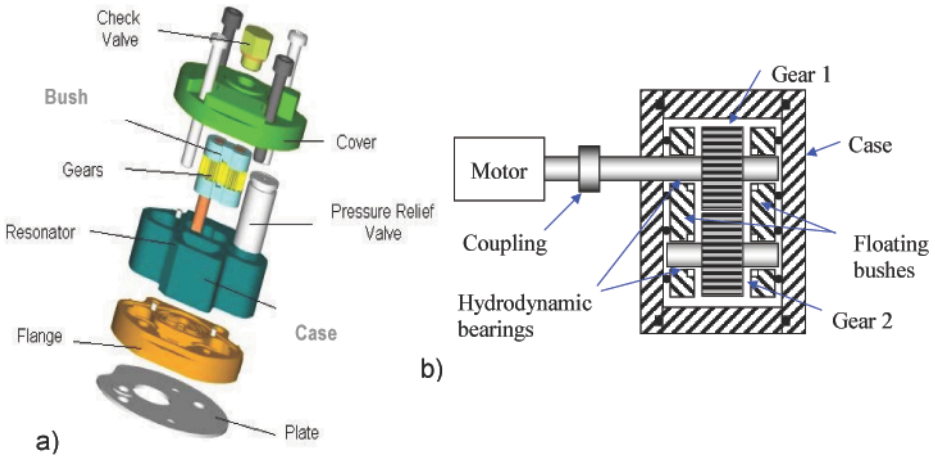

Figure A1.10 – (a) Exploded drawing and (b) scheme of the gear pump.

Gears and floating bushes are packed jointly inside a case that encloses both components and defines the isolated spaces carrying the fluid from the low to the high-pressure chamber. Moreover, the case houses the pressure relief valve and the two more empty spaces (see Figure 1.11.a), called resonators, aim at reducing the pressure fluctuation due to the not constant outlet pressure. The lateral floating bushes act as supports for gear shafts by means of two hydrodynamic bearings which are hydraulically balanced in order to avoid misalignments between gear shaft and journal bearing (see Figure A1.11.a). The fluid that fills the space bounded by the case and two successive gear teeth becomes isolated at the input port and is carried out towards the output port (from left to the right in Figure A1.11.b). This way, the isolated volume increases its pressure progressively until arriving at the high-pressure chamber. When gear teeth mesh,

there will be a trapped volume between gears that suffers a sudden volume reduction. This fact supposes a violent change in the pressure of the trapped volume. To avoid this, the trapped volume must be connected to the high or low-pressure chambers. That is the role of the relief grooves milled in the internal face of lateral bushes whose shape and location are so important in the resulting dynamic behaviour (Figure A1.12). Due to manufacturing tolerances, it is not possible to completely eliminate the pressure rise but its effect can be strongly reduced with an accurate design. Furthermore, lateral bushes should be also hydraulically balanced in axial direction with the aim of avoiding misalignments between gear shafts and journal bearings. To achieve that, a rubber seal located in the external face of the endplates (flange and cover) is used. This seal defines two areas on the external surface of the lateral bushes subjected to high or low pressure; such a pressure should balance the pressure exerted in the opposite face (internal surface) by the pressure of the isolated spaces.

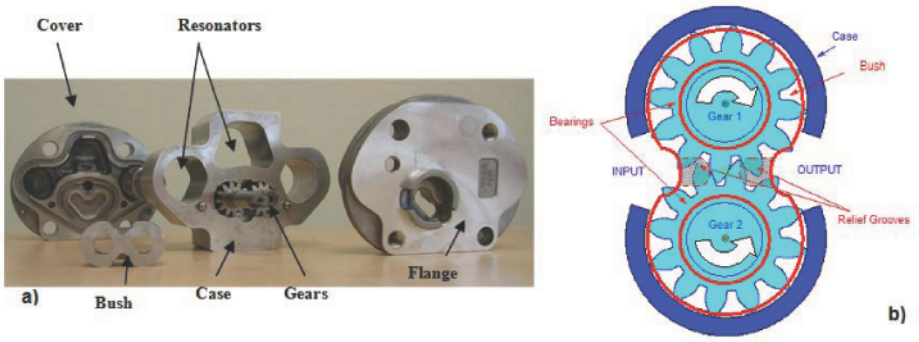

Figure A1.11 – (a) Enlarged photo and (b) detail of floating bushes and relief grooves.

Finally, the flange (Figure A1.13) and the cover (Figure A1.14) enclose the entire pump components above described. In particular, the flange connects the pump to the manifold and the cover houses the check valve and the relief valve. The check valve

is mounted in the pump for safety reasons; in fact, it allows the steering wheel to work also in case of failure of the electrical motor. On the other hand, the relief valve discharges the oil under pressure into the reservoir when the pressure exceeds a threshold value (for the pump under study the threshold value is 100 bar) in order to avoid damage to the mechanical components.

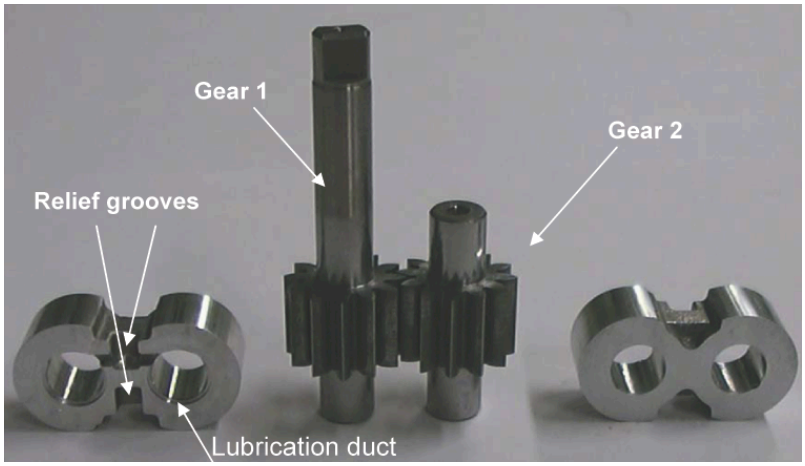

Figure A1.12 – Gears and bushes.

Power is applied to the shaft of one gear (gear 1, see Figure A1.12), which transmits it to the driven gear (gear 2) through their meshing. Gear 1 is connected by an Oldham coupling to an electrical drive allowing some misalignment between them. That is necessary because the driving gear shaft centre is moving with respect to the lateral bushes describing an orbit around a center that will depend on the working pressure and speed. In the considered case, the pump has twin spur gears with 12 teeth, pressure angle of 20 degrees, module of 1.15 mm and width of 12.1 mm. The operational pressure ranges from 3.5 to 100 bar and the angular speed from 1500 to 3400 rpm.

From the dynamic behaviour point of view, this type of pump presents two different excitations: the first excitation is due to the transmission error and time-varying meshing stiffness, the other

is related to the pressure distribution of the oil into the tooth spaces. Both of those excitations have the same fundamental frequency equal to the meshing frequency.

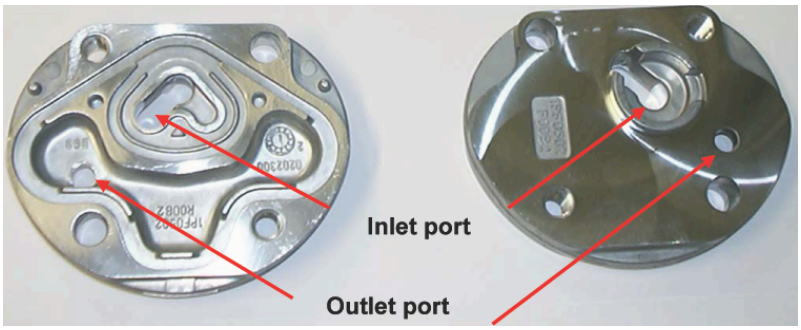

Figure A1.13 – Flange: internal (left) and external side (right).

Figure A1.14 – Cover: internal (left) and external side (right).

A1.3 Design parameters of the GENB gear pump

Before starting with the introduction of the LP model in the following chapter and with the introduction and description of the foremost section of this thesis part (see *Chapter A4*), i.e. the creation and study of the FE model identified with the coupled system (all the components of the gear pump), it is useful defining the geometry of the gear pump and the reference frames used. The displacement of the gears and of the bushes in axial direction

(i.e. the extrusion direction of the case) has been neglected as well as the pressure variation in axial direction. Therefore, the geometry taken into account is a plane geometry orthogonal to the extrusion direction of the case (see Figure A1.15).

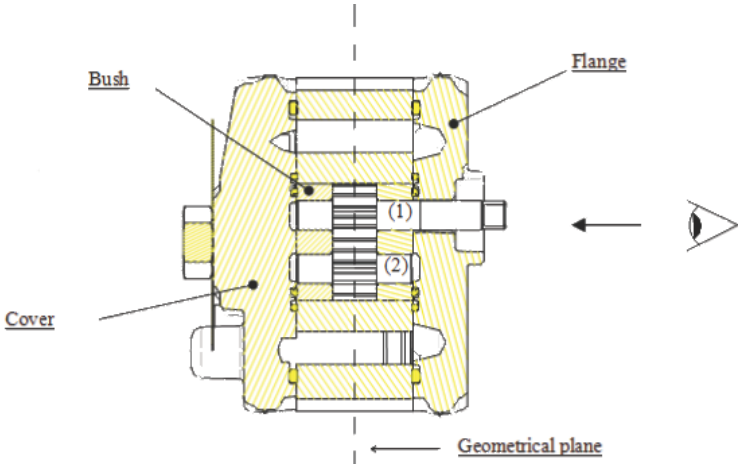

Figure A1.15 – Observation point of the geometry.

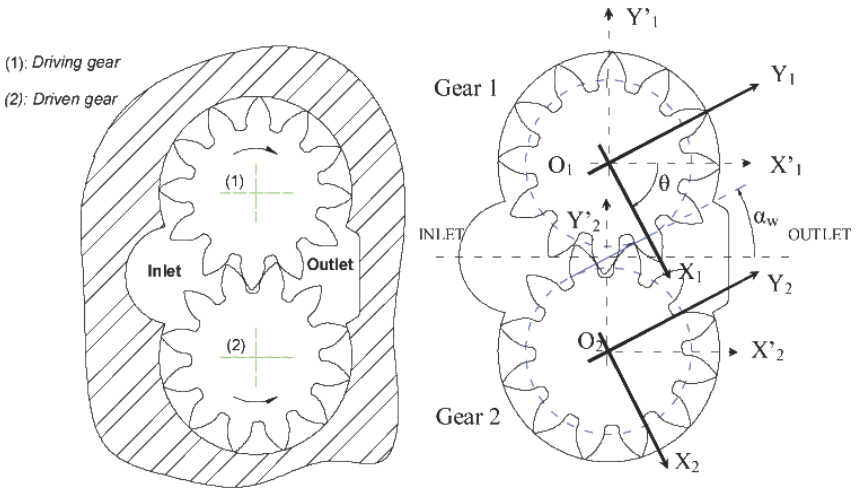

Figure A1.16 – Pump view in the geometrical plane (left) and reference frames of the gears (right).

The case is considered fix while the two gears and the bushes can move with respect to its. The observation point of the geometry is in the side of the flange, as shown on the right side of Figure A1.15, therefore the driving gear (gear 1) becomes depicted above the driven gear (gear 2), see Figure A1.16. Two difference reference frames for each gear are used (see Figure A1.16), both having their origins coincident with the centers of the gears; in reference frames $O_1X_1Y_1$ and $O_2X_2Y_2$, the X-axis is perpendicular to one of the lines of action and the Y-axis is parallel. On the other hand, in the reference frames $O_1X_1'Y_1'$ and $O_2X_2'Y_2'$, the Y'-axis is along the line connecting the centers of the gears and the X'-axis are orthogonal.

A1.3.1 Gear geometry

In the following subsections, the dimensions of both gears will be detailed with reference to the TRW pump manufactured at the present time, namely GENB. The geometrical dimensions and inertia properties of gear 1 (see Figure A1.17) are listed in the Table A1.1. It can be noted that mass, polar moment and torsional stiffness of gear 1 are obtained by the following expressions:

$$m_1 = \delta \cdot \pi \cdot \left(b_1 \cdot R_1^2 + R_s^2 \cdot \left(L1_1 + L1_2 \right) \right) \tag{A1.1}$$

$$J_1 = \frac{\delta \cdot \pi}{2} \cdot \left(b_1 \cdot R_1^4 + \frac{1}{3} \cdot R_s^4 \cdot L1_1 + R_s^4 \cdot L1_2 \right) \tag{A1.2}$$

$$K_T = \frac{G \cdot \pi \cdot R_s^4}{2 \cdot L1_1} \tag{A1.3}$$

Symbols and value	Description
$z_1 = 12$	Number of teeth
$\hat{m}_1 = 1.150$	Gear module [mm]
$\beta_1 = 0$	Helical angle (spur gear)
$b_1 = 12.1$	Gear thickness [mm]
$\alpha_1 = 20$	Pressure angle [deg]
$\alpha_{w1} = 27.727$	Pressure angle in working condition [deg]
$r_{b,1} = 6.484$	Base radius
$x_1 = **$	Addendum modification coefficient [mm] (not divulged)
$r_{ext,1} = 17.270/2$	Tip radius [mm]
$r_{root,1} = 11.478/2$	Root radius [mm]
$l_{t,1} = 0.249$	Tooth tip thickness [mm]
$L1_1 = 39.5$	Longer dimension length of the driving shaft [mm]
$L2_1 = 9.5$	Shorter dimension length of the driving shaft [mm]
$m_1 = 0.0404$	Mass of gear 1 [kg]
$R_{s,1} = 4$	Radius of the shaft [mm]
$J_1 = 4.2596e-007$	Polar moment of gear 1 $[kg \cdot m^2]$
$G = 7.91x10^{10}$	Shear modulus $[N/m^2]$
$K_T = 5.5x10^2$	Torsional stiffness of the driving shaft $[kg \cdot m^2]$

Table A1.1 – Gear 1 properties and dimensions.

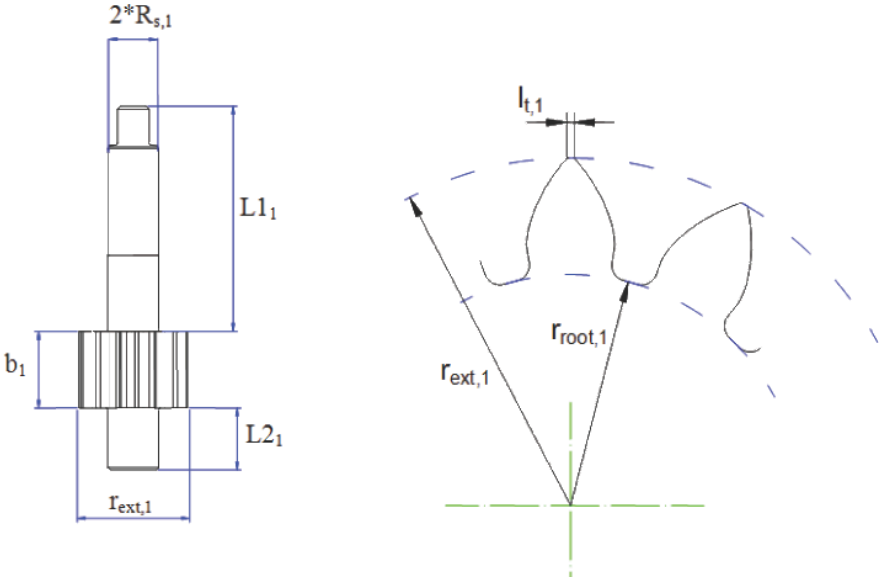

Figure A1.17 – Gear 1 geometry.

The geometrical dimensions and inertia properties of gear 2 (see Figure A1.18) are listed in the Table A1.2.

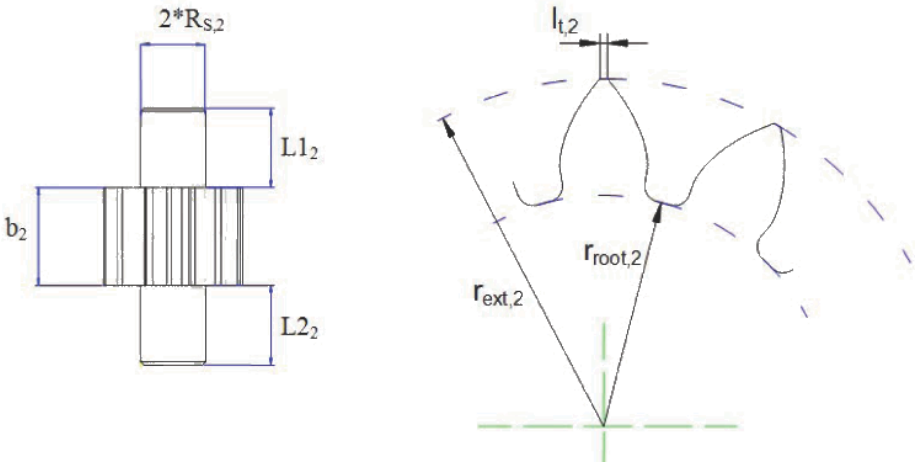

Figure A1.18 – Gear 2 geometry.

Symbols and value	Description
$z_2 = z_1 = z = 12$	Number of teeth
$\hat{m}_2 = \hat{m}_1 = \hat{m} = 1.150$	Gear module [mm]
$\beta_2 = \beta_1 = \beta = 0$	Helical angle (spur gear)
$b_2 = b_1 = b = 12.1$	Gear thickness [mm]
$\alpha_2 = \alpha_1 = \alpha = 20$	Pressure angle [deg]
$\alpha_{w2} = \alpha_{w1} = \alpha_w = 27.727$	Pressure angle in working condition [deg]
$r_{b,2} = r_{b,1} = r_b = 6.484$	Base radius
$x_2 = x_1$	Addendum modification coefficient [mm] (not divulged)
$r_{ext,2} = r_{ext,1} = r_{ext} = 17.270/2$	Tip radius [mm]
$r_{root,2} = r_{root,1} = r_{root} = 11.478/2$	Root radius [mm]
$l_{t,2} = 0.249$	Tooth tip thickness [mm]
$L1_2 = 9.5$	Longer dimension length of the driving shaft [mm]
$L2_2 = 9.5$	Shorter dimension length of the driving shaft [mm]
$m_2 = 0.0216$	Mass of gear 2 [kg]
$R_{s,2} = R_{s,1} = R_s = 4$	Radius of the shaft [mm]
$J_2 = 3.9564e-007$	Polar moment of gear 2 [$kg \cdot m^2$]

Table A1.2 – Gear 2 properties and dimensions.

It can be noted that mass and polar moment of gear 2 are obtained by the following expressions:

$$m_2 = \delta \cdot \pi \cdot \left(b_2 \cdot R_{p2}^2 + R_s^2 \cdot \left(L2_1 + L2_2 \right) \right) \tag{A1.4}$$

$$J_2 = \frac{\delta \cdot \pi}{2} \cdot \left(b_2 \cdot R_{p2}^4 + R_s^4 \cdot L2_1 + R_s^4 \cdot L2_2 \right) \tag{A1.5}$$

Another quantity that will be used in the following is the base pitch; the base pitch P_b is the distance between two consecutive teeth measured on the base circle of the gear and equals to the distance between the contact points of two meshing tooth pairs (see Figure A1.19):

$$P_b = \frac{2 \cdot \pi \cdot r_b}{z} \tag{A1.6}$$

where z is the number of teeth and r_b the base radius. The relation between the pitch measured on the base circle (P_b) and on the pitch circle (P_p, namely circular pitch) is:

$$P_b = P_p \cdot \cos(\alpha) \tag{A1.7}$$

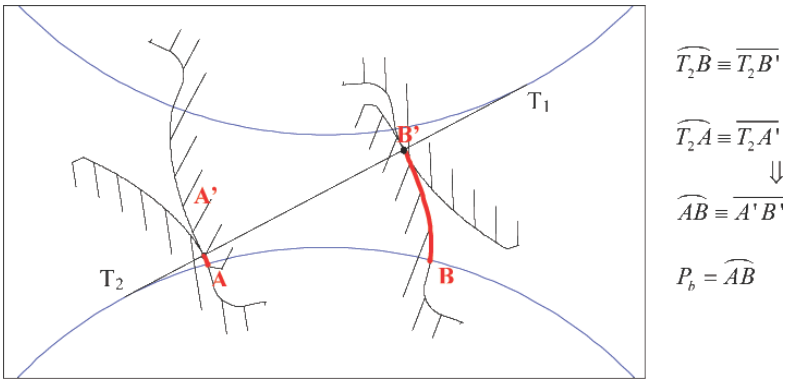

Figure A1.19 – Position of the gears when two tooth pairs are meshing.

A1.3.2 Pump case

Figure A1.20 detail the angles defining the beginning and ending of the isolated vanes, see Table A1.3. It can be noted that the nominal internal radius of the pump case equal the tip radius of the gears ($r_{ext,1}$, $r_{ext,2}$), however, taking into account the relative

geometrical tolerances, a clearance is always present between the two components.

Symbols and value	Description
$\Phi_{A1}, \Phi_{A2} = 339{,}68°$	Angles defining the ending of the isolated vanes for gear 1 and 2, respectively [deg]
$\Phi_{B1}, \Phi_{B2} = 200{,}32°$	Angles defining the beginning of the isolated vanes for gear 1 and 2, respectively [deg]

Table A1.3 – Angles defining the beginning and ending of the isolated vanes.

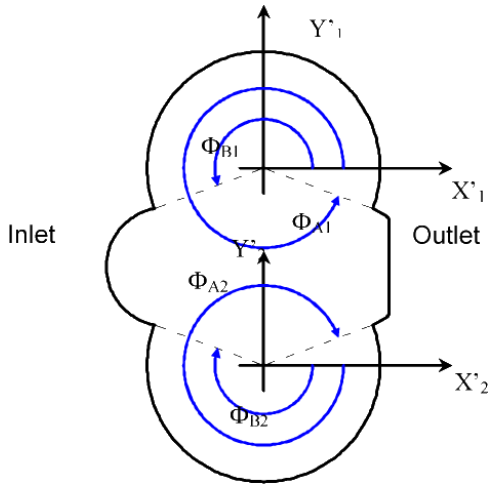

Figure A1.20 – Geometry of the pump case.

A1.3.3 Bush geometry

As mentioned before, the two gears, already described in the previous sections are assembled by a couple of lateral floating bushes acting as seals for the lateral ends, see Figure A1.10.a.

Figure A1.21 shows the geometry of the bush while all its design parameters are listed in the Table A1.4.

Symbols and value	Description
$R_b = 4$	Bearing radius [mm]
$r_{ext,b} = 17,20 / 2$	External radius of the bush (equal to the tip radius of the gears) [mm]
$r_d = 4,5$	Radius of the drainage circle [mm]
$a = 14,65$	Centre distance of gear pair [mm]
$b_b = 9,5$	Bush thickness [mm]

Table A1.4 – Bush design parameters.

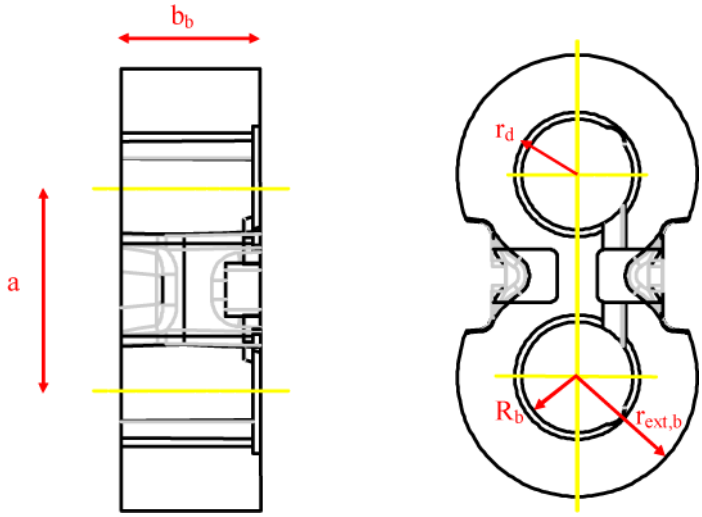

Figure A1.21 – Bush geometry.

In Figure A1.22 is shown the characteristic dimensions of the relief grooves milled in the bush.

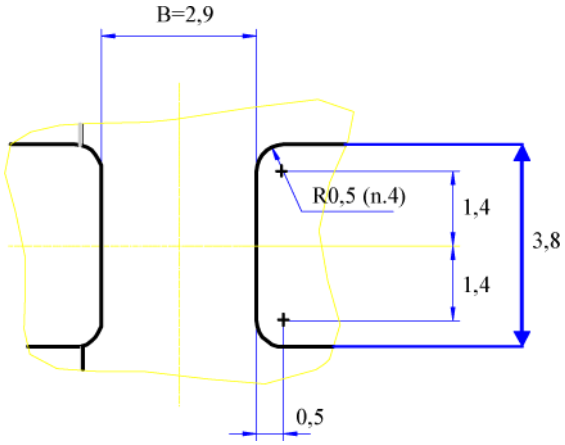

Figure A1.22 – Characteristic dimensions in [mm] of the relief grooves milled in the bush.

CHAPTER A2

The lumped-parameter kineto-elastodynamic model

This work concerns external gear pumps for automotive applications, which operate at high speed and low pressure. In this situation gear pumps have two main noise sources both of them sharing the same fundamental frequency: fluid borne noise, as a consequence of the flow from the low to the high pressure chamber (see Figure A2.1), and mechanical noise due to the gear meshing. Due to the complex nature and the combination of both excitation sources, design is a difficult task requiring a great number of experimental tests. This fact increases the interest in developing a model that simultaneously includes pressure and gear meshing effects. Gears are known to be one of the major

vibro-acoustic sources in rotating machineries and the prediction and control of gear vibrations is becoming particularly important in automotive, aerospace, and power generation industries.

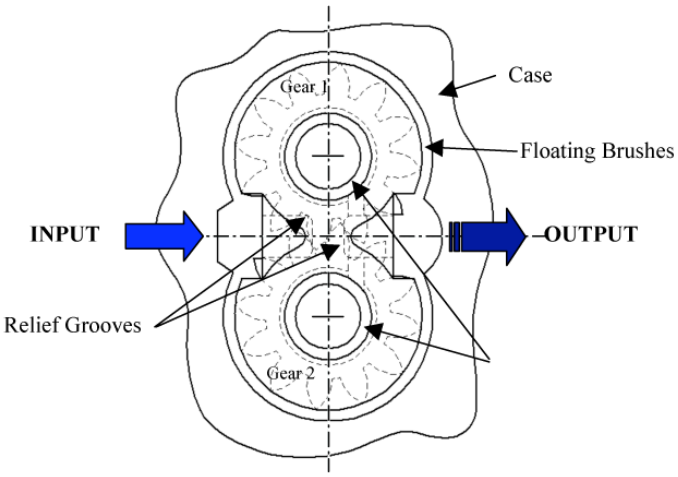

Figure A2.1 – Schematic representation of the fluid flow into the gear pump.

The dynamic behaviour of gear pairs for design and for noise and vibration reduction is a topic that has received the attention of several researchers: the majority of the simulations to date are based on rigid-body lumped parameter models with the meshing teeth assimilated to lumped stiffnesses. References [4-6] contain a good description of the mathematical models used to simulate this kind of transmission device. In our case we use the gear pair for a different objective that is the fluid movement. Nevertheless the system under study is a gear pair and its behaviour will be defined by its characteristics. The experimental results available seem to underline that the main source of noise excitation is related to the gear meshing frequency and its harmonics. This result must be taken with caution because hydraulic noise will also have the same principal frequency. The models found in literature extend from the more simple that only consider the torsional movement [7-9] to the spatial models that consider several additional degrees of freedom taking into account the

influence of case and bearings [10-13]. The simulation of the dynamic behaviour of a speed-increase gearbox was also carried out using FE methods [14], in particular a 3D contact FE model is used to model the time variable meshing stiffness of the gears and using tetrahedral solid elements to model the gearbox housing.

One of the main characteristics of the gear dynamics behaviour is the parametric excitation due to the change in the number of meshing teeth. This situation yields to a variable stiffness that increases the complexity of the analysis. Some works have analysed this problem analytically [15-16] and also numerically [17-19] with the objective of providing some simple expressions that describe the stiffness variation as a function of the gear pair contact position. The other important characteristic that governs the gear transmission response is the so-called transmission error both static as well as dynamic; the transmission error is defined as the difference between the actual and ideal position of the gears. Some authors focus their attention in the contact problem introducing the transmission error in the dynamic equations and solving the two problems at the same time [20-21], thus taking into account both the variable stiffness and transmission error.

The majority of works focus on spur gears but there are also models for helical gears. These are more complex due to the introduction of the helical angle in the model [22-24]. The non-linear behaviour caused by the backlash between teeth and into the journal bearings that could lead to a tooth separation has been studied in several works [24-25]. This situation is especially important in the case of gears working with reduced loads.

Apart from this research activity [27-30], works that only deal with the dynamic behaviour of gear pairs for design and NVH reduction [4-16], as well as the pressure evolution in a gear vane during the pump rotation [26] and the oil bearing behaviour [31-32] were found in literature, but these effects have been shown and discussed separately; conversely in the case of gear pumps all these important effects have to be considered in the

same model in order to take their interactions into account.

The developed LP model has six degrees of freedom and includes the main important phenomena involved in the pump operation as time-varying meshing stiffness, the time-varying oil pressure distribution on gears and hydrodynamic journal bearing reactions. Although below are quickly introduced these different aspects, the following sections will deal with their description in a more extended version, anyway describing them in a non detailed manner; this due to the fact that although the main point of this first part of the thesis is the creation of the FE model is also necessary to introduce the LP model. As already mentioned, the final result will be the generation of the hybrid model LP/FE. In particular, the steps and considerations that will be exhibited and explained not thoroughly in the following sections of this chapter will provide important informations relating to the real pump model, which in turns will be introduced in the form of data and assumptions in the creations stages of the gear pump FE model generated through the software LMS.VirtualLab.

The *meshing phenomena* have been well developed. In fact, this type of gears works at low load and consequently the effects of tooth profile errors and tooth separation could not be ignored. The model takes into account the parametric excitations due to the *time-varying meshing stiffness* (*Section A2.2*) and to the *tooth profile errors* (*Section A2.3*); the effects of the backlash between meshing teeth, the lubricant squeeze and the possibility of tooth contact on both lines of action were also included in the model. In the following will be only considered the spur gear case. Nevertheless the helical gear case is considered and addressed in [34].

To estimate pressure forces and torques (*Section A2.6*), model calculates *pressure distribution* and its variation during the rotation of the gears (*Section A2.5*); the model uses the formulation in [26], taking into account the displacement of the lateral floating bushes, the wear caused by the gears at the case during the run in process and the modeling of phenomena bound

to relief grooves that separate low-pressure camera to high-pressure camera. For the sake of simplicity these contributions are not exposed here in detail. More details about them can be found in [30][34]. However, as stated in *Chapter A1* for the latter contribution, i.e. relief grooves (see Figure A2.1), when two tooth pairs are in contact, a trapped volume between the two pairs of contact teeth is born. As the gear 1 turns, this trapped volume will have a reduction and as consequence the pressure rises. To avoid the closure of this trapped volume causing a rise in pressure, the relief grooves have been made with a breadth apt to evade the closure of the volume; thus, the trapped volume is always put in communication with low-pressure camera or high-pressure camera. Pressure transition from the high to the low-pressure regions was taken as linear.

The non-linear behaviour of the *hydrodynamic journal bearings* [31-32] is included (*Section A2.4*). The formulation proposed by Childs et al. [33], called "finite impedance formulation" is used. Briefly, this formulation consists of taking into account and composing the results gotten from the theories "short bearing" and "long bearing".

As a consequence, the model is highly non-linear. The non-linear differential equations of motion are numerically integrated in Simulink® environment (subject not treated here). With the aim to reduce the integration time, the average positions of the journal axes into the bearings are previously estimated (*Section A2.7*). For this calculation the periodically variable model parameters are set to constant values – equal to their mean values – and the "stationary" axis positions are computed as the solution of a non-linear system of algebraic equations. Thus, the variable pressure forces on gears can be approximately estimated from these average axis positions, before starting the numerical integration, obtaining an important reduction of the integration time. It was verified that this approach gives accurate results, see reference [30][34] and *Chapter A3*.

In order to build a simple model several assumptions were

made:

- Lateral floating bushes were taken as fix and parallel to the gear lateral sides, determining lateral clearances of constant height.
- Only one kind of gear is considered: the spur gear. Therefore assumption of a planar model was acceptable because of the reduced axial forces.
- Gear disks are assumed as rigid and the contact stiffness will be due to the tooth flexibility and Hertzian deformation.

Thus, the model is a plane model with 6 degrees of freedom ($x_1, y_1, \theta_1, x_2, y_2, \theta_2$) as presented in Figure A2.2. In order to develop the dynamic equations two reference frames are used, one for each gear (see *Chapter A1*, Figure A1.16). These reference frames will have their origins coincident with the centers of the gears. The X-axis is perpendicular to one of the lines of action and the Y-axis is parallel. For each gear, degrees of freedom are the displacements along the directions X and Y and the angular displacement: coordinates x_1, y_1, θ_1 are relative to gear 1 (driving), while coordinates x_2, y_2, θ_2 are relative to gear 2 (driven). The known model input is the coordinate θ_0, representing the angular displacement of the electrical drive, assumed to rotate at constant speed. Coordinate θ_0 is connected to θ_1 (gear 1) by a torsional spring-damper element that represents the dynamic behaviour of the shaft. The shaft torsional stiffness is indicated as K_T and the proportional damping as C_T ($C_T = \gamma_T \cdot K_T$).

A2.1 Gear meshing

The model [27-30,34] takes into account the possibility of tooth contact or separation on both lines of action. Figure A2.2b

shows the DLA and ILA blocks that represent gear meshing; their content is shown in Figure A2.3. Be *direct line of action* (*DLA*) the contact line where the force from gear 1 to gear 2 causes a momentum in agreement with the direction of rotation, and be *inverse line of action* (*ILA*) the contact line where the force from gear 1 to gear 2 causes a momentum in the opposite direction of rotation. The gears used are low contact ratio gears ($\varepsilon \cong 1.4$), so in each line of action there will be one or two meshing tooth pairs. To consider this situation, every one of the four possible pairs of teeth in contact is associated to a stiffness (K_a, K_b, K_c, K_d) and to a damper (C_a, C_b, C_c, C_d). This damper globally takes the structural damping as well as other damping into account. The damper coefficient is taken proportional to the corresponding stiffness if teeth are in contact; when there is tooth separation the damper coefficient is computed in order to represent the lubricant squeeze effect. The error functions E_a, E_b, E_c, E_d are the displacement excitations representing the relative gear errors of the meshing teeth; when two pairs of teeth come into contact there will be two separate error functions, each acting on a different spring and damper (see *Section A2.2*).

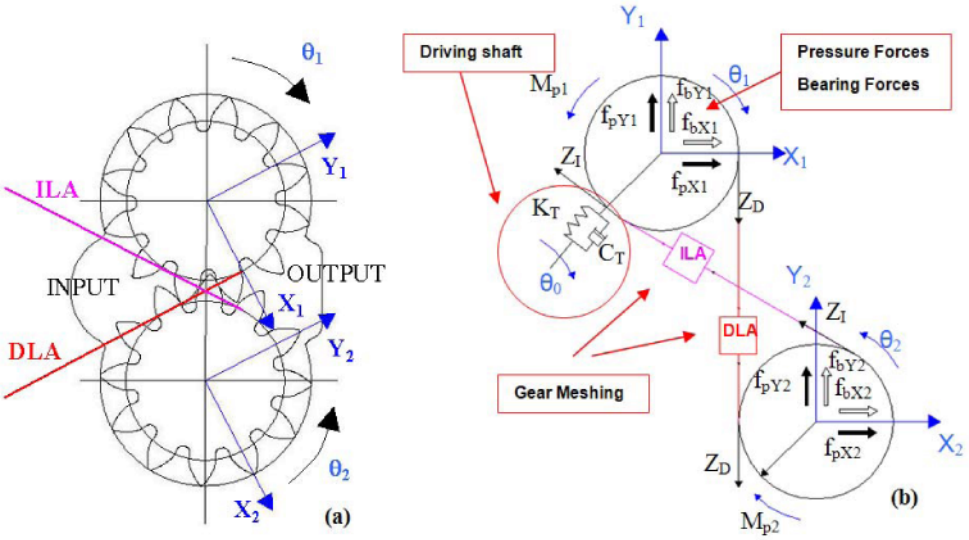

Figure A2.2 – (a) Reference frames and (b) scheme of the model.

As can be clearly noted by the Figure A2.2 and Figure A2.3, quantities with subscripts *a* and *b* are related to the pairs of teeth along the *DLA* while *c* and *d* to the pairs of teeth along the *ILA*. Moreover the backlash *g* along the line of action is considered; it is obtained by Wildhaber measurements. The following quantities are introduced taking as reference Figure A2.2 and Figure A2.3.

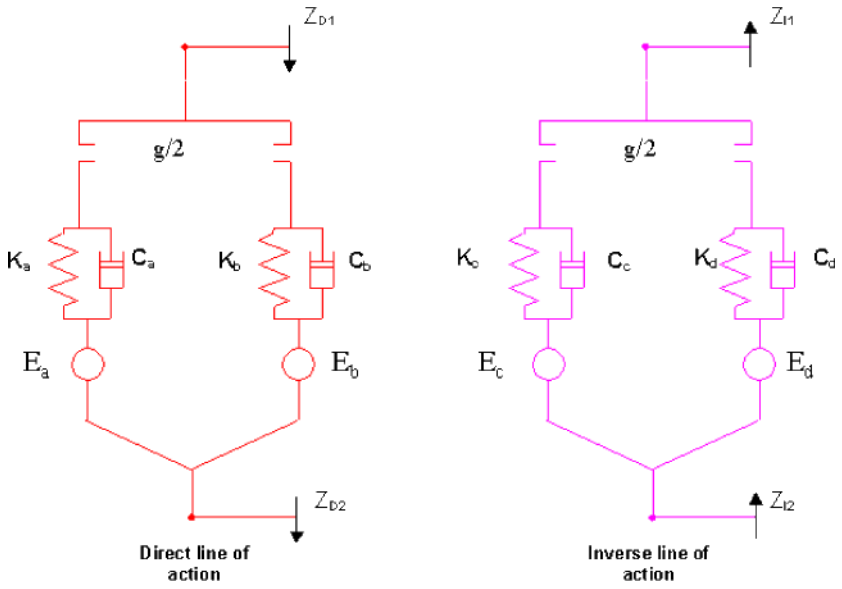

Figure A2.3 – Scheme of the gear meshing on both line of action.

$$z_{D1} = r_{b1}\theta_1 - y_1 \tag{A2.1}$$

$$z_{D2} = r_{b2}\theta_2 - y_2 \tag{A2.2}$$

$$z_{I2} = r_{b2}\theta_2 - x_2 \sin(2\alpha_w) - y_2 \cos(2\alpha_w) \tag{A2.3}$$

$$z_{I1} = r_{b1}\theta_1 - x_1 \sin(2\alpha_w) - y_1 \cos(2\alpha_w) \tag{A2.4}$$

$$z_D = z_{D1} - z_{D2} \tag{A2.5}$$

$$z_I = z_{I2} - z_{I1} \tag{A2.6}$$

The equations of motion can be written as second-order non-linear differential equations:

$$\begin{cases} m_1 \cdot \ddot{x}_1 = f_{bx1}\left(x_1, y_1, \dot{x}_1, \dot{y}_1, \dot{\theta}_1\right) + f_{px1}\left(x_1, y_1, \theta_1, \dot{\theta}_1\right) - \sin\left(2\alpha_w\right) \cdot f_{mgc}\left(z_I, \dot{z}_I, \theta_1\right) + \\ \quad -\sin\left(2\alpha_w\right) \cdot f_{mgd}\left(z_I, \dot{z}_I, \theta_1\right) \\ m_1 \cdot \ddot{y}_1 = f_{by1}\left(x_1, y_1, \dot{x}_1, \dot{y}_1, \dot{\theta}_1\right) + f_{py1}\left(x_1, y_1, \theta_1, \dot{\theta}_1\right) + f_{mga}\left(z_D, \dot{z}_D, \theta_1\right) + f_{mgd}\left(z_D, \dot{z}_D, \theta_1\right) + \\ \quad -\cos\left(2\alpha_w\right) \cdot f_{mgc}\left(z_I, \dot{z}_I, \theta_1\right) - \cos\left(2\alpha_w\right) \cdot f_{mgd}\left(z_I, \dot{z}_I, \theta_1\right) \\ J_1 \cdot \ddot{\theta}_1 = -r_{b1} \cdot f_{mga}\left(z_D, \dot{z}_D, \theta_1\right) - r_{b1} \cdot f_{mgb}\left(z_D, \dot{z}_D, \theta_1\right) + r_{b1} \cdot f_{mgc}\left(z_I, \dot{z}_I, \theta_1\right) + \\ \quad +r_{b1} \cdot f_{mgd}\left(z_I, \dot{z}_I, \theta_1\right) + K_T \cdot \left(\theta_0 - \theta_1\right) + C_T \cdot \left(\dot{\theta}_0 - \dot{\theta}_1\right) + M_{p1}\left(\theta_1\right) \\ m_2 \cdot \ddot{x}_2 = f_{bx2}\left(x_2, y_2, \dot{x}_2, \dot{y}_2, \dot{\theta}_2\right) + f_{px2}\left(x_2, y_2, \theta_2, \dot{\theta}_2\right) + \sin\left(2\alpha_w\right) \cdot f_{mgc}\left(z_I, \dot{z}_I, \theta_1\right) + \\ \quad +\sin\left(2\alpha_w\right) \cdot f_{mgd}\left(z_I, \dot{z}_I, \theta_1\right) \\ m_2 \cdot \ddot{y}_2 = f_{by2}\left(x_2, y_2, \dot{x}_2, \dot{y}_2, \dot{\theta}_2\right) + f_{py2}\left(x_2, y_2, \theta_2, \dot{\theta}_2\right) - f_{mga}\left(z_D, \dot{z}_D, \theta_1\right) - f_{mgd}\left(z_D, \dot{z}_D, \theta_1\right) + \\ \quad +\cos\left(2\alpha_w\right) \cdot f_{mgc}\left(z_I, \dot{z}_I, \theta_1\right) + \cos\left(2\alpha_w\right) \cdot f_{mgd}\left(z_I, \dot{z}_I, \theta_1\right) \\ J_2 \cdot \ddot{\theta}_2 = r_{b2} \cdot f_{mga}\left(z_D, \dot{z}_D, \theta_1\right) + r_{b2} \cdot f_{mgb}\left(z_D, \dot{z}_D, \theta_1\right) - r_{b2} \cdot f_{mgc}\left(z_I, \dot{z}_I, \theta_1\right) + \\ \quad -r_{b2} \cdot f_{mgd}\left(z_I, \dot{z}_I, \theta_1\right) + M_{p2}\left(\theta_2\right) \end{cases} \tag{A2.7}$$

where the meshing force of each pair of teeth is due to an elastic component and a viscous damping component:

$$f_{mgj} = f_{el.j} - f_{v.j} \qquad j = a,b,c,d \tag{A2.8}$$

These components for tooth pair "a" are computed as follows (see Figure A2.3):

$$\begin{cases} f_{el.a} = \left(z_D + E_a - \dfrac{g}{2}\right) \cdot K_a \\ f_{v.a} = \left(\dot{z}_D + \dot{E}_a\right) \cdot \gamma_m \cdot K_a \end{cases} \qquad if \left(z_D + E_a - \frac{g}{2}\right) \geq 0 \tag{A2.9}$$

$$\begin{cases} f_{el.a} = 0 \\ f_{v.a} = \left(\dot{z}_D + \dot{E}_a\right) \cdot C_{squeeze} \end{cases} \qquad if \begin{cases} \left(z_D + E_a - \dfrac{g}{2}\right) < 0 \\ \left(\dot{z}_D + \dot{E}_a\right) > 0 \end{cases} \tag{A2.10}$$

$$\begin{cases} f_{el.a} = 0 \\ f_{v.a} = 0 \end{cases} \qquad if \begin{cases} \left(z_D + E_a - \dfrac{g}{2} \right) < 0 \\ \left(\dot{z}_D + \dot{E}_a \right) < 0 \end{cases} \tag{A2.11}$$

Similar formulations are used for tooth pairs *b*, *c* and *d*. Equations (A2.9) to (A2.11) take into account the possibility of tooth contact and separation. If there is contact between teeth $\left(z_D + E_a - g/2 \geq 0 \right)$, the model calculates the elastic and the viscous damping forces; it is assumed that the damper coefficient for each pair of teeth is proportional to the pair stiffness, $C_j = \gamma_m \cdot K_j$, where the coefficient γ_m does not depend on time *t* and is called proportional damping factor. For further study and consideration on this proportional damping evaluation see reference [29-30] and [34]. Summarizing, the inaccuracy of initial damping estimation is mainly due to uncertainties on material physical properties as well as approximation in modeling the link geometry (see *Chapter A4*). As a consequence, the damping coefficients should be appropriately chosen in order to match experimental results. Then, the proportional damping factors will be tuned during the validation procedure in order to better match the experimental results (see *Section A3.2*). This proportional damping factors will be then introduced as input values in the FE model of the gear pump, see *Section A4.71*, in order to obtain a reliable and realistic numerical model of this mechanical system, i.e. the gear pump.

When tooth separation occurs $\left(z_D + E_a - g/2 < 0 \right)$, the elastic force is zero as well as the proportional viscous force, but the squeeze effect is considered if tooth profiles are approaching $\left(\dot{z}_D + \dot{E}_a > 0 \right)$; in this case the damper coefficient is computed by the following formulation [29]:

$$C_{squeeze} = 12 \cdot \pi \cdot \mu_l \cdot b \left[R_{eq} / \left(2 \cdot h \right) \right]^{3/2} \tag{A2.12}$$

where R_{eq} is an equivalent radius of the approaching surfaces

calculated as $1/R_{eq} = 1/r_{1m} + 1/r_{2m}$ and h is the instantaneous height of the meatus between teeth calculated along the line of action. The quantities r_{1m} and r_{2m} are the mean curvature radiuses of the approaching tooth flanks.

The rotation of each gear can be decomposed in two terms, one related to the rigid body rotation and the other due to small angle variations $\varphi_k(t)$ around the rigid body position:

$$\theta_k = \omega_k \cdot t + \varphi_k(t) \tag{A2.13}$$

where k is the number of the gear (k=1, 2). In order to simplify the meshing stiffness and the error function computation, it is a usual practice to take the gear angular speed (ω_k) as constant, and to neglect the small angle variations around the rigid body position. Thus, the position dependence on stiffness and error can be transformed in a time dependence form; in other words the time t periodically varies from 0 to the meshing period T that is equals to $60/n_{z_k}$ where n is labeled as the gear velocity in r.p.m.. This in turn gives the following expressions, only taking into account the first tooth pair case:

$$K_a(\theta_1(t)) = K_a(\omega_1 \cdot t + \varphi_1(t)) \Rightarrow K_a(t) \tag{A2.14}$$

$$E_a(\theta_1(t)) = E_a(\omega_1 \cdot t + \varphi_1(t)) \Rightarrow E_a(t) \tag{A2.15}$$

Likewise for K_b, E_b, K_c, E_c, K_d and E_d.

Placing eq. (2.8) in equations of motion (2.7) and reorganizing, isolating the acceleration terms in the left side, the following matrix equation can be obtained:

$$\begin{aligned}\{\ddot{q}\} = &(f_{el.a} + f_{v.a})\{B\} + (f_{el.b} + f_{v.b})\{B\} + (f_{el.c} + f_{v.c})\{D\} + \\ &+ (f_{el.d} + f_{v.d})\{D\} + \{F_p\} + \{F_b\} + \{F_s\}\end{aligned} \tag{A2.16}$$

where:

$$\{q\}^t = \{x_1, y_1, \theta_1, x_2, y_2, \theta_2\} \tag{A2.17}$$

$$\{F_p\}^t = \left\{\frac{f_{px1}(x_1, y_1, \theta_1, \dot{\theta}_1)}{m_1}, \frac{f_{py1}(x_1, y_1, \theta_1, \dot{\theta}_1)}{m_1}, \frac{M_{p1}(\theta_1)}{J_1}, \frac{f_{px2}(x_2, y_2, \theta_1, \dot{\theta}_2)}{m_2}, \frac{f_{py2}(x_2, y_2, \theta_1, \dot{\theta}_2)}{m_2}, \frac{M_{p2}(\theta_1)}{J_2}\right\} \tag{A2.18}$$

$$\{F_b\}^t = \left\{\frac{f_{bx1}(x_1, y_1, \dot{x}_1, \dot{y}_1, \dot{\theta}_1)}{m_1}, \frac{f_{by1}(x_1, y_1, \dot{x}_1, \dot{y}_1, \dot{\theta}_1)}{m_1}, 0, \frac{f_{bx2}(x_2, y_2, \dot{x}_2, \dot{y}_2, \dot{\theta}_2)}{m_2}, \frac{f_{by2}(x_2, y_2, \dot{x}_2, \dot{y}_2, \dot{\theta}_2)}{m_2}, 0\right\} \tag{A2.19}$$

$$\{F_s\}^t = \left\{0, 0, \frac{K_T(\theta_0 - \theta_1) + C_T(\dot{\theta}_0 - \dot{\theta}_1)}{J_1}, 0, 0, 0\right\} \tag{A2.20}$$

$$\{B\}^t = \left\{0, \frac{1}{m_1}, -\frac{r_{b1}}{J_1}, 0, -\frac{1}{m_2}, \frac{r_{b2}}{J_2}\right\} \tag{A2.21}$$

$$\{D\}^t = \left\{-\frac{\sin(2\alpha_w)}{m_1}, -\frac{\cos(2\alpha_w)}{m_1}, \frac{r_{b1}}{J_1}, \frac{\sin(2\alpha_w)}{m_2}, \frac{\cos(2\alpha_w)}{m_2}, -\frac{r_{b2}}{J_2}\right\} \tag{A2.22}$$

In eq. (A2.16) the first four terms are the meshing forces along the *DLA* and *ILA*; the other terms are the pressure forces (F_p), bearing forces (F_b) and the driving shaft torque (F_s).

A2.2 Meshing stiffness

One of the main characteristics of the gear dynamic behaviour is the parametric excitation due to the change in the number of tooth pairs in contact and to the tooth stiffness variation depending on the contact point. Kuang work [17-18] was selected to implement the variable gear mesh stiffness in the case

of spur gears, see reference [29-30] and [34] for additional considerations and description of the problem in more detail. Kuang employed a quadratic finite element model in deriving an empiric equation for the tooth stiffness constant (calculated in N/μm/mm) at successive contact positions. This formulation allows the introduction of tooth addendum modification and its validity range goes from 12 to 100 teeth. The stiffness constant for a single tooth is calculated by:

$$K'_p\left(r_p\right)=\left(A_0+A_1\cdot x_k\right)+\left(A_2+A_3\cdot x_k\right)\cdot\frac{r_p-R_{pk}}{\left(1+x_k\right)\cdot\hat{m}_k} \qquad \text{(A2.23)}$$

where R_{pk} and x_k are the pitch radius and the addendum modification for gear k respectively, whilst A_0, A_1, A_2, A_3 are empirical coefficient all evaluated in [34]. This stiffness constant is defined as the load necessary to deform a single gear tooth having 1 mm face-width by an amount of $1\mu m$ along the line of action. So $K'_p\left(r_p\right)$ is the stiffness constant for a single tooth of gear k when the contact takes place in the point defined by the radius r_p $\left(p=1,2,3,4\right)$. The subscripts p denotes the considered tooth flank of contact: 1 and 2 are the flanks of gear 1 and 2 respectively in contact along the DLA, whereas 3 and 4 are the flanks of gear 1 and 2 respectively in contact along the ILA. The radial distances of contact point for driving and driven gear along the DLA line are:

$$\begin{aligned} r_1(t)&=\sqrt{r_{b1}^2+\left[\sqrt{r_{\inf}^2-r_{b1}^2}+\frac{2\cdot\pi\cdot r_{b1}\cdot t}{z_1\cdot T}\right]^2} \\ r_2(t)&=\sqrt{r_{b2}^2+\left[a\cdot\sin\left(\alpha_w\right)-\sqrt{r_1^2-r_{b1}^2}\right]^2} \end{aligned} \qquad 0\le t<T \qquad \text{(A2.24)}$$

The total pair stiffness along the DLA is obtained assuming that the stiffness of each tooth in contact and the Hertzian

stiffness are springs connected in series; the total stiffness for pair a along the DLA taking into account the gear width (b in millimeter) is:

$$K_a = b \cdot \frac{K'_1(r_1) \cdot K'_2(r_2) \cdot K'_H}{K'_1(r_1) \cdot K'_2(r_2) + K'_2(r_2) \cdot K'_H + K'_1(r_1) \cdot K'_H} \tag{A2.25}$$

where K'_H is the Hertzian stiffness defined by Yang as:

$$K'_H = \frac{\pi \cdot E_Y}{4 \cdot (1 - \upsilon^2)} \tag{A2.26}$$

It can be noted that the Hertzian stiffness has to be calculated in $N/\mu m/mm$ for adding its to the above stiffness constant. When two pairs of teeth are in contact along the DLA line the total stiffness of the second pair b can be obtained using an analogous formulation, taking into account in eq. (A2.24) that the second pair has to be considered out of phase of a time corresponding to a pitch with respect to the first one, see reference [29-30] and [34] for more clarifications. The total stiffness of the tooth pair along the ILA is computed in a similar way using the following formulations for r_3 and r_4.

$$r_4(t) = \sqrt{r_{b1}^2 + \left[\sqrt{r_{\inf}^2 - r_{b1}^2} + \frac{2 \cdot \pi \cdot r_{b1} \cdot (t + T/2)}{z_1 \cdot T}\right]^2} \qquad 0 \le t < T/2 \tag{A2.27}$$

$$r_3(t) = \sqrt{r_{b2}^2 + \left[a \cdot \sin(\alpha_w) - \sqrt{r_4^2 - r_{b1}^2}\right]^2}$$

$$r_4(t) = \sqrt{r_{b1}^2 + \left[\sqrt{r_{\inf}^2 - r_{b1}^2} + \frac{2 \cdot \pi \cdot r_{b1} \cdot (t - T/2)}{z_1 \cdot T}\right]^2} \qquad T/2 \le t < T \tag{A2.28}$$

$$r_3(t) = \sqrt{r_{b2}^2 + \left[a \cdot \sin(\alpha_w) - \sqrt{r_4^2 - r_{b1}^2}\right]^2}$$

A2.3 Tooth profile errors

In Figure A2.4 is shown an example of generic tooth profile with profile error parameters for the tooth of the gears; in particular the profile is referred to the left flanks.

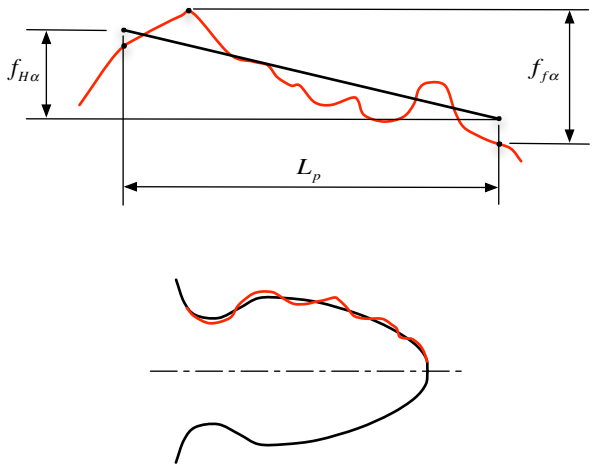

Figure A2.4 – Generic tooth profile with profile error parameters.

The error function of the single flank implemented in the model has been selected in order to reproduce the general trend of the measured errors. As can be seen by eq. (A2.29) the error function is composed by a linear term and by a sinusoidal one with appropriate generic frequency "f".

$$E_{fp}(s) = \frac{f_{H\alpha} \cdot (s - s_0)}{L_p} + \left[\frac{f_{f\alpha}}{2} \cdot \sin\left(\frac{2 \cdot \pi \cdot f \cdot (s - s_0)}{L_p} \right) \right] \qquad \text{(A2.29)}$$

Where s_0 is the start condition (for $s = s_0$, $E_{fp}(s) = 0$), $f_{H\alpha}$ and $f_{f\alpha}$ are the tooth profile error parameters whose values are obtained by measurements, and L is the length of the profile evaluation:

$$L = s(R_T) - s(R_{SV}) \tag{A2.30}$$

The quantities s is the distance between a point M of the tooth profile and the tangent point to base circle r_{bk}, see Figure A2.5. This diagram shows the profile error E_{fp} versus the coordinate s evaluated along the tangent to the base circle. It means that coordinate $E_{fp}(s)$ and s are measured in the same line. For this kind of gears the lower limit of r is R_{SV}=7.5 mm while the upper limit is R_T=8.25 mm corresponding to the tip radius, see eq. (A2.30).

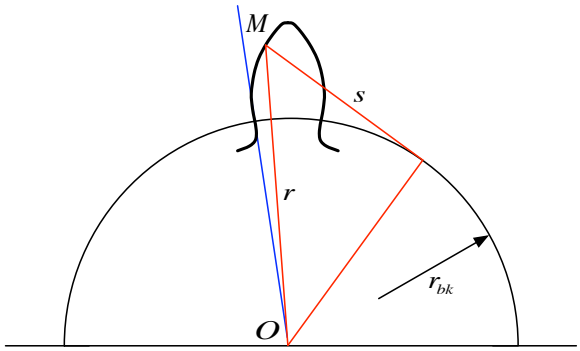

Figure A2.5 – Reference coordinates for profile errors.

The s dependence of the error function can be transformed in a time dependence form using the formulation of radial distances of contact point along the DLA, eq. (A2.24), or the ILA, eq. (A2.27) and eq. (A2.28):

$$E_{fp}\left(s\left(r(t)\right)\right) \Rightarrow E_{fp}\left(r(t)\right) \Rightarrow E_{fp}(t) \tag{A2.31}$$

The profile error of tooth pair a is obtained adding the two error distributions along the flank 1 and 2 in contact along the DLA:

$$E_a = E_1(t) + E_2(t) \tag{A2.32}$$

When two pairs of teeth are in contact along the DLA the profile error of the second pair *b* can be obtained using an analogous formulation, taking into account in eq. (A2.24) that the second pair has to be considered out of phase of a time corresponding to a pitch with respect to the first one, likewise for *Section A2.2*. In references [29-30] and [34] are presented some results for the pairs *a* and *b* relative to the contact along the DLA line and also for the pairs *c* and *d* relative to the contact along the ILA.

A2.4 Bearing behaviour

Oil bearings have an extended use in several machinery fields. There are a great number of works about oil-bearing analysis in the case of single-shaft rotor dynamic systems. The main concepts with an extensive analysis can be found in [31]. Recently, some specific works about the dynamic behaviour of gear pairs supported by oil-bearing systems have been published. In [33] the short bearing theory is used to model the bearing behaviour and the dynamic equations are numerically integrated. All the models that simulate the behaviour of the oil bearings start from the Reynolds' equation with some simplifications. Commonly two main simplifications are used: short and long bearing approximations that yield two simple forms of the Reynolds' equation. Comparisons between the results obtained by the application of the long and short theories and the results obtained by the numerical integration of the Reynolds' equation give the following conclusions: the *short bearing theory* (L/D<0.5, where L is the axial length of the bearing and D its diameter) provides good values for the bearing-reaction direction but the modulus magnitude of this reaction has an error that increases with high eccentricity ratios. On the other hand, the *long bearing theory* (L/D>1) provides an improved definition of the bearing

reaction magnitude with high eccentricity ratios also, but the reaction direction is not so accurate. Individually, these two solutions have a limited value due to their restricted range of application in both L/D (length to diameter) and eccentricity ratios. Since their application ranges do not coincide, the two solutions (short and long) of the Reynolds' equation can be combined together obtaining an approximate solution with extended range validity for finite-length bearings with all eccentricity ratios. In [33] is proposed the so-called "finite impedance formulation" that attempts to achieve the vectorial composition of the results obtained with the short and long theories. More details about this formulation can be found in [34]. The theory exposed by Childs [33] leads to calculate the reaction forces of the journal bearings in the pump under study. In particular, the baring reaction forces (f_b) can be defined as a function of the impedance value (W) in order to provide a relationship between the bearing reaction and the position and velocity of the shaft, see eq. (A2.33). As is clear from this equation the bearing reaction forces is obtained in a reference frame XY with origin in the centre of the journal bearings.

$$\begin{cases} f_{b,x} = -2 \cdot v_s \cdot \mu_l \cdot b_b \cdot \left(\dfrac{R_b}{C_r} \right)^3 \cdot W_x \\ f_{b,y} = -2 \cdot v_s \cdot \mu_l \cdot b_b \cdot \left(\dfrac{R_b}{C_r} \right)^3 \cdot W_y \end{cases} \tag{A2.33}$$

In order to explain the variables used in expression (A2.33) it is useful to define some kinematic quantities related to Figure A2.6 in which P is the centre of the journal, O the centre of the bearing, μ_ε and μ_Γ are the unit vector along and normal the eccentricity $\tilde{e}$. More details can be found in [33] and [34].

$$\varepsilon_P = \frac{\tilde{e}}{C_r} = \frac{\sqrt{x_P^2 + y_P^2}}{C_r} \tag{A2.34}$$

$$\Gamma = arctg\left(\frac{y_P}{x_P}\right) \tag{A2.35}$$

$$\varpi = \frac{\omega}{2} \tag{A2.36}$$

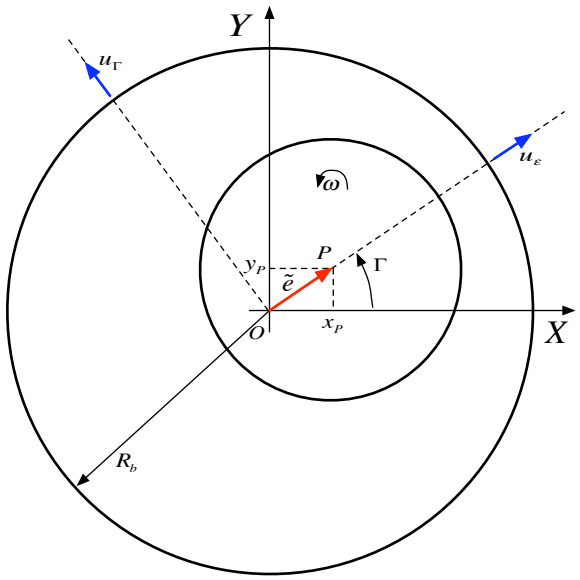

Figure A2.6 – Journal bearing scheme.

The eccentricity-ratio vector is labeled as ε_P whilst Γ is the eccentricity angle for the shaft position. This latter value with the shaft displacement $\tilde{e}$ define the gear centre location. Thus, the velocity magnitude can be calculated as:

$$|v_s| = \sqrt{\left(C_r\dot{\varepsilon}_p\right) + \left[C_r\varepsilon_p\left(\dot{\Gamma} - \varpi\right)\right]} \tag{A2.37}$$

The impedance magnitude in the XY reference frame is:

$$\begin{cases} W_x = W \cdot \cos\left(\zeta + \tilde{\alpha} - \psi\right) \\ W_y = W \cdot \cos\left(\zeta + \tilde{\alpha} - \psi\right) \end{cases} \tag{A2.38}$$

where the angles ζ and $\tilde{\alpha}$ are the attitude angle of v_s and ε_P respectively, see Figure A2.7. More details about the impedance magnitude and about the velocity magnitude can be found in [34].

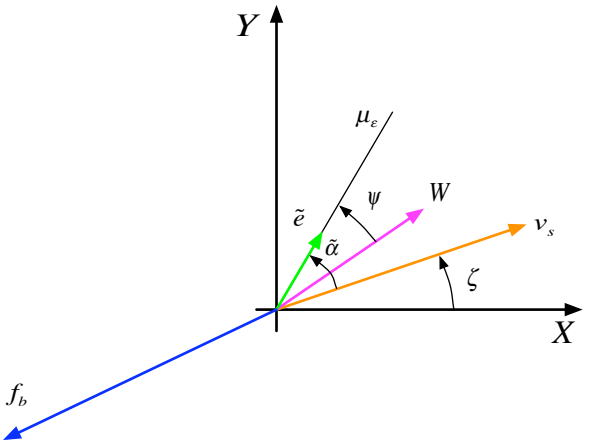

Figure A2.7 – Kinematic variables in the journal bearing impedance method.

A2.5 Pressure distribution

The pressure distribution around the gears yields a resultant force and a torque in each gear. These forces and torques are variable during the gear rotation and they are periodic with period equal to the meshing time. This situation determines an important interaction with the meshing forces and the transmission error excitation because of the same periodicity. The pressure increase in the travel from the low to the high-pressure region is more or less progressive but it is really conditioned by several dimensional and operational parameters as the clearances in the radial and axial sense, oil viscosity, outlet pressure and shaft speed. There are several publications that develop the calculus of the pressure value in the tooth spaces during the

rotation of the gears [26][31-33]. The differences among these models are minimum and are mainly in the account of a fix or variable clearance between the case and the gear and also in the number of control volumes defined (the volumes in which the pump is divided). In this study the formulation in [26] has been used taking the eccentricity of the gears into the case and the wear caused by the gears in the case during the run in process into account [34].

In order to study the pressure variation and following the Eulero's approach, the pump is divided in several "control volumes", i.e. the "sealed" spaces between teeth, bearing blocks and case. It should be noted that the number of the considered control volumes would be variable during the gear rotation because of the variation in number of isolated tooth spaces between the gear and the case. Applying to the opened thermodynamic system, i.e. the generic control volume, the first thermodynamic principle, the continuity equation and the steady-state fluid equation, under the hypothesis of adiabatic and isentropic transformation, the following relation is thus obtained (left side):

$$\frac{dp}{dt} = \frac{B_{oil}}{V}\left\{(\Delta Q) - \frac{dV}{dt}\right\} \Rightarrow \Delta Q = \left(\frac{V}{B_{oil}} \cdot \frac{dp}{d\theta} + \frac{dV}{d\theta}\right) \cdot \omega \qquad \text{(A2.39)}$$

Using this relation (on the left) it is possible to determine the pressure variation of the fluid (characterized by B_{oil}) contained in the control volume V caused by mass gain of ΔQ and by the volume variation of dV/dt. Considering that $dt = d\theta/\omega$, the continuity equation labeled on the left side can be expressed in terms of gear rotational angle θ (see right side). In order to solve eq. (A2.39) the calculus of the volume and its variation and the inlet and outlet flow rates has to be performed for each control volume. Thus it is necessary to understand how each volume communicates with each other through the clearances of the pump. The arrows in Figure A2.8 show the direction and sense of

the flows exchanged among the volumes.

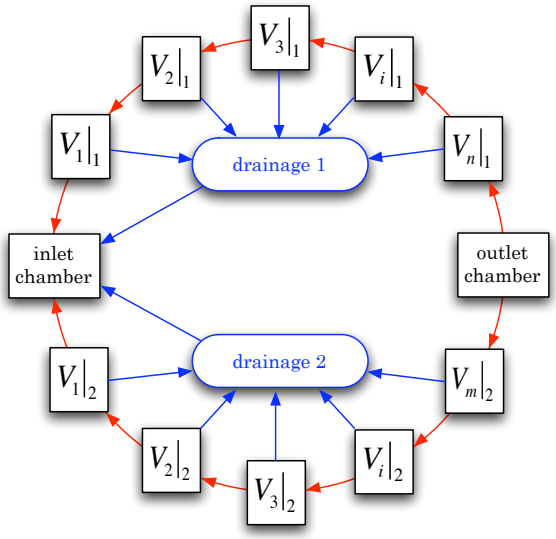

Figure A2.8 – Flows among control volumes.

Figure A2.9 shows the generic tooth space "*i*", edged between two consecutive tooth flanks (*i* and *i*+1) and the case. Each tooth space is connected with the lateral bushes (Figure A2.10) and with the drainage circle (Figure A2.9) through the clearance h_f, and with the next tooth space by the corresponding clearance between case and tooth tip. So the eq. (A2.39) applied to the generic tooth space "*i*" becomes:

$$Q_{h,i+1} - Q_{h,i} + 2\left(Q_{f,i+1} - Q_{f,i}\right) - 2Q_{d,i} = \left(\frac{V_i}{B_{oil}}\frac{dp_i}{d\theta} + \frac{dV_i}{d\theta}\right)\omega \qquad \text{(A2.40)}$$

It can be noted that the flow through the clearance h_f is double because two are the sides of the gear; moreover the flow rates $Q_{h,i}$, $Q_{f,i}$ and $Q_{d,i}$ are taken as positive when coming out of the tooth space *i*, whilst $Q_{f,i+1}$ and $Q_{h,i+1}$ are considered as positive when coming into the tooth space *i*.

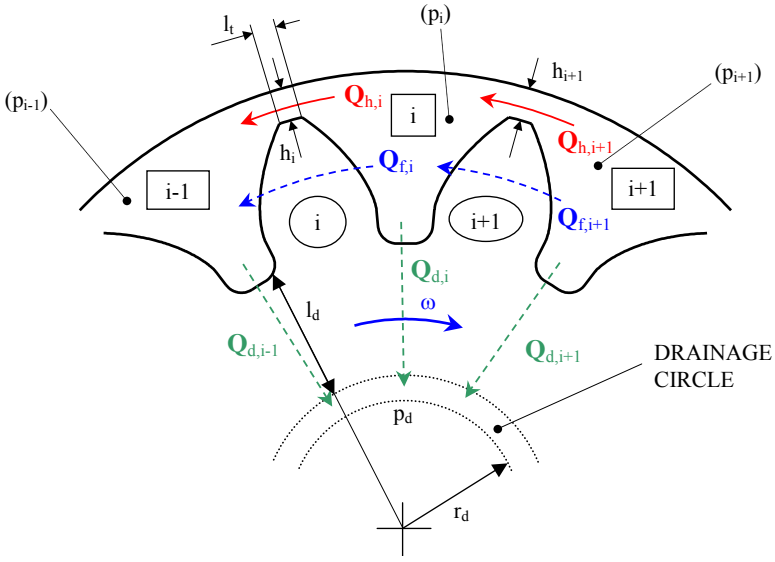

Figure A2.9 – Volumetric flow rates for the generic tooth space *i*.

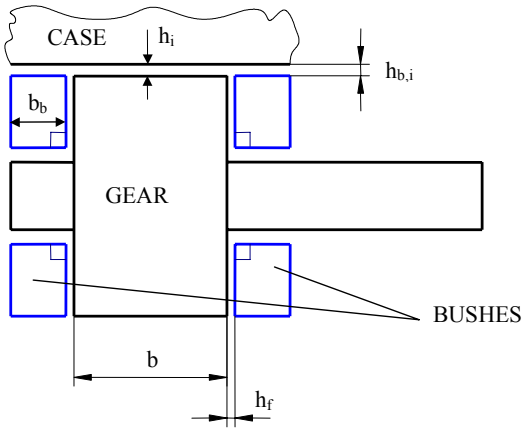

Figure A2.10 – Clearances between pump components.

The flow rates will be calculated taking into account the contributions of the pressure drop among adjacent volumes ($Q_{p,i}$, see Figure A2.11.a) and the entrained flow ($Q_{u,i}$, see Figure A2.11.b). The sense of both the quantities is from the tooth space *i* to the tooth space *i-1*, therefore the resulting expression becomes:

$$Q_{h,i} = Q_{p,i} + Q_{u,i} = \frac{bh_i^3}{12\mu_l l_t}\left(p_i - p_{i-1}\right) + \frac{b\omega r_{ext} h_i}{2} \tag{A2.41}$$

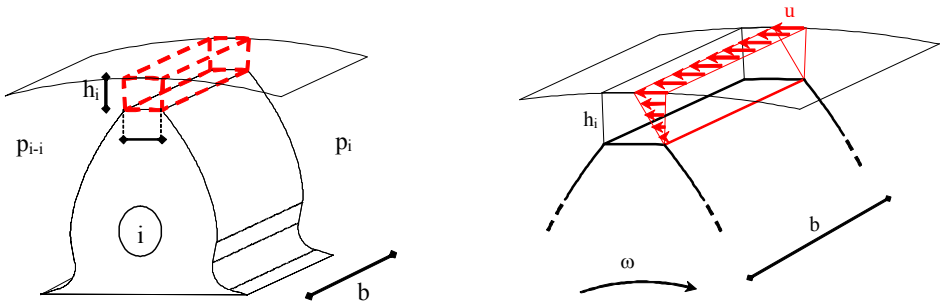

Figure A2.11 – Volumetric flow rate due to (a) pressure drop and (b) entrained flow in the clearance between case and tooth tip.

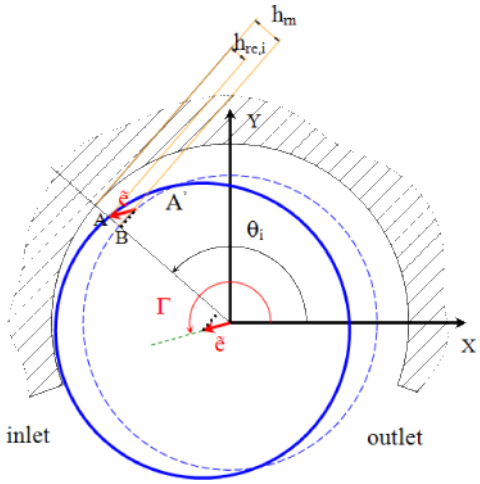

Figure A2.12 – Radial clearance.

The height of the clearance h_i between the tooth tip and the case depends on the position of the gear shaft (because of the eccentricity of the gear with respect to the case, see Figure A2.12) and on the case wear. So, the radial clearance will be different for each tooth along the gear. Through several steps, see reference

[34] for more details, the clearance height h_i of the tooth i is given by:

$$h_i = h_w(\theta_i) + h_{re,i} \tag{A2.42}$$

where $h_w(\theta_i)$ is the radial height of the wear profile for the tooth tip i. More details about the wear profile evaluation can be found in [34]. Therefore the model evaluates the pressure distribution adding the wear profile to the radial clearances between tooth tip and case.

In analogy with eq. (A2.41) the volumetric flow rate between the lateral bushes and the lateral flank of the tooth $Q_{f,i}$ is:

$$Q_{f,i} = \frac{b_f h_f^3}{12\mu_l l_f}(p_i - p_{i-1}) + \frac{b_f \omega r_m h_f}{2} \tag{A2.43}$$

Quickly comparing eqs. (A2.41)-(A2.43), is easy to note some differences in the nomenclature adopted. This is due to the fact that in the latter the relative velocity is variable and moreover the width and the length of the meatus are not geometrically defined. Thus, by the fact that the flow rate through this clearance is smaller than the flow through the clearance at the tooth tip, one may consider averaged values for u, b_f and l_f.

The drainage flow for the tooth space i is given by the following expression updating the quantities previously mentioned $\left(b \to b_f \to b_d, l_t \to l_f \to l_d\right)$ and neglecting the entrained flow term (its radial component is zero).

$$Q_{d,i} = \frac{b_d h_f^3}{12\mu_l l_d}(p_i - p_{i-1}) \tag{A2.44}$$

The last term to be calculated in eq. (A2.40) is the volume variation dV_i. This term for an angle rotation $d\theta$ of the gear is obtained by the difference of the shaded areas exposed in Figure A2.13 multiplied by the thickness b of the gear.

$$\frac{dV_i}{d\theta} = r_{ext} \cdot b \cdot \left(h_{i+1} - h_i\right) \tag{A2.45}$$

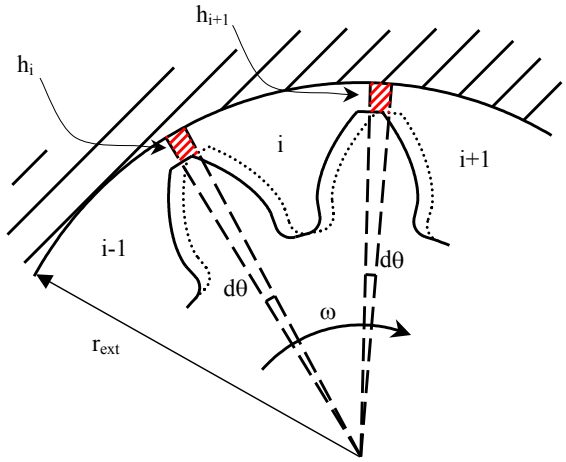

Figure A2.13 – Volume variation at the tooth tip.

So, taking into account all the previous terms and substituting in eq. (2.40), considering the volume V_i as constant and equal to the nominal value of the tooth space, the following equation for the generic tooth space can be obtained:

$$\frac{dp_i}{d\theta} = \frac{B_{oil}}{\omega \cdot V_i}\left[C_h \cdot \left(h_{i+1}^3 \cdot \Delta p_{i+1} - h_i^3 \cdot \Delta p_i\right) - K_h \cdot \left(h_{i+1} - h_i\right) + 2 \cdot C_f \cdot \left(\Delta p_{i+1} - \Delta p_i\right) - 2 \cdot C_d \cdot \Delta p_{d,i}\right] \tag{A2.46}$$

where:

$$\begin{cases} C_h = \dfrac{b}{12 \cdot \mu_l \cdot l_t} \\ C_f = \dfrac{b_f \cdot h_f^3}{12 \cdot \mu_l \cdot l_f} \\ C_d = \dfrac{b_d \cdot h_f^3}{12 \cdot \mu_l \cdot l_d} \\ K_h = \dfrac{b \cdot \omega \cdot r_{ext}}{2} \end{cases} \qquad \begin{cases} \Delta p_{i+1} = p_{i+1} - p_i \\ \Delta p_{d,i} = p_i - p_d \\ \Delta p_i = p_i - p_{i-1} \end{cases} \tag{A2.47}$$

Applying eq. (A2.46) to the isolated volumes of gear 1, a system of differential equations can be obtained and the unknown quantities, i.e. the pressure in all the control volumes, can be calculated. Such a system has to be solved for an angle variation equal to the pitch angle but due to the change in the number of isolated space, two different systems must be integrated one for N and one for N-1 equations. In other words, due to the rotation of the gear, there will be a change in the number of isolated spaces that will vary from a maximum (N) to a minimum (N-1) consequently varying the number of equations that must simultaneously be utilized in the system. Moreover, in order to solve this equation system, an initial value of the pressure distribution has to be known; for that reason the pressure values obtained at the end of the integration step are used as initial values for a new integration cycle. After several cycles the solution for the pressure distribution will be obtained. The same procedure can be applied to gear 2 in order to calculate the pressure distribution around the driven gear. More details and some examples about the relief grooves influence (which separate low pressure camera to high pressure camera) in the evaluation of the pressure distribution can be found in [34].

A2.6 Pressure forces and pressure torque

Once the pressure distribution for a complete rotation of the gears has been obtained, the resultant pressure force and the resultant pressure torque for each gear can be determined.

The pressure force is calculated as vectorial sum of the pressure around the gears multiply by the involved area. Taking as reference Figure A2.14, the pressure force in the vane q having direction as the symmetric axis of the vane itself and been reduced in the reference frame OXY (see Figure A1.16) can be calculated for gear 1 as follows:

$$\begin{cases} f_{px1} = -\sum_{q=1}^{z} f_{pv,q} \cdot \cos\left(\varphi_{1,vane,q}\right) \\ f_{py1} = -\sum_{q=1}^{z} f_{pv,q} \cdot \sin\left(\varphi_{1,vane,q}\right) \end{cases} \tag{A2.48}$$

where $\varphi_{k,vane,q}$ is the angular position of the axis of the vane q for gear k with respect to the X-axis (see Figure A1.16) and z is the vanes number of the gear. For more details and example about the pressure force evaluation for the spur gear see reference [30] and [34].

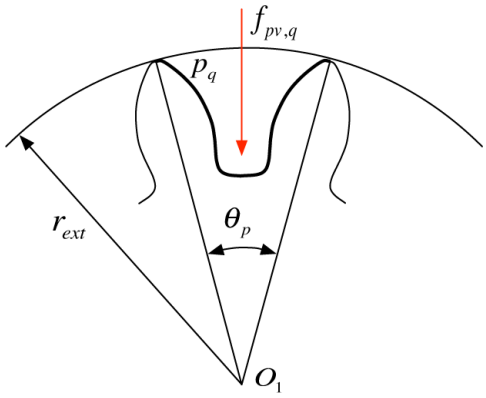

Figure A2.14 – Pressure force in a vane.

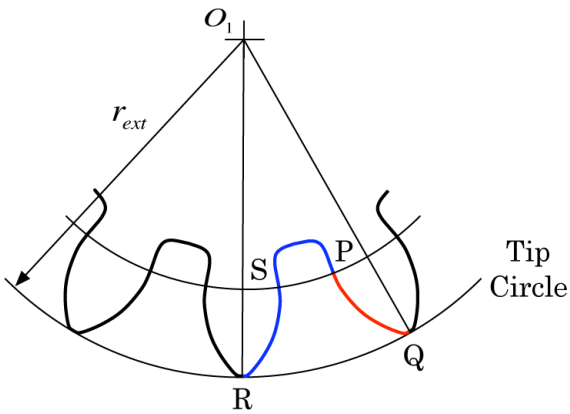

Figure A2.15 – Not balanced vane.

The pressure torque is due to the pressure difference in the tooth spaces of the meshing teeth. These will be the only tooth spaces not balanced. The rest of the tooth spaces will have inside a constant pressure and therefore a zero resulting torque. In order to calculate the pressure torque due to the not balanced vane, the region between the tip radius and the radius of the contact point P has to be taken into account (see Figure A2.15), in fact the pressure acting on the region between S and P and the pressure acting on the tooth tip determines a radial force that gives no torque. The pressure torque is just created by the tangential force pressure acting in the arc SR and PQ. Thus, the torque can be defined by the difference between the tip radius of the gear and the radius corresponding to the contact point along the contact line. As we are interested to introduce the torque in a dynamic model, it is better to express the torque magnitude as a function of the meshing period, obviously in relation to the DLA line:

$$\begin{cases} M_{p1}(t) = b \cdot (p_{out} - p_{in}) \cdot \left(\dfrac{r_{ext}^2 - r_1^2(t)}{2} \right) \\ M_{p2}(t) = b \cdot (p_{out} - p_{in}) \cdot \left(\dfrac{r_{ext}^2 - r_2^2(t)}{2} \right) \end{cases} \tag{A2.49}$$

where $r_1(t)$ and $r_2(t)$ define the position of the tooth pair in contact as detailed in *Section A2.2*, eq. (A2.24). The pressure torque due to the not balanced vanes along the Inverse Line of Action (ILA) is computed in a similar way taking into account the different sequence of meshing contacts along this line of action with respect to the DLA as explained in the previous sections. In conclusion the pressure torque in the ILA will be calculated by the same formulation as for the DLA, but using $r_3(t)\left(\rightarrow M_{p3}(t)\right)$ and $r_4(t)\left(\rightarrow M_{p4}(t)\right)$ for defining the position of the tooth pair in contact. More details about the pressure torque evaluation can be found in [34].

A2.7 Stationary position

Pressure calculation needs some seconds to solve the differential equation systems. With the aim at reducing the integration time, the average positions of the shaft axes inside the journal bearings are estimated before the integration of the dynamic model (equations of motion). Profile errors are not considered, pressure efforts for each angular position are reduced to average values and the contact between teeth is assumed as rigid. When the shaft centre is in the stationary equilibrium, the shaft centre velocity vanishes and the problem is to solve a non-linear equation system giving the shaft centre location. In this case, the acting forces for each gear, shown in Figure A2.16, are the mean pressure forces $\left(f_{pkm}\right)$, the mean pressure torques reduced to forces $\left(f_{Tm}\right)$ and the mean bearing reactions $\left(f_{bk}\right)$.

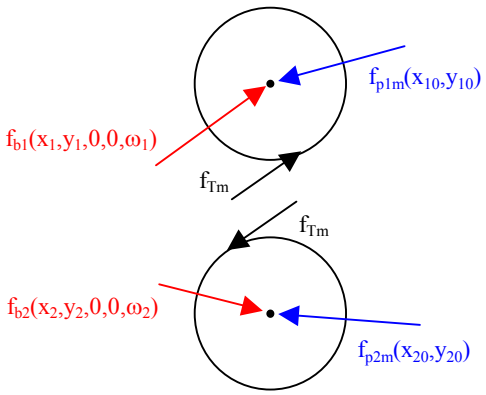

Figure A2.16 – Diagram of gear forces.

When the integration begins, an arbitrary shaft location is defined $\left(x_{k0}, y_{ko}\right)$. Then the pressure distribution and the corresponding force average values $(f_{pkm}\left(x_{k0}, y_{k0}\right))$ are calculated. The non-linear system is solved founding the shaft centre location $\left(x_k, y_k\right)$ where the bearing reactions balance the pressure forces.

Obviously the new centre location will be different from the initial position and the pressure force evolution for the new position must be recalculated repeating the same procedure described above until the difference between two consecutive positions is less than a threshold value. An additional control was included to take into account the mean force variation from one to the next calculated position. After some iteration the “stationary” centre location is obtained. This procedure is applied to each gear obtaining the stationary shaft centre location. Thus the variable pressure force on gears can be approximately estimated from these average axis positions, before starting the numerical integration, obtaining an important reduction of the integration time. More details about this “approach” used in order to calculate the orbit shaft axes position, the gear accelerations and the acting forces on gears are defined and described deeply in [34].

CHAPTER A3

Experimental validation of the LP model

The model developed must be verified and validated using experiments. A good model should be a good representation of the real machine and therefore should have a good correspondence with the experimental measurements; model parameters can be modified in order to approach real and simulated behaviour, improving the features of the model. This could be a critical task because good experiments are as rare as good theories and complex systems sometimes introduce additional difficulties associated with the availability of directly comparing measurement data with model outputs.

In literature, several investigators [35-36] have measured the time variation of tooth space pressure in an external gear

pump by using a pressure transducer fitted in the driving gear in order to obtain the so-called pressure distribution around the gears. In the following sections of this chapter will be presented another kind of validation procedure for the pump under study (the GENB pump) following a non-detailed path, that differs from that developed by the above-mentioned researchers by these important aspects:

- we are interested in validating the "dynamic model", i.e. the resulting acceleration on gears that not only takes the pressure distribution into account but the meshing forces and the bearing reactions as well (see *Chapter A2*);
- the experimental measurements carried out by the mentioned investigators were performed on medium size external gear pumps where the tooth vane dimension could house the sensor. In our case, the GENB pump is a small size external gear pump and it is quite hard to house the sensor in the tooth vane.

Model validation is not a simple task in complex systems like gear pumps where it is not easy to directly obtain vibration data concerning rotating components. The model validation is based on the comparison between simulations and experimental results concerning forces and moments: it deals with the external and inertia components acting on the gears, estimated by the LP model, and the reactions and inertia components acting on the pump case and on the test plate, obtained by means of measurements. These are the components that can excite case vibrations and produce noise; consequently, their estimation has a practical interest for noise reduction. The validation is carried out comparing the level of the waterfall maps in the frequency domain, with particular attention to identify system resonances. More details about the validation procedure and the validation results of this newest procedure adopted for the GENB pump can be found in detail in [34].

A3.1 Test set up

Tests were carried out on a test bench (Figure A3.1 left) available at TRW Automotive Italia SpA – Divisione Automotive Pumps. The pump under testing is fastened on an ergal plate (Figure A3.1 right and Figure A3.3.a) that also provides proper connections to low and high-pressure oil pipes. An electrical motor drives the pump with inverter having maximum angular speed of 5000 rpm; the plate has a hole for the driving shaft (see Figure A3.3.a).

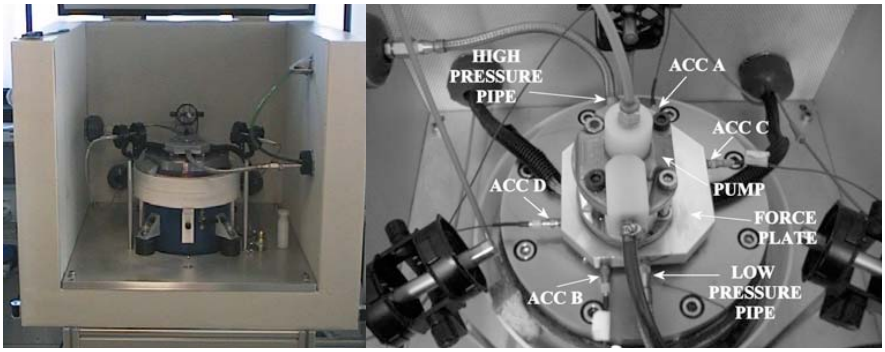

Figure A3.1 – Test bench on the left and pump under study on the right.

The test bench operation is controlled by a system based on software Labview. The reference frame considered for the plate is shown in Figure A3.2 and Figure A3.3: the origin is on the axis of the driving shaft (centre of gear 1, O_1) and Z-axis is downward (coordinate θ is clockwise). Figure A3.2 and Figure A3.3.a also shows the relationships between the reference frame of the plate (at which the pump case is fastened) – called RFC – and the reference frames of gears 1 and 2 – called hereafter RF1 and RF2, respectively. The plate is equipped with 4 high-impedance quartz-based triaxial force sensors (Kistler 9251, frequency range 0 to 30 kHz). These sensors, located as shown in Figure A3.1 and Figure A3.3.b, are used to form a force plate allowing the user to measure 6 variables: the three orthogonal X, Y and Z force components and the three moments about each individual axis. In addition, four

PCB 353B18 piezoelectric accelerometers (frequency range 1 to 10000 Hz) are mounted on the plate as shown in Figure A3.1 and Figure A3.3.b, in order to measure plate accelerations in the XY plane. The eight signals (4 force sensors and 4 accelerometers) are recorded on DAT, acquired and processed using LMS Scadas SC305 Front-end and controlled by software LMS Test.Lab.

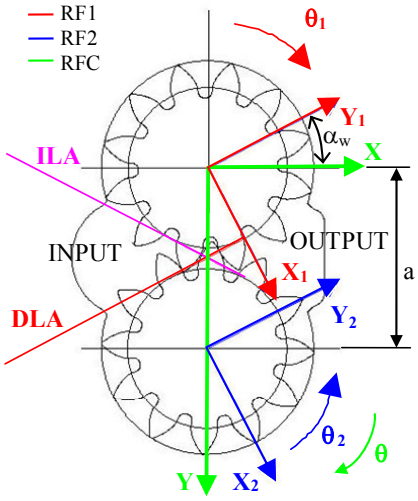

Figure A3.2 – Reference frame.

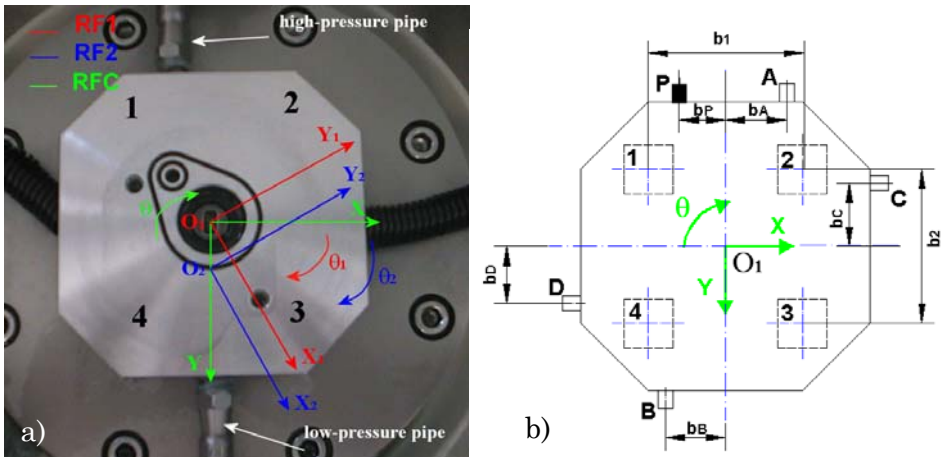

Figure A3.3 – (a) Force plate with reference frames and (b) scheme of the force plate: locations of force sensors (1,2,3,4) and accelerometers (A,B,C,D).

In order to validate the model, D'Alembert's equations of the whole system composed of the pump and the force plate (the pump case is rigidly fixed to the plate) are considered, where some terms are obtained by measurements and others are simulation results. Considering that only forces and moments in the plane orthogonal to the gear axes are taken into account and thus using the reference frame shown in Figure A3.2, D'Alembert's equations are:

$$\begin{cases} \sum F_{eX} + \sum F_{igX} + \sum F_{iCX} = 0 \\ \sum F_{eY} + \sum F_{igY} + \sum F_{iCY} = 0 \\ \sum M_{eO_1} + \sum M_{igO_1} + \sum M_{iCO_1} = 0 \end{cases} \tag{A3.1}$$

where F_{eX}, F_{eY}, M_{eO_1} are the force components, $F_{igX}, F_{igY}, M_{igO_1}$ are the inertia components concerning gears that are firstly expressed in the reference frames of the gears and then transformed to the reference frame of the force plate, and $F_{iCX}, F_{iCY}, M_{iCO_1}$ are the inertia components concerning the pump case and the force plate. While the gear inertia components are given by the simulation results in terms of gear accelerations, the inertia components concerning pump case and force plate can be evaluated by acceleration and force measurements. After a series of steps and considerations that for simplicity here are not introduced, but can be found in detail in [34], the eq. (A3.1) can be reorganized in order to put the terms given by measurements on the left side and the terms given by simulation on the right side, the following equations are obtained:

$$\begin{cases} R_{X12} + R_{X34} + \sum F_{iCX} = -\sum F_{igX} \\ R_{Y14} + R_{Y23} + \sum F_{iCY} = -\sum F_{igY} \\ \left(R_{X12} - R_{X34}\right) \cdot \dfrac{b_2}{2} + \left(R_{Y23} - R_{Y14}\right) \cdot \dfrac{b_1}{2} + \sum M_{iCO_1} = -\sum M_{igO_1} - M_S \end{cases} \tag{A3.2}$$

where M_S is the driving shaft torque. The terms on the right side

of these equations load the pump case and the plate and produce the reactions and the inertia forces on the left side. In operational conditions these are the components that can excite case vibrations and produce noise. Consequently, their estimation has a practical interest.

A3.2 Comparing experimental results and simulations

As mentioned before, the validation is carried out using data in frequency domain (in [34] is detailed also the validation using time domain); the model parameters were preliminarily evaluated on the basis of both design and literature data (see *Chapter A1*). The values of damping factors γ_T and γ_m (proportionality factor between damper constant and stiffness for the driving shaft and the tooth meshing, respectively) are tuned in order to better match experimental results, their values are $\gamma_T = 10^{-9} s$ and $\gamma_m = 10^{-10} s$.

The validation results in frequency domain concern two linear run-up tests from 2000 to 3350 rpm, with operational pressure of 34 bar and 90 bar as well, conducted with the apparatus described in the previous section. The run-ups have been acquired using sampling frequency of 25.6 kHz and frequency resolution of 3.125 Hz. During the run-up tests 67 spectra of the quantity on the left side of equations (A3.2) has been acquired. These spectra are taken at speed intervals of 20 rpm between 2000 to 3350 rpm and they are shown as waterfall maps. In order to compare simulation data with the experimental run-ups, 27 simulations has been conducted at operational pressure of 34 bar and 90 bar and angular speed interval of 50 rpm from 2000 to 3350 rpm. The simulations were carried out for a time corresponding to 48 meshing periods *T*, using display frequency of 48 kHz. For each simulation the quantity on the

right side of equations (A3.2) was evaluated and its frequency spectrum was calculated. Figure A3.4 to Figure A3.9 show these amplitude spectra as waterfall maps.

As mentioned the model is non linear and natural frequencies could not be defined; more details about this aspect can be found in [34] under the heading "model linearization". However it can be useful to evaluate the natural frequencies and mode shapes of an undamped linearized model, in order to compare these natural frequencies with the experimental resonances exhibited in the waterfall maps. With the aim at obtaining the conventional matrix formulation with masses and stiffnesses, the variable meshing stiffness is replaced by its mean value, while the bearing forces are linearized in the stationary centre position (*Section A2.7*, $x_{ks}, y_{ks}, k = 1,2$) by the expansion in a Taylor series giving a bearing stiffness matrix coefficients. More details about the procedure for obtaining the undamped linearized model can be found in [34]. However, whishing to provide a minimum amount of information, the above considerations with all the treatment made in the previous chapter leads to the following linear system of equations of motion in order to perform the model linearization:

$$[M]\cdot\{\ddot{u}\}+[C]_L\cdot\{\dot{u}\}+[K]_L\cdot\{u\}=\{f_{bs}\}+\{f_p\}+\{f_T\} \tag{A3.3}$$

The natural frequency can then be estimated solving the following equation of motion obtained from eq. (A3.3) where the terms on the right side and the terms proportional to the velocity have been neglected (normal modes):

$$[M]\cdot\{\ddot{u}\}+[K]_L\cdot\{u\}=0 \tag{A3.4}$$

It is worth noting that in the equation of motion of the undamped linearized model, eq. (A3.4), mass matrix is constant for each operational condition whilst the stiffness matrix $[K]_L$ changes as a function of operational speed and pressure. In

particular the stiffness terms obtained by the bearing reaction linearization depend on the stationary centre position and therefore these terms depend on the output pressure and rotational speed. Table A3.1 and Table A3.2 show the natural frequencies at different operational conditions estimated by the undamped linearized model (LP model).

	34 bar 2000 rpm	34 bar 2600 rpm	34 bar 3200 rpm	34 bar 3350 rpm
$\omega_{n1}[Hz]$	3366	3387	3408	3413
$\omega_{n2}[Hz]$	4130	4130	4130	4130
$\omega_{n3}[Hz]$	5001	5031	5061	5069

Table A3.1 – Natural frequencies of the linearized model at 34 bar.

	90 bar 2000 rpm	90 bar 2600 rpm	90 bar 3200 rpm	90 bar 3350 rpm
$\omega_{n1}[Hz]$	4130	4130	4130	4130
$\omega_{n2}[Hz]$	5415	5427	5439	5442
$\omega_{n3}[Hz]$	8047	8065	8083	8087

Table A3.2 – Natural frequencies of the linearized model at 90 bar.

The experimental waterfall maps (Figure A3.4 to Figure A3.9) show some resonance regions: from about 500 Hz to 2.5 kHz in X and Y-directions and at about 3.4 kHz, 4.2 kHz, 5.2 kHz, 8 kHz and 10 kHz in all the components. The last two resonances (8 kHz and 10 kHz) can be identified as the natural frequencies of

the whole system composed of the pump and the force plate supported by the force sensors (Kistler 9251). In fact, considering that the sensor stiffness is 1000 N/mm in X and Y-directions of Figure A3.3, the system natural frequencies are 8.281 kHz for the vibration modes in the X and Y-directions and 10.675 kHz for the rotational mode (θ-direction). These frequencies cannot be obviously found in the model results because they concern a system not included in the model. At the operational pressure of 34 bar, the experimental resonances at about 3.4 kHz, 4.2 kHz, 5.2 kHz satisfactorily agree with the natural frequencies estimated by the linearized model (Table A3.1). At high pressure (90 bar), the first two natural frequencies of the model (Table A3.2) can be found in the experimental waterfall maps, while the third natural frequency at about 8 kHz is in the same region as one of the natural frequencies of the whole system pump-force plate, thus they can not be distinguished.

For the comparison between the experimental and simulation spectral maps, presented in Figure A3.4 to Figure A3.9, it is worth noting that they have different resolutions: the frequency resolution is 3.125 Hz for experimental spectra and for the simulation ones ranges from 8.3 to 14 Hz; the resolution in the rpm-axis is 20 rpm for the experimental spectra and 50 rpm for the simulation ones. The amplitude grey scale is the same for the pairs of maps relative to the same direction and operational condition. As previous mentioned, the resonance regions at about 8 kHz and 10 kHz cannot be found in the simulation maps. In the other frequency ranges, there is a quite good correspondence in the X-direction maps at both pressure levels and in the Y-direction maps at 34 bar. The correspondence is good in the momentum maps, especially around the resonances at about 4.2 kHz. The discrepancies between experimental and simulation results could be also due to the approximations introduced in equation (A3.2), when it has been considered that the pump case is rigidly fixed to the plate and that the pressure variation of the high-pressure pipe is negligible.

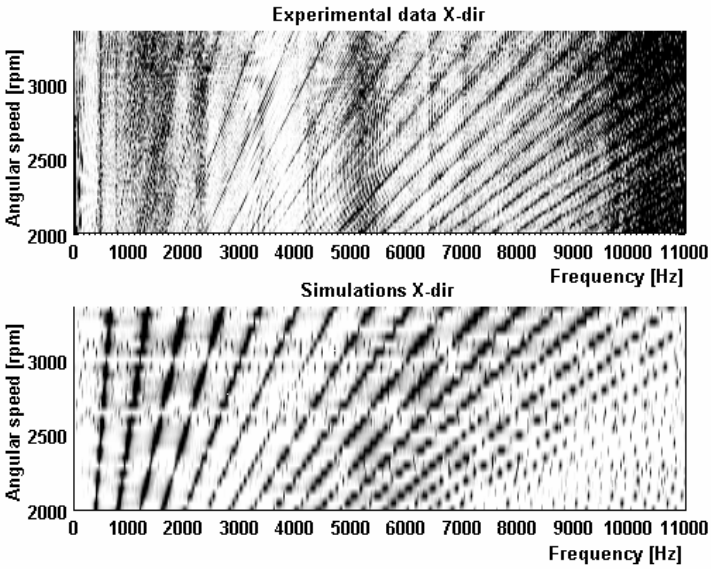

Figure A3.4 – Waterfall maps of force spectra in X-direction at 34 bar: experimental and simulation results.

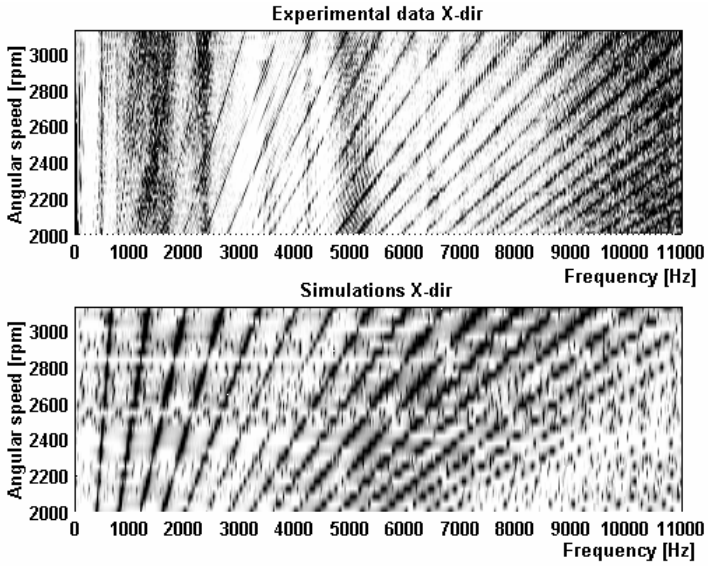

Figure A3.5 – Waterfall maps of force spectra in X-direction at 90 bar: experimental and simulation results.

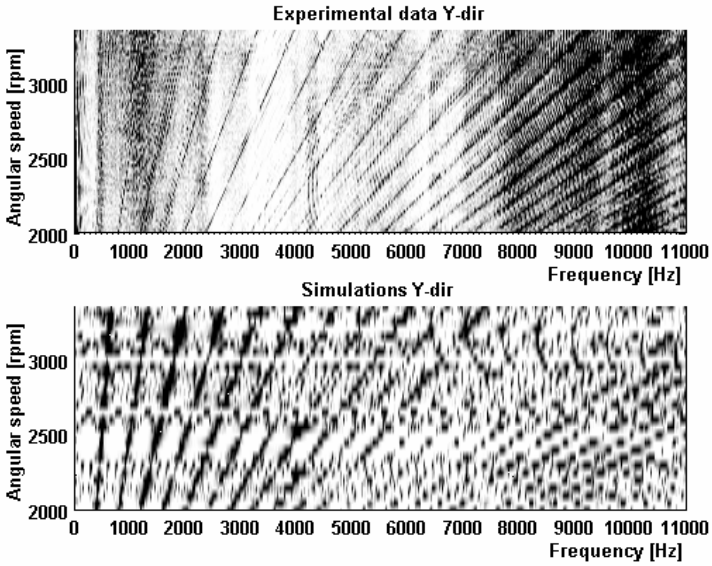

Figure A3.6 – Waterfall maps of force spectra in Y-direction at 34 bar: experimental and simulation results.

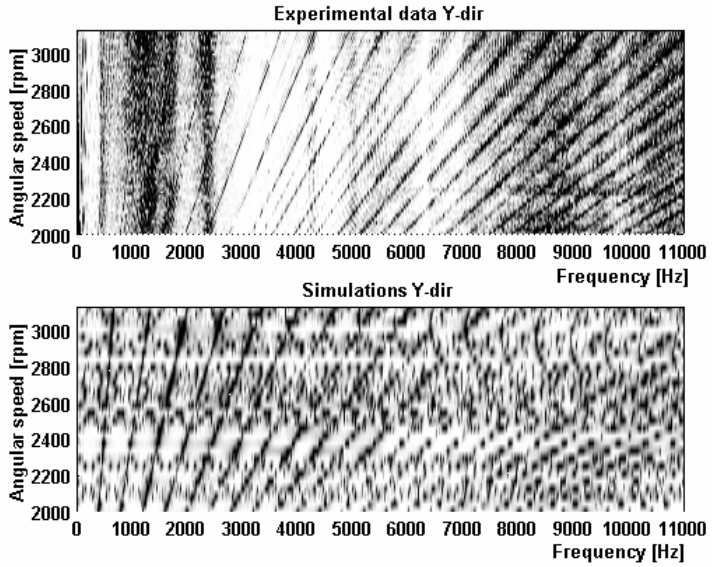

Figure A3.7 – Waterfall maps of force spectra in Y-direction at 90 bar: experimental and simulation results.

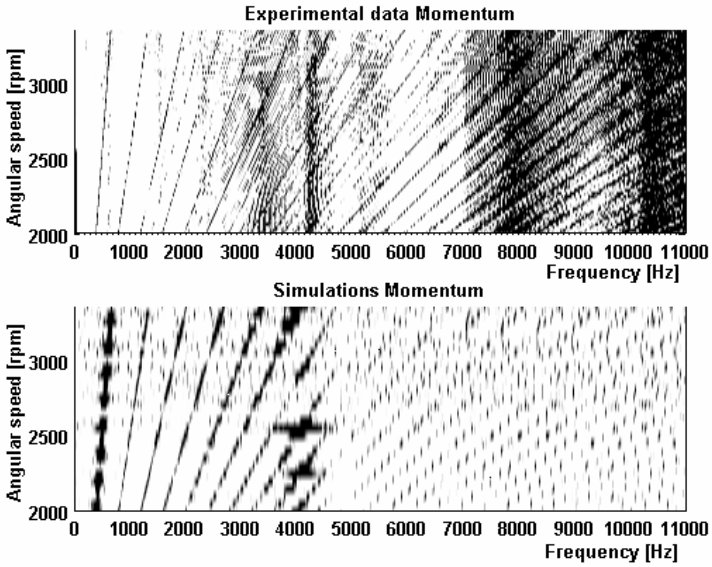

Figure A3.8 – Waterfall maps of momentum spectra at 34 bar: experimental and simulation results.

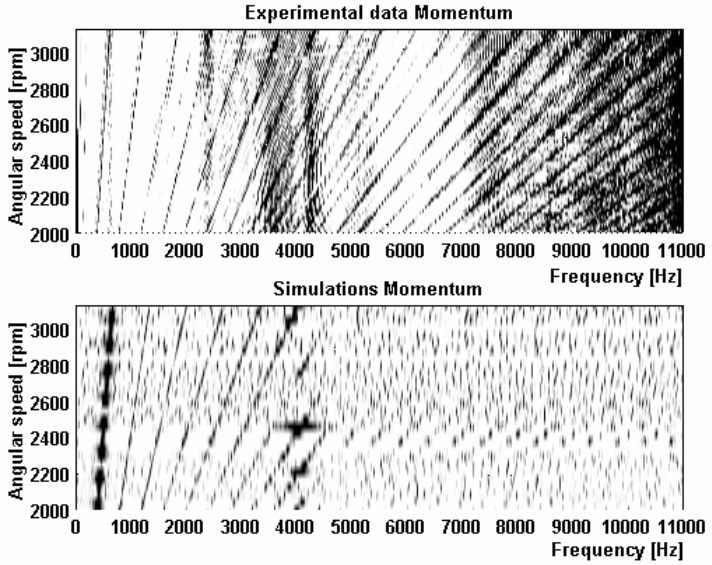

Figure A3.9 – Waterfall maps of momentum spectra at 90 bar: experimental and simulation results.

CHAPTER A4

The hybrid FE/LP model of the pump

In this Chapter an FE model of the gear pump already described in the previous chapters is built up with the aim at evaluating the acceleration on the exterior part of the gear pump (external surface of the case, flange, cover) during operational conditions. The evaluation of the vibrations on the external surfaces are so important for the company and customers because they are the vibrations that directly produce noise and they transfer vibration to the neighbouring structures (e.g. car chassis). In particular, the model will be described in *Sections* from *A4.1* to *A4.5*. The FE model not only regards the gear pump, but also the plate to which the pump is fastened during the experimental test. In fact the model must be validated using

experiments and therefore it has been modeled the same apparatus used for the experimental measurements, i.e. the pump, the ergal plate and the four force sensors supporting the plate as stated in *Chapter A3* and shown hereafter in Figure A4.1.a and A4.1.b. Two different FE dynamic analyses have been performed using the FE model (*Section A4.6*): a modal analysis (SOL 103 in MSC.Nastran) with the aim at evaluating the fundamental eigenfrequencies and an FRF analysis (SOL 111 in MSC.Nastran) in order to estimate the accelerations in some locations of the external surface of the gear pump to compare them with the accelerations acquired by experiments. In *Section A4.7* the experimental measurements carried out will be detailed. Two linear run-up tests have been performed from 2000 to 3350 rpm, with operational pressure of 34 bar and 90 bar as well; in these tests the experimental accelerations in two locations of the external pump case have been acquired. The tests were carried out on a test bench (Figure A3.1) available at TRW Automotive Italia SpA – Divisione Automotive Pumps, that is the same test bench used for the validation procedure of the lumped-parameter model treated and briefly presented in *Chapter A3*. Moreover, an experimental modal analysis of the system under test, composed by the pump and the plate supported by the force sensors (see Figure A3.1) has been carried out with the aim of evaluating the modal damping necessary in the finite element FRF analysis. Then, in *Section A4.8* the validation procedure for the assessment of the hybrid FE/LP model will be described: the experimental case accelerations measured during the run-up tests will be compared with the simulated accelerations coming from the FE model. In particular the FRFs (case accelerations divided by the internal dynamic forces) obtained from the FE model will be multiplied by the dynamic forces calculated by the LP model described in *Chapter A2* in order to evaluate the case accelerations. Then, the amplitude spectra of such accelerations will be compared with the experimental quantities. In this phase, with the aim to better match the experimental results, some

model parameters have been adjusted.

The hybrid model can be effectively used for evaluating the effect of all the design and operational parameters on the pump external surface acceleration. In other words, the model is able to predict the effects of variations of some parameters; for instance, it is possible to predict the consequence of the clearance alteration due, for example, to wear or improper assembling. For example, it is possible to predict the effect that a modification in the clearance into the journal bearings and between case and tooth tip has in the dynamic forces and in gear accelerations. Moreover the effect of operational pressure and speed, the influence of the variation of the oil viscosity due to the temperature, the effect of design parameters such as profile errors, dimension and shape of the relief grooves can be evaluated and predicted through the model. As an example, in *Section A4.9*, the assessed hybrid FE/LP model will be used in order to evaluate the external accelerations (dynamic response of the system) as a function of the design parameter "length of the relief grooves".

A4.1 FE model description

How the pump has been modelled using the FE method is described starting by this section. The mechanical system already presented in the previous chapters is shown in Figures A4.1.a and A4.1.b: it is the whole gear pump composed by the case, the two end-plates (the lower one is indicated as flange and the upper one as cover), the gears, the valves, the bushings as well as the four force sensors and the ergal plate to which the pump is fastened on the test bench available in TRW. To better understand the shape, the size and the placement of each component constituting the gear pump in order to facilitate the next stage namely "solid modeling", an external view of the pump in its compact form, an internal view of the pump highlighting all its internal component,

the path that follows the oil within the pump and an exploded view of the gear pump are shown from Figure A4.2.a to Figure A4.2.d respectively.

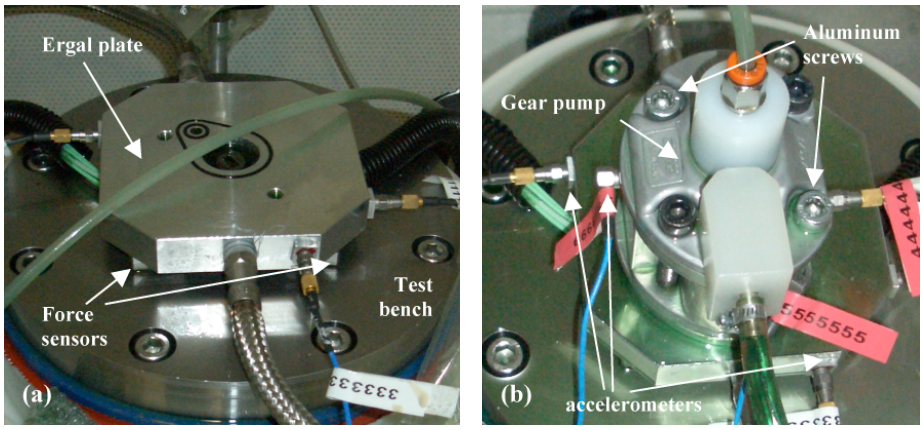

Figure A4.1 – (a) Ergal plate and (b) mechanical system under test.

Figure A4.2.a – External view of the pump in its compact design.

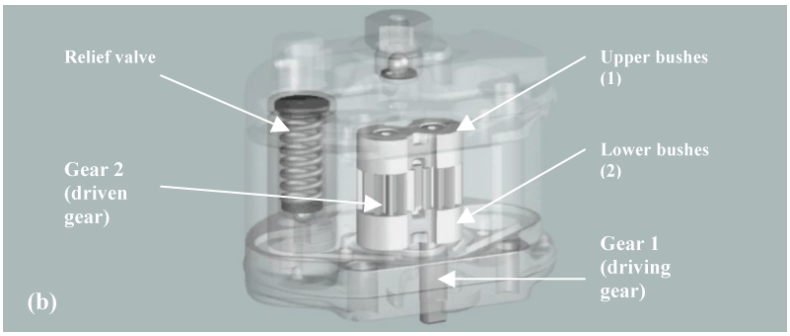

Figure A4.2.b – Inner view of the pump.

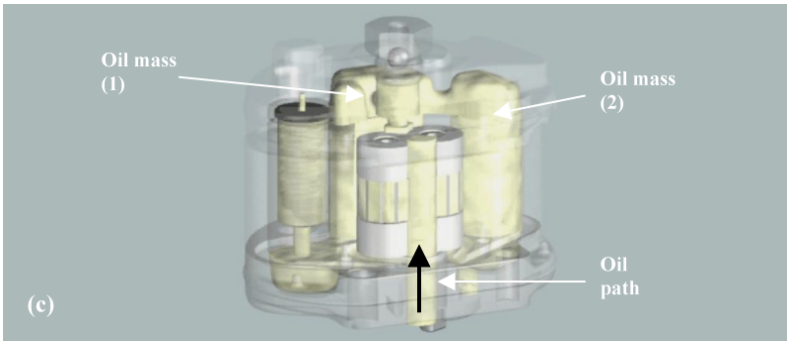

Figure A4.2.c – Oil path within the pump.

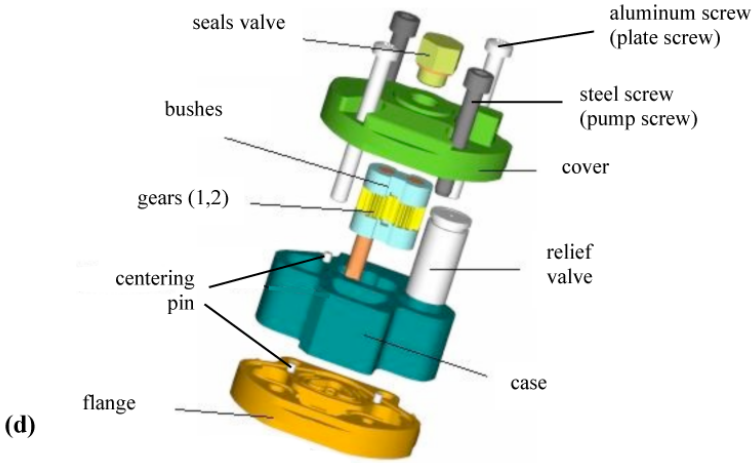

Figure A4.2.d – Exploded drawing of the gear pump.

The case and the two end-plates have been meshed using tetrahedral elements as shown in Table A4.1. It can be noted that the case and the end-plates have different Young Modulus and density because the case is made of aluminum whereas the end-plates are made of steel. In the actual pump, the 3 components are fastened together by means of two steel screws (M6, length 65 mm) as shown in Figure A4.1.b and Figure A4.2.a. The two screws, by means of the tightening torque guarantee the connection between the case and the end-plates. The two screws have been modelled with beam elements having the same cross

section area and inertia properties of the actual screws. These screws are than joined to the surrounding mesh of the cover and the flange by means of rigid spiders as shown in Figure A4.3 and Figure A4.4. The tightening torque has not been applied to the screws in the model because it represents a static torque and therefore it has no contribution in a dynamic analysis. Moreover, the tightening torque produces the effect of joining the case surface to the end-plates surfaces. Therefore in order to model this, rigid spider connections (Card RBE2 in Nastran) have been used in order to connect the case surface with the end-plates surfaces as shown in Figure A4.4.

System compo-nents	**# nodes**	**# elements**	**Element type**	**Young modulus [*GPa*]**	**Density** $[kg/m^3]$
Case	46024	27398	Tetrahedral, 10 nodes (card CTETRA)	70	2700
Flange	38554	22192	Tetrahedral, 10 nodes (card CTETRA)	210	7800
Cover	37605	22120	Tetrahedral, 10 nodes (card CTETRA)	210	7800
Pump screws	2	1	Beam (card CBEAM)	210	7800
Ergal plate	39478	24740	Tetrahedral, 10 nodes (card CTETRA)	70	2700
Plate screws	2	1	Beam (card CBEAM)	70	2700

Table A4.1 – Properties of system components.

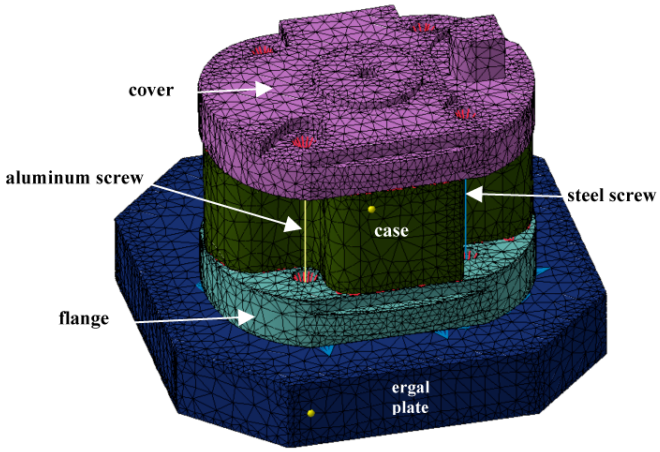

Figure A4.3 – FE model of the mechanical system under test.

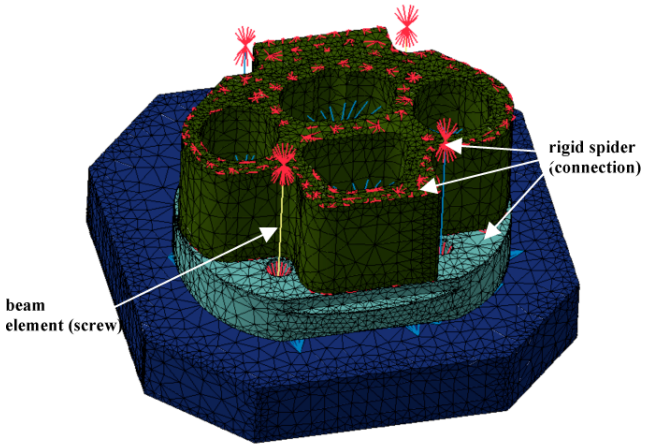

Figure A4.4 – Screws modeled with beam elements (yellow plate screws – blue pump screws) and joined to the end-plates mesh by means of rigid spider (in red).

Moreover, as already mentioned, the presence of the pump internal components (gears, bushings, oil and relief valve) has been taken into account. Each of these components has been modelled by means of a concentrated mass and relative inertia momentum (Card CONM2 in Nastran) located on its centre of mass and connected to the surrounding mesh by means of interpolation spiders (Card RBE3 in Nastran). Table A4.2 lists all these internal components properties and how they appear in the

FE model is shown in Figure A4.5.

Internal system components	**Mass [*kg*]**	**Inertia matrices** $[kg \cdot m^2]$	**Young modulus [*GPa*]**	**Density** $[kg/m^3]$
Bushings (1),(2)	0.01	$I_{XX} = 3.048e^{-7}$ $I_{YY} = 7.752e^{-7}$ $I_{ZZ} = 9.189e^{-7}$	70	2700
Driven gear (2)	0.022	$I_{XX} = 1.304e^{-6}$ $I_{YY} = 1.304e^{-6}$ $I_{ZZ} = 3.984e^{-7}$	210	7800
Driving gear (1)	0.032	$I_{XX} = 7.774e^{-6}$ $I_{YY} = 7.774e^{-6}$ $I_{ZZ} = 4.818e^{-7}$	210	7800
Relief valve	0.07	$I_{XX} = 1.187e^{-5}$ $I_{YY} = 1.187e^{-5}$ $I_{ZZ} = 3.159e^{-6}$		5878
Oil (1)	0.0156			
Oil (2)	0.0082			

Table A4.2 – Properties of internal system components. The inertia values are those located on the centre of mass of each component.

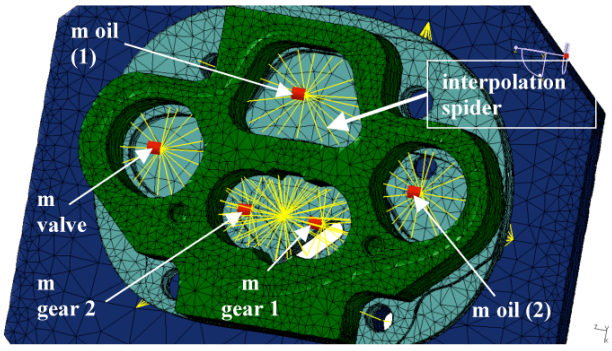

Figure A4.5 – Concentrated masses (red) connected with the surrounding mesh (green) through interpolation spider (yellow).

The ergal plate of the test bench (Figure A4.1.a) has been modelled using tetrahedral elements. The ergal plate is connected to the pump by means of two screws made of aluminum (Figure A4.1.b and Figure A4.3). The two screws have been modelled using beam elements in the same way as for the steel screws and then connected to the ergal plate and to the pump by means of interpolation spiders. Moreover, rigid spiders have been used between the end-plate (the flange) lower surface and the ergal plate upper surface for modelling the connection between the two surfaces and in order to avoid penetration between the surfaces themselves as shown in Figure A4.6. Finally, the ergal plate is connected to ground by four triaxial force sensors located as shown in Figure A3.3.b. These sensors have been modelled by means of spring elements having the nominal stiffness of each sensor as collected in Table A4.3. Furthermore, the spring elements (not visible in figure) are joined to the plate mesh by means of rigid spiders as depicted in Figure A4.7.

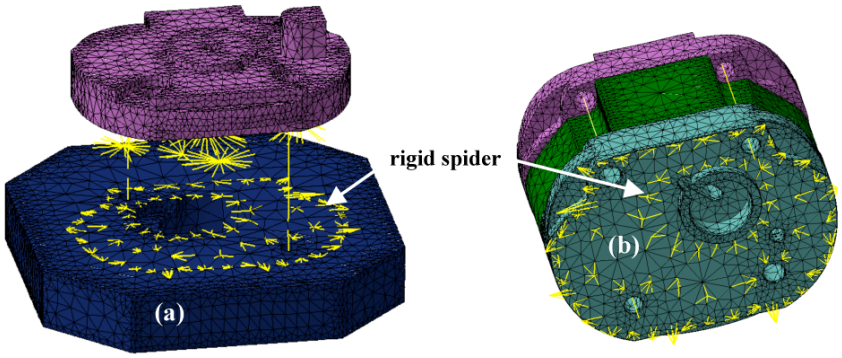

Figure A4.6 – Rigid spiders (in yellow) between ergal plate (a) and flange (b).

	X'-direction	Y'-direction	Z'-direction
Stiffness [N/m]	1E9	1E9	2.6E9

Table A4.3 – Stiffness of the spring elements in the lower surface of the ergal plate (values taken from sensor data).

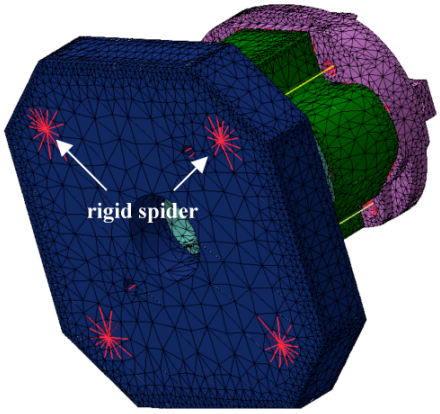

Figure A4.7 – Rigid spiders (in red) connecting ergal plate mesh and sprig elements (not visible in figure) modeling the force sensor between ground and the ergal plate.

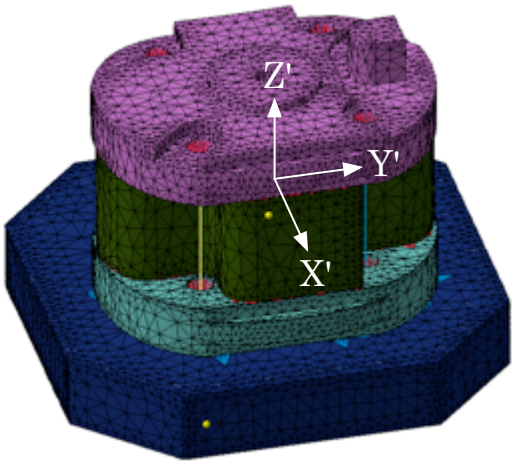

Figure A4.8 – Reference frame X'Y'Z' of the FE model.

The stiffness values of the spring elements positioned on the lower surface of the ergal plate and the inertia values of the internal system components (relief valve and driven and driving gears) listed in Table A4.3 and A4.2 respectively, are based on the reference system shown in Figure A4.8. This point will be

recovered in the following sections. However, to give a small advance, it is easy to understand why these inertia and nominal stiffness values are equal in the X and Y-directions. This is due to the rotational symmetry of these components depending by the reference frame adopted.

A4.2 Overview of the FE model creation

In this section the necessary steps and the expedient required to enable the realization of a reliable and realistic FE model of the pump including the ergal plate will be exhibited and explained. The achieving of this goal will be permitted through the use of the following software: DS CATIA®, LMS Virtual.Lab® and MSC.Nastran®. Each of this softwares corresponds to a well-defined functionality that, combined with the peculiarities of their complete interface allows performing an overall study of the components constituting the mechanical system under test; i.e. starting with the modeling phase (geometry creation), carrying on with the setup phase of the analysis to which the components must be subjected, and ending with the achievement of the results. A further phase will follow that attempts to check the validity and goodness of the FE model thanks to a comparison with the results coming from the experimental tests.

In essence, the *first step* identified as the design phase is handled by CATIA software, that allows the designer to firstly realize the geometry of the mechanical components under study (see *Section A4.3*), and secondly, to create and control the mesh of the component [37]. The "mesh control" means the possibility to choose the type of the meshing element (tetrahedral, quadrangular) and the possibility to make the mesh more or less dense, or make it denser only in some precise locations of the component such as edges, corners, connections and holes; obviously depending by the time consuming and by the computing

power of the used machine. Considering all the components making up the FE model an average accuracy of the mesh has been assumed. This choice is supported by the two following considerations: (i) due to the enormous computational time that is required for very dense mesh, which would increase significantly during the numerical simulations and, (ii) because of negligible differences in the results obtained for different mesh accuracies. Obviously, these components are those listed in Table A4.1 except for the pump and plate screw due to the fact that these latter are modeled by beam elements. The CATIA software will provide an output file, having extension ".CATPart", containing all the component information regarding its geometry and its solid mesh properties, which thanks to a perfect interface with LMS Virtual.Lab software can be easily opened by the latter and than modeled to designer liking.

As announced, the *second step* is related to the operations performed in Virtual.Lab environment, which allows managing all the setting operations and the analysis arrangement contained in the pre and post-processing phases. This software is implemented by a series of "packages", each one designed to operate in a specific application field, clearly within the pre and post-processing framework. In turn each package is divided into a number of additional "sub-packages" in order to guide the designer to choose the most appropriate procedure for achieving the desired study (see Figure A4.9).

Important aspect is defined by the complete interface between the various packages, which allows moving quickly and efficiently from one feature to another simply clicking on the package of interest, without the need to close the application or save the data already arranged. Among the various packages available in Virtual.Lab (Motion, Durability, Acoustics and Optimization), two are those on which the attention will be pointed in order to conduct the study of the mechanical system under test: the "*Noise & Vibration*" and "*Structures*" packages [38]. Obviously, depending by the package used will follow the

choice of specific workbench in order to direct the study in accordance with a precise "study path", which are: the "*General pre/post for structural analysis*" and "*Assembly definition and analysis*" workbench for the Structures package and the "*System analysis*" workbench for the Noise & Vibration package respectively (see the packages and workbench highlighted in blue in Figure A4.9).

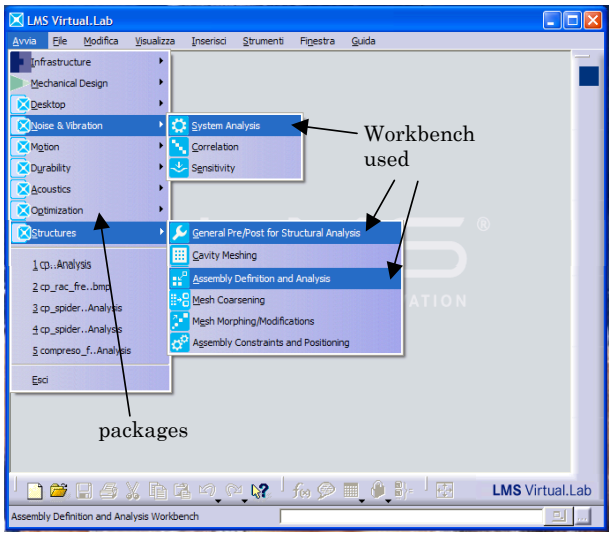

Figure A4.9 – LMS Virtual.Lab framework.

The *System Analysis* workbench offers several capabilities allowing to prepare and set the model for all those analyses that at a later stage should be performed, such as: (i) set loads and boundary conditions, (ii) collect, check and display data coming from other numerical models or experimental tests, (iii) evaluate the accordance degree between two modal data sets, (iv) provide the effect of simple changes that could be made to the basic model through the study performed on the FRF and modal data, (v) display the modal contributions coming from different components, and so on.

The *General pre/post for structural analysis* workbench offers to designers and engineers the possibility to simulate in a

single work session structural features and components/sub-components performance. Standard solver such as MSC.Nastran, Ansys or Elfini elaborates the structural analysis solutions, here defined and set for a generic FE model. As already mentioned above, MSC.Nastran is the solver used for the evaluation of the results coming from the pump FE model, which, through a perfect interface with LMS Virtual.Lab will support the following analysis: (i) linear (Sol 101) and non linear (Sol 106) static analysis, (ii) real (Sol 103) and complex (Sol 107, 110) modal analysis, (iii) direct (Sol 111) and modal (Sol 108) FRF analysis, (iv) steady state heat transfer (Sol 153) and (v) Buckling analysis (Sol 105).

The *Assembly definition and analysis* workbench allows the user to assemble the components forming the global system from both experimental tests and numerical models. These components are connected (rigidly or with supports and bushings) in order to constitute the complete system. In other words this workbench allows generating a finite element model of the hybrid system (such as a complete vehicle) composed by the individual sub-systems contained in it (which may come from experimental tests or from FE models) and by all the connection properties. The sub-FE models can be represented by means of complete or reduced modal models (the models based on experimental tests are always in a reduced modal model form).

The *last step* is handled by the software MSC.Nastran that working as a solver allows performing all the calculations providing the required results.

Essentially, through the LMS Virtual.Lab software (pre and post-processing stages) all the input data to the FE model are defined (analysis type, loads, constraints, materials, components properties, etc) and the output quantities are chosen (frequencies, accelerations, FRF, displacements, mode shapes, stresses and strains, etc). In this manner all the informations that attempts to characterize the components under study are firstly introduced and the output quantities that at the end of the simulation will be

displayed and studied in order to get feedback on the goodness of the FE model created are finally evaluated. The file generated in Virtual.Lab environment that contains all the input informations have extensions ".bdf" or ".dat" that, in turns, is assimilated by the solver MSC.Nastran [2] that provides the output file containing the solutions, having extensions ".xdb" or ".op2". This latter file is than opened by Virtual.Lab, which will proceed through the use of appropriate methodologies to their display, their comparisons and study, constituting in this manner a new suitable stage for considerations and estimations on possible improvements on the methodology followed or possible changes on the components studied.

A4.3 Geometric CATIA models

In this section will be presented the solid components models (see component listed in Tables A4.1 and A4.2) created and shaped through the software CATIA [37]. These models will constitute the basis on which the following analyses managed in Virtual.Lab environment will be performed. The components, already listed in *Section A4.1*, that needs to be modelled are the case, the two end-plates (flange and cover), the end-plates sealing components and the ergal plate for the external view of the system under test (see Figures A4.1 and A4.2.a) and, the upper and lower bushings, the driving and the driven gears and the relief valve for the inner view of the system under test (see Figure A4.2.b). Through a comparison between the above components and those listed in the Tables A4.1 and A4.2 it is important to define two aspects in relation to the external and internal components forming the system under test (see Figure A4.1.b):

- With regard to macro-components, i.e. the external components, the screws used for the connection

between the pump components and between the pump and the plate of the test bench were not considered. These pairing components are listed in Table A4.1 and labeled as pump and plate screws. This assumption is made possible by the fact that it would be unnecessary and time consuming to create a geometrical model in CATIA environment of these screws components since they can be directly introduced in Virtual.Lab environment through the use of special elements such as beam elements (see Figures A4.3 and A4.4).

– The gaskets, not visible in any of the figures presented above, useful only for the oil sealing and interposed between the two cases surfaces and the two end-plates (the cover and the flange) will not take part to the complete FE mechanical system creation and therefore to any kind of analysis. This is because the presence in the analysis of two rubber elements characterized by thickness values too small compared to that of the other elements forming the global FE model, and by different mechanical characteristics of the material used, would only lead to a "heavier" model without making any improvement or any significant change from the vibratory point of view. The reason for their creation will be defined and explained in *Section A4.4*.
– With regard to internal components must be remembered that they will be introduced in the FE model creation stages in the form of lumped masses and then connected to the surrounding mesh elements through the use of specific elements such as interpolation spider elements (see Figure A4.5). These internal components are those listed in Table A4.2 and labeled as bushings, driving and driven gear and relief valve. The reason why these elements have been created in CATIA environment is said; a proper placing of a lumped mass in an FE model requires information

on its weight and on its inertia principal components in addition to the definition of its location according to the reference frame chosen (see values listed in Table A4.2). These informations can be directly obtained through the creation of the geometrical model of the aforementioned components performed in CATIA environment.

– The latter "component" listed in Table A4.2 and labeled as the oil, obviously cannot be modeled in the same manner as the other components. Thanks to the knowledge of the path followed by the oil within the pump case and consequently by the knowledge of the areas where it has a greater concentration (see Figures A4.2.c), it is than possible to calculate the fluid volume in these sectors, than switching to the determination of the mass values (m oil 1 and m oil 2 in Figure A4.5). In this manner the two masses, whose values are given in Table A4.2, are evaluated and consequently placed in the centre of the two locations containing the oil as shown in Figure A4.5.

In the following sections the solid models for both external and internal components forming the mechanical system under test, created in CATIA environment, will be presented. The characteristics of each component, such as mechanical properties, type of material, type of mesh elements, number of elements and nodes forming the mesh, masses and inertia momentum are given in Tables A4.1 and A4.2.

A4.3.1 External components

The external mechanical components forming the complete mechanical system under test already presented in the previous

chapter and shown in Figures A4.1.a and A4.1.b are: the case, the two end-plates (the lower one is indicated as flange and the upper one as cover), the sealing components and the ergal plate to which the pump is fastened on the test bench available in TRW.

The *case* component, already represented in Figure A4.2.d, identifies the central component of the gear pump in which all the internal components reside. First step is the creation of the geometry through the use of several features available in the "*part design*" workbench supplied by CATIA software (see Figure A4.10.a). Second step is the application of the mesh on the component just created through the "*advanced meshing tools*" workbench available in CATIA environment, which allows the user to define the type of meshing element, the mesh precision and other informations relating to its quality (see Figure A4.10.b). As already explained in *Section A4.2* all these informations regarding the case component will be contained in an output file having extension ".CATPart". This file will be directly imported into Virtual.Lab environment thus creating the bases on which develop any kind of analysis.

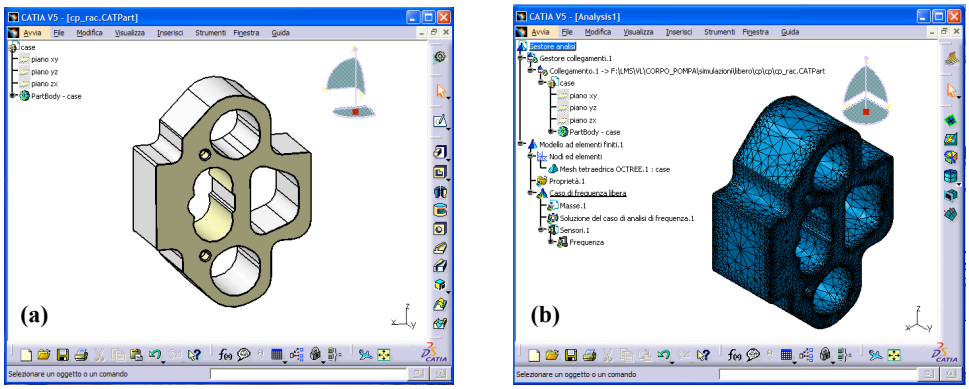

Figure A4.10 – (a) Case geometry and (b) case mesh.

In Figures A4.11.a and A4.11.b is shown the geometry of the *flange* component that is placed between the case and the ergal plate (see Figure A4.1.b and A4.3), whilst the *cover* component geometry that is placed on the upper surface of the case (see

Figure A4.1.b and A4.3) is shown in Figures A4.12.a and A4.12.b.

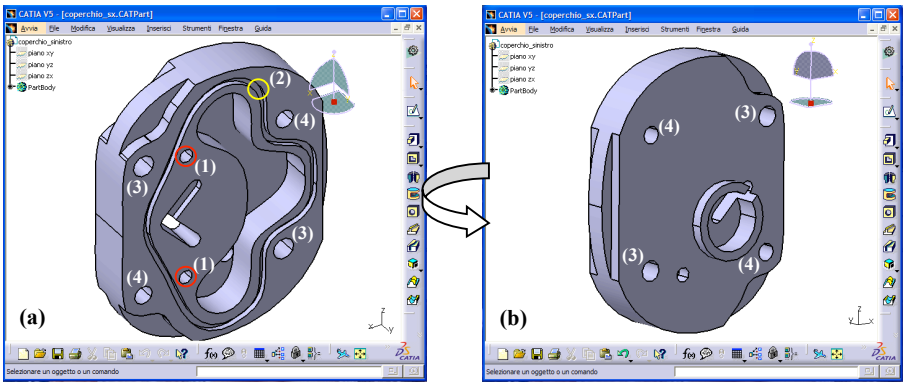

Figure A4.11 – Flange geometry, (a) front and (b) rear view.

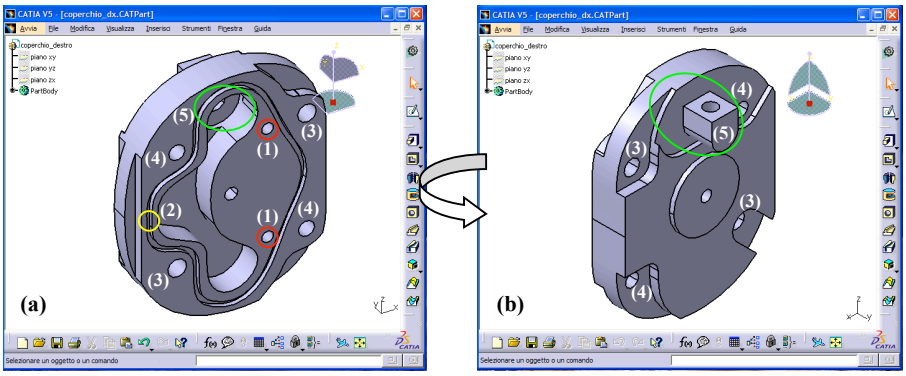

Figure A4.12 – Cover geometry, (a) front and (b) rear view.

Observing these components figures, some indications can be given relating to the link that this elements have with the other forming the whole mechanical system:

(1) Pin housing; only used for the centering in the assembly stage of physical components.

(2) Gasket housing; only used for the oil sealing and interposed between the two cases surfaces and the two end-plates.

(3) Aluminum screws housing; used for joining together the pump case and the ergal plate.

(4) Steel screws housing; used to make compact the pump, joining together the case and the end-plates.

In addition to the flange component, the cover component is characterized by another housing that is:

(5) Relief valve housing (see Figure A4.2.d).

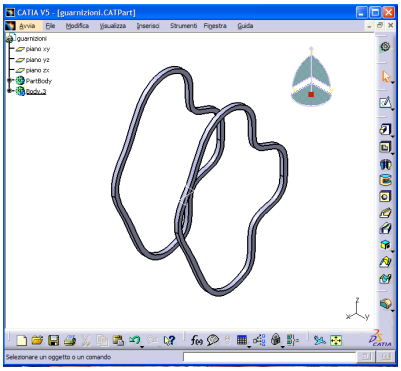

Figure A4.13 – Cover geometry, (a) front and (b) rear view.

In Figure A4.13 is shown the geometry of the two gaskets, the sealing components interposed between the case and the two end-plates (see point 2 of Figures A4.11 and A4.12). In this representation these seals, used for hydraulically balance in axial direction (Y-direction) the lateral bushings with the aim of avoiding misalignments between gear shafts and journal bearings, are spaced in the Y-direction by an interval equal to the thickness of the case. As mentioned above, even if they do not take place in the whole FE system and hence they will not be used in the analyses developed in Virtual.Lab environment, they will be useful for carrying out a solution that will make the global FE study of the mechanical system easier.

In Figures A4.14.a and A4.14.b is shown the geometry of the ergal plate component (see Figures A4.1.a and A4.3) that is connected to the pump by means of two aluminum screws and to the ground by four triaxial force sensors located as shown in Figure A3.3.b. As already detailed in *Section A4.1*, these sensors have been modelled by means of spring elements having the

nominal stiffness of each sensor as collected in Table A4.3. Observing this component figures, some indications can be given relating to the link that this elements have with the other forming the whole pump:

(1) Aluminum screws housing; used for joining together the pump case and the ergal plate.
(2) Plate housing; used for operational reasons (hole for the driving shaft) and for the centering in the assembly stage of physical components (see Figure A4.11.b).

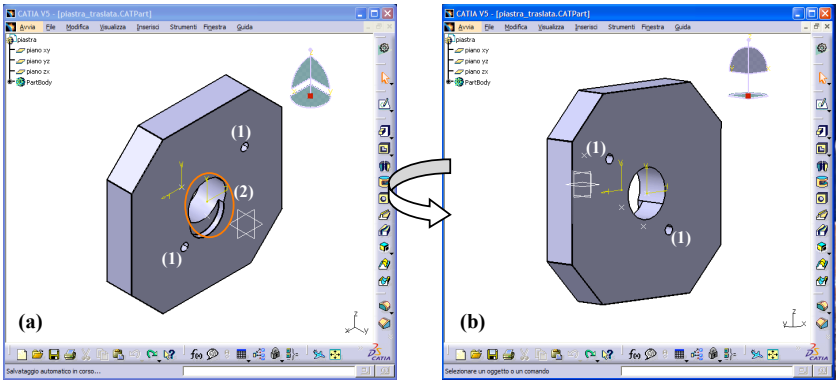

Figure A4.14 – Plate geometry, (a) front and (b) rear view.

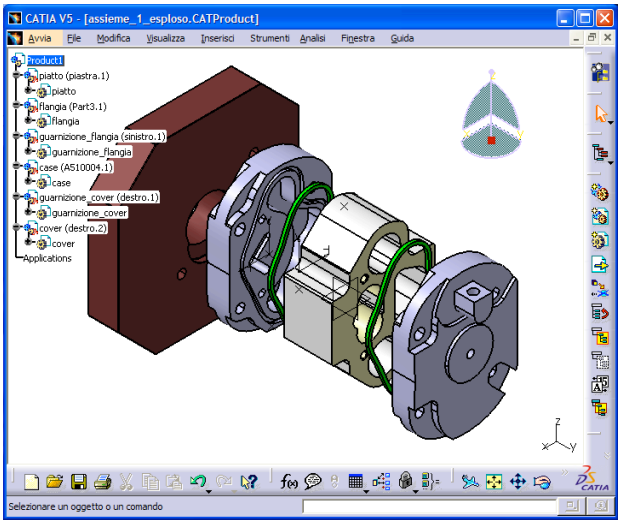

Figure A4.15 – Exploded view of the mechanical system.

In Figure A4.15 is represented an exploded view of the whole mechanical system under study without taking into account all the internal components. It is worth noting that each of these components has been subjected to a change in relation to the reference system, moving by the local reference frame (that characterize each individual component) to the global reference frame shown in Figure A4.8 (that characterize the whole FE model).

A4.3.2 Internal components

The internal mechanical components completing the whole mechanical system under test already presented in the previous chapter and shown in Figures A4.1.a and A4.1.b are the driven and driving gears, the relief valve and the bushings. It is worth remembered that all these components are housed inside the case component.

In Figure A4.16.a is shown the *bushing* geometry housed in the case component as depicted by Figures A4.2.b and A4.2.d. As already mentioned in the previous chapters these lateral floating bushings were taken as fix and parallel to the gear lateral side and used both for the centering of the gears and especially for separate low-pressure camera to high-pressure camera through the relief grooves milled in its internal face. This latter consideration, adopted for avoid the violent change in the pressure of the trapped volume between the twin gears that suffers a sudden volume reduction, is of considerable importance in relation to the modeling of the dynamic effects that are established during the pump working; aspect already treated in *Chapter A2*. On the other hand, with regard to solid modeling, and thus with regard to the creation of the FE model of the mechanical system under test, the presence of the relief grooves in the bushing does not involve significant considerations on the

effectiveness of the FE model. Therefore, because of this judgment and by the fact that the mass removed by the presence of the relief grooves would be insignificant compared to the total mass of the component, thus not making any improvement in the study of the whole system, the bushing will be created without grooves (see Figure A4.16.a). As described in *Section A4.3*, the placement of the lumped masses on the FE model is permitted through the introduction of some information in Virtual.Lab environment. These informations are those listed in the "*table properties*" depicted in Figure A4.16.b. However these values have already been reported in Table A4.2. It is worth noting that prior to introducing these values (inertia values) in the FE model it is important to verify that the local reference frame, by which the sub-components are created, coincides with the global one, by which all the sub-components are assembled forming the whole system (see Figure A4.15).

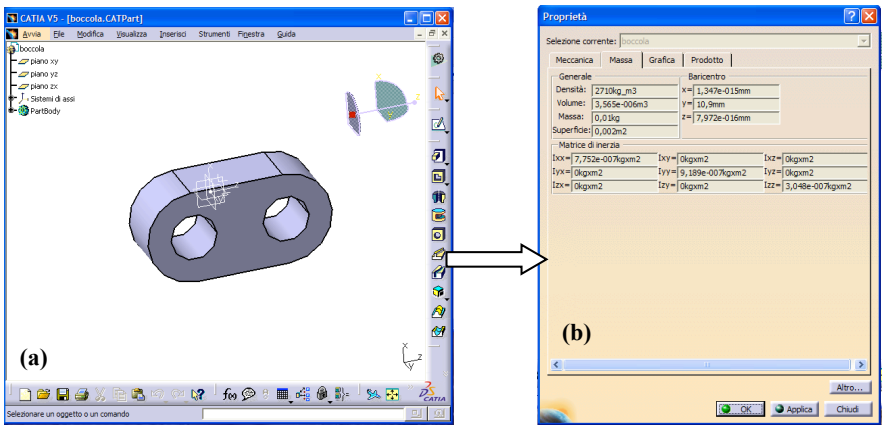

Figure A4.16 – Bushing (a) geometry and (b) properties.

In Figures A4.17.a and A4.18.a are shown the *driven* and *driving gear* geometry respectively, packed jointly with the floating bushings inside a case that encloses both components and defines the isolated spaces carrying the fluid from the low to the high-pressure chamber. The gears properties are listed in the form of Figures A4.17.b and A4.18.b.

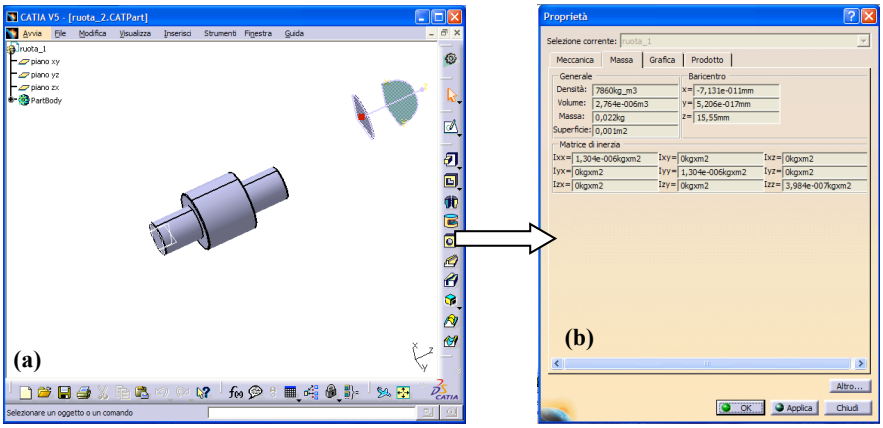

Figure A4.17 – Driven gear (a) geometry and (b) properties.

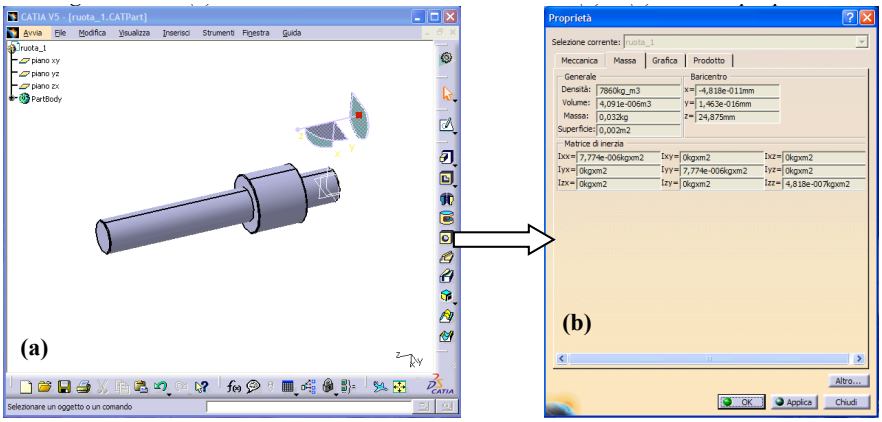

Figure A4.18 – Driving gear (a) geometry and (b) properties.

To create in CATIA environment the cylinder corresponding to the location of the teeth was chosen as radius, the primitive radius.

The case houses another component, the latter taken into account in this section, i.e. the pressure relief valve shown in Figure A4.19.a. This valve, as clearly shown in Figure A4.2.b, is not a simple cylinder like the one represented in Figure A4.19.a, but is composed by several internal components, each having different shapes, material and therefore different properties; thus producing difficulties in relation to the material that has to be adopted for modeling the valve. In order to remedy to this

inconvenient, it has been calculated the equivalent density of the component through the knowledge of the relationship between its volume and weight, quantities easily determinable having the physical component (see Figure A4.19.b). The properties of the relief valve are listed in the form shown in Figure A4.19.c.

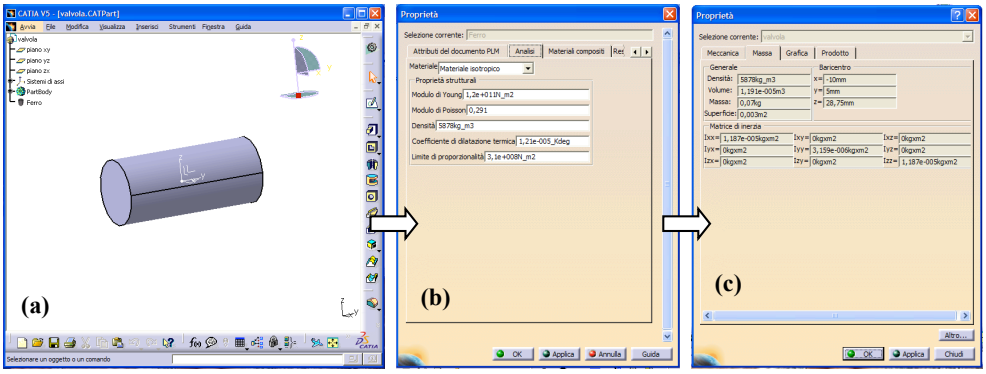

Figure A4.19 – Relief valve (a) geometry, (b) material and (c) properties.

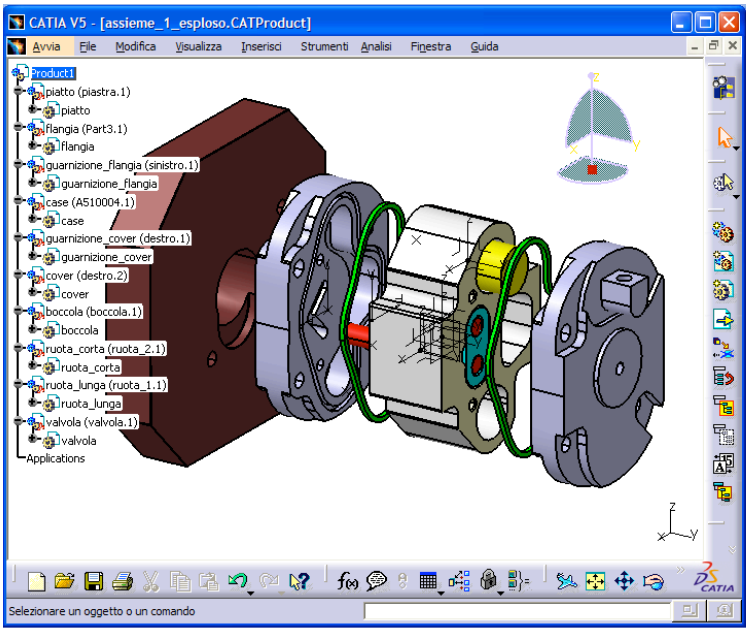

Figure A4.20 – Exploded view of the whole mechanical system including internal components.

In Figure A4.20 is represented an exploded view of the whole mechanical system under study including all the internal components. It is worth noting that each of these components has been subjected to a change in relation to the reference system, moving by the local reference frame (that characterize each individual component) to the global reference frame shown in Figure A4.8 (that characterize the whole FE model). Giving a quick look it is possible to note that all the components have been properly created both in relation to the dimensions and to the locations according to the global reference frame; in fact no penetration between surface components is found. It is worth noting that all the internal components will be eliminated and replaced by lumped masses using the informations outlined above.

A4.4 Arrangement of the external FE components

The external components, shown in *Section A4.3.1*, before being assembled in order to form a single FE model representing the whole mechanical system under test, must be prepared and arranged; for example the local reference systems of the components, each one characterized by the coordinates X, Y, Z, must be adjusted both in their orientation and location according to the global reference frame (coordinate X', Y', Z' of the reference frame shown in Figure A4.8), the materials must be set, the presence of the force sensors on the lower surface of the ergal plate must be modeled. All these suggestions will certainly make easier the next stage, which is the components assembly stage. The components that in this section will be subjected to this arrangement will be, the case, the end-plates and the ergal plate.

Firstly taking into account the case component, it is important to make a consideration on its geometry, which for operational reasons will change. In fact, the case will not be more

the one showed in Figure A4.10 but will become the one shown in Figure A4.21.c.

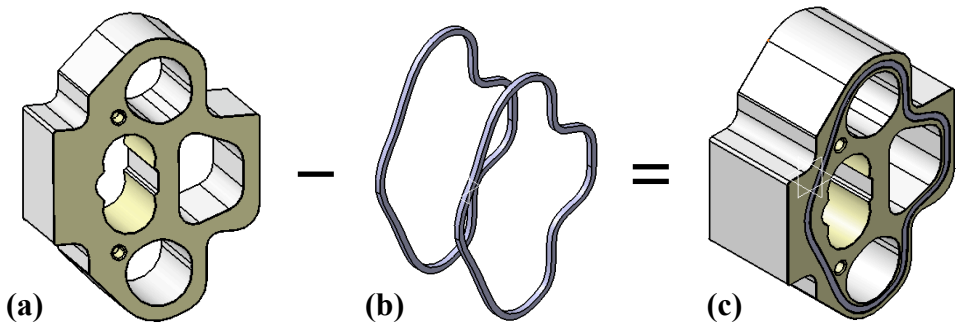

Figure A4.21 – (a) Original case, (b) rubber seals and (c) modified case geometry.

In essence, the modified case is obtained by subtracting the "original" case with the rubber seals (see Figure A4.13 and A4.21.a). This expedient has become essential to facilitate the union of the external components forming the gear pump. Specifically, to facilitate connecting operations between neighboring nodes of different component mesh; for example the connection between the surfaces of the case and the two end-plates. More details about these connections can be found in *Section A4.5*. The presence of the grooves generated on the axial surfaces of the case by the rubber seals can provide reference points, otherwise null, in order to achieve a precise and accurate connection between neighboring nodes of different components mesh. Furthermore, as it is clear from Figure A4.21, the characteristic dimensions of these grooves are considerably lower compared to that of the case, thus producing on the component negligible effects from the vibratory point of view. Therefore the analysis carried out using this "modified" case will not be affected by the presence of these micro-grooves.

The case component is placed in the assembled vision between the flange and the cover. The contact between the surfaces of the case and the adjacent surfaces of the end-plates is

modeled by means of rigid spider elements (Card RBE2 in Nastran). Moreover the centering of the end-plates on the case component is facilitated by the presence of four pins, two between the case and the cover and the latter between the case and the flange (see Figure A4.2.d). The presence of these pins is modeled by means of the same elements used for the simulation of the contact between surfaces. The rigid spider connections (blue element in Figure A4.22), which are nothing more than elements characterized by infinite stiffness values, are then applied in the positions where the pin are located, thus connecting the nodes of the case mesh on the outer circumference of the pins housing. Of course it is important to define the degree of the constrained DOFs of these nodes, which are the nodes linked together through these rigid spider. In this case, the nodes of the mesh have been completely constrained (all the displacements and rotations are contrained) due to the fact that the pin blocks any movement or rotation on the areas next to it. The same procedure is repeated for each pin location on the case component.

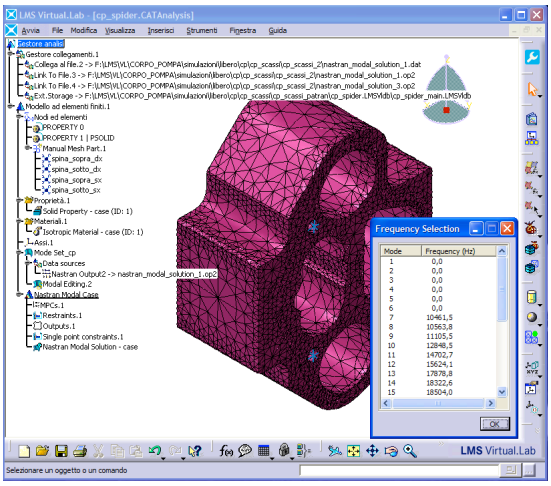

Figure A4.22 – Rigid spiders (in blue) applied on the pin housing.

In Figures A4.23 and A4.24 are shown the updated model of the flange and cover component respectively. For these

components a number of rigid spider connections higher than that seen for the previous component has been set. Indeed, both these components, similarly for the case component, show in addition to the pin housing the presence of four holes located at their "corners".

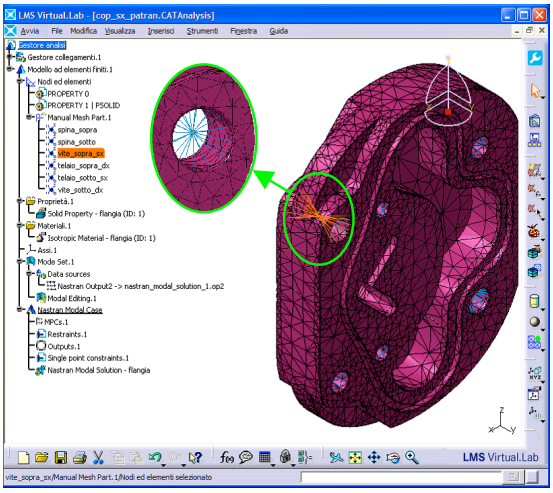

Figure A4.23 – Rigid spiders (in blue) for modeling pin and screws on the flange component.

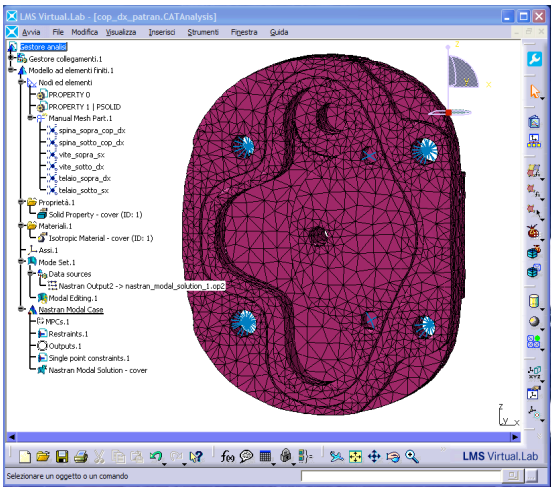

Figure A4.24 – Rigid spiders (in blue) for modeling pin and screws on the cover component.

This is due to the presence in the whole system of two screw pairs; two for keeping compact the gear pump assembly and the latter two to join the pump with the ergal plate. These holes must be modeled in order to simulate the presence of these screws. The methodology used in order to achieve this behaviour is the same as that used to model the presence of the pins (see blue connection in the figures below).

In relation to the plate component additional considerations must be carried out to those made for the other three components. The difference does not consist in modeling the screw locations, which are obviously modeled in the same manner as the previous cases, but differs because of its link with the surrounding environment. In fact, the case and the two end-plates are studied under free-free conditions, while the plate is connected to ground by four triaxial force sensors located as shown in Figure A3.3.b.

The presence of each of these sensors, positioned on the lower surface of the plate, is highlighted in its FE model by the application of some "*definition points*" also called "*IO points*" (see Figure A4.25). These elements, represented as yellows spheres, are considerably important in the creation of the FE model because they enables to:

- Attach loads on the nodes selected in the FE model;
- Select input and output points on the transfer functions set;
- Select input and output points in the analyses cases;
- View and identify more effectively the nodes on the component mesh.

Obviously these IO points will be applied on some specific nodes of the component mesh. Therefore, the nodes chosen to model the presence of the four sensors has to be found at their centers, because of their finite dimensions (red circles in Figure A4.25).

These sensors have been modelled by means of spring elements having the nominal stiffness of each sensor as collected in Table A4.3. Through the help of the IO points is now easy to

find the application point of these spring elements.

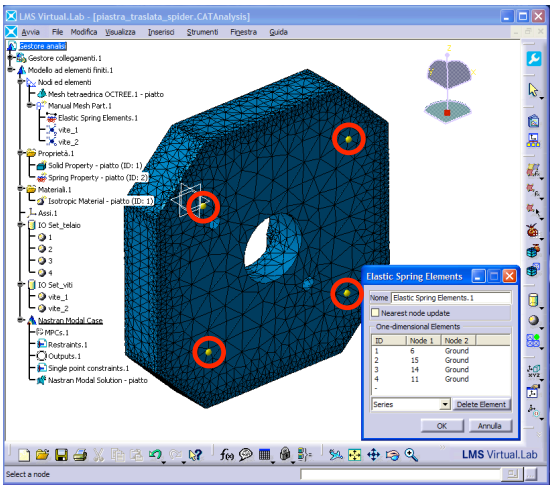

Figure A4.25 – IO points (in yellow) defining the four force sensors positions (red circles).

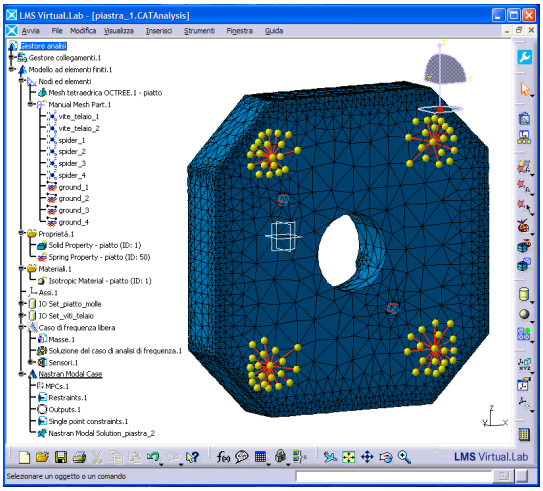

Figure A4.26 – IO points (in yellow) defining the four force sensors.

In reality, the force sensors applied on the lower surface of the plate have finite dimensions. Therefore, to achieve a realistic modeling, these sensors cannot be approximated to a single node. In other words, the contact areas between sensors and plate are

not covered by a point but by an area having extension equal to that of the sensors used. To get around this inconvenient the number of IO points directly applied on the plate mesh has been increased (see Figure A4.26). In order to simulate the presence of a rigid element such as the force sensor, these IO points have been connected together by means of rigid spider elements. In particular, each node has been connected to a single central node, on which the spring element has been applied (see red connections in Figure A4.26). Finally, these spring elements (not visible in figure) are joined to the plate mesh by means of rigid spiders.

A4.5 The global FE model creation

In this section a single file containing all the informations regarding the whole mechanical system on which will be performed the modal analysis and the FRF analysis will be generated. This FE model will include: (i) all the FE models of the external components already presented in *Section A4.4* and (ii) all the internal components having the properties and characteristic already described in *Section A4.3.2* and placed in the model in the form of lumped masses. Figure A4.27 shows the FE model of the mechanical system under test.

Giving a look at the items listed in the "*modeling tree*" exposed on the left side of the figure below it is possible to note that:

- Under the item "*Nodes and Elements*" are listed all the properties and the geometries of all the components forming the complete FE model. In detail are listed: (i) four properties (Card PSOLID in Nastran) regarding the presence of four solid elements (case, flange, cover, plate), (ii) three properties (Card PELAS in Nastran)

regarding the presence of the spring elements on the lower surface of the plate (X', Y' and Z' directions) and, (iii) one property (Card RBE2 in Nastran) relating to the presence of rigid connections between nodes of the mesh components (screws holes and pin housing).

– Under the item "*Materials*" are listed all the materials of the components forming the assembly; each characterized by an identification number: 1 for the flange, 2 for the case, 3 for the cover and 5 for the plate.
– Under the item "*Properties*" are listed the properties that link the components to the corresponding materials and the stiffness parameters in the X, Y and Z directions to the springs elements.

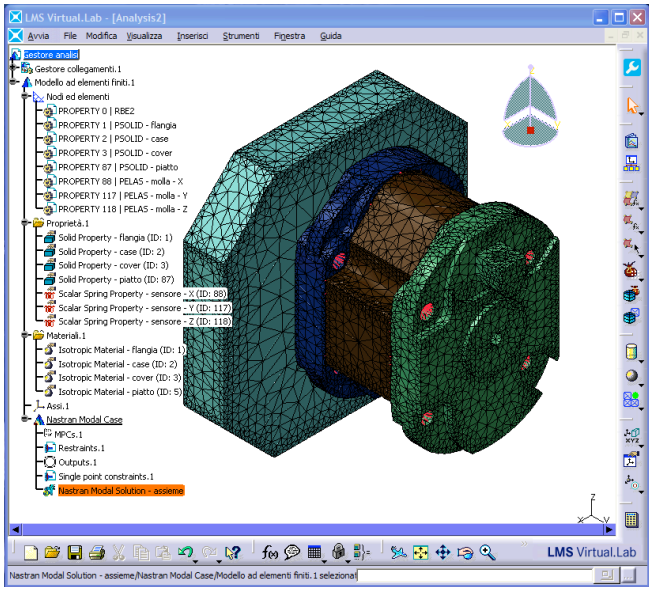

Figure A4.27 – FE model of the mechanical system under test.

Completed this first stage it is possible to continue with the introduction of additional components in order to ultimate the creation of this FE model, thus making it as close as possible to the real mechanical system under test. In the following will be introduced the clarifications regarding the introduction in the FE

model of the remaining components, which are identified by (i) two steel screws to make compact the gear pump, (ii) two aluminum screws to join the pump with the ergal plate and (iii) the internal components including the oil. Moreover will than be introduced the explanation of the step used to model the (iv) union of all the components forming the whole mechanical system, in order to simulate the real contact between the surfaces of the components and thus the real behaviour of the system assembled.

In the gear pump, the case and the two end-plates are fastened together by means of two steel screws (M6, length 65 mm) as shown in Figure A4.1.b and Figure A4.2.a. The two screws, by means of the tightening torque guarantee the connection between the case and the end-plates. The two screws have been modelled with beam elements having the same cross section area and inertia properties of the actual screws. These screws are than joined to the surrounding mesh of the cover and the flange by means of rigid spiders as shown in Figure A4.28 (see green line).

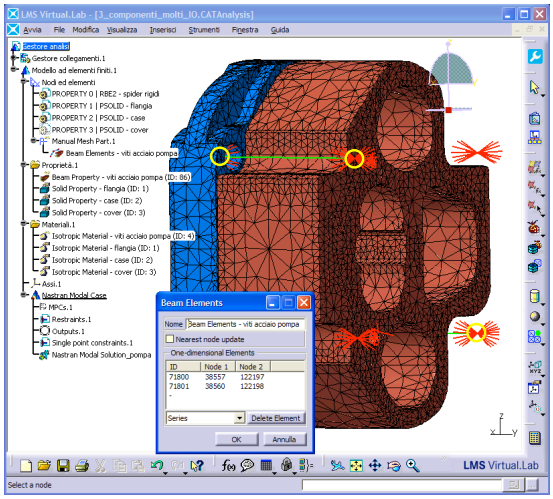

Figure A4.28 – Steel screws introduction in the FE model.

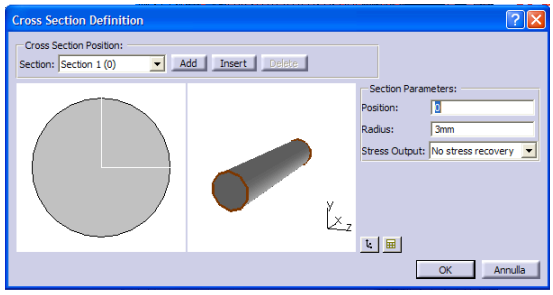

Figure A4.29 – Table for the cross section definition.

The introduction of these beam elements in the model is simplified by the preparation procedure brought about on external components performed in the previous section. In fact, the nodes on which the beam elements must be connected (see yellow circles in Figure A4.28) have already been defined in the previous section by modeling the screw holes through rigid spider elements (see also red connection in Figure A4.28). In order to complete the characterization stage of the screws in the model, in addition to the choice of their reference frame according to the global, it is important to define the type of beam section. In the table shown in Figure A4.29 are listed the geometrical dimensions that characterize the steel screws such as the cross section parameters (radius 3 mm because of an M6 screw).

Obviously the same considerations made for the steel screws are still valid for the aluminum screws, used for the union of the gear pump with the plate. Apart from the material, the only difference is due to the creation of four beam elements instead of two (as defined in the previous study case). This is because the aluminum screw must pass through three different components: the cover, the flange and the ergal plate. Therefore, it is essential to firstly connect one component to the following through one beam element (the cover and the flange), just like for the steel screws, and finally connect the flange with the ergal plate. Figure A4.30 graphically reflects this view. The region highlighted in blue defines the first beam connection (cover-flange) whereas the green one highlights the second beam connection (flange-plate).

It is worth noting that the mechanical characteristics of these screws have already bean introduced in Table A4.1 in *Section A4.1*.

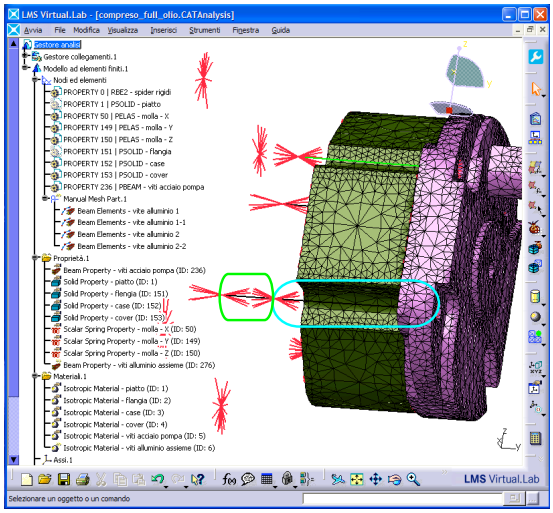

Figure A4.30 – Aluminum screws introduced in the FE model.

The tightening torque has not been applied to the screws in the model because it represents a static torque and therefore it has no contribution in a dynamic analysis. Moreover, the tightening torque produces the effect of joining the case surface to the end-plates surfaces. Therefore, in order to model this, rigid spider connections (Card RBE2 in Nastran) have been used in order to connect the case surface with the end-plates surfaces as shown in Figure A4.33.

Giving a look at the items listed in the "*modeling tree*" exposed on the left side of the figure above and comparing it with the one presented in Figure A4.27, it is important to note that the items listed under "*Nodes and Elements*", "*Properties*" and "*Materials*" have increased in number. This increase is due to the introduction in the FE model of new elements such as the screws. In other words, each component introduced in the model will take place in its modeling tree thus allowing the designer to quickly and precisely note any variation in the FE model; thus

consequently allows to precisely and carefully localize appropriate changes or improvement on the model created.

The presence of the pump internal components (gears, bushings, oil and relief valve) and their introduction in the FE model will be explained below. As already introduced, each of these components has been modelled by means of a concentrated mass and relative inertia momentum (Card CONM2 in Nastran) located on its centre of mass and connected to the surrounding mesh by means of interpolation spiders (Card RBE3 in Nastran). Table A4.2 lists all these internal components properties and how they appear in the FE model is shown in Figure A4.5. Thanks to the creation of these internal components in CATIA environment (see *Section A4.3.2*), their inertia and mass values are available, while, thanks to the global reference frame adopted for the assembly stage (see Figure A4.8) and to the locations of these internal components within the case, it is possible to define their application positions. In other words through the knowledge of these informations it is possible to clearly define the nodes on which the lumped masses has to be applied (centre of mass of the component). These nodes will be used only as a reference point for the introduction of the lumped masses (see for example the green point shown in Figure A4.31). Figure A4.32 shows the lumped masses that identify the internal components (in red) and consequently their application nodes. In yellow are also represented the interpolation spider elements that allow to model the connection between these internal components with the surfaces of the case in which they are housed.

Simply counting the number of concentrated masses depicted in Figures A4.5 and A4.32, it is possible to note a discrepancy between this number (5) and the number of internal components listed in Table A4.2 (6). The missing node or the missing mass is that related to the bushings. Its absence is permitted on a purely geometric feature. Looking at Figure A4.2.b can be seen that the two bushings are applied in the same manner on the spur gears and all housed in the same case cavity.

So, instead of further complicating the model with the introduction of additional nodes, lumped masses and connections through spider elements between the nodes of the mesh, it is much easier to sum up the mass of a bushing with that of one of the two gears, and the other bushing mass with that of the remaining gear.

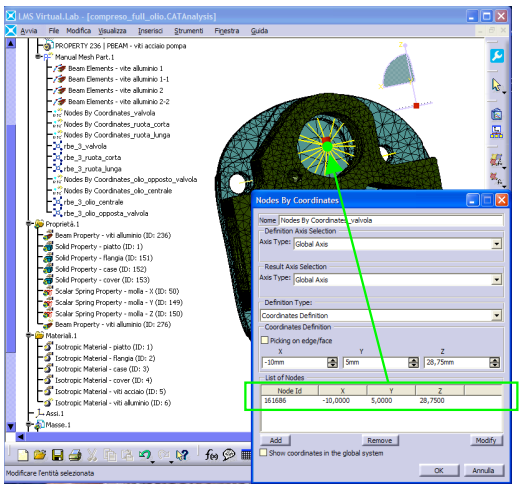

Figure A4.31 – Nodes (in green) for the exact identification of the lumped mass location.

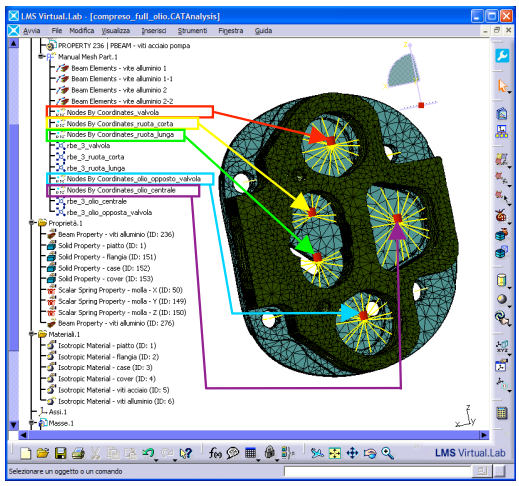

Figure A4.32 – Introduction of the internal component in the FE model.

In addition, because of the bush positions in the mechanical system under test, the sum of their mass with that of the two gears does not cause any change in terms of the coordinates for the application of the lumped masses. This solution simplifies the model without altering its validity, provided that the mass introduced relatively to the gears take into account the presence of the bushings masses. Therefore, the masses of the two gears will become: $m_{gear1} = 0.042kg$ and $m_{gear2} = 0.032kg$.

In order to simulate the real contact between adjacent surfaces of different components and to prevent their penetration has been used rigid spider elements, as already announced in the previous sections and shown in Figure A4.6. To accomplish this important task the IO Points have been used, already defined in *Section A4.4* regarding the arrangement of the plate. Basically, wanting to join two adjacent surfaces of generic components, the methodology used will be the follows:

- Create a first IO Point set for the first surface component. If the number of IO Point defined for the surface is too extensive, it is desirable to achieve a set of IO Point defined for each zone or sector of the surface of the component that has to be connected.
- Create a second IO Point set for the second surface component. The same consideration outlined for the first point is still valid.
- Create the connections through the rigid spider element. The two IO Point set defined in the two previous methodology point simplifies this operation. In fact, at this stage, each IO Point contained in the first set has to be connected with that contained in the second set through rigid spider.
- Perform the same procedure for all the component pairs in contact.

Some considerations regarding the step just exposed can be made in order to simplify the operations. With regard to the

definition of the IO Point at the nodes of the mesh of the components that has to be linked, it is important to adopt an identification number. This number will allow the designer to find easily which pair of nodes, contained in both the IO set, has to be connected. Considering for example the connection between the upper surface of the case and the lower surface of the flange. Due to the high number of nodes on both the surfaces that has to be linked, the choice of the nodes belonging to the two surfaces to be connected become really difficult and time-consuming. To overcome this problem is important to find homologous reference points on the two surfaces. The complexity of the geometry of the case and of the flange and the lack of reference points and/or zones that can help in the selection of the nodes to be connected, it has opted for modeling the case component as illustrated in Figure A4.21. The groove generated in both the surface of the case allows having a guide, which if followed by the designer provides clear reference points for the connection of the nodes. Therefore, as illustrated in Figures A4.33.a and A4.33.b, along this groove are applied several IO Points (yellow spheres) both in the surface of the case and in the surface of the flange. Obviously, the higher the number of IO Point in the model, the higher the number of connection and the higher the accuracy of the solution.

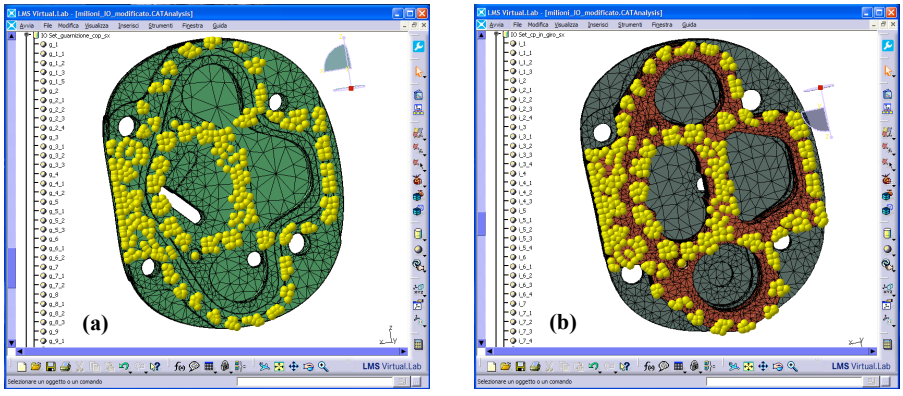

Figure A4.33 – IO Points used for realizing the connection between (a) the flange and (b) the case surfaces (only one visible in the figure above).

Figure A4.34.a and A4.34.b show the IO Point set introduced in the model in order to simulate the connection between the plate and the flange. Figure A4.35 shows rigid the connections by means of rigid spider elements using as guide the IO Points previously generated.

The same considerations can be applied for connecting the case with the cover.

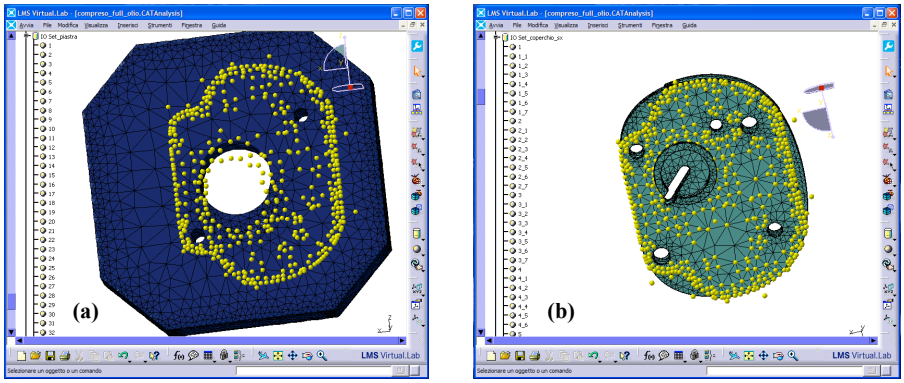

Figure A4.34 – IO Points used for realizing the connection between (a) the ergal plate and (b) the flange surface.

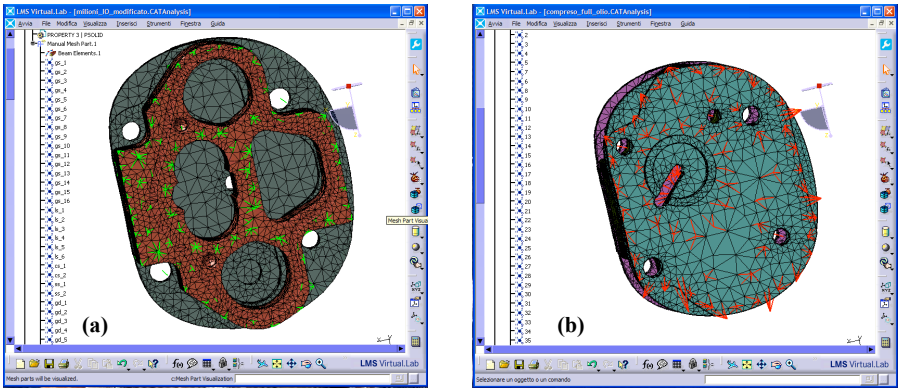

Figure A4.35 – Rigid spider elements (in red) used for realizing the connection between (a) the case and the flange and (b) the flange and the ergal plate (not visible in the figure above).

A4.6 Dynamic analyses using the FE model

The first dynamic analysis performed using the FE model described above is a modal analysis (SOL 103 in MSC.Nastran) with the aim of evaluating the fundamental eigenfrequencies and mode shapes in the frequency range of interest (till 6 kHz). Furthermore, an FRF analysis (SOL 111 in MSC.Nastran) has been carried out to estimate the accelerations in some locations of the gear pump external surfaces and to compare them with the accelerations acquired by experiments. The damping values introduced in the FRF analysis has been estimated by means of an experimental modal analysis, as described in *Section A4.7*.

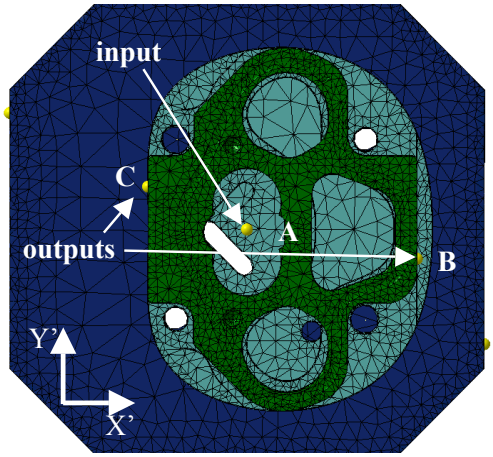

Figure A4.36 – Input and output point set in the FRF analysis.

In particular, the input point (A) has been located in the centre of the cavity where the gears are housed, as seen in Figure A4.36 and the output points (B and C) have been placed in the two opposite external surfaces of the case. As can be clearly noted by Figure A4.37, the input node is connected with the nodes of the surrounding mesh by means of interpolation spider. These connections are performed in the same manner as that carried out for the lumped masses (see *Section A4.5*).

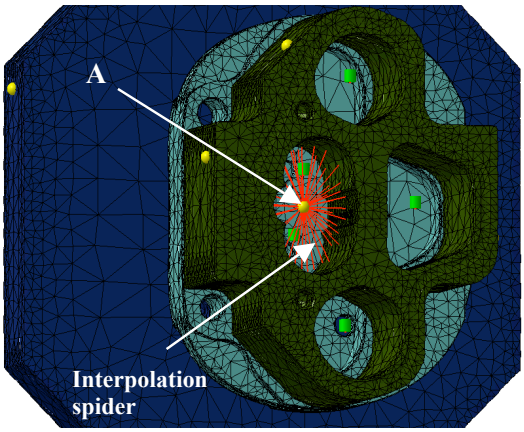

Figure A4.37 – Input point (A) connected with the surrounding mesh by means of interpolation spider (in red).

Let us denote with $H_{i,j}$ the FRF between a force applied in the j-point (input) and the acceleration measured in the i-point (output); so for example $H_{Bx',Ay'}$ denotes the FRF where the input force is applied at the point A in Y'-direction and the acceleration is calculated in the point B and X'-direction.

Let us analyse the simulation results in terms of eigenfrequencies, eigenmodes and FRFs. Table A4.4 collects the first 10 eigenfrequencies of the FE model described in the previous sections. The first natural frequency (at 2143Hz) represents a bending mode around the Y'-axis and therefore the nodes of the pump case have prevalent movement in X'-direction. This behaviour is confirmed by the FRF analysis, in fact, the $H_{Cx',Ax'}$ (FRF with input in A and output in C along the X'-direction) shows, at such a frequency, a peak (see Figure A4.38). The second eigenmode (at 2378Hz) represents a bending mode around the X'-axis and therefore the nodes of the pump case have prevalent movement in Y'-direction. The situation is opposite to what happened in the first mode, in fact the FRFs with excitation in Y'-direction show a peak (Figure A4.38 in green line). In the third mode at 4135Hz, the deformation involved mainly the ergal plate in Z'-direction, and therefore the pump nodes will have a

displacement in Z'-direction; so none of the calculated FRFs can show a peak at that frequency because these FRFs refer to X'- and Y'-directions. Finally, the 4th mode at 4189Hz is a torsional mode, in which the pump case has a displacement mainly in the X'Y'-plane, so this natural frequency can be found in FRF plot as depicted in Figure A4.38.

	1^{st}	2^{nd}	3^{rd}	4^{th}	5^{th}	6^{th}	7^{th}
Eigenfrequency [Hz]	2143	2378	4135	4189	4736	4836	5063

Table A4.4 – Eigenfrequencies.

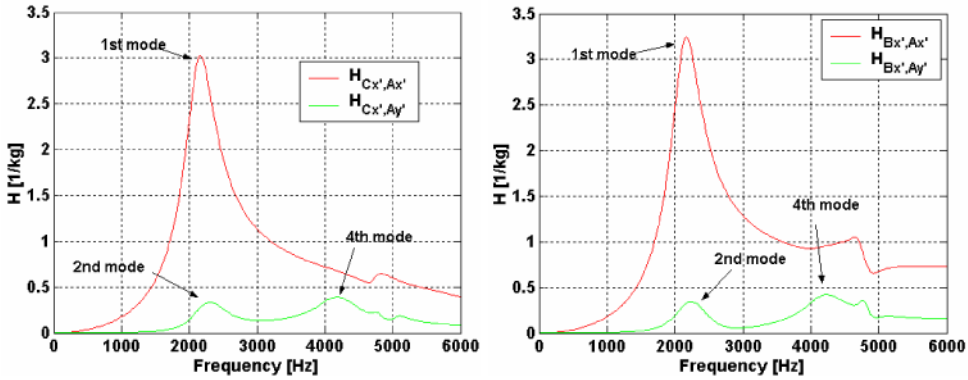

Figure A4.38 – FRF amplitudes: (a) comparison between $H_{Cx',Ax'}$ and $H_{Cx',Ay'}$ and (b) comparison between $H_{Bx',Ax'}$ and $H_{Bx',Ay'}$.

A4.7 Experimental tests

A4.7.1 Experimental modal analysis

An experimental modal analysis (EMA) of the whole system

composed of the pump and the ergal plate, where the pump is fastened to the plate, has been carried out to evaluate the modal damping as a function of frequency. The system under study is a complex system due to the clearances between each subcomponent and due to the presence of the lubricant oil; therefore the system is highly non-linear and the results of the experimental modal analysis (EMA) can not easily compared with the results of the FE modal analysis described in *Section A4.6*. The results of the EMA will be only used in order to evaluate a global damping value as a function of frequency that has been used in the FE dynamic analysis (FRF analysis described above). The comparisons with the hybrid model will be performed in terms of FRFs (as shown in *Section A4.8*). Six PCB piezoelectric accelerometers (frequency range 1 to 10000 Hz) are mounted on the pump case and on the ergal plate as shown in Figure A4.1.b in order to measure the response in terms of acceleration. Moreover a hammer PCB 068C04 has been used to excite the system in 24 measurement points both in direction X' and Y' (see Figure A4.39.a). The procedure used in order to perform the EMA is the conventional procedure in which both excitation and response are measured simultaneously for obtaining the so-called *Inertance*, i.e. the FRF between acceleration and force. The response points have been maintained fixed during the test, while the excitation moves from one measurement point to another in order to obtain the FRF among all the considered points. The signals were acquired using a sample frequency of 40960 Hz and frequency resolution of 1.25Hz; furthermore the FRFs are calculated by using the H1 estimator available in LMS Test.Lab. Figure A4.39.b shows the PSD of the hammer force concerning all the measured points: it is effectively excited the frequency range up to 7 kHz, which includes the frequency range of interest. Curve-fitting methods have been used in order to evaluate the modal parameters: they can operate both on the response characteristics in the frequency domain, i.e. on the frequency response functions themselves, and in the time domain as well. The latter method

uses the fact that the Inverse Fourier Transform of the FRF is itself another characteristic function of the system that represents the response of the system to a single unit impulse as excitation. In particular, two modal parameter extraction methods have been used: the LSCE method (Least Square Complex Exponential) operating in the time domain and the PolyMAX method operating in the frequency domain, both available in LMS Test.Lab.

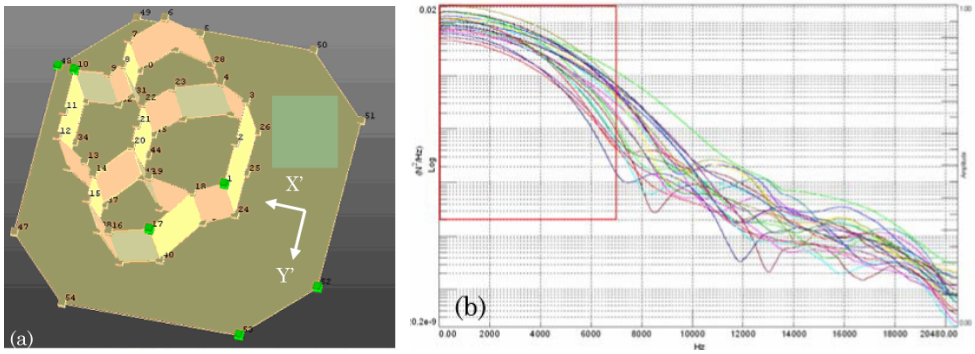

Figure A4.39 – (a) Measurement points and (b) power spectrum density (PSD) of the excitation force concerning all the measured points.

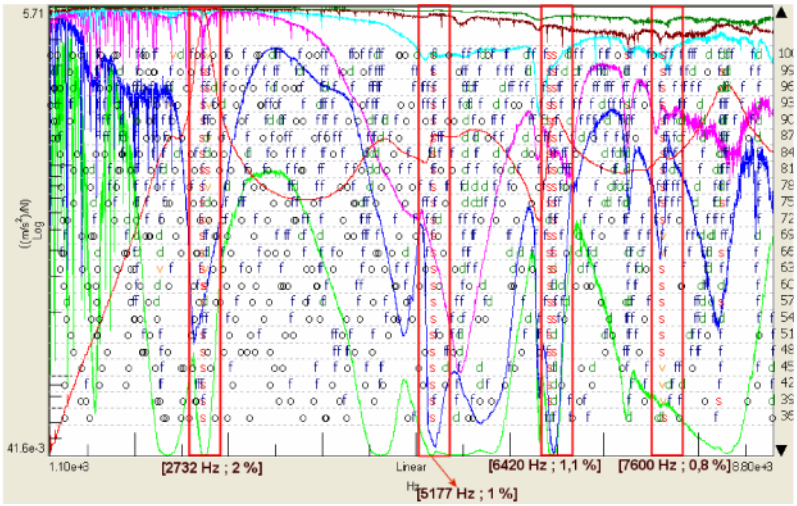

Figure A4.40 – Stabilization diagram obtained using LSCE.

The complete formulation of such methods can be found in [2 *PART B*]. As an example, the stabilization diagram obtained using the LSCE method is depicted in Figure A4.40 in order to show the complexity of the analysis; once the stable poles have been chosen, the modal damping can be evaluated. Figure A4.41 depicts the modal damping in the frequency range of interest obtained averaging the values coming from the LSCE and PolyMAX methods.

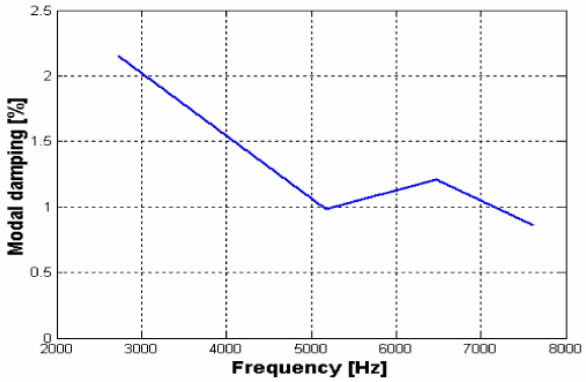

Figure A4.41 – Model damping (in percentage) as a function of frequency of the whole system composed by the pump and the plate.

A4.7.2 Run-up tests

The tests were carried out on a test bench available at TRW Automotive Italia SpA, see Figure A4.1.b, that is the same test bench used for the validation of the LP model (*Chapter A3*). Two PCB piezoelectric accelerometers (frequency range 1 to 10000 Hz) are mounted on the pump case as shown in Figure A4.1.b in the locations identified by the points B and C, in order to measure case accelerations (see also Figure A4.36). Two linear run-up tests from 2000 to 3350 rpm, with operational pressure of both 34 bar

and 90 bar, have been conducted with this apparatus. The acceleration signals were acquired and processed using LMS Scadas SC305 Front-end controlled by software LMS Test.Lab. The run-ups were acquired using sampling frequency of 25.6 kHz and frequency resolution of 0,78 Hz. During the run-up tests 57 spectra (from 2000 to 3350 rpm) of the accelerometer signals in the points B and C were acquired. These spectra are shown as waterfall maps in *Section A4.8*, Figure A4.43 to Figure A4.46.

A4.8 Validation of the FE/LP model

In this section the experimental accelerations measured during the run-up tests in the points B and C (Figure A4.1.b) will be compared with the simulated accelerations coming from the model. In order to evaluate the simulated accelerations, the FRF analysis described in *Section A4.6* has been performed using as damping the modal damping evaluated by the EMA described in *Section A4.7.1*. Moreover, the parameters of the FE model were preliminarily evaluated on the basis of design data (Young modulus, density, spring stiffness, etc) as shown in Tables A4.1, A4.2 and A4.3 and then the spring stiffness between ground and ergal plate are tuned in order to better match the experimental results obtaining the values collected in Table A4.5. Therefore, from the FE dynamic analysis the following four FRFs can be calculated:

- $H_{Cx',Ax'} \rightarrow$ FRF with input in A (X'-direction) and output in C (X'-direction).
- $H_{Cx',Ay'} \rightarrow$ FRF with input in A (Y'-direction) and output in C (X'-direction).
- $H_{Bx',Ax'} \rightarrow$ FRF with input in A (X'-direction) and output in B (X'-direction).

– $H_{Bx',Ay'} \rightarrow$ FRF with input in A (Y'-direction) and output in B (X'-direction).

Then, the dynamic forces calculated by means of the LP model to obtain the case accelerations multiply each FRF.

	X'-direction	Y'-direction	Z'-direction
Stiffness [N/m]	3E8	3E8	2.6E9

Table A4.5 – Stiffness of the spring elements in the lower surface of the ergal plate (adjusted values).

The dynamic forces that will be multiplied with the above FRFs are the dynamic forces exciting the case and they consist in both the bearing reactions and the pressure forces both acting on the pump case. The LP model described in *Chapter A2* gives as outputs the dynamic forces acting on gears that obviously have the same modulus and direction but opposite sense of the forces acting on the case as shown in Figure A4.42. In order to maintain the validation procedure simple, the pressure forces $\left(f_p\right)$ and bearing forces $\left(f_b\right)$ acting on the case and depicted in Figure A4.42 have been summed obtaining a global force acting in the centre of the gear house (point A on the right side of Figure A4.42 and on Figure A4.36) and that can be decomposed in the X'- and Y'-direction $\left(F_{Ax'},F_{Ay'}\right)$.

In order to obtain the acceleration amplitude as a function of frequency in X'-direction in the point B $\left(a_{Bx'}\right)$ and in the point C $\left(a_{Cx'}\right)$ the following expressions have been used:

$$a_{Bx'}(f) = H_{Bx',Ax'} \cdot F_{Ax'} + H_{Bx',Ay'} \cdot F_{Ay'} \tag{A4.1}$$

$$a_{Cx'}(f) = H_{Cx',Ax'} \cdot F_{Ax'} + H_{Cx',Ay'} \cdot F_{Ay'} \tag{A4.2}$$

where $F_{Ax'}$ and $F_{Ay'}$ are the spectrum of the global dynamic forces acting on the point A in X'- and Y'-directions, respectively. The input point A of the FE model is then connected to the surrounding mesh (gear house) by means of interpolation spiders (see Figure A4.37). The spectrum of the accelerations on the points B and C $\left(a_{Bx'},a_{Cx'}\right)$ are obtained by multiplying the dynamic forces in X' and Y'-direction by the relative FRF estimated using the FE model.

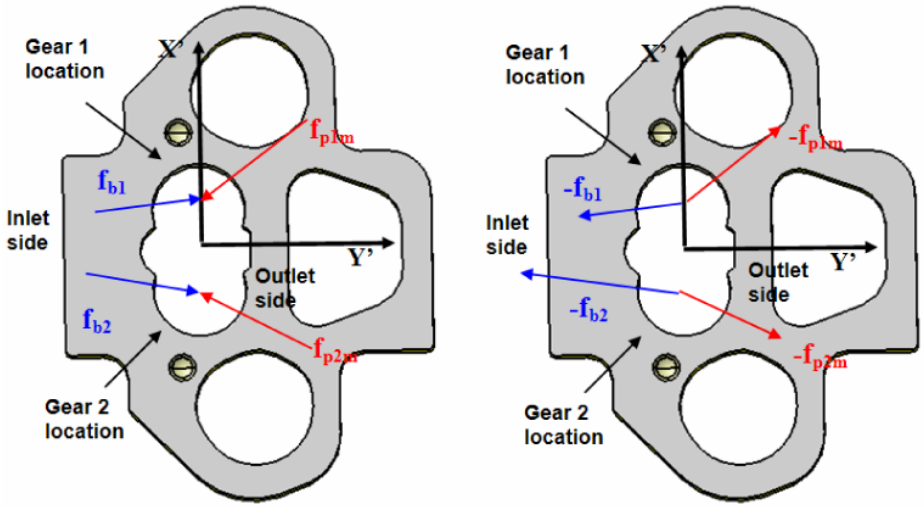

Figure A4.42 – Location and direction of forces acting on gears (left) and on the case (right).

In order to compare the simulation data $\left(a_{Bx'},a_{Cx'}\right)$, with the experimental run-ups, the dynamic forces obtained by the 27 simulations already conducted in *Chapter A3* at operational pressure of 34 bar and 90 bar and angular speed interval of 50 rpm from 2000 to 3350 rpm have been used. The simulations were carried out for a time corresponding to 48 meshing periods T, using display frequency of 48 kHz. For each simulation the dynamic forces $F_{Ax'}$ and $F_{Ay'}$ were evaluated and introduced in the expressions (A4.1) and (A4.2) for the evaluation of the

accelerations. Figure A4.43 to Figure A4.46 shows these accelerations, in terms of amplitude spectra as waterfall maps. About the comparison between the experimental and simulation spectral waterfall, it is worth noting that they have different resolutions: the frequency resolution is 0.78 Hz for experimental spectra and for the simulation ones it ranges from 8.3 to 14 Hz; the resolution in the rpm-axis is 20 rpm for the experimental spectra and 50 rpm for the simulation ones. The amplitude scale is the same for the pairs of waterfall relative to the same point and operational conditions.

The experimental waterfall maps (Figure A4.43 to Figure A4.46 on the left side) shows two resonance regions in the frequency range till 6kHz: at about 2.2kHz and at about 4kHz that can be clearly observed also in the simulation maps both in the measurement points B and C and at 34 and 90 bar as well. Moreover, the amplitude level is the same for the pairs of waterfall (simulation-experimental) relative to the same point and operational conditions. Therefore, the hybrid model is able to foresee the resonances of the system and to estimate the amplitude of the accelerations on the external surfaces of the pump. It can be noted that this validation procedure not only assesses the effectiveness of the FE model, but also can be considered as a global validation procedure for the hybrid FE/LP model since the validation procedure uses the dynamic forces coming from the LP model.

It is interesting to observe that in the validation procedure in *Chapter A3*, the pump case was considered rigidly fixed to the plate while herein the flexibility of both ergal plate and pump case has been taken into account by means of the FE method.

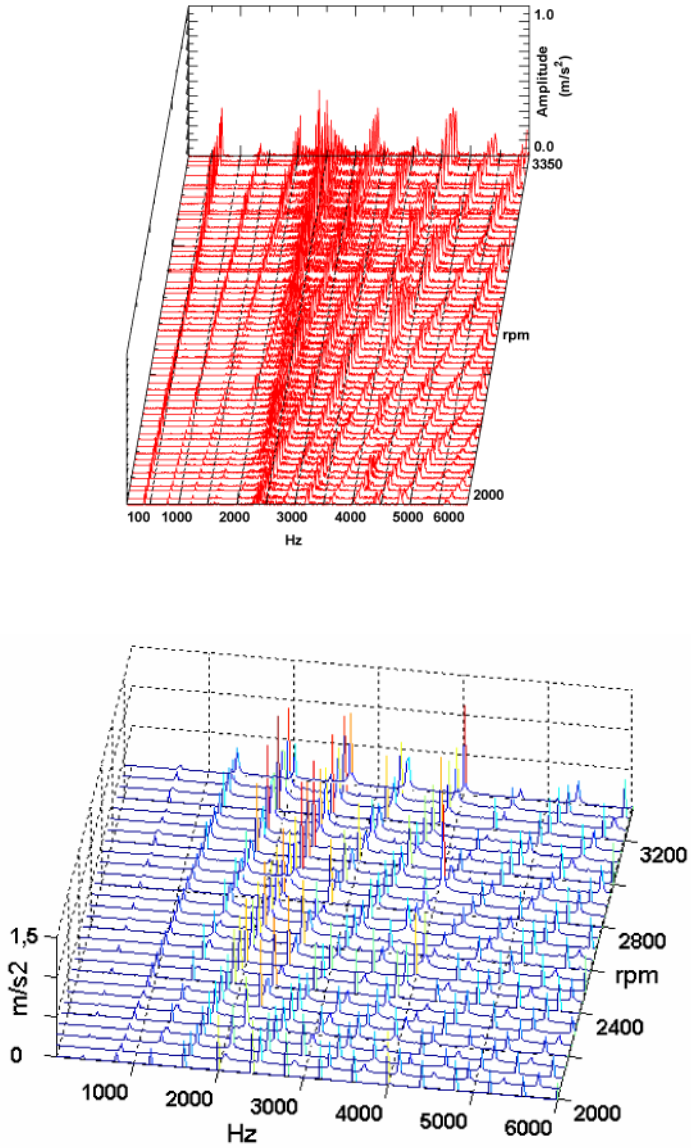

Figure A4.43 – Waterfall maps of acceleration spectra in point B at 34 bar: experimental (left) and simulation (right) results.

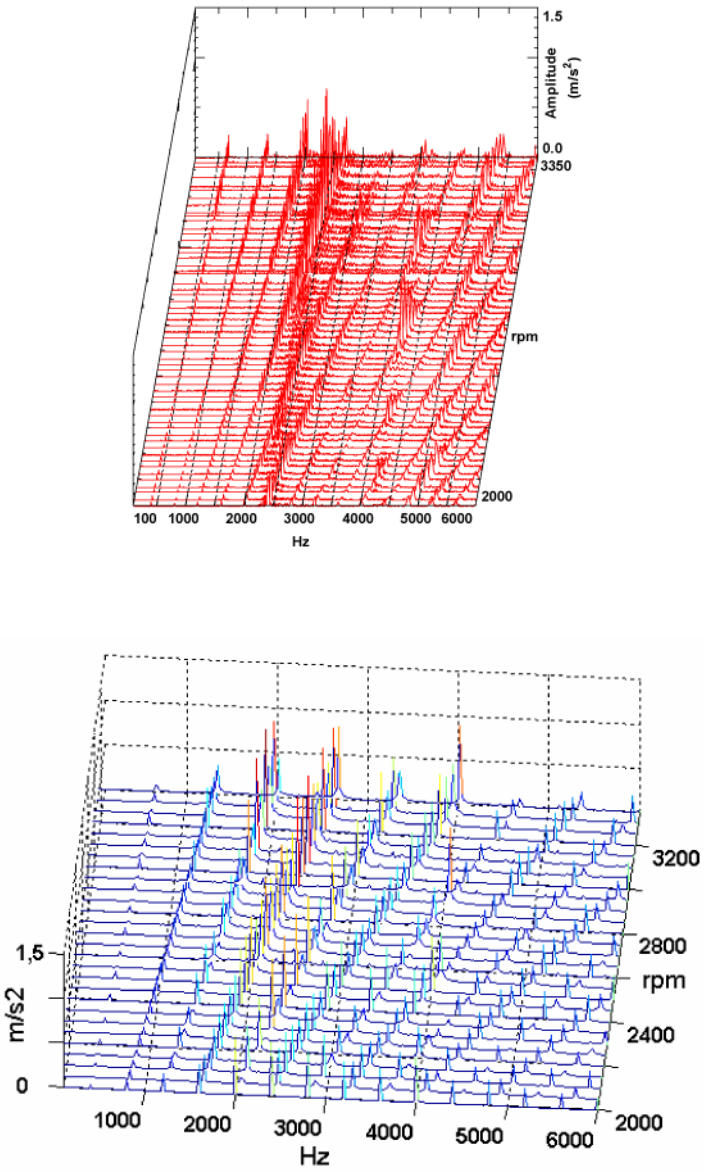

Figure A4.44 – Waterfall maps of acceleration spectra in point C at 34 bar: experimental (left) and simulation (right) results.

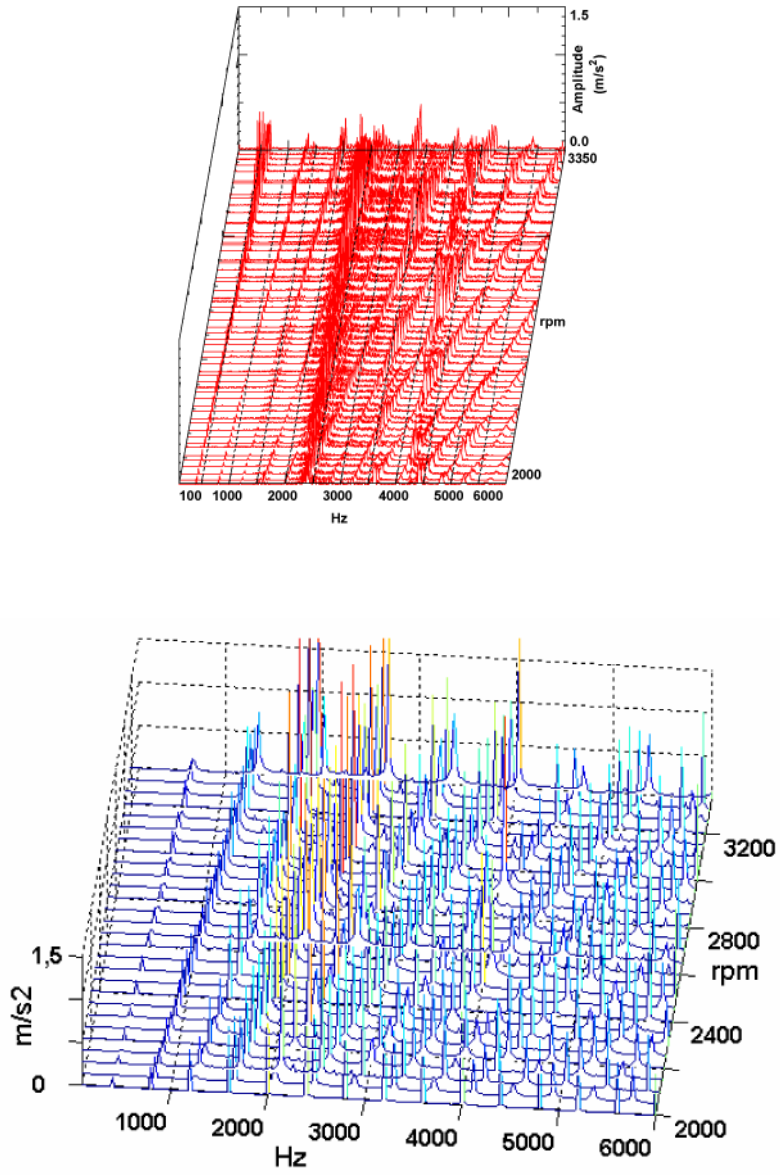

Figure A4.45 – Waterfall maps of acceleration spectra in point B at 90 bar: experimental (left) and simulation (right) results.

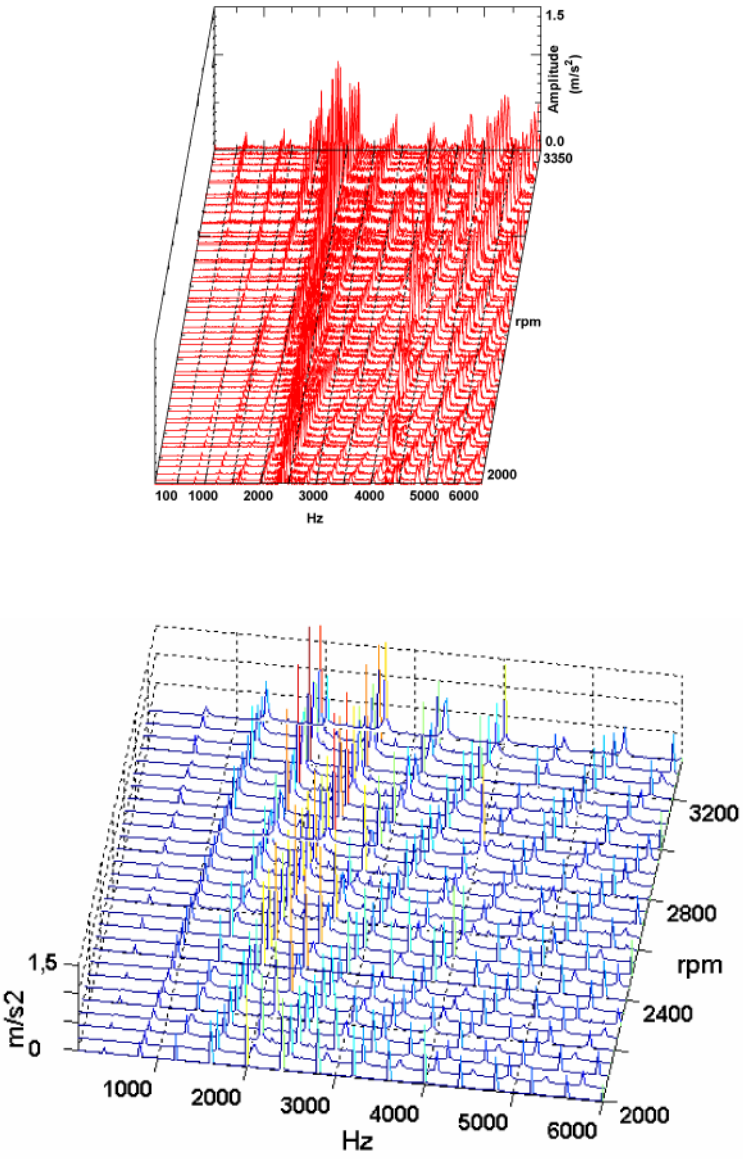

Figure A4.46 – Waterfall maps of acceleration spectra in point C at 90 bar: experimental (left) and simulation (right) results.

A4.9 Applications

As an example of application, the assessed hybrid FE/LP model will be used in this section in order to evaluate the external accelerations in case of design modification such as length of the relief grooves. The effect in terms of case accelerations by using the FRFs already estimated by the FE model and the dynamic forces coming from the LP model is shown through the following figures. In particular, Figure A4.47 and Figure A4.48 shows the comparison at 3350 rpm and 20 bar between the case acceleration in the points B and C with different kinds of relief grooves. It can be noted that the relief grooves with 2.9 mm length determine larger oscillations than with other relief groove lengths.

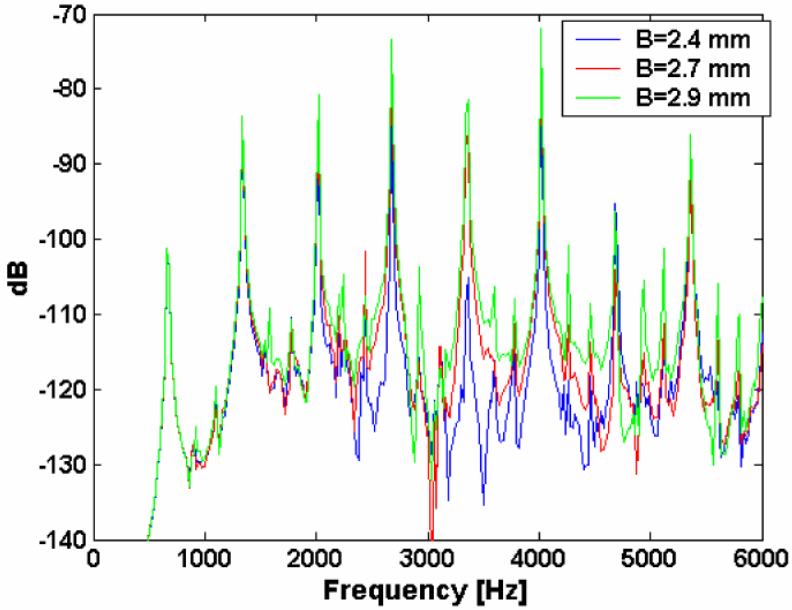

Figure A4.47 – Case accelerations at operational conditions of 3350 rpm and 20 bar with different dimensions of the relief grooves (length B of 2.4, 2.7 and 2.9 mm) in point B.

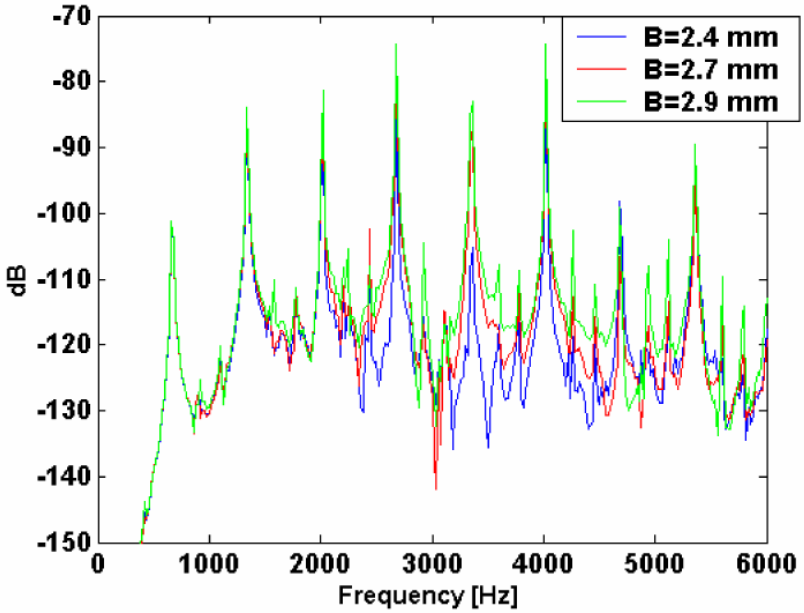

Figure A4.48 – Case accelerations at operational conditions of 3350 rpm and 20 bar with different dimensions of the relief grooves (length B of 2.4, 2.7 and 2.9 mm) in point C.

PART B

This second part of the thesis, identified as *Part B*, is firstly aimed at reviewing structural modification techniques and secondly, at establishing a new methodology for vibration reduction by the application of damping patches to selected component areas. This methodology can be applied to improve the dynamic characteristics of a generic system, such as the external gear pump considered in *Part A,* or any other mechanical system.

The dynamic characteristics of a structure, in particular its natural frequencies and mode shapes, are determined by its mass, stiffness and damping distributions. The properties provided by

these distributions are often called the structure spatial properties. Its natural frequencies and mode shapes are its modal properties. Spatial properties are often quantified using a mathematical model of the structure, such as a finite-element (FE) model. This model translates the physical properties of the structure, such as its dimensional, geometrical and material properties, into distributed mass and stiffness properties. Structural modification using an FE model can be determined in terms of mass and stiffness changes. Changes that can be introduced on a structure through the application of thin layer characterized by high damping properties.

However, with real-life structures, it is more important to determine the structural modification in terms of physical parameters (such as for example the thickness, length, number of patches) changes. There are three main reasons for carrying out structural modifications.

- Firstly, an existing structure may exhibit unsatisfactory dynamic characteristics. This is not unusual, since it is customary for design engineers to consider static loading and balance when designing a structure or a component, even if the structure may eventually work in an environment with dynamic loading.
- Secondly, the design of a structure, which will be located in a dynamic working environment, needs to satisfy certain defined criteria, such as the avoidance of vibration resonance.
- Thirdly, the demands on the higher performance capacities of complex mechanical and structural systems, such as machine tools, automobiles, railway vehicles, aerospace systems and high speed rotating systems, which require sound dynamic design, i.e. including desired dynamic characteristics, such as vibration response, resonances, dynamic stability and mode shapes.

With some exceptions, any physical or spatial change to a structure should theoretically result in modal property changes. This implies that, almost any sufficiently great structural change may cause modal property changes (for instance, natural frequency changes). Therefore, physical changes would seem to offer numerous possible solutions to structural modification problems. The reality is very different from this optimistic notion.

- Firstly, practical design and performance requirements often impose restrictions on structural modifications. Only a limited number of modifications are practically feasible.
- Secondly, for a simple proposal regarding modal property changes, such as natural frequency changes with the aim of limiting excitation frequency ranges, restrictions should be imposed on changes unintentionally caused to other modal properties.
- Thirdly, other physical constraints, such as minimum total mass structural adaptations, may be required.

Structural Modification can be used in order to overcome these problems by firstly predicting accurately and quickly at computer level the effect of possible modifications such as the addition of masses, beams, layers and dampers etc. or of configuration changes on the dynamic characteristics of the structure, and then effecting modifications. Another important objective for structural modification is the prediction of the magnitude and location of the modifications in order to shift the resonances or improve other dynamic performance parameters. This objective could thus be viewed as something more like design synthesis. These methods naturally look beyond this aim in order to bring about optimal modifications. Many practical structural modifications have very simple objectives. The most common objective is to change the natural frequency of a structure in order to avoid excitation frequency and prevent excessive vibration. Resonance and anti-resonance phenomena are critical to this analysis. It is often a justifiable assumption that changing

excitation forces is not feasible. This leaves modifying the structure to optimize its dynamic characteristics as the only way to remedy the problem of excessive vibration. However, adding a substructure to the original structure can also cause structural modifications (for example the patches application). The use of this latter kind of application to carry out structural modifications and consequently to remedy the problem of excessive vibration is treated in *Chapter B2*, and more precisely is referred to a patch application.

Chapter B1 provides a brief introduction regarding the techniques that have been developed and adopted by researchers over the last few decades regarding structural modifications (see *Section B1.1*). At higher frequencies, the dynamic behaviour of a structure cannot be expressed in terms of the magnitude and phase response at a defined structure location and frequency. In fact, difficulties arise due to the high order modes which contribute to the response and also because high frequency responses are strongly affected by uncertainty and variability regarding the construction of the physical system. So, instead of using a matrix perturbation and analytical approach, *energy-based approaches* are often adopted (*Section B1.2*). *Statistical Energy Analysis* (*SEA*) is a method for high frequency vibrations which gives a "broad-brush" description of the dynamic behaviour of a structure. This method predicts average vibration levels, that are time, frequency and space averaged. Thus, it gives a rough approximation of structural behaviour. SEA is particularly valuable from a conceptual point of view in that it establishes a link between stored energy and energy flow. *Section B1.2* will present some explicit formulations of the relationships between energy and energy flow within a structure. These explicit formulations, that shows a clear correlation between the input power to a structure, its potential energy and its loss factor (that is unknown), can guide the identification of "hot spots" within an elastic structure which, if locally damped, can be best suited to global vibration reduction, i.e. in the entire frequency range. This

kind of target can be reached by estimating potential energy distribution within a structure. Unwanted vibrations in structures are a common problem in industry. In practice, platelike structures (such as those found in washing machines, refrigerators and motor enclosures) are often damped by applying constrained layer-damping material over the entire surface of the structure or the part of the structure which is accessible, at the expense of increased manufacturing time and product cost. Paradoxically, structure radiated noise can also be increased by arbitrarily applying damping material onto the structure and thus, unknowingly causing the damped vibrational pattern to radiate sound more efficiently than the original undamped vibrational pattern. Therefore, careful placement of damping patches is important for product cost, noise and vibration reduction (see *Chapter B2*).

This research aims at being a step towards the goal of determining damping placement on a structure in order to ensure noise reduction and therefore, to improve structural vibrational behaviour. *Chapter B3* acts as an introduction to attaining this aforementioned final goal. Using all the informations shown in *Chapters B3*, *B4*, *B5* and *B6* the aim is to shown how potential energy distribution estimation can define the placing of constrained layer damping patches onto a structure in order to reduce its amplitude vibration level. All the considerations and results are based on numerical data obtained by evaluating potential energy distribution and normal velocity on a steel plate (see *Chapter B5*) and a steel bracket (see *Chapter B6*), characterised by different loading and boundary conditions. As for the plate, also for the bracket component, the kind of numerical simulations performed through the methodology created are three:

- ✓ Potential energy evaluation studying the component behaviour at a single characteristic frequency;
- ✓ Potential energy evaluation studying the component behaviour on its entire frequency range;

- ✓ Velocity evaluation studying the component behaviour on its entire frequency range.

Through these numerical simulations the potential energy trend regarding the study at a single natural frequency and the potential energy distribution regarding the study on the entire frequency range will be obtained. The first will be essential in order to precisely define the location of the patches, while the second can be used to identify which patches arrangement produce the highest improvement (the highest amplitude vibration reduction level). In reality, this latter task will be entrusted by the velocity evaluation. In essence, the results concerning the estimation of potential energy values in addition to those concerning the velocity values, both relating to the entire frequency range, will be useful to clearly define the impact that each patch configuration has on the overall amplitude vibration reduction of the component studied.

The numerical simulations presented in *Chapter B4* addresses two different aspects of vital importance for the appropriate development of this research, which are, the potential energy evaluation (*Section B4.1*) and the definition of how the patches should be applied to the component surface (*Section B4.2*), respectively. In essence, the results obtained in these sections approve and validate the methodology, as do the comparisons of the results and considerations that will be carried out in *Chapter B5* and *Chapter B6*.

CHAPTER B1

Structural Modification

Structural modification [1-7,50-52] under the banner of modal analysis technology refers to a technique to modify local physical properties of a structure in order to change or optimize its dynamic characteristics. This differs from structural modification for a static analysis, where changes are made to satisfy criteria of statics such as the reduction of static stress concentration.

The dynamic characteristics of a structure, usually referred to as its natural frequencies and mode shapes, are determined by its mass, stiffness and damping distributions [6-7]. The properties outlined by these distributions are often called the spatial properties of the structure. The natural frequencies and mode

shapes are its modal properties. The spatial properties are often quantified by a mathematical model of the structure, such as a finite-element (FE) model. This model translates the physical properties of the structure, such as its dimensional, geometrical and material properties, into distributed mass and stiffness properties. For structural modification using an FE model, it is possible to determine the modification in terms of mass and stiffness changes. However, for a real-life structure, it is more important to determine the structural modification in terms of physical parameter (such as thickness, length, diameter, etc.) changes. There are two main reasons for structural modification.

First, an existing structure may exhibit unsatisfactory dynamic characteristic, such as for the gear pump treated in the previous part. This is not unusual, since it is customary for design engineers to consider static loading and balance when designing a structure or a component, even if the structure may eventually work in an environment with dynamic loading.

Second, the design of a structure that is known to experience a dynamic working environment needs to satisfy some defined criteria such as averting vibration resonance.

With exceptions, theoretically any physical or spatial change (or their combinations) of a structure should result in modal property changes. This implies that, for a proposed modal property change (say a natural frequency change), almost any structural change of sufficient extent may realize it. Therefore, it seems to have numerous possible solutions of physical changes for a structural modification problem. The reality is different from this optimistic notion.

Firstly, practical design and performance requirements often impose restrictions on structural modification. There are only limited modifications that are practical or feasible (see *Chapter B2*). Secondly, for a simple proposition of modal property change such as a natural frequency change to avert excitation frequency range, there are restrictions on changes brought unintentionally on other modal properties. Thirdly, other physical constraints,

such as minimum total mass change to the structure, may be required.

Many practical structural modification cases have very simple objectives. The most common objective is to change a natural frequency of a structure so that the frequency of excitation can be avoided and excessive vibration prevented. It is often a justifiable assumption that changing excitation forces is not feasible. This leaves modifying the structure to optimize its dynamic characteristics as the only avenue for remedying the problem of excessive vibration.

Most of the structural modification methods aim to change a structure's modal properties by modifying the existing physical or spatial properties. As a result, the total number of degrees of freedom (DOFs) of the mathematical model used to describe the dynamics of the structure does not alter. In fact, often even the load paths are kept unchanged. This means no new physical connections will be introduced. However, adding a substructure to the original structure can also carry out structural modification. An example is the modification by using a single-DOF (SDOF) mass damper. In this case, structural modification relies on sub-structural coupling analysis.

The spatial pattern of the vibrations of a coupled system is given by its eigenfunctions (mode shapes) and the systems frequency response characteristics depend on its resonance frequencies. In general, a system formed by connecting two finite systems has mode shapes and resonance frequencies that differ from those of the two component systems. The power flow between the two systems may be expected to depend on the degree of matching between the resonance frequencies of the two systems, on the degree of similarity of their mode shapes, on the location of the joint with respect to nodes of the two systems, and on how the damping is distributed in the two systems. Clearly, any attempt at developing a complete description of the vibrations of coupled systems with more than four nodes is bound to encounter crushing complexity.

As will be shown by *Cremer et al.* (1988) [52], for finite systems subject to random excitation, the power flow can be related to some simple parameters, and in some cases this power flow may be expressed rather simply in terms of the damping and the transmission efficiencies for the corresponding infinite systems. The fact that these relations hold only in a certain average sense (in general, they apply only to the mean-square velocities, averaged over space and frequency) is not necessarily a disadvantage. In practice, the details of a structure, and especially its boundary conditions, usually are not known well enough to enable one to calculate the exact modal properties of the structure, so that the above-mentioned average quantities usually are the only ones of practical significance.

The approach introduced here and described in *Section B1.2* of this chapter has come to be known as "*Statistical Energy Analysis*" (*SEA*). "*Statistical*" indicates that averages are involved and that some randomness is assumed in the excitation, the distribution of resonances frequencies, and the matching conditions of the various modes. "*Energy*" refers to the fact that the average quantities used are closely related to the energy and power in the system (*see Section B1.3*).

B1.1 Historical development

Structural modification evolved with the development of structural dynamics. The first useful formulation of structural modification was based on a matrix *perturbation approach* [3-5,7,21-23] to derive an approximate solution for the modal properties of the modified structure (*Rayleigh* 1945 [24]). *Rayleigh* found that an increase in the mass of any part of a vibrating system is attended by a prolongation of all the natural periods. His approach was later expanded by researchers to broaden the formulation and to include second-order approximation. The

practical application of this perturbation approach was developed in the 1970s and 1980s by a number of researchers. Their work allows specified constraints on frequencies and mode shapes and links physical parameter changes of a structure, such as the cross-sectional area of a beam element, to its modal properties. The main problem associated with a perturbation approach is that the modification has to be "small" to have accurate solutions.

The *analytical approach* of structural modification began in 1960s. The models used in the study were largely mass-spring systems because of their simplicity in both the number of DOFs and the absence of rotational DOFs. A significant early study on local structural modification from the mass and stiffness characteristics of a structure was carried out by *Weissenburger* (1968) [25]. He formulated the relationship between a simple lumped mass and stiffness alteration of an undamped linear dynamic system and its dynamic characteristic changes. This work was later expanded by *Pomazal & Snyder* (1971) [26], who analysed the effects of adding springs and dampers to a viscously damped linear system. The complete solution of the original system is a prerequisite of the analysis that, in today's analysis, appear to be over-demanding. These works often treated structural modification from the viewpoint of a *direct problem*. Therefore, they are more conveniently used as the reanalysis tools for a modified system.

Another significant *analytical approach* was developed by *Ram & Blech* (1991) [27], who theorized the effects of modification at one DOF by different mass and stiffness attachments. They proved that the consequence of connecting a vibratory system to the ground through a simple SDOF oscillator is to increase the natural frequencies of the system, which are lower than the natural frequency of the oscillator, and to decrease the natural frequencies that are above. This conclusion can be applicable to continuous systems as well as to lumped systems. The findings, though not readily applicable to structural modification, provide interesting insights to the dynamic behaviour of a structure

before and after a simple modification.

The merit of *reanalysis* in structural modification is to provide an efficient and reliable analytical solution of the dynamic characteristics of the modified structure after structural modification has been nominated [1-5,19-20]. A notable pioneering work in reanalysis was reported by *Wang* (1987) [28]. Reanalysis is particularly useful in the design optimization process [47-49]. This perhaps explains why much literature for reanalysis appears in FE-related journals and conference proceedings. The modal-analysis-based reanalysis is known as *structural dynamic modification* (*SDM*). It relies on the modal properties of a structure and proposed modifications to predict the new modal properties of the modified structure.

Sensitivity analysis has been a useful tool for structural modification. It forms a type of reanalysis. The sensitivity of modal properties of a structure with respect to its physical properties has been developed by many researchers in the last three decades. The focus of their study was to determine the derivatives of the eigenvalues and eigenvectors of a dynamic system with respect to system changes. The presumption of small structural changes ordains sensitivity analysis to be ineffective for a significant extent to modification unless iteration is used.

Structural modification as an *inverse problem* was formulated as an inverse eigenvalue problem by many researchers (see for example *Tsuei & Yee* 1987; *Bucher & Braun* 1993 [29-30]). An inverse eigenvalue problem is to determine matrix changes that will result in a proposed eigenvalue and/or its eigenvector. This can be achieved using modal data (*Bucher & Braun* 1993) or using frequency-response function (FRF) data (*Tsuei & Yee* 1987). The latter method requires only FRF data from modification DOFs. This is particularly convenient and effective for modal testing. The method was further developed (see *He & Li* 1995 [31]) to study the relocation of an anti-resonance of a structure and cancellation of a resonance with an anti-resonance for a selected FRF.

Historical development of *local structural modification* in terms of dynamic absorbers can also be traced back decades ago. The work by *Den Hartog* (1956) [32] and *Timoshenko* (1995) [33] in this area has been frequently referred to by researchers. To date, many dynamic absorbers have been studied (*Hunt* 1979) [34]. A majority of these absorbers involves adding extra DOFs to a structure for dissipating energy rather than modifying its existing mass and stiffness distributions.

Another significant structural modification approach that moves away from all the aforementioned approaches is referred to be the *energy based approach*. This kind of approach represents the theoretical basis on which the study described in this second part will be exposed.

The energy transmission in vibrating structures is a phenomenon the importance of which concerns both vibration theory and practice. The energy balance law universally applies to all forms of wave motions, vibratory and acoustic. Computational and measurement methods have been developed by means of which the energy flow in vibrating structure can be traced. Most energy methods use a statistical notion of the global vibration field (*Lyon & Jong* 1995 [60] and *Langley* 1989 [61]). Owning to its ostensible simplicity the *Statistical Energy Analysis* has become the most used energy-modeling concept. Attempts to establish an equivalent *SEA* based on local energy variables [53-55] has not yielded results comparable to the original lumped parameter *SEA*.

Relating to the deterministic approach, the literature on energy distribution and energy flow in structure is rare (*see Maysenhölder* 1994 [56], *Auld* 1990 [57] and *Alfredsson* 1997 [58]). However the practical applicability of these exact approaches is not as wide as is that of statistical ones. The exception is the evaluation of energy flow that has received some considerable attention. It is worth noting that, while various techniques have been developed on the topic of energy flow, the estimation of energy in structures was fairly neglected. In

particular, the estimation of potential energy was never considered as an issue.

B1.2 Energy based approach

At higher frequencies, the dynamic behaviour of a structure cannot be expressed in terms of the magnitude and phase of the response at discrete structure location and frequency. In fact, difficulties arise due to the high order modes that contribute to the response and also because the response at high frequencies is strongly affected by the uncertainty and variability, on the physical system construction. So, energy-based approaches are often adopted.

The *Statistical Energy Analysis* (*SEA*) is a method for high frequency vibrations that give a "broad-brush" description of the dynamic behaviour of a structure. This method predicts average vibration level, that is time, frequency and space averaged. So, it gives a coarse idealisation of the structure behaviour.

A particular value of *SEA* from the conceptual point of view is that it establishes a link between the stored energy and the energy flow. Classical *SEA* refers to the stored energy as the total mechanical energy of the system concerned, like the sum of kinetic and potential energies. In *SEA* applications it is assumed that the two constituent energies are equal. The practical importance of this assumption allows expressing the stored energy in terms of kinetic energy, the one which is much easier to handle. While in systems of high modal density the two energies are indeed practically identical in the global sense, their spatial distributions (the kinetic and potential energy densities) are not. Moreover, the total energy density is not uniformly distributed across a vibrating structure that hinders the use of global concepts, such as the *SEA*, at the local level. Attempts to establish an equivalent *SEA* based on local energy variables [53-55] have

not yielded results comparable to the original, lumped parameter *SEA*.

Relating to the deterministic approach, the literature on energy distribution and energy flow in structure is rare [56-58]. However the practical applicability of these exact approaches is not as wide as is that of statistical ones. The exception is the evaluation of energy flow that has received some considerable attention. It is worth noting that, while various techniques have been developed on the topic of energy flow, the estimation of energy in structures was fairly neglected. In particular, estimation of potential energy was never considered as an issue.

The next chapters concern the estimation of potential energy and velocity for structural components carried out with I-DEAS software estimated in their entire frequency range. The aims of the numerical simulations are twofold: firstly the evaluation of energy distribution and energy flow within a structure; secondly to give the correct patch location, which are used in order to decrease the structure vibration level.

Hereafter will be presented some explicit formulation of the relationship between energy and energy flow.

The relationships presented in the next section will constitute the basics on which the study is referred.

B1.3 Estimation of energy flow within a structure

Some basic relationships are presented here to estimate the energy flow within a structure. The study will be focalized to define the link between the input power and the potential energy.

Globally, taking into account sinusoidal vibration the relationship between the real input power P and the global energy E is usually expressed by an approximation [59-60]:

$$\bar{P} \approx \eta\omega\bar{E} \tag{B1.1}$$

where $\bar{}$ denotes time average, ω denotes frequency and η denotes system damping (loss factor). The symbol E denotes the total mechanical energy like the sum of potential and kinetic energies, $E = E_p + E_k$. It can be further simplified by assuming equality between the time averaged kinetic and potential energies (*see Section B1.2*):

$$\bar{E}_k \approx \bar{E}_p \Rightarrow \bar{P} \approx 2\eta\omega\bar{E}_k \tag{B1.2}$$

Taking into account a linear system excited by multiple force [59], the overall time-averaged kinetic energy and total net input power can be expressed in terms of single modal summation:

$$\begin{aligned} \bar{E}_k &= \frac{m\omega^2}{4}\sum_r |U_r|^2 \\ \bar{P} &= \frac{m\omega}{2}\sum_r \eta_r\omega_r^2 |U_r|^2 \end{aligned} \tag{B1.3}$$

If a single mode dominates close to its resonance frequency, the simple eq. (B1.2) for kinetic energy becomes valid:

$$\omega \to \omega_r \quad \Rightarrow \quad \begin{aligned} \bar{E}_k &\approx \frac{1}{4m}\frac{|f_r|^2}{\eta_r^2\omega^2} \\ \bar{P} &\approx \frac{1}{2m}\frac{|f_r|^2}{\eta_r\omega} \end{aligned} \quad \Rightarrow \quad \bar{P} \approx 2\eta\omega\bar{E}_k \tag{B1.4}$$

where r is the modal indices, U_r the complex modal amplitude, m the total mass, ω_r the natural frequency and f_r the complex modal force (see [59] page 47).

Equation (B1.4) is given in terms of kinetic energy only. General form of potential energy cannot be assessed by modal approach the same way as that of kinetic energy, eq. (B1.3), because the potential energy depends on the particular characteristics of the system considered.

The kinetic and potential energies are almost equal at resonance, but not at other frequencies. Below the resonance potential energy of a particular mode is larger than kinetic, while the opposite applies above the resonance. In the case of high modal overlap, at any particular excitation frequency, the kinetic energy of modes having the eigenvalues above the excitation frequency will become compensated by the kinetic energy of lower modes. Inverse compensation effect will apply to potential energy. As a result, the kinetic and potential energies in modally overlapped systems can be shown to match closely at all frequencies except below the first resonance where the compensation cannot take place. This justifies approximation of eq. (B1.2).

Since both the system energy and input power can be reduced to a single modal summation, the terms under the summation sign represent modal kinetic energy $e_{k,r}$ and modal power p_r:

$$\begin{aligned} e_{k,r} &= \frac{m\omega^2}{4}\left|U_r\right|^2 \Rightarrow \bar{E}_k = \sum_r e_{k,r} \\ p_r &= \frac{m\omega}{2}\eta_r\omega_r^2\left|U_r\right|^2 \Rightarrow \bar{P} = \sum_r p_r \end{aligned} \tag{B1.5}$$

The relationship between the energy and the power can now be brought to the modal level:

$$p_r = 2\omega\eta_r\left(\frac{\omega_r}{\omega}\right)^2 e_{k,r} \tag{B1.6}$$

The modal relationship has the same form as the approximate relationship (B1.2) except for the factor equal to the ratio square of eigenfrequency and excitation frequency. This factor explains the nature of power-energy relationship with respect to frequency: below a resonance the kinetic energy is overestimated by the input power, while above a resonance it is underestimated.

The potential energy of a single-degree-of-freedom (sdof) system is related to its kinetic energy via the same frequency ratio factor as appearing in eq. (B1.6).

$$E_p = E_k \left(\frac{\omega_{res}}{\omega} \right)^2 \tag{B1.7}$$

where ω_{res} is the resonant frequency. Since any multi-dof system can be represented as a canonical circuit of a series of single-dof systems, it could be demonstrated that the modal relationship between the potential energy and input power can be obtained by inserting eq. (B1.7) into eq. (B1.6) to yield the eq. (B1.8), valid for any system with *N* degrees of freedom.

$$p_r = 2\omega\eta_r e_{p,r} \tag{B1.8}$$

As clearly defined by *G. Pavic* [59] it is possible to represent the net input power by a function of potential energy, free from the frequency weighted factor appearing in eq. (B1.6), that will hold exactly as long as the loss factor remain constant for all the modes.

$$\bar{P} = 2\eta\omega\bar{E}_p \tag{B1.9}$$

An alternative validation of this central equation will be provided in *Section 3* "Local distribution of energy and energy flow within a structure" of a paper by *G. Pavic* [59] using a non-modal approach.

Equations (B1.1) and (B1.3) are valid for the whole structure exhibiting resonant behaviour. These cannot be applied at the local level like analysis of energy distribution within a structure.

Locally, the complex intensity divergence fully determines the energy density within an elastic vibrating object. The two following equations represent a fundamental relationship between the energy density and energy flow in an elastic damped structure [59]:

$$\begin{aligned} \mathrm{Re}\left(\nabla \cdot \mathrm{I}\right) &= -2\eta\omega\overline{e}_p \\ \mathrm{Im}\left(\nabla \cdot \mathrm{I}\right) &= -2\omega\left(\overline{e}_k - \overline{e}_p\right) = -2\omega\overline{\ell} \end{aligned} \qquad \text{(B1.10)}$$

where ℓ denotes the Lagrangian density $\left(\ell = e_k - e_p\right)$, ω denotes the frequency, η denotes the loss factor and e_p and e_k the potential and kinetic energy densities respectively.

The density of energy flow, the *intensity*, is given as a linear combination of products between stresses and velocities (see *Appendix B* "Energy density, intensity and intensity divergence" of a paper by *G. Pavic* [59]). Under the complex notation, used to represent sinusoidal time variations these products are transformed into complex products between stress amplitudes and conjugate velocity amplitudes. The real part of complex energy flow corresponds exactly to the temporal mean value of true energy flow, which is the net energy flow.

The divergence of complex intensity vector I and the kinetic and potential energy densities, e_p and e_k, are linked through the following equation:

$$\nabla \cdot \mathrm{I} = \mathrm{Re}(\nabla \cdot \mathrm{I}) + j\,\mathrm{Im}(\nabla \cdot \mathrm{I}) = 2\omega\left[\bar{e}_p(j-\eta) - j\bar{e}_k\right] \tag{B1.11}$$

Equation (B1.11) is very general as any damping in a linear, sinusoidally vibrating system can be represented by an approximate complex elasticity modulus. It has been assumed that the loss factors relative to compression and shear moduli are identical, equal to η in eq. (B1.11). Assuming the loss factor constant across the whole vibrating object, the kinetic and potential energies of the vibrating body can be expressed as simple functions of total complex mechanical power supplied.

$$\bar{E}_p = \frac{\mathrm{Re}\left(\bar{P}_{in}\right)}{2\eta\omega} \tag{B1.12a}$$

$$\bar{E}_k = \frac{\mathrm{Re}\left(\bar{P}_{in}\right) + \eta\,\mathrm{Im}\left(\bar{P}_{in}\right)}{2\eta\omega} \approx \frac{\mathrm{Re}\left(\bar{P}_{in}e^{-j\eta}\right)}{2\eta\omega} \tag{B1.12b}$$

$$\bar{L} = \bar{E}_k - \bar{E}_p = \frac{\mathrm{Im}\left(\bar{P}_{in}\right)}{2\omega} \tag{B1.12c}$$

Equations (B1.12a) and (B1.12b) shows that the equivalence between power exchange and energy is related to the potential energy only. As mentioned before, the simplified expression (B1.2) that involves kinetic energy is not completely correct, in particular where the local field variables are concerned; anyway the use of local kinetic energy to express the local power dissipation is quite common. While one part of losses of a small portion of a vibrating structure could indeed be attributed to its motion and thus to its kinetic energy it seems unphysical to link the internal losses to kinetic rather than potential energy.

Even if the loss factor for typical structures is very small this should not imply that the second term in the numerator of

equation (B1.12b) could be neglected. In fact the imaginary part of input mechanical power could often be much larger than the real part. Close to resonant frequencies the imaginary part is small in comparison to the real part and consequently the kinetic and potential energies will become almost identical at resonance.

If the loss factor is not constant over the vibrating body, see eq. (B1.13), the quantity responsible for energy dissipation within the structure is defined by the product between the local loss factor and potential energy rather than global values of these two quantities.

$$\bar{P}_{in} = 2\omega\left(j\bar{L} + \int_V \eta e_p \, dV\right) \tag{B1.13}$$

where V is the body volume of the structure, P_{in} is the total complex mechanical power supplied to the structure and $\bar{L}$ the mean Lagrangian energy density. Equations (B1.11-B1.13), obtained by direct integration of fundamental elasticity relationships, do not rely on limitations of modal approach. The only assumption was that on material linearity and on dissipation that was taken in the form of an isotropic, frequency dependent, internal loss factor. This makes these equations applicable to finite as well as infinite systems, to stationary vibration as well as to wave fields. The principal advantage of the simple energy-power relationships (B1.12-B1.13) is their independence of excitation. In cases where the damping satisfies the stiffness proportionality criterion, the four relationships, once established, will hold for any excitation. This is of particular value in all cases where the structure is excited at more than a single point.

In reality damping will rarely be uniformly distributed or stiffness proportional across a structure. Due to the fact that in reality damping is never uniformly distributed across a structure, the study is done taking into account the total potential energy and how it is distributed within the structure.

Summarizing, on the *global* level, the temporal mean value

of the total vibratory power input to a structure is proportional to the product between the loss factor and the potential energy evaluated in the entire frequency range if the damping is isotropic and uniformly distributed across within a structure. In this case the potential energy can be obtained from the known input power to the structure and the known loss factor. If the damping is not uniformly distributed but remains isotropic, an integral representation based on the product of the local loss factor and potential energy density is applicable, eq. (B1.13). *Locally*, the mean intensity divergence is proportional to the product of internal damping and potential energy density. If the intensity is represented in complex form, the imaginary value of intensity divergence is proportional to the mean Lagrangian energy density at a given point. These explicit formulations that enable to estimate the energy flow within a structure are demonstrated through several examples in the Journal of Sound and Vibration paper by *G. Pavic* [59].

The established proportionality between the net intensity divergence and the potential energy density can be used for un improvement of experimental vibration analysis by identifying "hot spots" within an elastic structure which, if locally damped, can be best suited for vibration reduction in its frequency range. This kind of target can be reached by the estimation of potential energy distribution that is a task easier by far than any direct evaluation of intensity divergence. Indeed, the *Chapters B5* and *B6* attempts to estimate in an easy way the potential energy distribution of a precise structure. Even if not treated in this thesis, for what mentioned above, the knowledge of the potential energy distribution within a structure with the knowledge of the input power to the structure will allows to determine the loss factor of the structure in the case of isotropic damping. Whereas the internal damping of a structure is unknown, the methodology that will be outlined in the next chapters will provide a great help on the possibility of determining these values of loss factor of the structure.

CHAPTER B2

Damping mechanisms

In *Chapter B1* has been introduced some informations regarding the vast field of structural modification. Purpose of the following chapters will be focalized on the improvement of the vibrational behaviour of some generic structures; i.e. plate and bracket, by applying on them structural modifications techniques and by studying, observing and validating their vibrational behaviour through an energy approach (*Section B1.2*). The structural modification techniques adopted and applied to the base structure will make changes on the mass, stiffness and damping properties itself. These changes on the base structure properties will be made through the introduction and application of some little components, i.e. patch, directly applied on the

surface of this base structure and characterized by high damping properties. This kind of application is usually referred as "*surface damping treatment*",

As is clear from this brief introduction is simple to understand, before starting with the practical applications, that is essential to treat some important aspects such as the particular case of structural modification defined as surface damping treatment and the effects of damping on the structures.

Therefore, before starting with an explanation and exposure of the work that I have done during a period of training and research for 13th months at INSA university (*Chapter B3*, *B4, B5* and *B6*), this chapter will deal with some fundamental aspects regarding damping effects on a structure and the surface damping treatments treaty in such a general form, all followed by the exposition of several cases of their applications already studied and addressed by other scientists and researchers.

B2.1 Introduction

In engineering practice, controlling vibration and noise in structures and machines is partly art and partly science. This is because, though one can in principle obtain from analysis or experiment the data needed to develop and optimize the appropriate control measures, in practice one is constrained by factors of time, equipment, and economics and is often obliged to make decisions concerning the control measures without having complete information. This means that guesses must be made, past experience must be drown on, and less than optimum measures must be sought which do the job without necessarily being the most perfect solution.

One of the least understood aspects of the design of a damping treatment is determination of how much damping is really needed to deal with a given problem. This question cannot

be resolved unless there exists an understanding of how much damping there is in the original structure. The definition of this initial damping is very important, because all improvements are related to that value.

To illustrate this matter, consider the difference in structural response between built-up structures, i.e. complex diesel engine blocks, and welded structures, i.e. muffler of shells and blades. Built-up structures are joined together or assembled by mechanical fasteners, such as rivets, bolts and screws. Built-up structures usually have high initial structural damping, which could give a loss factor as high as 0.05. Such values are considerably higher than those found in welded structures because the joint damping is then minimal, and the measured structural loss factor is comparable to that for the material, on the order of 10^{-4} or 10^{-5} for steel or aluminum structures. Thus increasing the built-up structure damping by a factor of 10 is considerably more difficult than for welded structures.

In other words the knowledge of the initial damping of the original structure, or of the structure whose vibrational behaviour has to be improved, is crucial for proper inspection of the vibration control.

For that reason in the following chapters each kind of structural material adopted in this work will be strictly joined by specific initial structural damping values.

B2.2 Effects of Damping

During the course of daily life we only occasionally encounter structures that have little or no damping [1-2,6,50], and hence we rarely have the opportunity to observe the absence of a phenomenon that we take almost completely for granted. When a structure possesses no damping, no mechanism exists to remove the vibrational energy in it, implying that any vibratory motion,

once set up, will continue forever. Clearly this can never happen in the real world, but close approximations do occasionally occur. The first example that comes to mind is the bell, a structure designed through ancient experience to vibrate for a long time at frequencies selected for its pleasing sound effect. The bell is designed in such a way that movement at the support location is very small, hence minimizing one group of energy dissipation mechanisms, and only one mode of vibration is strongly excited when the bell is impacted.

Most of the time structures built by humans or nature have so many mechanisms built in for dissipating vibrational energy, that the presence of extraneously excited vibrations is rarely noticed. It is for this reason that the need for damping is often not recognized. Nowadays, as we continue to build ever more efficient and economical structures for various purposes and increase the demands we place on these structures, we also tend to eliminate many of the sources of damping which, though without full recognition, helped such structures to survive their service environments in the past. So more and more frequently we must take special efforts to return the damping we took away, and sometimes add more, in a reliable, safe, durable and cost-effective way. To do this it is desiderable to understand what damping is all about. As in the study of most physical phenomena, damping is frequently best understood in terms of what it does, that is, how its presence, or absence, will affect the vibratory motion of the structure.

The first, easily observed effect of damping on structural response is that associated with free vibration. If deforms a cantilever beam and then release it from rest, it will begin to oscillate regularly, and the amplitude of each successive oscillation will be smaller than the one before, the ratio of successive amplitudes being a measure of the amount of damping. If the beam is undamped, the oscillation, once set up, will continue indefinitely. If the beam tip is joined to ground by a viscous damper for which the force applied to the beam is directly

proportional to and in opposition to the instantaneous velocity, then the response will die away with time, slowly for a light damper and quickly for a heavy damper. Theoretically the motion will take an infinite time to die away completely, but in practice other mechanisms of damping will eventually be greater than the velocity-dependent contributions of the damper and will bring the system to rest in a finite time. One such mechanism is dry friction in which the damping force is constant but changes sign each half cycle so as to always opposite the velocity at each instant. Clearly the vibrations of damped structures will normally die away with time at a rate that may be used as a measure of the amount of damping.

Looking at damping from a purely phenomenological point of view, that is, with respect to its effect on structural response we can observe the influence on damping effect on the final steady state amplitude attained by a structure when excited by a harmonically oscillating force, i.e. forced vibration. If the oscillating force is applied at time $t = 0$, the response will rapidly build up until the system is in dynamic equilibrium, as illustrated in Figure B2.1 where F represents the oscillating force and W the oscillation amplitude. At most frequencies the influence of damping will not be too great. At low frequencies the stiffness of the structure will provide the dominant restoring force, whereas at high frequencies it will be the inertial force. Somewhere in between, depending on the precise values of mass and stiffness, a resonance will occur. At this precise frequency, in the absence of damping, no dynamic equilibrium can be attained, and the system will be subjected to ever-increasing oscillation amplitudes. In practice some damping will always exists and will bring the system to equilibrium at higher or lower amplitudes, depending on the magnitude of the damping forces. A measure of damping is suggested by the observed behaviour, namely:

$$\eta = \frac{\omega_2 - \omega_1}{\omega_{res}} \qquad \text{(B2.1)}$$

where ω_{res} is the resonant frequency and ω_1 and ω_2 are the frequencies on either side of ω_{res} for which the amplitude is $1/\sqrt{2}$ times the resonant amplitude. η is known as the system loss factor and increases as the damping increases. The measure of damping will be unique for certain types of damping, such as viscous or hysteretic, but will depend on the amplitude for other types of damping, such as dry friction, and must therefore be used with some caution, as indeed is the cause for all measures of damping.

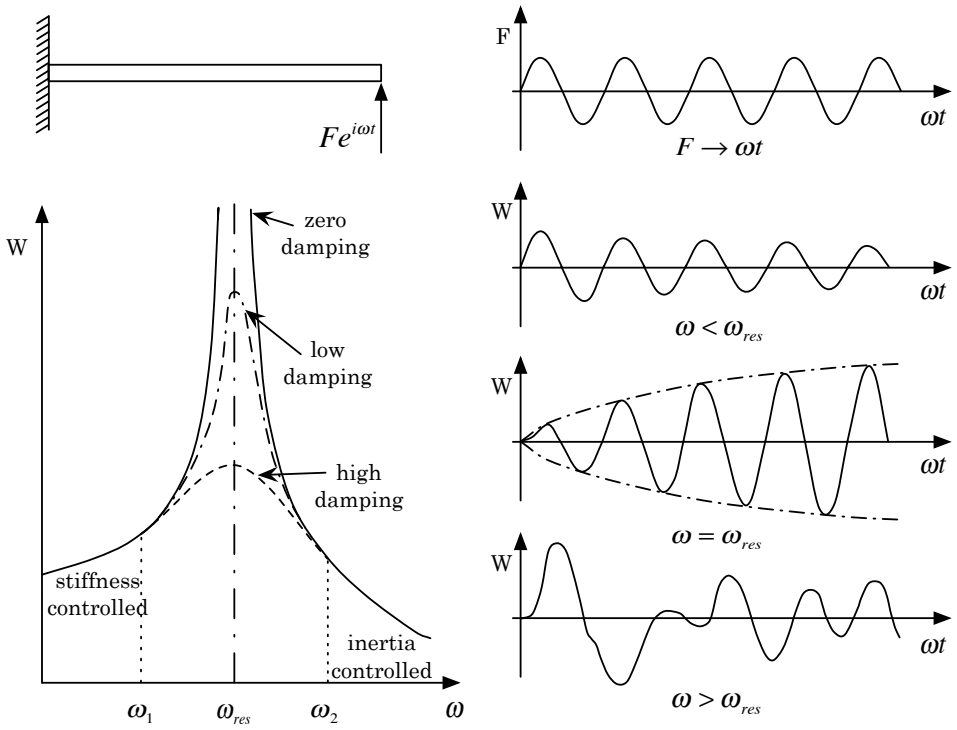

Figure B2.1 – Effect of damping on forced vibration.

For these reasons the vibrational improvement of some generic components such as plate and bracket, which will be made

in the *Chapters B5* and *B6*, will be based on the study of their resonance frequencies. In other words, to define the positions on the surface of the base component on which apply the components characterized by high damping properties, i.e. viscoelastic materials, is essential to rest upon the study of the resonance frequencies of the principal structure.

Obviously, the same consideration here treated will be expanded and dealt with in more detail in the next chapters.

B2.3 Types of damping

There is some form of mechanical-energy dissipation in any direct system. In the modeling of systems, damping can be neglected if the mechanical energy that is dissipated during the time duration of interest is small in comparison to the initial total mechanical energy of excitation in the system. Even for highly damped systems, it is useful to perform an analysis with the damping terms neglected, in order to study several crucial dynamic characteristics, i.e. modal characteristics (undamped natural frequencies and mode shapes) [1-2,6,50].

Several types of damping are inherently present in a mechanical system. If the level of damping that is available in this manner is not adequate for proper functioning of the system, external damping devices can be added either during the original design or in a subsequent stage of design modification of the system. Two general types of external dampers can be added to a mechanical system in order to improve its energy dissipation characteristics. They are passive and active dampers. A passive damper is a device that dissipates energy through some motion, without needing an external power source or actuator. Active dampers have actuators that need external sources of power. They operate by actively controlling the motion of the system that needs damping. Dampers may be considered as vibration

controllers.

Anyway, three primary mechanisms of damping are important in the study of mechanical systems. They are the internal, structural and fluid damping.

Internal (material) damping results from mechanical-energy dissipation within the material due to various microscopic and macroscopic processes. Structural damping is caused by mechanical-energy dissipation resulting from relative motions between components in a mechanical structure that has the common points of contact, joints or supports. Fluid damping arises from the mechanical-energy dissipation resulting from drag forces and associated dynamic interactions when a mechanical system or its components move in a fluid.

For reasons directly related to the specified path followed in the present work and to the considerations in it, hereafter will be deepened only the internal or material damping case.

Internal damping of materials originates from the energy dissipation associated with microstructure defects, such as grain boundaries and impurities; thermo-elastic effects caused by local temperature gradients resulting from non-uniform stresses, as in vibrating beams; eddy-current effects in ferromagnetic materials; dislocation motion in metals; and chain motion in polymers. Several models have been employed to represent energy dissipation caused by internal damping. This variability is primarily a result of the vast range of engineering materials; no single model can satisfactorily represent the internal damping characteristics of all materials. Nevertheless, two general types of internal damping can be identified: *viscoelastic damping* and *hysteretic damping*. The latter term is actually a misnomer, because all types of internal damping are associated with hysteresis-loop effects. The stress σ and strain ε relations at a point in a vibrating continuum possess a hysteresis loop, such as the one shown in Figure B2.2.

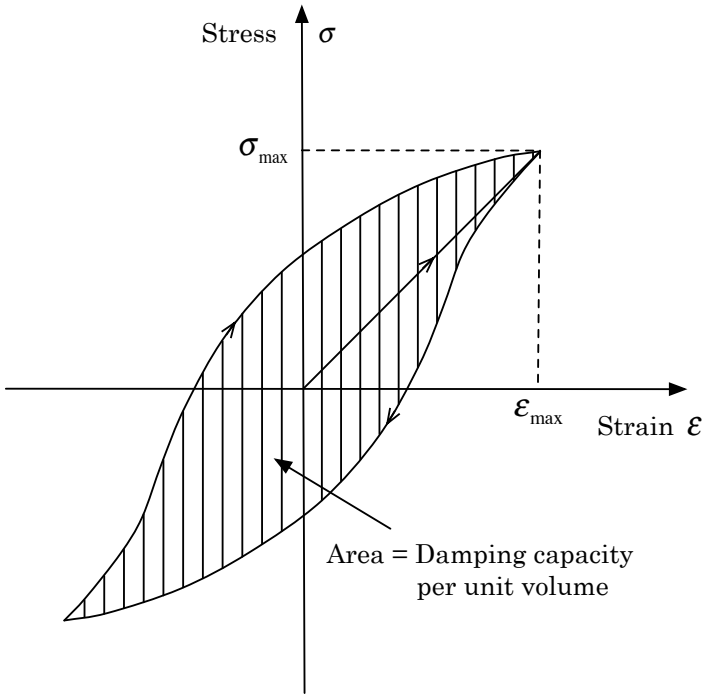

Figure B2.2 – A typical hysteresis loop for mechanical damping.

The area of the hysteresis loop gives the energy dissipation per unit volume of the material, per stress cycle. This is termed per-unit-volume damping capacity, and is denoted by d. It is clear that d is given by the cycle integral:

$$d = \oint \sigma \, d\varepsilon \tag{B2.2}$$

In fact, for any damped device, there is a corresponding hysteresis loop in the displacement-force plane as well. In this case, the cyclic integral of force with respect to the displacement, which is the area of the hysteresis loop, is equal to the work done against the damping force. It follows that this integral (loop area)

is the energy dissipated per cycle of motion. This is the *damping capacity*, which, when divided by the material volume, gives the per-unite-volume damping capacity as before.

It should be clear that, unlike a pure elastic force, i.e. spring force, a damping force couldn't be a function of displacement q alone. The reason is straightforward. Consider a force $f(q)$ that depends on q alone. Then, for a particular displacement point q of the component, the force will be the same regardless of the magnitude and direction of motion, i.e. the value and sign of $\dot{q}$. It follows that, in a loading and unloading cycle, the same path will be followed in both directions of motion. Hence, a hysteresis loop will not be formed. In other words, the net work done in a complete cycle of motion will be zero. Next consider a force $f(q,\dot{q})$ that depends on both q and $\dot{q}$. Then, at a given displacement point q, the force will depend on $\dot{q}$, as well. Hence, even at low speeds, force in one direction of motion can be significantly different from that in the opposite direction. As a result, a hysteresis loop will be formed, which corresponds to work done against the damping force, i.e. energy dissipation. One can conclude than that damping force has to depend on a relative velocity $\dot{q}$ in some manner.

B2.4 Viscoelastic materials

Viscoelastic damping [6,50,52,63-64,73,77] is exhibited strongly in many polymeric and glassy materials, and this mechanism of internal damping has many possibilities for industrial application and is consequently the material adopted for the realization of the work described in this second part (*Part B*). Polymeric materials are made up of long molecular chains, such as the organic chain illustrated in Figure B2.3. The carbon atoms join strongly together and can be branched so that the long

chains can be strongly or weakly linked, according to the composition and processing of the polymer. The damping arises from relaxation and recovery of the polymer network after it has been deformed, and a strong dependence exists between frequency effects and temperature effects because of the direct relationships between material temperature and molecular motion.

Glasses are characterized not by long networks, as in polymers, but by short-term order and long-term disorder, as illustrated in Figure B2.3.

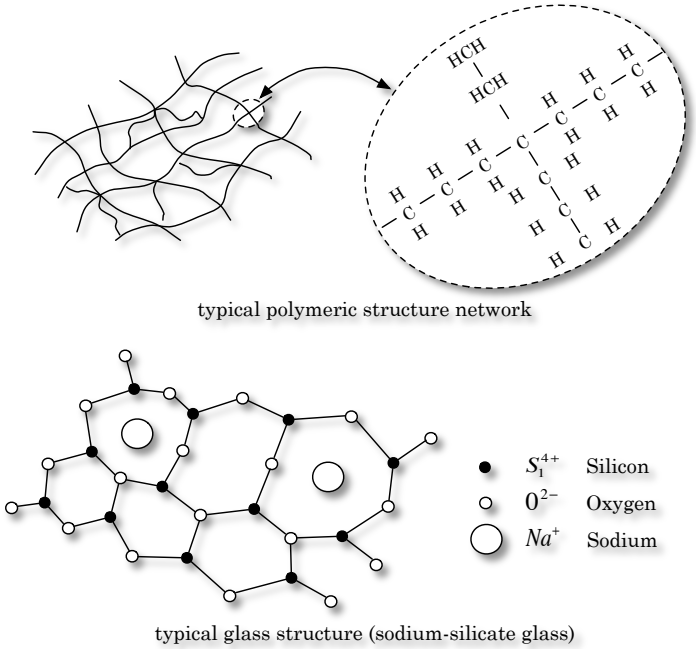

Figure B2.3 – Polymer and glass structures.

Inorganic oxides of which the glass is composed form different lattice geometries, depending on the elements involved and their proportions. Damping again arises from relaxation processes after deformation of the glass, recovery being due not to the original distribution of short networks but to other conditions of thermodynamic equilibrium. Since the glass is not cross-linked,

as can also happen in a polymer, creep can occur, i.e. deformation under continuous load application. For a cross-linked polymer, however, the static stiffness can be quite high, and creep will not occur. By proper tailoring, polymeric materials can be manufactured to possess a wide variety of damping, strength, durability, creep resistance, thermal stability and other desirable properties over selected temperature and frequency range. Similar tailoring can be accomplished for glasses at higher temperatures. In each case of course distinct natural limitations exist, which should be respected, such as upper temperature limits of each material before irreversible damage occurs.

The viscoelastic material adopted in the present work, used to reduce the vibrational behaviour of some prescribed structure and characterized by high damping property is referred to be the *asphalt*. In other words, to improve the vibrational behaviour of a plate and a bracket will be carried out the surface damping treatment by placing on them a prescribed number of thin layer asphalt patches. The mechanical characteristics of this viscoelastic material will be shown in the next chapter, see *Section B3.2*.

B2.5 Surface damping treatment

Surface damping treatments are often used to solve a variety of resonant noise and vibration problems, especially those associated with sheet metal structure vibration. Such treatments can easily be applied to existing structures and provide high damping capability over wide temperature and frequency ranges. The surface damping treatments are usually classified in one of two categories, according to whether the damping material is subjected to extensional or shear deformation.

Extensional damping is one of the most commonly used treatments. Sometimes this treatment is referred to as the

unconstrained- or *free-layer damping treatment* [6,75]. The treatment is coated on one or both sides of a structure, so that whenever the structure is subjected to cyclic bending, the damping material will be subjected to tension-compression deformation. This type of damping treatment is illustrated in fig. B2.4.

As shown by Figures B2.4 and B2.5 can be defined that E is the Young's modulus of elasticity, H is the thickness and η is the system loss factor. Subscript *1* refers to the base structure, subscript *2* to the damping layer and subscript *3* to the constraining layer.

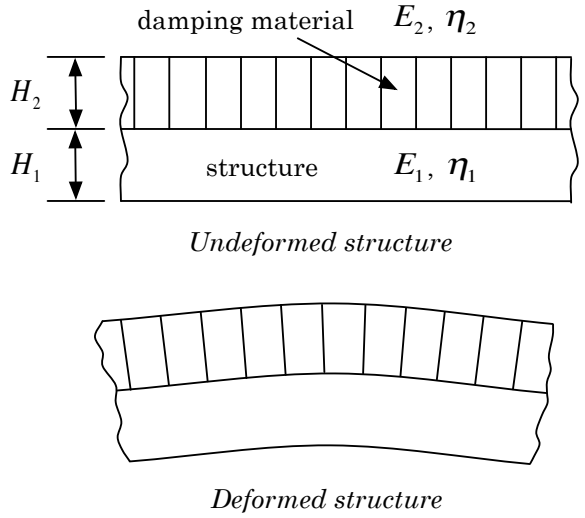

Figure B2.4 – Unconstrained or free-layer damping treatment.

For a given weight, the shear type of damping treatment is more efficient than the *unconstrained-layer damping treatment*. However, this efficiency is balanced by greater complication in analysis and application. The treatment is similar to unconstrained-layer type, except the viscoelastic material is *constrained* by a metal *layer*. Therefore, whenever the structure is

subjected to cyclic bending, the metal layer will constrain the viscoelastic material and force it to deform in shear. The shear deformation is the mechanism by which the energy is dissipated. This concept is illustrated in Figure B2.5.

To illustrate this case further, consider two extremes of the middle layer damping properties for Figure B2.5.

At low temperatures, where the material is in its glassy region, both the structure and the constrained layer become rigidly coupled. In this case, whenever the system is subjected to cyclic bending, little shear deformation occurs in the middle layer, and hence the energy dissipation is also small.

On the other hand, at high temperature, where the viscoelastic material is in its rubbery region and soft, both the structure and constrained layer become almost uncoupled. The energy dissipation in this case is also minimal, even though the shear deformation in the middle layer is high. This is because the shear modulus of the middle layer is low.

Between these two extremes, the material possesses an optimal modulus value, so that energy dissipation for the constrained layer goes through a maximum. The maximum shear deformation in the middle layer is a function of the modulus and the thickness of the constrained layer, the thickness of the damping layer and the wavelength of vibration in addition to the properties of the damping material.

The performance of the *constrained-layer damping treatment* depends to a large extent on the geometry and type of constraining layer [63-64,68-69,73-74,78]. Usually, it is desiderable to have the constraining layer as stiff as possible to introduce the maximum shear strains into the viscoelastic layer. However, the constraining-layer stiffness should not normally exceed that of the structure. Therefore the maximum amount of shear strain is usually accomplished whenever the constraining layer is of the same type and geometry as that of the structure to be damped. This is usually referred to as the *sandwich damping treatment* and is illustrated in Figure B2.5b [67,76].

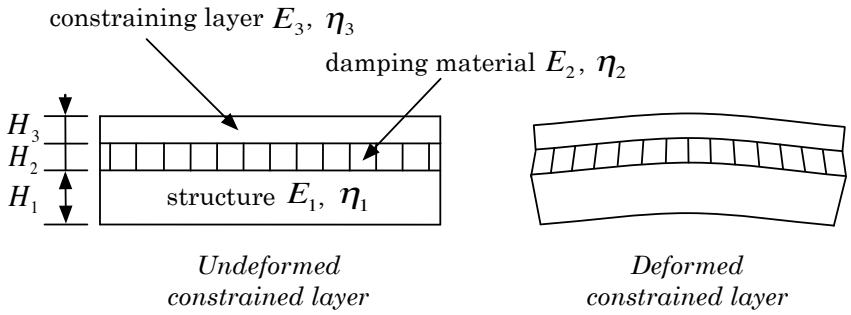

(a) Constrained-layer treatment

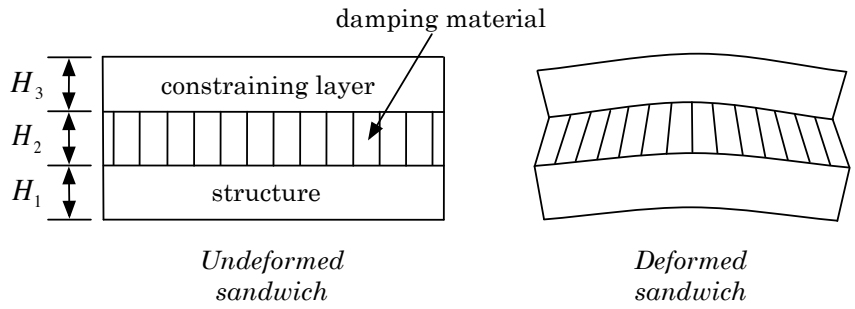

(b) Sandwich panel

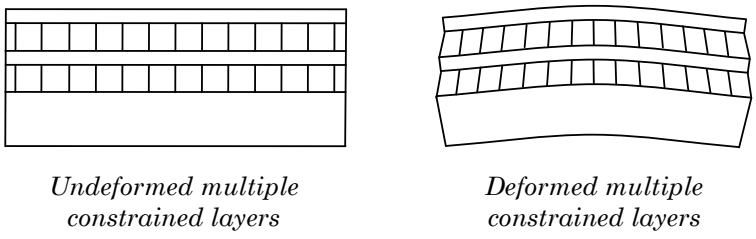

(c) Multiple constrained layers

Figure B2.5 – Various constrained damping treatments: (a) Constrained-layer treatment, (b) Sandwich panel, (c) Multiple constrained layers.

Multiple constrained-layer treatments are usually used as a means for increasing the damping introduced to a structure [72]. Increasing the number of layers as the same effects as increasing the thickness of the constrained layer, but with slight variations. Figure B2.5c illustrates two constrained layer treatments on a structure. As a result of many tests on the performance of the multiple constrained layers, it has been found the most of the shear deformation occurs in the first damping layer, closest to the structure. In other words, all subsequent layers work mainly to increase the stiffness of the constraining layer to which the first damping layer is subjected.

All the aforementioned cases relating to the surface damping treatments are directly affected by changes of some specific characteristics, i.e. temperature, multiple materials, thickness, initial structural damping, frequency and wavelength and partial coverage.

As usual, *temperature* is the first parameter of importance with respect to the damping performance of a constrained- or unconstrained-layer treatment. Obviously, it is very important to select and match the appropriate material for the desired environment over which it needs to operate. There are a number of commercially available materials whose transition regions occur over different temperatures, ranging from as low as -200° F to as high as 2000° F.

Several attempts have been made to broaden the damping performance of the layer treatments with respect to temperature. One of the easiest ways to reach it is by selecting *several materials* with different properties. These optimum properties must occur at two or more different temperatures. For instance, if the temperature range for which the treatment has to operate is from -50° F to 150° F, it may be necessary to select one material that has its optimum value around 0° F and another material that has its optimum value approximately 100° F. It will than be possible either to place one material layer on one side of the structure and one on the other or both on top of each other so that

their performances are combined to give wide temperature coverage.

Having selected a damping material with optimum damping capability over the desired temperature range of operation, the next variable to be investigated is the *thickness* of the damping material relative to that of the structure. Increasing the thickness of the viscoelastic material higher damping can be achieved in the system. However, it is also evident that this increase in damping is not a linear function of thickness. This is because if the damping material thickness is much greater than that of the structure, the composite system damping approaches that of the viscoelastic material itself, and it is not possible to obtain higher composite damping than that of the viscoelastic material. On the other hand, for small thickness the increase in damping is almost linear with respect to the thickness; that is, if the thickness is doubled, the amount of damping in the system is also doubled. This case is accurate only if the damping properties of the material do not change greatly with frequency. The performance of a constrained-layer damping treatment depends not only on the thickness of the viscoelastic material, as in the case of the unconstrained layer treatment (defined above), but also on the thickness and type, i.e. geometry, of the constraining layer.

Regarding general discussion concerning the performance of constrained- and unconstrained-layer damping treatment, it could be assumed an *initial structural damping* equal to zero. However, in many cases the structural damping is significant and should be included in the analysis. This is particularly true for structures with many joints and/or subcomponents that are likely to contribute to the overall damping. For example some diesel engine components could have modal loss factor values as high as 0.05. Hence, adding small amounts of an unconstrained or constrained layer damping treatment to such a structure might not result in significant improvement beyond the 0.05 initial modal damping, and it would be necessary to utilize the material in much higher thickness for significant improvement to be

achieved.

It is very difficult to separate the effects of *frequency* and *wavelength* on the performance of constrained-layer damping treatments. However, the direct effects of frequency are small compared to those of the wavelength of vibration because the properties of the material do not change very much with frequency, but the performance is a function of the square of the semiwavelength of vibration. Taking into account the variation of the composite damping loss factor, with temperature, for different semiwavelength of vibration, it can be seen that the peak loss factor occurs at a lower temperature for the lower semiwavelength of vibration [6]. The phenomenon is related to the fact that lower wavelengths of vibration have higher modal stiffnesses associated with them; hence the constrained-layer treatment is capable of introducing the same shear strains at lower temperatures.

Since high damping is usually best achieved when the damping material is subjected to large cyclic deformations, the locations of the damping material on the vibrating structure are important, i.e. *partial coverage* [65-66,70,77-79]. Therefore, knowledge of the vibrational mode shapes of interest is necessary to determine the location where the maximum bending stresses occur. For the first mode of vibration of a simply supported beam, the maximum bending stress occurs around the center of the beam. Therefore, by concentrating the material around the center of the beam, better performance will be achieved than if the same amount of material is distributed uniformly over the beam. Unfortunately for most cases it is not practical to do this because damping is usually required for many modes covering a wide frequency range, and conflicting optimum locations occur.

All the abovementioned kind of changes that could affects the surface damping treatments are defined and verified through several examples in a textbook by *Nashif et al.* [6].

B2.6 Surface damping treatment development

In many practical plate and machinery casing structures, it is difficult to treat the whole surface with constrained layer viscoelastic material. Further, it may indeed be desirable to selectively apply one or more damping patches to control certain resonances.

Patch damping design is an efficient and cost effective concept for solving noise and vibration problems [6,65,72]. However, there is a limited body of scientific literature on this topic and it therefore remains a somewhat ill understood and empirical technique.

Elastic beams with constrained layer viscoelastic material have been analyzed by many investigators, as evident from the extensive references and studies described in the book on vibration damping by *Nashif et al.* [6]. However, much of the prior work has been limited to full coverage [65-67], i.e., viscoelastic material added to one or both sides of the beam in a uniform manner. Conversely, only a very few publications have dealt with partially covered sandwich beams [65-66,70,72,77-79].

In practice, non-uniform and/or partial damping treatment is necessary because of material, thermal, packaging, weight or cost constraints. And in some applications multiple damping patches at selected locations are more desirable. None of the mathematical models, as available in the literature, appears to be directly applicable to this problem. Consequently a clear need exists for a more refined analysis which this thesis part's with the aid of some other articles attempts to fulfill.

Single or double constrained layer patches have been computationally examined by using higher order differential equation theory [6], the Rayleigh-Ritz method [6,65,66,72,76-77], or a finite element procedure [67,73-74]. Experimental methods of investigation have included modal testing [6,65,66,72], structural intensity mapping [79] and modal strain energy methods used to study the energy dissipation pattern in vibrating structures with a viscoelastic damping layer [63-64].

Nokes and *Nelson* [78] were among the earliest investigators to provide an analytical solution to the problem of a partially covered sandwich beam. In their formulation, damped mode shapes are assumed to be the same as the undamped eigenvectors, and the modal loss factor was calculated as the ratio of energy dissipated to the total modal strain energy. A more thorough analytical study was carried out by *Lall et al.* [77]. In their Rayleigh–Ritz approach, both flexural and longitudinal shape functions were incorporated in the eigenvalue problem for a plate with a single damping patch. Through this approach they calculated the natural frequencies and modal loss factors also reporting a parametric study on the patch size and location.

Kung and *Singh* [65] have studied this simply supported plate case again for the sake of the verification and for create an analytical method to predict modal properties of a damped structure through an energy-based approach.

This latest work represents an extension of another analytical and experimental methodology proposed by the same authors for sandwich beams. In this other work *Kung* and *Singh* [72] have developed an analytical method employing a Rayleigh–Ritz minimization scheme that considers flexural, longitudinal, rotational and shear deformations in all layers of a sandwich beam verifying the method by comparing results for a single patch with those reported in the literature [77] and with modal measurements. Through this approach are also estimated the unknown material properties of viscoelastic material used in the experimental study and finally are examined critical issues such as the patch boundary conditions and discontinuity in the material.

Another work extends prior work [65,72] by proposing some approximate analytical methods applied to plate examples to seek some insight into the patch damping design process. Once more, *Kung* and *Singh* [66] developed tractable formulations that identify the role of some parameters, i.e. material properties, viscoelastic layer thickness, patch size, number of patches and

their locations.

By the 1990s, active constrained layer damping had begun to receive more attention. The active constrained layer damping treatments consist of a layer of viscoelastic material bonded to the host structure and constrained by an actuator. These treatments control vibrations by means of several mechanisms: the actuator increases the dissipation of energy by increasing the shearing in the viscoelastic layer, and simultaneously it controls the vibrations by applying forces to the host structure through the viscoelastic layer. Some analytical formulations of active constrained layer damping treatments were then proposed [71,80].

Earlier works on constrained layer damping are mainly contributed to the passive constrained layer damping. In some of these works with objective to minimize the integrated global vibrational energy of the base structure over a frequency range of interest, a genetic algorithm (GA) based penalty function method is further employed to search for the optimum of the locations and lengths of the constrained layer damping patches [68-70].

Experimental results done by several researchers like *Spalding* and *Mann* [79] shows how structural intensity can predict where to locate small-constrained layer damping patches to attain either local or global velocity changes on a plate. If damping is applied to a region of low shearing reactive structural intensity magnitude, a local velocity change is seen. If damping is applied to a region of high shearing reactive structural intensity magnitude, a global velocity change is seen. In addition, the researchers noted that large damping patches produce global velocity changes.

CHAPTER B3

Vibration reduction through patch applications: introduction to the methodology

Unwanted vibrations in structures are a common problem in industry. In practice, platelike structures (such as those found in washing machines, refrigerators and motor enclosures) are often damped by applying constrained layer-damping material over the entire surface of the structure or the part of the structure that is accessible at the expense of increased manufactured time and product cost. Therefore, careful placement of damping patches is important for product cost, noise and vibration reduction.

This research aims at being a step towards the goal of determining damping placement on a structure in order to ensure noise reduction and therefore, to improve structural vibrational

behaviour. In the following will be shown how potential energy distribution could define the placement of constrained layer damping patches on a plate in order to produce changes in the velocity pattern of the structure. All the considerations and conclusions are derived from the numerical results obtained by the numerical simulations carried out on two specific mechanical component: one steel plate and one steel bracket different by boundary conditions and by dimensions (the thickness of the component). Goal of this chapter is to present the general methodology used for carrying out numerical simulations with the aim to reduce the level of unwanted vibrations in mechanical components through the bright application of some specific component characterized by high damping properties. The numerical simulations carried out on two aforementioned principal components (plate and bracket) will be used in order to assess their potential energy distribution and normal velocity values. The results coming from the simulations performed on these two different components will be used to determine the best placement of thin layer damping patches in order to ensure vibration reduction. In turns, these quantities can provide important information on the effective reduction of the component amplitude vibration level.

B3.1 Why this choice?

Concerning this subject, referred as the vibration reduction through patch application, one of the most significant observations from experimental results is that local or global changes in vibration amplitude can be achieved using *structural intensity* to guide the placement of constrained layer damping material. Local velocity changes occurred when damping was placed over an area of low intensity. Global velocity changes occurred when damping was placed over an area of high intensity.

These results represent important practical information because it is very useful in practice to produce velocity reductions at some frequencies in order to reduce sound radiation while maintaining the vibration at other frequencies that already radiate sound very inefficiently. Thus the measured intensity can be used to determine the appropriate location of small-constrained layer damping patches to attain desired vibration reductions at specified frequencies without inadvertently changing the vibration pattern at other frequencies.

In this work will be used a new approach that want to attempt the same final goal, referred as the improvement of the vibrational behaviour of some mechanical structures, without the need to evaluate the bending/shearing intensity values or intensity mapping and especially to overcome all the problems directly related to their difficult assessment and estimation. In other words, the desired target referred as the identification of "hot spots" within an elastic structure which, if locally damped, can be best suited for vibration reduction on the entire frequency range, will be reached by the estimation of potential energy distribution that is a task easier by far than any evaluation of intensity or intensity divergence.

In this study the formulations in [59] have been considered taking all the considerations and conclusions to be helpful. Briefly, these formulations consist of evaluating the system's loss factor in systems with non-proportional and non-homogeneous damping. In [59] three energy definitions of loss factor were tested corresponding to equations (B1.1), (B1.2) and (B1.9) presented in *Section B1.3* of *Chapter B1*. The difference between the three is in the type of energy involved. The basic definition referred as eq. (B1.1) comprises the sum of kinetic and potential energies, the simple definition replaces the total energy by twice the kinetic energy, eq. (B1.2), and the present definition, based on eq. (B1.9), uses twice the potential energy instead. These cases shows that the loss factor estimate using the potential energy formulation, eq. (B1.9), gives much better results than the

classical formulation, eq. (B1.1), which just vaguely indicates the correct trend of the global loss factor with frequency. The estimate via the kinetic energy is not only much inferior to the former two, but shows the frequency trend which is contrary to the true value.

These latter informations provide further confirmation about the validity of the procedure followed in the creation of the methodology and about the basis on which the study is based.

In reality damping will rarely be uniformly distributed or stiffness proportional across a structure (*Chapter B2*). Due to the fact that for real structure damping is never uniformly distributed across it, the study is done taking into account the total potential energy and how it is distributed within the structure. In such a way, it is desirable to assess the potential energy values for prescribed structure and to classify the mode shapes of the component due to its potential energy values.

Through the knowledge of the potential energy that came from the study of the mechanical component, it will be possible to find and define the areas on it where the surface damping treatments (patch) needs to be applied and exploited to solve a variety of resonant noise and vibration problems.

B3.2 Overview of the practical study

From all the previous considerations it is simple to comprehend which way will follow the practical study addressed to decrease the structure vibration level in order to improve the vibratory behaviour of the structure in the entire frequency range. The knowledge of these quantities allows to evaluate the energy distribution within a structure and consequently to quantify without any doubtful point the improvement extent regarding the structure vibratory behaviour. Important aspects of the procedure created and adopted in this thesis are: (i) the knowledge of potential energy and velocity values avoids determining the

intensity amplitude of the structure facilitating the results achievement, (ii) the time needed for the results achievement is considerably reduced, (iii) the amplitude vibration level of a mechanical component is certainly reduced, (iv) potential energy evaluations normally doesn't fails close to sources or discontinuities, which instead happens to vibration intensity estimations. Therefore, the evaluation of potential energy attempts to improve the robustness and precision of energy flow estimation within the structure.

Hereafter will be summarily presented the methodology adopted in the evolution of the work and the procedure followed to make feasible the measure of the energy flow within a defined structure. Through this approach, the potential energy distribution and the velocity values, specific quantities of the mechanical component subjected to precise boundary condition, can be easily and safely evaluated. These quantities are evaluated in all the frequency range on which the mechanical component is studied. Both for the plate as for the bracket such quantities will be estimated in order to assess their vibratory behaviour until their sixth mode shape (sixth mode shape included). In other words these frequency range will be comprised into a range between 0 and 170 Hz for the plate case and between 0 and 180 Hz for the bracket component respectively.

In order to validate the procedure, the methodology created will be performed studying two different components characterized by different shapes and different boundary conditions, but keeping unchanged the mechanical characteristics of the patches and of the base structure. For each component a forced analysis will be performed. It is important to remember that the force should not be applied on component symmetry positions in order to have the certainty to excite all the modes of the structure.

To perform an intelligent and suitable study of both the principal structures took into account (a plate and a bracket) the work will follow some simple steps summarily outlined below:

- Introduction to the methodology followed for create the FE model and for arrange it to the accomplishment of the analysis;
- Estimation of potential energy density and normal velocity values related to the base structure on its entire frequency range;
- Estimation and comparison of the results derived by different configurations, both for the plate and for the bracket.

The first two steps are performed in I-DEAS® environment whereas the last one is granted through Matlab®, that allows to treat all the results obtained by the numerical simulations in order to better display and compare the values that comes from the different simulations.

The aim of the numerical simulations are twofold: firstly, the evaluation of energy distribution and energy flow within a structure achieved through the potential energy estimation; secondly, to give the correct patch locations, which are used in order to decrease the structure vibration level of the entire structure. In other words, through the knowledge of the potential energy density that came from the study of the basic component, i.e. only the structure without any patch (initial or unrefined configuration), it will be possible to define the areas on it where is necessary to put the thin patches for improve its vibrational behaviour. Therefore, it will be fundamental to define the best-suited positions on the surface of the structure where the material damping will take place in order to reduce vibrational energy. *Chapters B5* shows two possible ways both leading to a correct patch location on the surface of the unrefined structure. In both cases, the patches are placed on the component (the plate or the bracket) according to the potential energy extent. The only difference between these two ways lies in the modality on which the presence of the patches is highlighted. These considerations will be treated extensively in *Chapter B5*.

As broadly defined in *Chapter B2*, several possibilities concerning the type of patches that could be applied on the surface of the structure still exist, i.e. free layer damping treatment, constrained layer damping treatment, sandwich damping treatment, multiple constrained layer damping treatment and partial coverage treatment. This thesis part is focused on the study and improvements of mechanical components, representing elementary parts or subcomponents of more complex systems. These components are usually characterized by a narrow space in which act in order to make improvements, and therefore it is not possible to act on the entire surface of the component. Hence, the case of partial coverage damping treatment will be took into account, then all the patch application cases performed during this thesis part will be referred to the partial coverage case.

Material damping, i.e. the patch, enable to adds stability to the system and it becomes generally more efficient at high frequencies, obviously depending by the kind of the material damping adopted, by the extent on which the material with high damping properties is applied on the surface of the base component and by the number of the patches directly applied on it. However is made the choice of the material which forms the patch, it will always be a material contained in the family of viscoelastic material, see *Section B2.4*. Regarding the studies related to the plate and to the bracket respectively, the same material is considered, characterized by the mechanical characteristics of those listed in *Table B3.1*. In addition to the mechanical characteristics of the two materials adopted during the simulations (steel and asphalt), are also listed the correspondent values of structural element damping coefficient or initial structural damping as mentioned in *Section B2.1* and *B2.5*.

	E_Y $[Pa]$	ρ $\left[kg/m^3\right]$	υ	η_h	*component*
steel	2,1e11	7800	0,30	1%	**plate/bracket**
asphalt	1,2e10	2100	0,21	17%	**patch**

Table B3.1 – Mechanical characteristics of the components

This value, clearly higher for the patch compared to the basic component, will allow the software to take into account the simultaneously influence of different damping values in relation to the two different materials constituent the modelled structure (basic component with patches). In practice, by introducing the initial structural damping it will be possible to model the real influence of the contact between the plate/bracket and the patches applied on them. As a matter of fact, considering general discussion concerning the performance of constrained- and unconstrained-layer damping treatment could be assumed an initial structural damping equal to zero, see *Section B2.5*. However, in many practical cases the structural damping is significant and should be included in the analysis. This is particularly true for structures with many joints and/or subcomponents, i.e. the positive displacement pump studied in *Part A*, which is likely to contribute to the overall damping. For example some diesel engine components could have modal loss factor values as high as 0.05. Hence, adding small amounts of an unconstrained or constrained layer damping treatment to such a structure might not result in significant improvement beyond the 0.05 initial modal damping, and it would be necessary to utilize the material in much higher thickness for significant improvement to be achieved. Although in the present work some generic components (plate and bracket) will be studied, it will be difficult that the initial structural damping of these base

components will be significant compared to the base component-patch assembly. Despite this, in order to create a proper methodology for reduces unwanted vibrations in mechanical components the aforementioned aspect has to be taken into account. This quantity, labeled as the hysteretic damping η_h is directly took into account through the introduction in I-DEAS of the percentage correspondent to the specific kind of material utilized (see *Section B5.2*, Tables B5.1.a, B5.1.b and B5.1.c).

It is important to underline that the definition of the correct patch location, which is used in order to decrease the structure vibration level, comes from the study of the base or unrefined configuration. By means of the simple structure study it is possible to define, for each natural frequency of the component, the best-suited position for the application of the patches. As already mentioned, in the evolution of this work will be taken into account only the first six natural frequencies for the plate as well as for the bracket. This choice is supported by the fact that the study of the higher frequencies is not so important from the structural point of view (the highest frequencies are hardly excited during operational conditions), furthermore the vibratory behaviour of the component at those higher frequencies become misleading. For each natural frequency of the base component the potential energy distribution will be estimated. The knowledge of this quantity will provide necessary and accurate informations about the position and the size of the patches that have to be applied on the surface of the component, in order to reduce his overall amplitudes vibration level just acting locally (directly acting on each natural frequency). In other words, the patches will act in some restricted areas of the surface of the component in order to affect the global behaviour of the base structure (reduction of the amplitude vibration level in all the frequency range of interest). The potential energy values estimated through the numerical simulations performed in I-DEAS environment are expressed in the form of a range of values. This means that all the potential energy values evaluated for a generic component

subjected to a dynamical loading are included between their maximum and minimum thresholds values. The same thing can be seen in the form of a component colours mapping, in which "hot colours" symbolize the highest potential energy values whereas the lowest are symbolized by "cold colours" (see Figure B3.1.a).

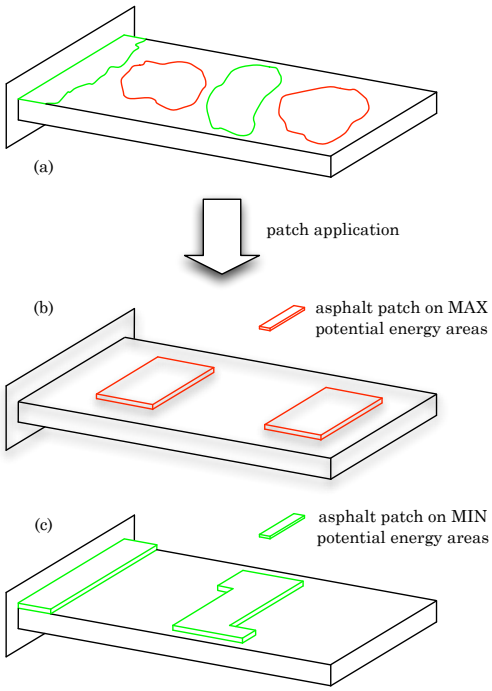

Figure B3.1 – Patches application on the surface of the plate for a generic natural frequency.

Thanks to this, the asphalt patches will be placed on the component surface according to the knowledge of the areas in which the highest potential energy density is localized (see red areas in Figure B3.1.a). Furthermore, the knowledge of the extension and number of these "hot colours" areas, in turns will define the dimensions, the location and the number of the patches that has to be used (see Figure B3.1.b). In order to increase the

awareness of the reliability of the approach adopted, the patches were applied also on the areas in which the lowest potential energy density is localized (see green areas in Figure B3.1.a and Figure B3.1.c). Regarding potential energy evaluation, the vibratory amplitude reduction is greater in the case of patches application in areas of highest potential energy density rather than in the lowest potential energy areas. This point will be explained and demonstrated in *Chapters B5* and *B6* for the plate and for the bracket respectively.

As will be shown in the next chapters and already shown in Figure B3.1, the patches are nothing more than parallelepipeds having the mechanical characteristics of a viscoelastic material already defined in Table B3.1. Hence, the study of the first six natural frequencies (frequency range in which the plate and the bracket are studied) will lead to the creation of six different configurations (six different FEM models), each one clearly marked by a different placement of the patches on the surface of each component. In fact, Figure B3.1 shows the distribution of the potential energy and thus the placement of the patches in relation to a generic natural frequency of the plate component. Another "configuration" will be generated studying the same component referred to another natural frequency. This means that the dynamic analysis performed on the plate component by studying its second natural frequency, will lead to a potential energy distribution that will be different from that obtained by studying its third natural frequency. This will imply a different placement of the patches on the surface of the plate. Although the placement of the patches is assigned by the study of each natural frequency of the plate, in addition to influence the same frequency, these thin layer components also affect the other frequency comprised in the frequency range of the plate, thus generating with a particular impact an overall reduction in the amplitude vibration level of the plate. Hence, achieving this methodology on a broad frequency range of the component studied, it will be possible to know which "natural frequency modelling" will lead to larger

reduction of the amplitude vibration level. Of course, depending on the operational conditions of the system in which the component work, it is possible to only act on a specific dangerous frequency, thus improving its vibratory behaviour.

To simplify and make more reliable the choice of the patch configuration that produce the best contribution in relation to the vibration reduction, the velocity values of the component subjected to a dynamical loading (plate and bracket) needs to be evaluated. In order to give this important information, this quantity should be assessed throughout the entire frequency range of the component studied. In this manner, through the numerical simulation generated via I-DEAS, the normal velocity values estimated into the entire frequency range of interest will be evaluated. However, these velocity values generated by the numerical simulations still require additional expedients. A simple example may help the reader to understand this point.

During the numerical simulation, the software will calculate for each mesh nodes of the basic structure the velocity values. If 3000 nodes compose the FEM model of a generic mechanical component, through the numerical simulation the software will generate an output file containing 3000 velocity values in a complex form in relation to the X, Y and Z directions. Pointedly the direction of interest for the evaluation of the velocity will be the perpendicular to the surface of the plate, that through the knowledge of the reference system leads to the study of the velocity in the Y direction only (Z direction for the bracket). In this case, every velocity value will be directly dependent by the temporal (t) and physical components of each node (x, y, z). Obviously the velocity values calculated in this way are unstable, therefore it is desirable to “remove” the time dependence, that is cause of instability in the numerical simulations, and ensure their dependence by the coordinates (x, y, z) only. This means moving from a level in which the velocity values are directly dependent by the specific instant of time, to another level in which the velocity values are temporally averaged.

To move around this problem, which then lead to the normal velocity values determinations related to the entire frequency range of the component studied, the effective velocity values or RMS velocity values will be calculated.

$$v_{eff} = v_{RMS} = \sqrt{\bar{v}(t)^2} \qquad -= \frac{1}{T}\int_{\substack{0 \\ T\to\infty}}^{T} (\ )dt \tag{B3.1}$$

In eq. (B3.1) the symbol $\bar{}$ denotes the temporal average. Through some simple steps, this equation can be adapted to become the following:

$$v_{eff} = v_{RMS} = \sqrt{\frac{1}{N}\sum_{n=1}^{N}|v_n|^2} \tag{B3.2}$$

where n denotes the n-th nodes while N denotes the maximum node numbers of the component mesh, and clearly v_n identify the velocity values for the n-th nodes that come from the numerical simulations performed in I-DEAS environment. As already mentioned, these values are specifically the velocity values in the Y direction for the plate and in Z direction for the bracket (depending by the reference system adopted). Thru eq. (B3.2) each velocity value generated through the numerical simulations will be translated into the corresponding value of effective velocity. Thanks to this "expedient" it will be possible to graph the velocity trend in the entire frequency range.

Treating these data and than chart them for the base component (plate or bracket) as well as for all the other configurations (base component with the patches added on it) will allow to define in a clear and unambiguous way for which natural frequency modelling will be produced the highest reduction in the overall vibration amplitude level of the component studied.

Summarizing, it is possible to define some key points relating to the study generated and widely explained in *Chapter B5* and *Chapter B6*.

(i). The potential energy distribution evaluation, in relation to the base structure, enable to define the best patches location, which are used in order to decrease the structure vibration amplitude level;

(ii). The potential energy distribution estimation is performed in correspondence of each natural frequency of the basic structure comprised in the entire frequency range of interest. For each one of these is realized a potential energy density mapping that represents the energy propagation within the structure;

(iii). Thru the knowledge of the two aforementioned points it is possible to put the patches on the base component, i.e. on the areas where is greatest the potential energy density;

(iv). For each one of the configuration generated (for each one of the natural frequency comprised in the entire frequency range) the velocity values are evaluated. These values will then be converted in effective velocity value or RMS value;

(v). Through the knowledge of these RMS values it is possible to define which configuration is the best between all those generated. This means defining which patch positions (patch configuration) leads to the maximum abatement of the structure vibration amplitude level.

As already mentioned, the results obtained following the guidelines presented and explained in this section for the two principal component studied (the plate and the bracket), will be presented in *Chapter B5* and *Chapter B6* along with all the considerations and informations adopted in their FEM model creation.

CHAPTER B4

Confirmative numerical simulations

This chapter attempts to provide some information about the effectiveness of the methodology created by introducing some numerical simulations, which allows to increase the robustness of the methodology created giving at the same time important information about the validity of the results obtained in the next chapters.

As mentioned in *Chapter B3*, in the following chapters will be presented all the information introduced in the FEM model of two principal components (the plate and the bracket) along with all the results obtained for these two cases. For both the cases will be generated numerical simulation by measuring the potential energy distribution and normal velocity values; in turns these

informations will be used to determine the best placement of damping patches to ensure the overall amplitude vibration reduction of the plate and of the bracket. Before dealing with the exhibition of this results needs to be introduced other specific numerical simulation with the aim to confirm the validity of some crucial steps of the procedure followed for carrying out this work. In other words, through the numerical simulations presented in *Sections B4.1* and *B4.2* will be addressed two aspects that are the potential energy evaluation and the manner in which the patches has to be applied on the surface of the component respectively. These sections attempts to answer some questions of fundamental importance for the proper success of the procedure created and adopted in this thesis part. Some of the questions are: have we full confidence that the procedure followed in the evaluation of the potential energy through the I-DEAS software is correct? Have we full confidence that the simulations performed provide the "true" values of potential energy of the component? Considering that we are working on a FEM model and not with experimental tests, are we sure that the patches are applied properly on the surface of the structure hosting them? Are we sure that the base component feel the presence of the patches on it and that the latter are not only rest on its surface?

Sections B4.1, *B4.2*, *B5.1* and *B5.2* will find answers to each of these questions by leaving the certainty of reliability and accuracy of the procedure followed for reach the overall reduction of the amplitude vibration level on a generic component.

B4.1 Potential energy evaluation

To confirm the validity of the procedure followed in relation to the creation of the component FEM model and to the potential energy and normal velocity evaluations is studied a beam component following two different ways.

Namely, potential energy values will be calculated at precise frequencies values (far from the resonant frequencies values) for the beam component, on which will be applied a single force at certain coordinates following two different ways: (i) an analytical way that will provide the exact potential energy values of the beam component and, (ii) a numerical way following the methodology previously accounted by using the I-DEAS software.

Obviously, if the methodology created reflects a correct process, the potential energy values obtained by the two ways should be very close to each other. If not, the methodology created and adopted could not in any way provide informations on the positions on the component surface of the patch application, and therefore would be useless for our purposes.

Hereafter will be exposed the characteristic dimensions of the beam component (Figure B4.1), the location of the force on the surface of the beam, the mechanical characteristic of the steel beam, and the frequencies on which the study is based, see Table B4.1.

Mechanical characteristics	Characteristic dimensions	Force applications	Frequency values
$E_Y = 2e11\ Pa$	$l = 1\ m$	$g = 0.7\ m$	$\omega = [20,50,100,200]\ Hz$
$\rho = 7800\ kg/m^3$	$b = 0.05\ m$	$n = 0.025\ m$	
$\upsilon = 0.3$	$h = 0.01\ m$		

Table B4.1 – Modes on which apply the patches.

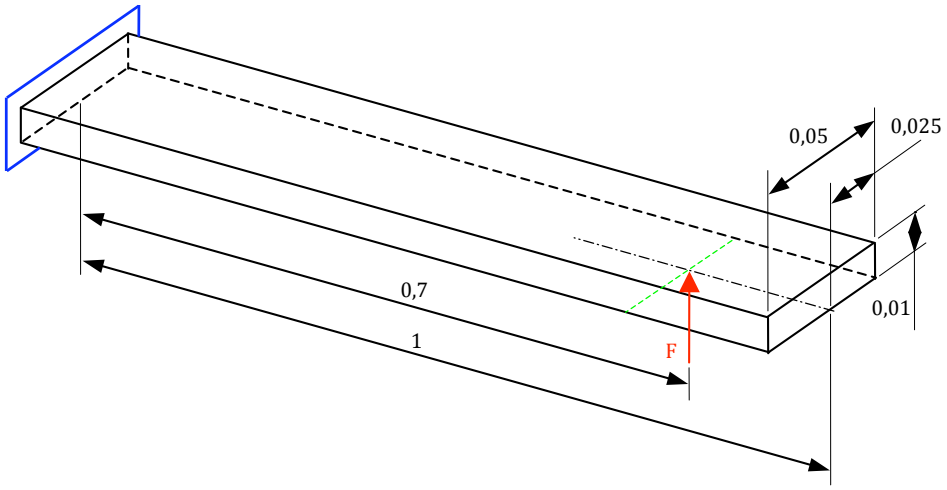

Figure B4.1 – Characteristic dimensions of the beam component and location of the force.

From Figures B4.2 to B4.2.f are shown the fem model of the beam component and its first six mode shapes respectively.

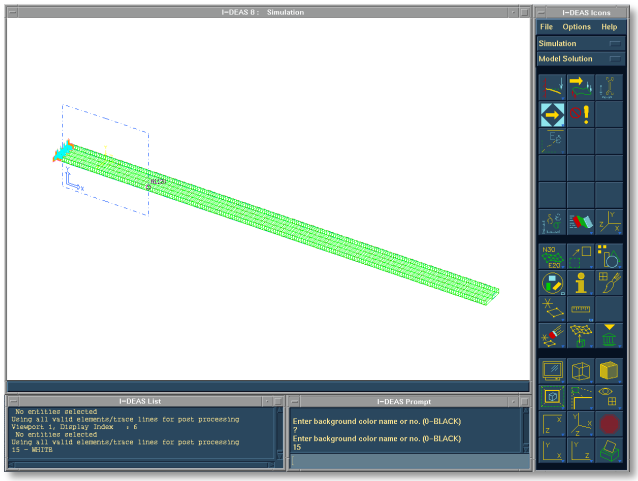

Figure B4.2 – Beam fem model.

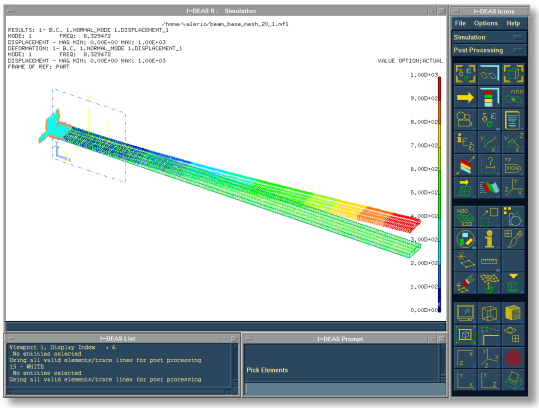

Figure B4.2.a – First mode shape of the beam component.

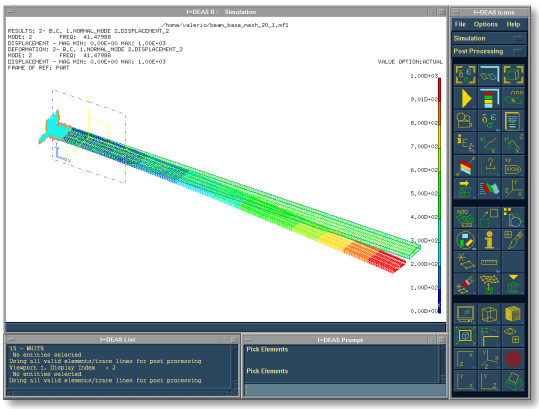

Figure B4.2.b – Second mode shape of the beam component.

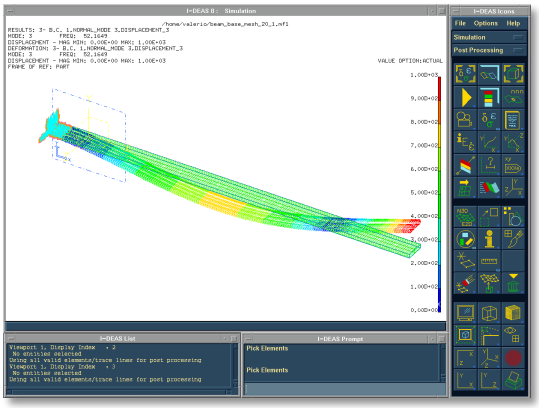

Figure B4.2.c – Third mode shape of the beam component.

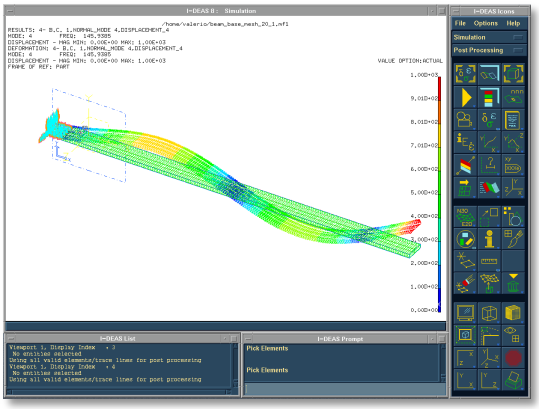

Figure B4.2.d – Fourth mode shape of the beam component.

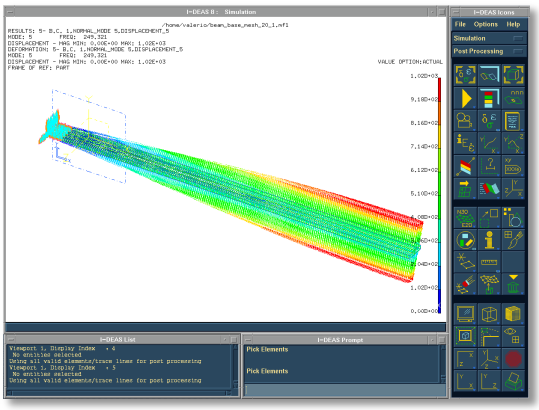

Figure B4.2.e – Fifth mode shape of the beam component.

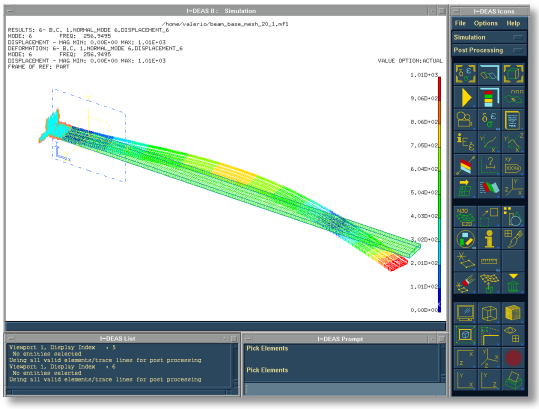

Figure B4.2.f – Sixth mode shape of the beam component.

In Figures from B4.3.a to B4.3.d are shown the comparisons of the potential energy values obtained by the two different ways previously mentioned starting from the study of the first frequency value (20 Hz) and ending with the study of the fourth frequency value (200 Hz) contained in the "range" exposed in Table B4.3. In all the cases, the blue line identifies the potential energy trend calculated through the analytical way (Matlab® code), while the red line identifies the potential energy trend obtained by the methodology created and performed through I-DEAS® software.

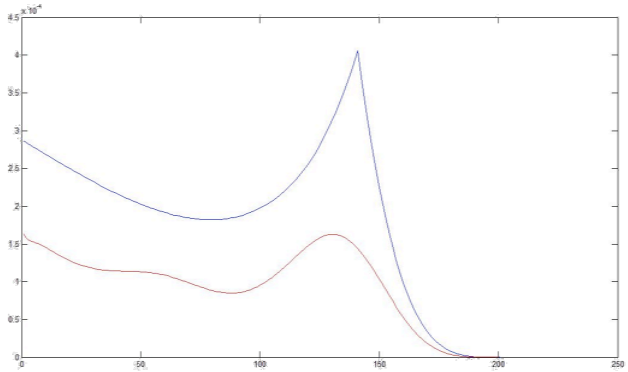

Figure B4.3.a – Potential energy trend: analytical way (blue), numerical way (red) for the first frequency study case (20 Hz).

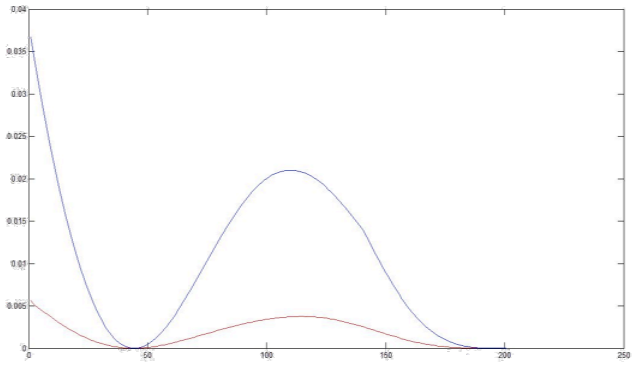

Figure B4.3.b – Potential energy trend: analytical way (blue), numerical way (red) for the second frequency study case (50 Hz).

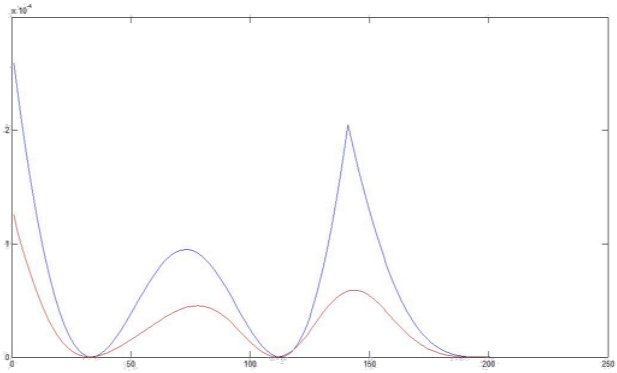

Figure B4.3.c – Potential energy trend: analytical way (blue), numerical way (red) for the third frequency study case (100 Hz).

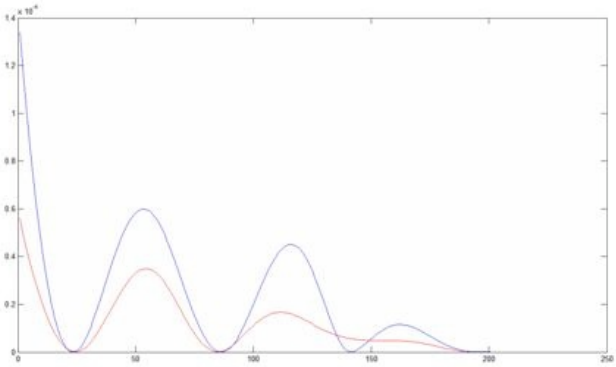

Figure B4.3.d – Potential energy trend: analytical way (blue), numerical way (red) for the fourth frequency study case (200 Hz).

As can be seen by the trends for all the frequencies considered, the potential energy values measured using the created numerical methodology follows in a very satisfactory way the exact potential energy trend calculated through the certainty of the analytical way, then sign of a proper and reliable procedure.

Using the analytical procedure, in reality the force was applied on the surface of the component in a distributed manner (along the green line in Figure B4.1), while the results and the graphs previously reported all concerns to the application of the

force on a single node. To further approach to this condition, the force was applied on three nodes along the green line. Were only considered three nodes due to the fact that the realized beam mesh has a maximum of three nodes for each “mesh line”, see Figure B4.2.

In Figures from B4.4.a to B4.4.d are shown the comparisons of the potential energy values obtained by the two different ways for the same frequency values but increasing the number of nodes on which the force is applied.

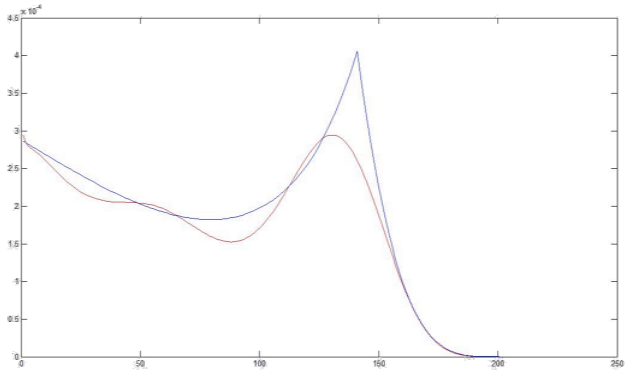

Figure B4.4.a – Potential energy trend: analytical way (blue), numerical way (red) for the first frequency study case (20 Hz) applying the force on three nodes.

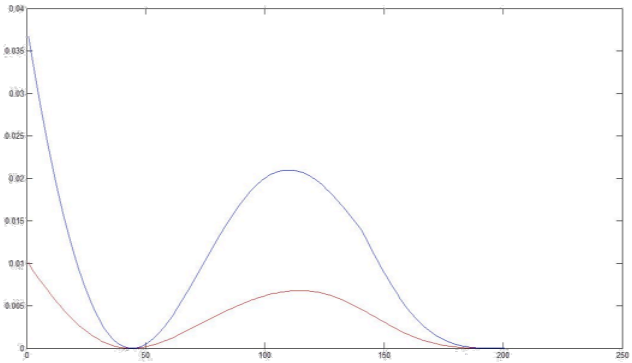

Figure B4.4.b – Potential energy trend: analytical way (blue), numerical way (red) for the second frequency study case (50 Hz) applying the force on three nodes.

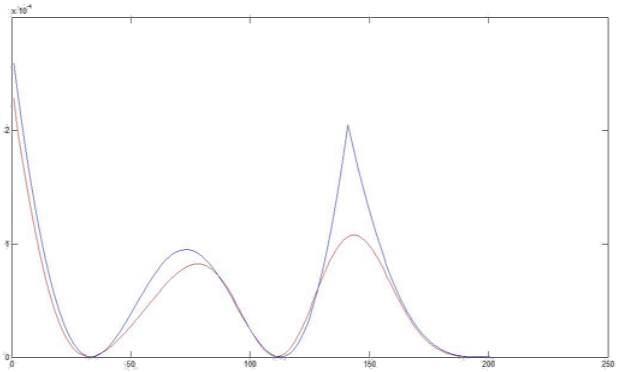

Figure B4.4.c – Potential energy trend: analytical way (blue), numerical way (red) for the third frequency study case (100 Hz) applying the force on three nodes.

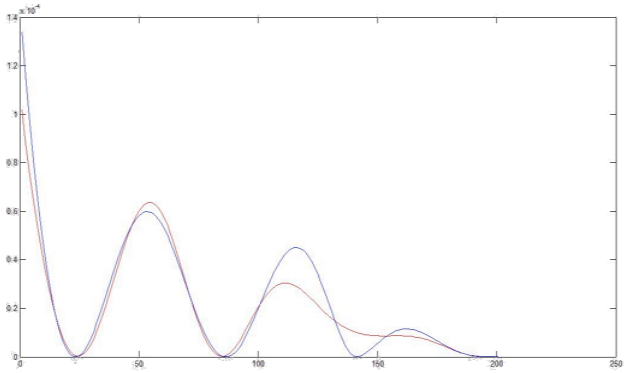

Figure B4.4.d – Potential energy trend: analytical way (blue), numerical way (red) for the fourth frequency study case (200 Hz) applying the force on three nodes.

In this second case can be seen as the increase in the nodes number on which the force is applied lead to the improvements of the results, giving back the potential energy values calculated using the method developed very close to the true values (analytical method). Then, applying the force in a distributed manner along the (green) line, not only on three nodes, will lead to virtually identical values of potential energy.

Considering all the graph presented in this section, it is

possible to see that the only graph on which the two curves obtained through the two different ways reflect trend less close to each other than any other graphics is shown in Figures B4.3.b and B4.4.b, referred on the study case relative to the frequency equal to 50 Hz.

This behaviour is caused by the proximity of the resonant frequency, which then changes the potential energy behaviour. In fact, as can be seen from Figures B4.2.b and 4.2.c relating to the representations of the second and third mode shapes of the beam component, the characteristic frequencies are 41 Hz and 52 Hz respectively, so very close to the frequency used in the study (50 Hz).

This example provides important informations on the validity of the procedure created and exhibited in *Chapters B5* and *B6*, giving in turns clear expectations about the fairness of the results obtained through it.

B4.2 Patch application on component surface

To confirm the validity of the procedure followed with regard to the methodology adopted for applying the patches on the surface of the base component and in relation to the study of the coupled system (base component plus patches), the following numerical simulation is realized.

The study will be characterized by the generation of three numerical simulations in order to assess the potential energy and frequencies values for three FEM models different by characteristic dimensions. Each of the three models will be characterized by the same mechanical properties as those listed in the Table B4.1, which are therefore related to the steel material.

The first numerical simulation will be characterized by the study of a beam component constrained at both the ends (see Figure B4.5.a) and defined by the geometric dimensions listed in

the first column of the Table B4.2.

The second simulation is characterized by the study of the previous component on which a single patch is applied on its upper surface (in red in the picture). The patch has the same mechanical characteristics of the base component (the beam). As can be seen from Figure B4.5.b, the patch will completely cover the base component and the geometric dimensions listed in the second column of the Table B4.2 characterize it. The only variation on the geometric dimensions will be in the thickness of the patch; its length and width will coincide with those of the beam component.

Obviously, the patch will be applied on the surface of the beam component following the same methodology adopted for carrying out the numerical simulations performed in *Chapters B5* and *B6*.

beam	patch	coupled system
$l = 200\ m$	$l = 200\ m$	$l = 200\ m$
$b = 50\ m$	$b = 50\ m$	$b = 50\ m$
$h = 10\ m$	$h = 4\ m$	$h = 14\ m$

Table B4.2 – Characteristic dimensions of the component.

The third simulation will be characterized by the study of a single component, see Figure B4.5.c, whose characteristic dimensions will be equal to those obtained by welding the two components (beam plus patch) adopted in the previous numerical simulation. In the third column of the Table B4.2 will be listed the geometrical dimensions of the component adopted for the realization of this latter numerical simulation.

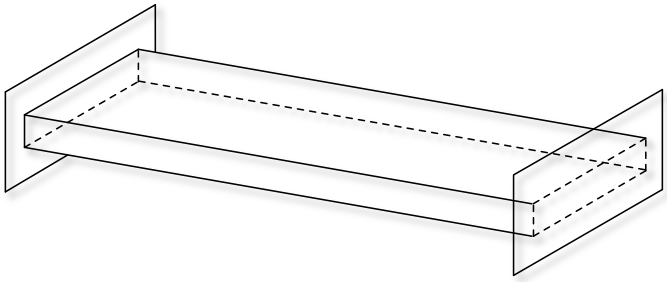

Figure B4.5.a – Configuration first numerical simulation.

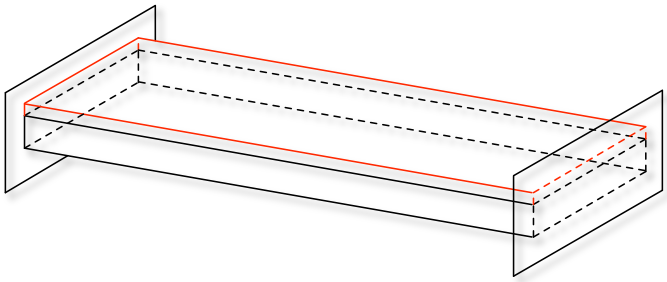

Figure B4.5.b – Configuration second numerical simulation.

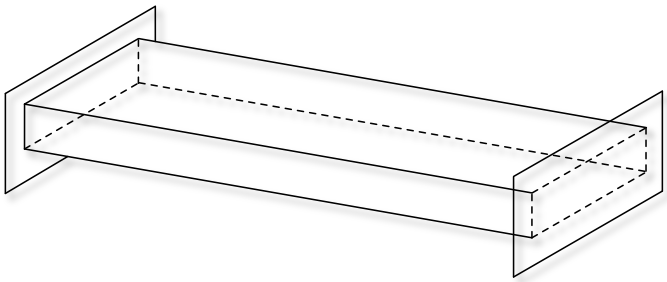

Figure B4.5.c – Configuration third numerical simulation.

Theoretically, if the methodology adopted for the application of the patches on the basic component is correct, the second and third simulations should give the same numerical results with respect to the characteristic frequency and potential energy values of the components adopted in these simulations. A first

information about the validity of the procedure is given by the deformed configuration of the coupled system (see Figure B4.5.b). During the animation of the deformed shape the patch exactly follows the beam component hosting it. This behaviour can also be seen in the next chapters in Figure B5.18 and in Figure B6.9.

This information, although positive, is not enough to validate the procedure created and adopted in this thesis work. The missing information is therefore provided through this example. In essence, the nodes of the patch mesh must match the nodes of the beam component mesh. In other words, the two components nodes that match because of their physical contact should be characterized by the same values of displacement and energy. Essentially, in the case of a correct union of two different components, these two nodes could be considered as a unique node, created by the two, which regardless of the component contact maintains its fundamental characteristics. Indeed, the second and third numerical simulations bring finally to the determination of the same potential energy and frequency values. This then gives the missing evidence to validate beyond reasonable doubt the methodology created for the application of patches on the base or unrefined component, automatically providing information about the correctness of the values obtained from the numerical simulations performed in *Chapter B5* and *Chapter B6*.

CHAPTER B5

Vibration reduction in a plate through patch applications

This chapter defines the attainment of the goal, labeled as the determination of the damping placement on a structure in order to ensure its noise reduction and obviously the improvement of its vibrational behaviour. In the following will be shown, through numerical simulations and data elaborations, how potential energy distribution can define the placement of constrained layer damping patches on the surface of a plate in order to produce changes (reduction) in the velocity pattern of the structure and thus in the overall vibrational behaviour of the unrefined component. However, in the previous chapter has already been introduced and explained the interaction between

the potential energy distribution and the patches positioning; while in *Chapter B1* has been explained the reason that why is the potential energy distribution to determine the patches application positions.

In this chapter all the informations introduced in the plate FEM model has been presented, and therefore all the results obtained for this study case will be shown. In other words, through this approach, several numerical simulations will be performed on the plate by measuring the potential energy distribution and normal velocity values, with the aim to attenuate and reduce its level of unwanted vibrations through the bright application of specific component characterized by high damping properties, i.e. the patches. Finally, the results coming from the numerical simulations performed on the plate will be used to determine the best placement of damping patches to ensure the highest amplitude vibration reduction into the entire frequency range of interest.

In the following chapter another mechanical components, a bracket, will be studied with the purpose to prove the methodology created. Of course, the same considerations made and the same methodology followed for the plate component, will overstay also for the bracket component (see *Chapter B6*). For this reason, in *Chapter B6* only the fundamental considerations and all the results regarding the bracket component will be shown and described.

Through *Sections B4.1* and *B4.2*, in which two confirmative numerical simulations are performed, the certainty to follow the correct path to reach the final goal will be provided. Through the numerical simulations presented in the previous chapter two aspects will be correctly addressed; (i) the reliability of the procedure that ensure the correct evaluation of the potential energy distribution (*Section B4.1*) and, (ii) the reliability of the procedure that ensures the correct application of the patches on the surface of the component studied (*Section B4.2*).

In essence, the methodology created and adopted in this

thesis part is approved and validated by the results obtained in these sections (*B4.1* and *B4.2*) and by those generated through the following numerical simulations performed on the plate.

B5.1 Plate study overview

During the discussion treated in this section will be considered and explained the following points regarding the study of a single plate, that are still valid for any other mechanical component.

(i). Definition of the methodology followed for develop the FEM model;

(ii). Definition of the informations directly related to the component study and subsequently introduced in its FEM model;

(iii). Introduction of some figures, illustrative of the steps made in I-DEAS environment in order to clarify certain concepts;

(iv). Data processing of the results obtained through the software, using Matlab;

(v). Considerations about the methodology validity and the results accuracy.

B5.2 Methodology explanation

In the following the methodology used to obtain the velocity and potential energy values into the entire frequency range of the plate component is presented. The methodology is made up of nine macro-steps, eight of which are realized in I-DEAS environment in order to enable the model creation/establishment

for the implementation of the analysis, while the last carried out in Matlab environment. This last step allows post-processing the results obtained through I-DEAS software and making them more readable and suitable for subsequent studies.

1. Geometry creation

   l = 1000 mm

   b = 600 mm

   h = 10 mm

2. Material definition

   Steel (plate) → $E_Y = 2.1e11\ Pa$

   $\upsilon = 0.3$

   $\rho = 7800\ kg/m^3$

   $\eta_{h,plate} = 1\%$

   Asphalt (patch) → $E_Y = 1.2e10\ Pa$

   $\upsilon = 0.21$

   $\rho = 2100\ kg/m^3$

   $\eta_{h,patch} = 17\%$

3. Boundary conditions definition
4. Mesh definition
5. Model solution definition

   Type of solution → Normal mode dynamic-Lanczos

   Options → Chose modal damping

   Define number of modes

   Output selection → Mode shapes

   Displacements

Potential energy

Kinetic energy

6. Response analysis definition

Frequency function → Force

Translational

Real

Equation:

- Abscissa min = 0
- Abscissa increment = 0.1
- Max number data points = 1701
- Force value = 100 N

Filename:

- “value_force”

Create event → Event type:

- Frequency

Element data recovery

- Element formulation

Add force:

- Define node application
- Define direction (Y)
- Insert the function created

ω_n :

- Insert viscous damping

7. Results evaluation

Response domain → Start/end point:

Output start frequency = 0

Output end frequency = 170

Decimation order = 1

Velocity (nodes)

Potential energy (elements)

8. Post-processing with I-DEAS®

Potential energy for each mode

Displacement for each mode

9. Post-processing with Matlab®

Potential energy on the entire frequency range

Velocity on the entire frequency range

In order to simplify all the concepts so far listed, in the following the same methodology using the real passage in I-DEAS environment first, and then in Matlab environment will be presented.

The first step is identified by the creation of the component plate geometry (see Figure B5.1), characterized by the geometrical dimensions reported in the first point of the above listed methodology (1000x600x10 millimeters). This first point is followed by the definition and application of the mechanical characteristic to the mechanical components. As mentioned above and in the previous chapters (*Chapter B3* and *B4*), the material that forms the base component is steel, whose mechanical properties are also listed in the table presented in Figure B5.2, values that come from I-DEAS environment.

Third step is characterized by the application on the plate component of the boundary conditions. As can be clearly seen

from Figure B5.1, the plate is constrained at its left side then blocking all its movements and all its rotations in all the directions. Also at this stage, it is important to remember to create a boundary condition set, see Figure B5.3. This step is crucial in the fem model preparation and in the generation of the first analysis, the latter leading to the displacements, natural frequencies and potential energy values determinations.

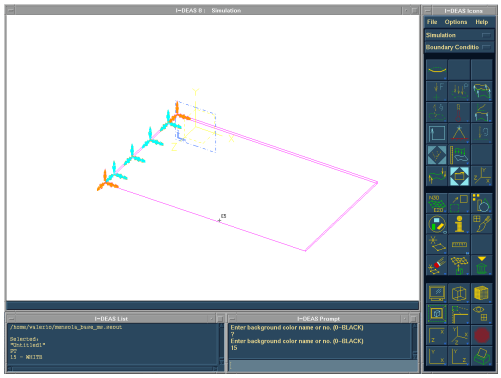

Figure B5.1 – Plate geometry, clamped at one end.

Figure B5.2 – Table containing the plate material properties.

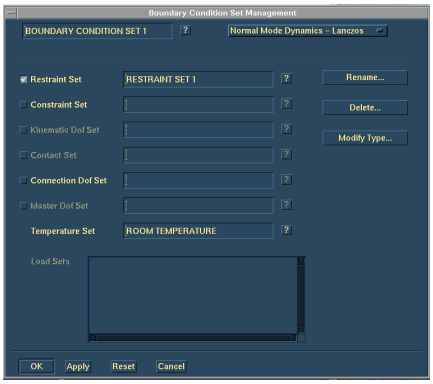

Figure B5.3 – Boundary condition set creation.

Fourth step is correspondent to the generation of the component mesh, see Figure B5.4. In this case is generated a mesh-type solid using the mapped mesh option that allows to create an uniform mesh, characterized by keeping equal the size of each individual blocks forming the mesh. This consideration will be of considerable importance in the later steps, namely the steps in which the patches will be placed on the surface of the plate. In other words, this kind of mesh will allows to provide reference points on the upper surface of the plate, thus facilitating the placements of the patches.

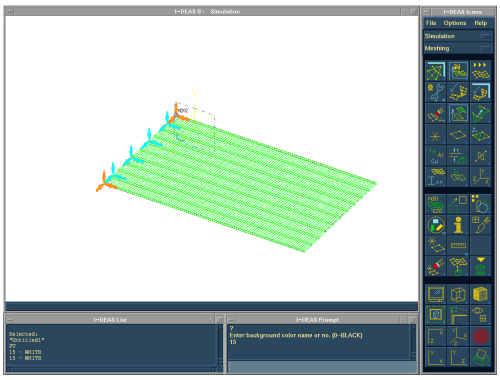

Figure B5.4 – Mesh creation on the plate component.

In the fifth step will be introduced in the fem model the first informations in order to define the type of solution that has to be

carried out. Is essential to create a *solution set* which will contain all the analysis informations. As can be seen from Figure B5.5, it is possible to chose/introduce a lot of information that will characterize the kind of analysis by clicking on the "*options*" (see Figures B5.6.a and B5.6.c) and "*output selections*" (see Figure B5.6.b) buttons. In addition, the type of solution (i.e. normal mode dynamics) and the boundary conditions set (see Figure B5.3) can be defined and introduced. By choosing the "*options*" button it is possible to (i) define the number of modes that should be considered in the normal mode dynamic analysis (Figure B5.6.c) and to (ii) introduce in the evaluation the modal damping contribution (Figure B5.6.a). Through the output selection form shown in Figure B5.6.b it is possible to define the kind of output that is desirable to achieve through the analysis performed. Several solutions could be chosen, such as mode shapes, potential and kinetic energy. Of course, these quantities could be graphically displayed depending by the natural frequency of the component. The modal damping toggle located on the solution options form (see Figure B5.6.a) allows the estimation of modal damping factors, such as the hysteretic and viscous damping factor.

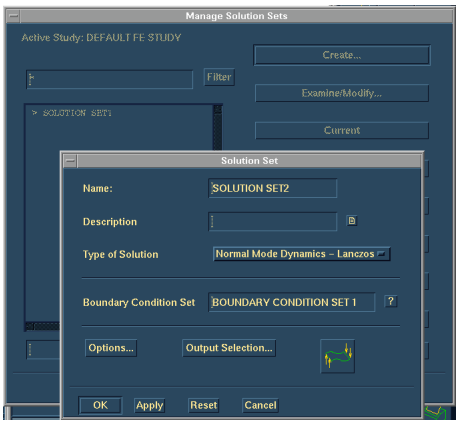

Figure B5.5 – Solution set creation.

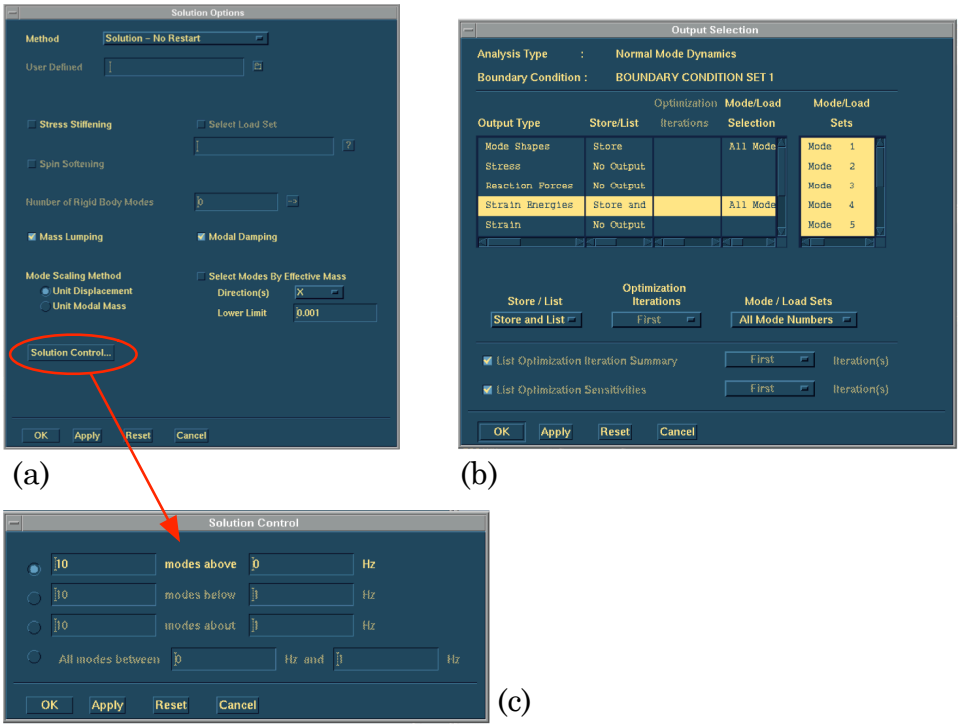

Figure B5.6 – Solution set options (a), output selection (b) and solution control (c) form.

In order to take into account the hysteretic damping factor in the plate FE model, it is desirable to specify a percentage value in relation to the *structural element damping coefficient*, that is a characteristic value of the material adopted in the model. Typically this value is set between 0.005 and 0.001. The software calculates modal damping twice: once to calculate hysteretic damping (structural damping) and a second time to calculate viscous damping (damper elements). The modal damping values are the diagonal terms in the modal damping matrix. Once the software has calculated modal damping, it converts the modal damping values to modal damping factors. To perform this conversion, the software divides the modal damping values by the critical damping value for each mode. The resulting modal damping factors represent the fraction of critical damping. The

software lists both the modal damping values and factors in the solver output (.lis) file. The software also stores the modal damping factors with the displacement mode shapes so that it is possible to use these factors in the response analysis. In this thesis part only the hysteretic damping factor will be utilized and introduced in the fem model. In addition, the software lists a confidence factor in the solver output file. The confidence factor is a measure of the relative size of the off-diagonal terms in the modal damping matrix. The software ignores the off-diagonal terms when it calculates the modal damping values. After the software normalizes the modal damping matrix, it sums these off-diagonal terms and compares them to the diagonal element. A confidence factor of 1.0 indicates that the sum of the off-diagonal terms is zero, whereas a confidence factor of 0.5 indicates that the sum of the off-diagonal terms equal the value of the diagonal element. Ideally, the confidence factor for each mode (or, at least, most modes) should be greater than 0.5. A confidence factor less than 0.5 indicates that the structure is heavily damped and normal mode analysis may not be appropriate (see Table B5.1.c).

To give an idea of the contribution brought about by the choice of the modal damping values and therefore by the introduction in the fem model of the structural element damping coefficient, a part of the file ".lis" generated by the software I-DEAS is represented below. Table B5.1.a shows the values of frequency, hysteretic and viscous damping and all the confidence factors for the first ten natural frequencies of the plate, in the case where no structural element damping coefficient is provided. The values contained in the hysteretic damping column for this case are obviously all zero. If the structural element damping coefficient for the steel plate is directly introduced in the fem model ($\eta_h = 1\%$), its contribution will be taken into account by the modal damping item (see Figure B5.6.a), which will result in the change of the values contained in the ".lis" file (see Table B5.1.b).

MODE	FREQUENCY	HYSTERETIC DAMPING VALUE	HYSTERETIC DAMPING FACTOR	VISCOUS DAMPING VALUE	VISCOUS DAMPING FACTOR	CONFIDENCE FACTOR
1	8.53	.000E+00	.000	.000E+00	.000	1.000
2	31.22	.000E+00	.000	.000E+00	.000	1.000
3	53.03	.000E+00	.000	.000E+00	.000	1.000
4	103.76	.000E+00	.000	.000E+00	.000	1.000
5	145.88	.000E+00	.000	.000E+00	.000	1.000
6	162.49	.000E+00	.000	.000E+00	.000	1.000
7	206.30	.000E+00	.000	.000E+00	.000	1.000
8	234.29	.000E+00	.000	.000E+00	.000	1.000
9	294.73	.000E+00	.000	.000E+00	.000	1.000
10	349.57	.000E+00	.000	.000E+00	.000	1.000

Table B5.1.a – Values obtained without the introduction of the structural element damping coefficient.

MODE	FREQUENCY	HYSTERETIC DAMPING VALUE	HYSTERETIC DAMPING FACTOR	VISCOUS DAMPING VALUE	VISCOUS DAMPING FACTOR	CONFIDENCE FACTOR
1	8.53	3.330E+08	.010	.000E+00	.000	1.000
2	31.22	2.463E+09	.010	.000E+00	.000	1.000
3	53.03	1.214E+10	.010	.000E+00	.000	1.000
4	103.76	2.137E+10	.010	.000E+00	.000	1.000
5	145.88	5.325E+10	.010	.000E+00	.000	1.000
6	162.49	3.982E+10	.010	.000E+00	.000	1.000
7	206.30	8.345E+10	.010	.000E+00	.000	1.000
8	234.29	1.196E+11	.010	.000E+00	.000	1.000
9	294.73	3.186E+11	.010	.000E+00	.000	1.000
10	349.57	3.150E+11	.010	.000E+00	.000	1.000

Table B5.1.b – Values obtained with the introduction of the plate structural element damping coefficient.

MODE	FREQUENCY	HYSTERETIC DAMPING VALUE	HYSTERETIC DAMPING FACTOR	VISCOUS DAMPING VALUE	VISCOUS DAMPING FACTOR	CONFIDENCE FACTOR
1	8.69	5.289E+08	.015	.000E+00	.000	.512
2	31.48	3.089E+09	.012	.000E+00	.000	.650
3	53.76	1.742E+10	.014	.000E+00	.000	.524
4	104.58	2.664E+10	.012	.000E+00	.000	.650
5	146.98	6.498E+10	.012	.000E+00	.000	.562
6	163.00	4.359E+10	.011	.000E+00	.000	.658
7	207.75	1.032E+11	.012	.000E+00	.000	.654
8	235.22	1.344E+11	.011	.000E+00	.000	.861
9	296.58	3.908E+11	.012	.000E+00	.000	.589
10	351.41	3.782E+11	.012	.000E+00	.000	.672

Table B5.1.c – Values obtained with the contemporaneously introduction of the structural element damping coefficient concerning the coupled system.

Is important to underline that all the values contained in these two tables (*Tables B5.1.a* and *B5.1.b*) are only concerning to the base plate study, with no patches applied on it. The presence of the patches will obviously change all the values contained in both the previous tables because of the presence in the patches of a structural element damping coefficient ($\eta_{h,patch} = 17\%$) clearly different in relation to that of the plate ($\eta_{h,plate} = 1\%$). The Table B5.1.c shows the values of frequency, hysteretic and viscous damping in addition to the confidence factors for the first ten natural frequencies of the coupled system, i.e. the plate with the patches. As can be seen from the values contained in Table B5.1.c, all the hysteretic damping and the corresponding confidence factors values are different from those reported in the Table B5.1.b. In fact, at this stage, all these values are directly dependent by the contemporaneously presence of the structural element damping coefficient in relation to both the component forming the coupled system. In addition, as mentioned earlier, the ideal confidence factor for each mode (or, at least, most modes) should be greater than 0.5. In this case all the ten confidence factor values are greater than 0.5. Thanks to the values listed in Table B5.1.c it is certain that the methodology followed for perform the study of a coupled system like that studied here, is reliable and accurate.

Returning to the study case, before starting with the sixth step of the above methodology is appropriate to realize a first numerical simulation based on the data released so far, in order to provide information about the goodness of the process followed. These numerical simulations will lead to the determination of the plate mode shapes and to its potential energy values. Figures from B5.7.a to B5.7.f shows the first six natural frequencies and therefore the first six mode shapes obtained for the plate study case.

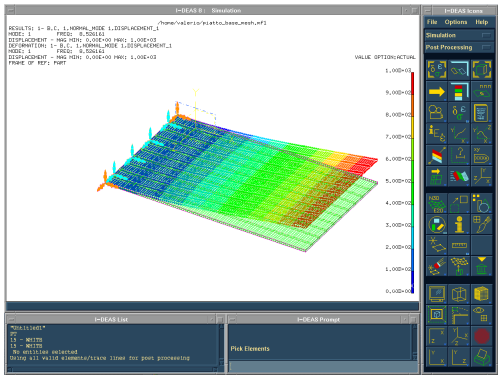

Figure B5.7.a – First mode shape of the steel plate.

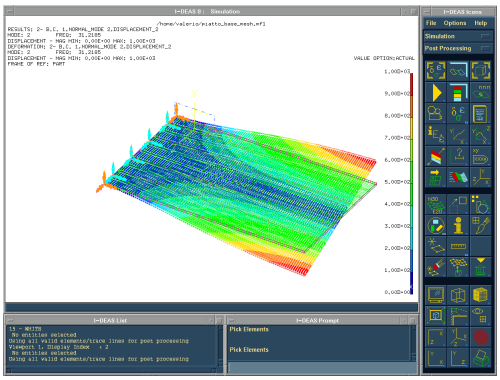

Figure B5.7.b – Second mode shape of the steel plate.

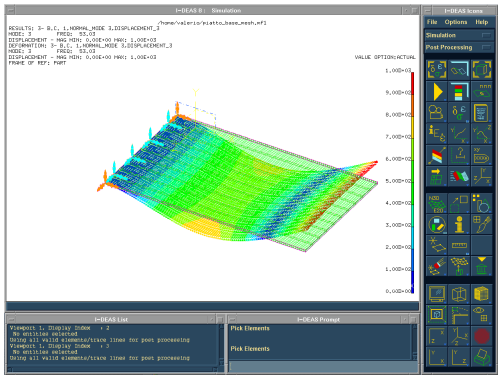

Figure B5.7.c – Third mode shape of the steel plate.

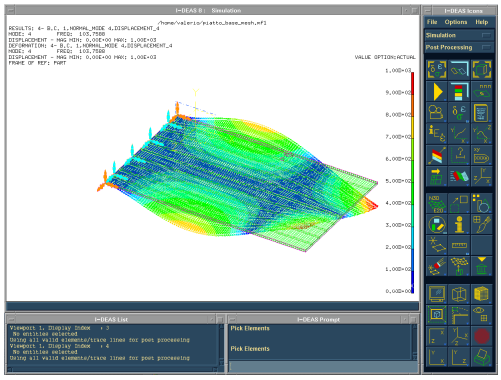

Figure B5.7.d – Fourth mode shape of the steel plate.

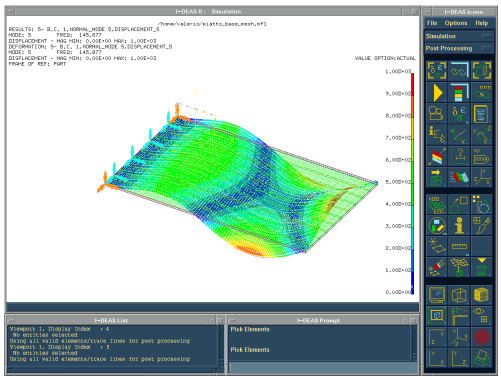

Figure B5.7.e – Fifth mode shape of the steel plate.

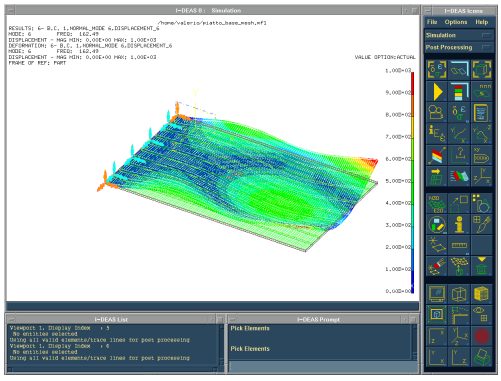

Figure B5.7.f – Sixth mode shape of the steel plate.

The sixth step of the methodology allows setting the model in order to get it ready for the beginning of the second part of the

component study, that introduce the potential energy and velocity evaluation cases. As can be clearly seen by the methodology listed in the beginning of this section, this sixth step is subdivided into two sub-phases that are referred to the dynamical loading application. Specifically in this section will be introduced information about (i) the creation of the force that has to be applied on the component (creation of the frequency function) and, (ii) the definition of the general settings followed by the choice of the node on which this force has to be applied.

As defined by the methodology previously exposed and by the figures presented below (Figures from B5.8.a to B5.8.e), the frequency function creation follow this guideline: creation of a real, translational force, characterized by an equation defined according to the knowledge of the constructive characteristics of the plate fem model and to the type of numerical simulation that has to be carried out, ending with the definition of the force amplitude. For the sake of the clarification, in the following will be explained the methodology adopted by which will be done the choice of the information that has to be introduced in the fem model regarding the creation of a proper equation.

Basically, the kind of numerical simulations performed are three:

- ✓ Potential energy evaluation at a single characteristic frequency (Figures B5.8.a and B5.8.b);
- ✓ Potential energy evaluation for all the frequency range of the component (Figures B5.8.c and B5.8.d);
- ✓ Velocity evaluation for all the frequency range of the component (Figures B5.8.e).

Let's consider the first numerical simulation case that is the analysis performed on the plate for reach the potential energy values corresponding to the component behaviour at a precise natural frequency (obviously contained in the frequency range of the component). In turn, this quantity will be fundamental in order to clarify and identify the location of the patches that has to be applied on the surface of the plate.

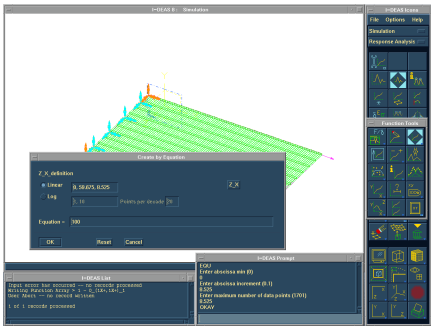

Figure B5.8.a – Equation informations for potential energy study case relating to a single frequency.

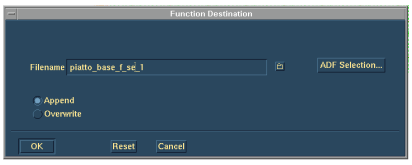

Figure B5.8.b – Frequency function filename for potential energy study case.

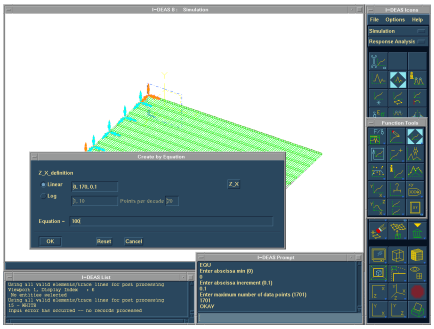

Figure B5.8.c – Equation informations for potential energy study case relating to the entire frequency range.

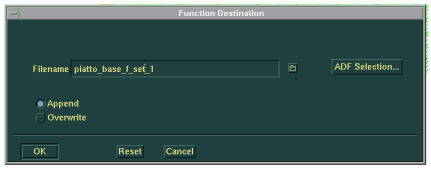

Figure B5.8.d – Frequency function filename for potential energy study case relating to the entire frequency range.

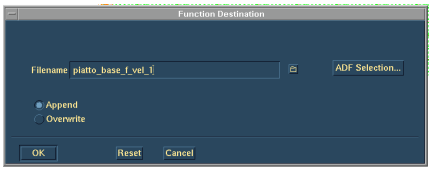

Figure B5.8.e – Frequency function filename for the velocity study case on the entire frequency range.

As shown in Figure B5.7.a the first natural frequency of the plate is equal to 8.525 Hz, so the aim is to study the behaviour of the plate component exactly at this value; due to the fact that has no physical sense apply the patches on the surface of the base component on the basis of studies carried out between the resonance frequencies.

The informations required to generate a proper equation are the introduction of the minimum abscissa value, its increment and the maximum number of points on which the file containing the results will be composed. Essentially, thanks to the introduction in the fem model of these informations, the graph obtained (as an output of the numerical simulations) will represent the potential energy trend for the single natural frequency considered. This means that on the abscissa axes will be present the numbers of the elements forming the mesh of the plate component. In this manner, through the knowledge of the potential energy trend, it is possible to know for which mesh elements the potential energy value will be maximum or minimum, than providing important informations on the location where is needed the patch application. Obviously, the patches will cover the mesh elements characterized by the highest potential energy values. Then, knowing the position of the mesh elements, it will be possible to know the exact position of the surface of the component that requires the use of the patches.

The usefulness of these considerations and why it is here presented in detail will be clear in the next section, when all the informations here introduced will be indispensable to correctly graph the potential and normal velocity values.

In order to perform a study on a precise characteristic frequency (the first in this case) and on the entire frequency range of the plate component, the values listed in Table B5.2 will be introduced in one of the I-DEAS form. Through these values, directly introduced in the sixth step of the aforementioned methodology, the potential energy values for the plate component will be evaluated. Then, through the numerical simulations the potential energy trend regarding the study of the component behaviour at a single natural frequency and the potential energy distribution regarding its study on the entire frequency range will be obtained. The first will be essential in order to precisely define the location of the patches, while the second can be used to identify which patches arrangement produce the highest improvement. In reality, this latter task will be entrusted by the velocity evaluation.

	Potential energy *first frequency*	Potential energy *frequency range*	Velocity *frequency range*
Abscissa min	0	0	0
Abscissa increment	8.525	0.1	0.1
Max. number of data points	100	1701	1701

Table B5.2 – Values introduced in the plate fem model for the characterization of the frequency function for different cases.

The values listed in the first two columns of Table B5.2 allow to define the precise frequency (8.525 Hz – first plate natural

frequency) and the entire frequency range (0-1701 Hz) in which the numerical simulations has to be performed in order to obtain the potential energy values (trend and distribution respectively).

Considering the determination of the entire frequency range extension, needs to be established the number of plate natural frequencies that has to be taken into account during the study. Suppose, therefore, to consider the first six natural frequencies of the plate. Giving a look on the mode shape presented in Figure B5.7.f is known that the sixth natural frequency of the plate is equal to 162.49 Hz, thus providing informations about the extension of the frequency range that must be introduced in one of the software forms. Assuming to consider the last frequency equal to 170 Hz that allows to keep all the first six natural frequencies of the plate component, and knowing that the study should be done taking into account the exact values of the natural frequencies, will be set 0.1 as the increment value whereas 1701 as the maximum number of data points (see values listed in Table B5.2). It was chosen 0.1 as the increment values because it allows going significantly closer to all the natural frequency values of the plate. Obviously, a further reduction in the increment value (for example from 0.1 to 0.05) will leads to greater accuracy in the numerical simulations, but also to a significant increase in the calculation time. Clearly, the product between the maximum number of data points and the increment value will provide the maximum frequency value at which the numerical simulation will end. The same considerations will take place also for the last study case, i.e. the velocity evaluation for the entire frequency range of the component. Also for this case, the graph will show the velocity trend compared to the frequency values, the latter reported in the abscissa axes. Obviously, both the quantities evaluations (potential energy and velocity) are referred to the same frequency range (see Table B5.2).

As mentioned before, this sixth step of the methodology presented in the beginning of this section allows setting the model in order to get it ready for potential energy and velocity

evaluation cases. Due to the fact that the first sub-phase that deals with the creation of the force that has to be applied on the component (creation of the frequency function) and with the definition of some general settings introduced to manage the plate fem model are already explained, still remains the second sub-phase explanation regarding the choice of the node on which this force has to be applied. In fact, as reported by the Figures B5.9.a and B5.9.b, this second sub-phase will lead to the introduction in the plate fem model of the latest information relating to the response analysis definition. In essence, an "event" will be created that will define the force on the component and its application locations.

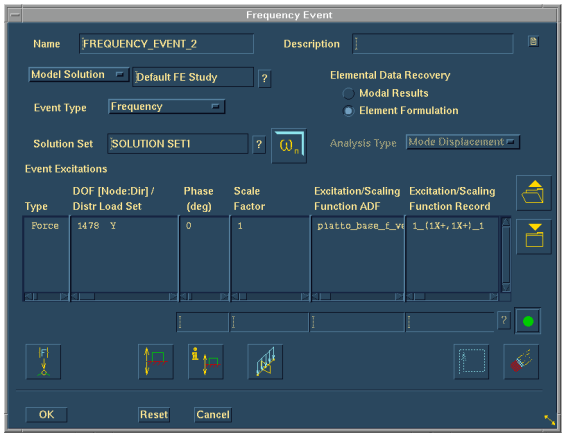

Figure B5.9.a – Frequency event form.

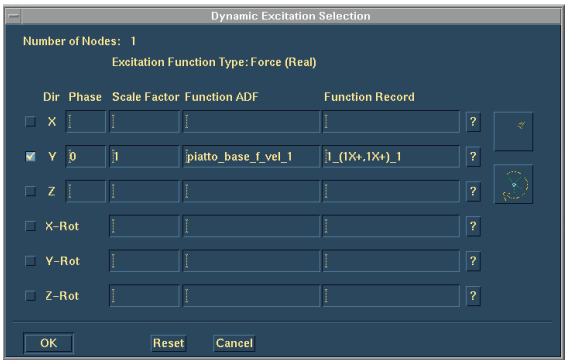

Figure B5.9.b – Dynamic excitation selection form.

Taking a look at Figure B5.9.a, many information can be introduced in the fem model, like the event name, its description, the model solution and the solution set (defined above). Considerable importance lies in the selection of the event type and in the data recovery. Relating to the first case, the choice is simple, due to the considerations made previously at every stage of the fem model creation. The event type will be therefore a "*frequency event*". For the second case will be chose "*element formulation*" that means that all the potential energy values are evaluated for each solid element forming the mesh of the plate component. Another important button is present in Figure B5.9.a, that is the button with a force drowns above it, that when pressed allows to chose the mesh node on which apply the force. Of course, for all the numerical simulations regarding the study of the plate, the node for the application of the force will be always kept constant. As already mentioned in the previous chapter the force should not be applied on component symmetry in order to be sure to excite all the component modes. For example, if the force were applied on plate symmetry, its contribution to the second mode shape would be null because of the second mode shape of the plate component is a torsional shape around the symmetry line of this component (see Figure B5.7.b). The force will be applied on the upper surface of the plate at the coordinates reported by the Figure B5.10. Once the node is chosen, a table will automatically appear (Figure B5.9.b) which will allow to choose the direction of the force (Y in this case) and the frequency function to which it will be matched. The frequency function that has to be introduced in this table, which will contain all the informations about the force type and its value, has been created in the previous sub-phase. In this case (see Figure B5.9.b) is the frequency function created for the velocity study case (see Figure B5.8.e).

This terminates the analysis setup, thus making the component ready for the generation of the estimations leading to the potential energy end normal velocity values in order to study the overall vibratory behaviour of the plate.

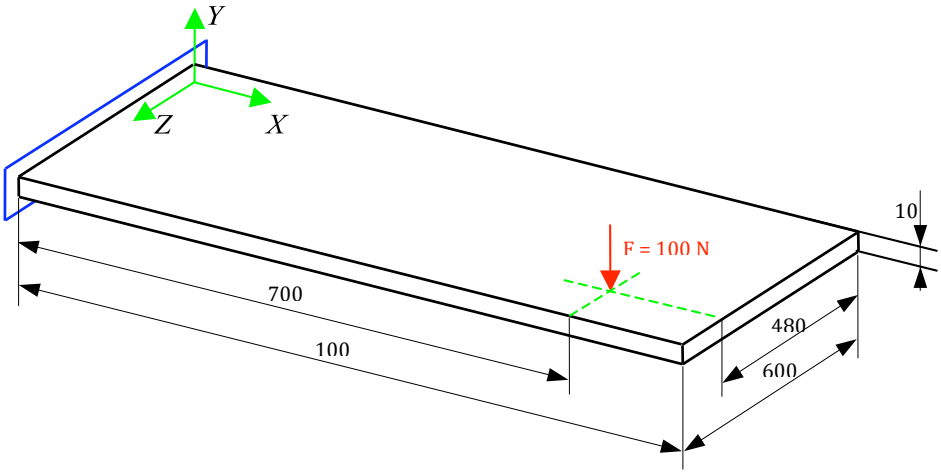

Figure B5.10 – Force location on the upper surface of the plate.

The seventh stage enables to carry out the numerical simulations in order to obtain, dependently by the study case, the potential energy and velocity values of the plate component.

Suppose now to consider the potential energy evaluation case relating to the single natural frequency of the component. As can be seen from Figure B5.11.a, it is possible to choose the type of output and the response domain. Obviously, the output quantity for this case is nothing more the potential energy, but less obvious is the choice of the response domain that shows two possible options. The first option, i.e. "*function selection*", will present the potential energy trend, on which can be selected through a cursor the frequency values for which generate the study. The second option, i.e. "*start/end point*", allows entering the values that has already been included in the frequency function creation process. In this case, choosing the second option has assessed the potential energy and velocity values. By clicking the "*evaluate*" button found in the lower part of the form presented in Figure B5.11.a, the software provides the possibility to choose the component mesh elements of the plate on which the potential energy evaluation will be performed. Obviously, this measure should be made taking into account all the mesh

elements. After the selection of these elements the software will automatically calculate the results, providing an output file characterized by the extension ".unv", which contains all the informations introduced in the fem model of the plate in addition to the results required by the type of analysis generated (potential energy evaluation for a single frequency in this case). This file will be treated and manipulated by a specific code generated through Matlab (see following sections). The same considerations are still valid for the potential energy and velocity evaluation case evaluated in the entire frequency range, i.e. between 0 to 1700 Hz. Obviously, in these latter cases, the data that has to be placed in the results form (see Figure B5.11.b) will be different compared to that for the previous study case (see Figure B5.11.a).

In order to perform the study on a precise natural frequency (first plate natural frequency in this case) and on the entire frequency range of the plate component the values listed in Table B5.3 will be introduced in one of the I-DEAS form (see Figures B5.11.a and B5.11.b). Through these values, directly introduced in the seventh step of the aforementioned methodology, the potential energy values for the plate component will be evaluated.

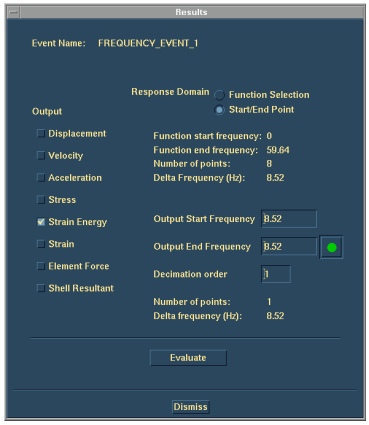

Figure B5.11.a – Results form for the potential energy evaluation case at the specific natural frequency.

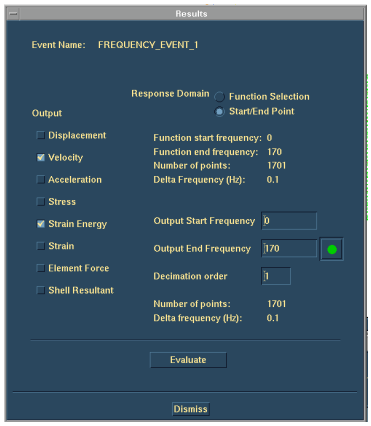

Figure B5.11.b – Results form for the potential energy and velocity evaluation cases on the entire frequency range.

	Potential energy *first frequency*	Potential energy *frequency range*	Velocity *frequency range*
Output start frequency	8.525	0	0
Output end frequency	8.525	170	170
Decimation order	1	1	1

Table B5.3 – Values introduced in the plate fem model for the evaluation of different quantities.

The eighth step represents the last phase that requires the use of the software I-DEAS. In this latter step, that represents the post processing stage, the results evaluated through the

numerical simulations can be listed (see Figure B5.12). As can be seen from this figure it is possible to choose the values to graph from a variety of possibilities such as the plate displacements (see Figures B5.7.a to B5.7.f).

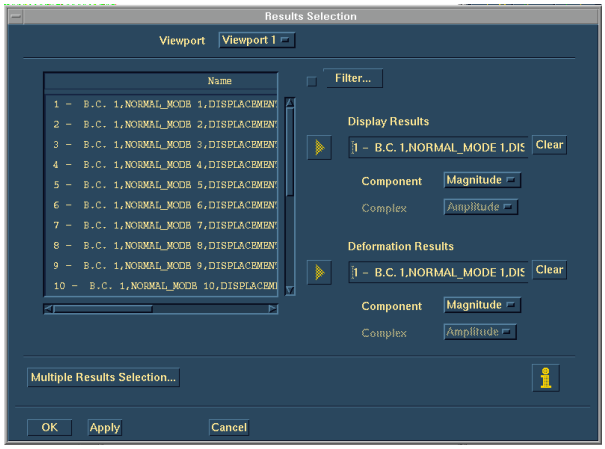

Figure B5.12 – Results selection form.

This point conclude the creation and the establishment stage of the plate fem model realized in I-DEAS environment related to the study of the base plate or to the study of its unrefined configuration, i.e. only the plate without any patch applied on it with the aim to improve its vibratory behaviour.

From this point, all the results thus obtained will be developed in Matlab environment in order to make them more readable and understandable for perform practical considerations. In essence, the results concerning the estimation of potential energy values regarding the specific natural frequency of the plate component will be useful to understand in which location the patches has to be applied; the results concerning the estimation of potential energy values in addition to those concerning the velocity values, both relating to the entire frequency range, will be useful to clearly define the impact that each natural frequency of the plate has on its overall amplitude vibratory behaviour. This in turns will provide in addition to the

knowledge of the input power to the component important information about the loss factor estimation (aspect not treated here). It is important to remember that the specific numerical simulations carried out in *Sections B4.1* and *B4.2* help to give certainty on the accuracy and reliability of the methodology created.

B5.3 Result presentation

Following the methodology outlined in the previous section of this chapter will be obtained through the numerical simulations performed in I-DEAS environment a series of files relating to (i) the study of the unrefined configuration of the plate component, that is nothing else that the plate without any patch applied on it and (ii) the study of all the configurations that coming from the study of the first six natural frequencies of the plate, each one characterized by a precise location of the patches on its upper surface.

Essentially, the configurations that will be explained and presented below will be the following:

(i). Base configuration (only the plate);
(ii). First patch configuration (in relation to the study of the plate behaviour at its first natural frequency);
(iii). Second patch configuration (in relation to the study of the plate behaviour at its second natural frequency);
(iv). Third patch configuration (in relation to the study of the plate behaviour at its third natural frequency);
(v). Fourth patch configuration (in relation to the study of the plate behaviour at its fourth natural frequency);
(vi). Fifth patch configuration (in relation to the study of the plate behaviour at its fifth natural frequency);
(vii). Sixth patch configuration (in relation to the study of the

plate behaviour at its sixth natural frequency);

B5.3.1 Base configuration

The files that are generated through the aforementioned methodology according to the information given in *Section B5.2* and therefore introduced in the plate fem model are the following:

- Potential energy evaluation regarding the study of the plate behaviour at its first natural frequency;
- Potential energy evaluation regarding the study of the plate behaviour at its second natural frequency;
- Potential energy evaluation regarding the study of the plate behaviour at its third natural frequency;
- Potential energy evaluation regarding the study of the plate behaviour at its fourth natural frequency;
- Potential energy evaluation regarding the study of the plate behaviour at its fifth natural frequency;
- Potential energy evaluation regarding the study of the plate behaviour at its sixth natural frequency;
- Potential energy evaluation regarding the study of the plate behaviour on the entire frequency range (0-170 Hz);
- Velocity evaluation regarding the study of the plate behaviour on the entire frequency range (0-170 Hz);

Essentially, two files will be generated in relation to the evaluation of the potential energy and velocity values, both estimated in all the frequency range; in addition to a series of files (six in this case) containing the potential energy values evaluated for certain natural frequencies of the plate. These eight files will contain all the information needed to perform a comprehensive study on the overall vibratory behaviour of the plate component.

As describe above, the first six files represent the potential

energy trend assessed at a precise natural frequency. In the abscissa axes will be shown the mesh element numbering of the plate. From Figures B5.13.a to B5.13.f are presented the potential energy trends compared to the mesh element numbers, starting from the first plate natural frequency until the sixth. As can be seen by the numerical values reported in the abscissa axes of these graphs, the plate mesh is made up of 1000 elements. In this case, the 500th element number corresponds to the plate geometric symmetry. Obviously, at this precise mesh element will be generated the potential energy trend symmetry (see Figures B5.13.a to B5.13.f). Suppose now to set a threshold value of potential energy. Each plate mesh element that is located above this value (that has to be decided) will require the presence of the patch. For example, taking into account the potential energy trend shown in Figure B5.13.a, and establishing a threshold value equal to 1.2 x 10^3 Nm, all the mesh element above this value requires the presence of the patches. Hence, the 299th mesh element requires the patch presence, while the 301st doesn't require it. Unfortunately, the greater the frequency the more the potential energy trend become misleading (see Figure B5.13.f), thus making difficult the determination of the plate mesh elements that requires the patches presence. In addition, this procedure, although accurate, requires a lot of time in doing this. Moreover, the time should be doubled because the elements must be found both in the potential energy graph, both on the component mesh.

To avoid this problem and to speed up the patch location search on the surface of the component has been created a Matlab code has been created. This code allows generating a better representation, allowing to quickly define the areas of highest potential energy density and hence the areas on which the patches shall be applied. From Figures B5.14.a to B5.14.f the potential energy density maps for all the six natural frequencies of the plate are shown, replacing the graph presented in Figures B5.13.a to B5.13.f. In essence, Figure B5.14.a will correspond to

Figure B5.13.a, and so on for all the other plate natural frequency considered.

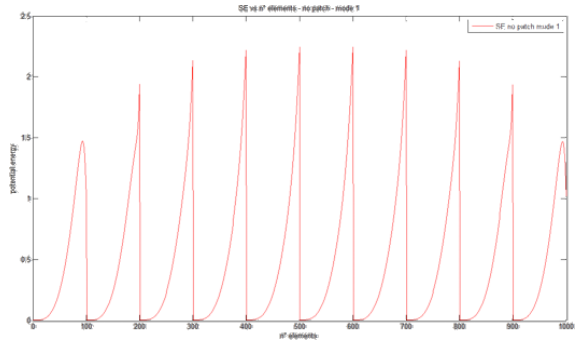

Figure B5.13.a – Potential energy trend for the first natural frequency study equal to 8.52 Hz.

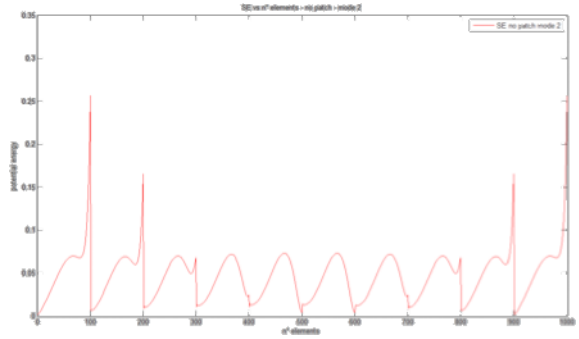

Figure B5.13.b – Potential energy trend for the second natural frequency study equal to 31.21 Hz.

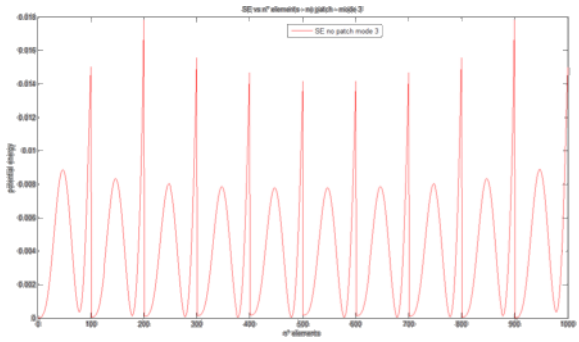

Figure B5.13.c – Potential energy trend for the third natural frequency study equal to 53.03 Hz.

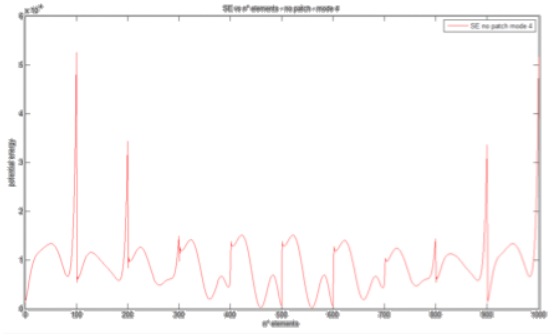

Figure B5.13.d – Potential energy trend for the fourth natural frequency study equal to 103.75 Hz.

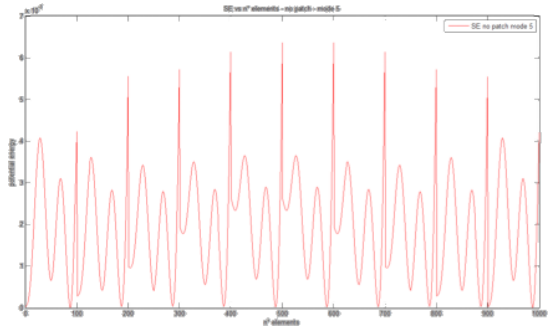

Figure B5.13.e – Potential energy trend for the fifth natural frequency study equal to 145.87 Hz.

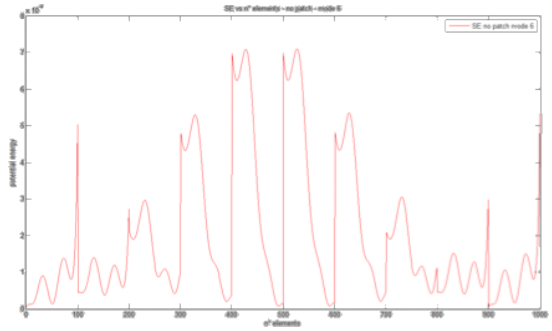

Figure B5.13.f – Potential energy trend for the sixth natural frequency study equal to 162.49 Hz.

Giving a quick look at the six figures presented below, the basis on which the potential energy density is presented is exactly

the plate, thus making very simple the definition of the mesh elements of the plate that corresponds to the highest level of potential energy (hot colors). In reality, the figure presented here shows the potential energy density perfectly slapped on the plate surface, while not presented here, were also determined the same potential energy density maps characterized by a raw visualization of this values, giving the presence of each mesh elements in a clear manner. This then leads to the display of stair-step (due to the difference in color) between two consecutive mesh elements. In this manner a "grid" is created on the surface of the plate exactly equal to the plate mesh grid. This form of visualization is less beautiful but much more important because it already provides the exact and rapid identification of the mesh element that should be covered by the patches.

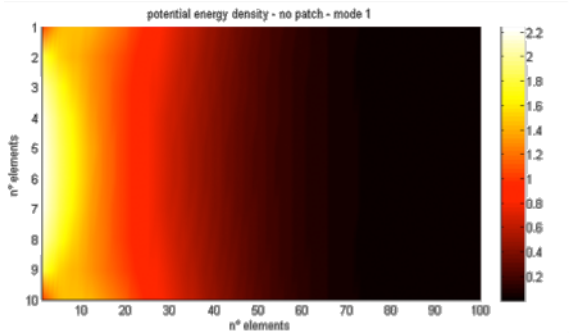

Figure B5.14.a – Potential energy density map for the first natural frequency study equal to 8.52 Hz.

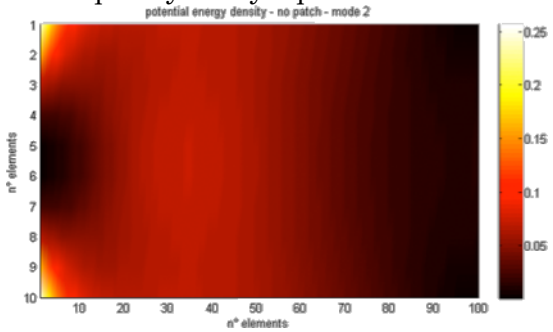

Figure B5.14.b – Potential energy density map for the second natural frequency study equal to 31.21 Hz.

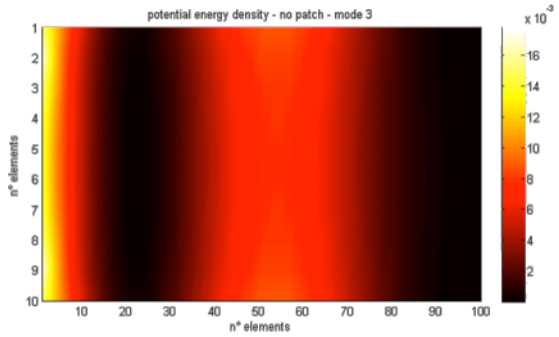

Figure B5.14.c – Potential energy density map for the third natural frequency study equal to 53.03 Hz.

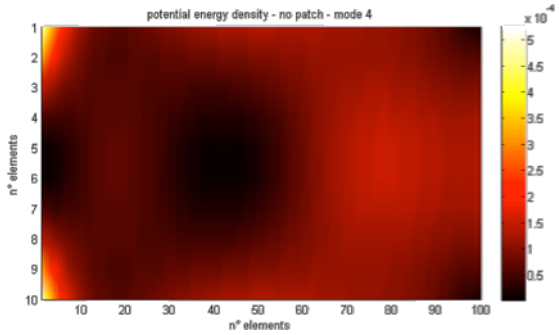

Figure B5.14.d – Potential energy density map for the fourth natural frequency study equal to 103.75 Hz.

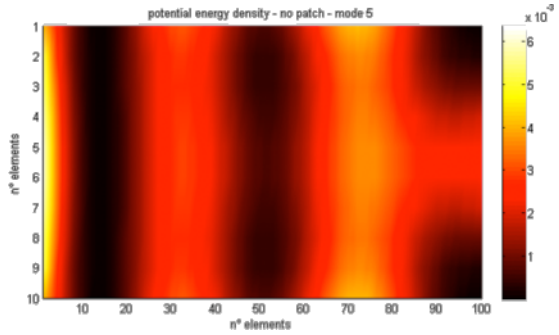

Figure B5.14.e – Potential energy density map for the fifth natural frequency study equal to 145.87 Hz.

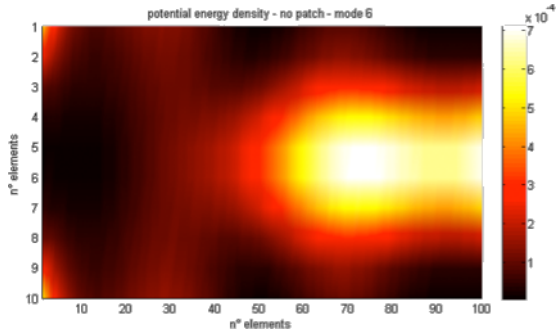

Figure B5.14.f – Potential energy density map for the sixth natural frequency study equal to 162.49 Hz.

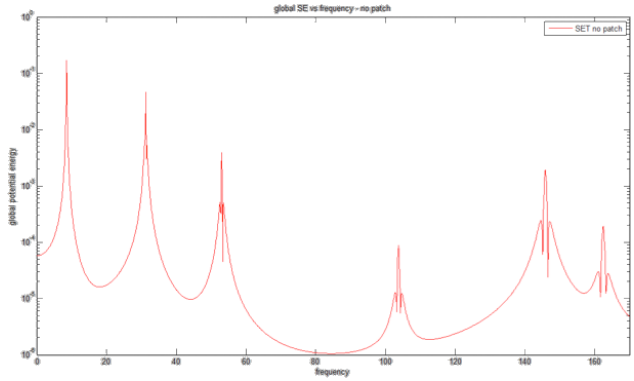

Figure B5.15 – Potential energy trend obtained for the entire frequency range.

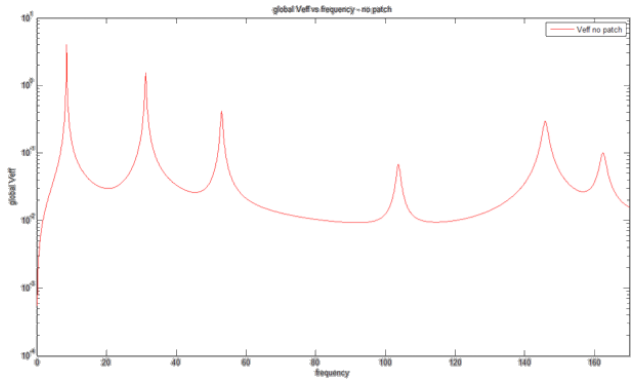

Figure B5.16 – Velocity trend obtained for the entire frequency range.

Returning to the introductory phase, two are the files that still remain, that are the potential energy and normal velocity estimation on the entire plate frequency range. Both these quantities will be estimated generating a "broad-brush" at all the frequencies contained in the plate frequency range. To make them more readable, another Matlab code will be used. In Figures B5.15 and B5.16 are shown the potential energy and normal velocity trend, displayed as a function of frequency. Regarding the normal velocity evaluation, further investigations are needed; investigations that has already been introduced in *Section B3.2*, see equations (B3.1) and (B3.2). Summarizing, thru eq. (B3.2) each velocity value obtained from the simulation performed in I-DEAS environment, will be translated into the corresponding value of effective velocity (each velocity value will be temporally averaged).

With this last considerations ends the study phase of the base plate component (unrefined configuration). In the following sections the results obtained regarding the study of the coupled system, i.e. the plate with the patches applied on it, will be presented.

B5.3.2 First patch configuration

The files that are generated through the aforementioned methodology according to the information given in the *Section B5.2* and therefore introduced in the plate fem model are the following:

- Potential energy evaluation regarding the entire frequency range of the coupled system;
- Velocity evaluation regarding the entire frequency range of the coupled system;

Essentially, two files regarding the potential energy and

velocity evaluations for the coupled system will be generated. These files, in turns, will provide improvement on the vibratory behaviour of the plate by reducing its amplitude vibration level. For this first case, the patches are applied on the surface of the component by studying the behaviour of the plate in correspondence of its first natural frequency (see Figure B5.13.a and B5.14.a). Figure B5.17 shows the plate fem model (green mesh) in addition to the patch (blue mesh) realized in I-DEAS environment. Again, as in the previous case, it is possible to represent the mode shape configuration for the coupled system. In this case, only the fifth mode shape of the coupled system is shown (see Figure B5.18), having the purpose of showing as the deformed configuration of the patch exactly follows that of the plate. This latter consideration, in addition to the confirmative numerical simulations presented in *Chapter B4* gives an idea about the correctness of the procedure established.

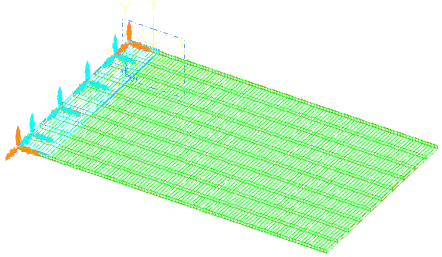

Figure B5.17 – Coupled system configuration for the study of the first natural frequency of the plate.

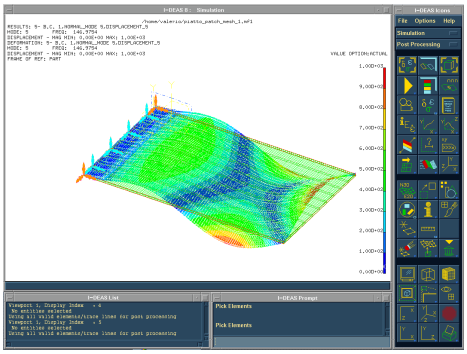

Figure B5.18 – Fifth mode shape of the coupled system configuration.

Due to changes in the system (the coupled system) because of the presence of the patch, the potential energy distribution at the first natural frequency changes. Therefore, it is possible to study this variation, and to define a new potential energy distribution that takes into account the presence of the patch. Figure B5.19 takes into account this change.

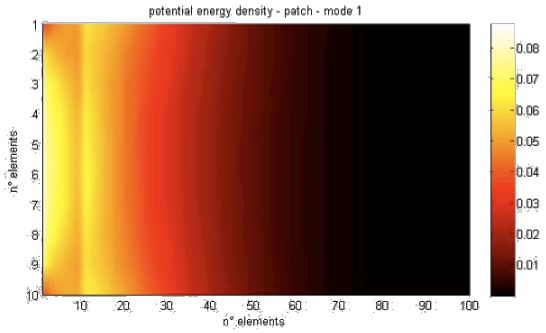

Figure B5.19 – Potential energy density map for the first natural frequency study (8.52 Hz) applying the patch.

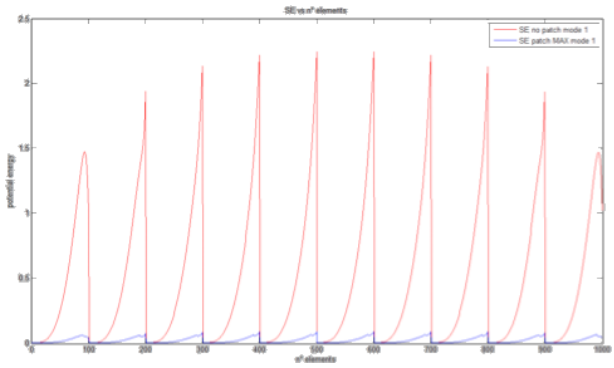

Figure B5.20 – Comparisons between the potential energy density trend for the base (red) and first (blue) configurations.

From a quick comparison between Figure B5.14.a relative to the potential energy density map obtained without the application of the patch and Figure B5.19 characterized by the application of the patch, can be clearly noted that the areas corresponding to the highest potential energy distribution has been reduced. In

addition, the amplitude levels of potential energy values for the second case (maximum value equal to 0.08) are decreased compared to the first case (maximum value equal to 2.2). The same thing can be clearly noted by Figure B5.20 that represents the comparison between the potential energy trends for the two cases (the red line corresponds to the base configuration and the blue line corresponds to the first configuration). It is easy to understand how the patch application, if appropriately located, causes a significant decrease on the potential energy level.

Following the same path adopted in the previous section, are represented below the potential energy (Figure B5.21) and velocity trend (Figure B5.22) obtained for this first configuration.

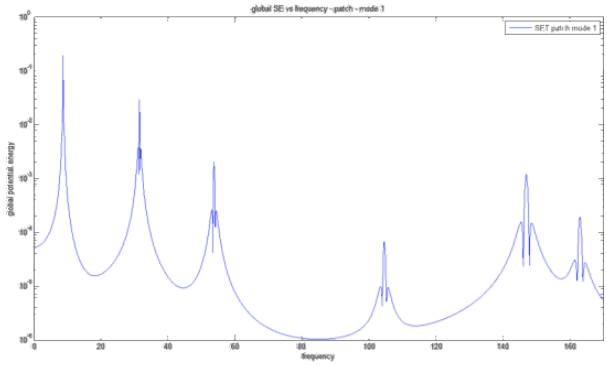

Figure B5.21 – Potential energy trend obtained for the first configuration of the coupled system.

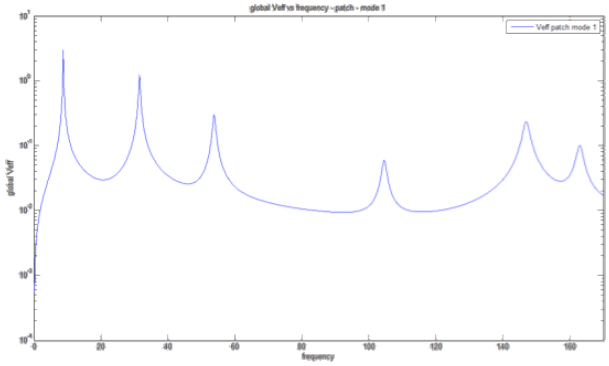

Figure B5.22 – Velocity trend obtained for the first configuration of the coupled system.

The results hereafter presented are obtained through the generation of numerical simulation in which the patch is applied on MAX potential energy density areas (see Figure B3.1.b, *Section B3.2*). Wishing to further validate the methodology for the patch application in order to achieve the improvement of the vibratory behaviour of the base component, the patch will be also applied on the MIN potential energy density areas (see Figure B3.1.c, *Section B3.2*). Although the application areas of the patches are different, even for their extension, it is important to keep the same total patch volume applied on the surface of the component regarding the two different numerical simulations. In other words, considering Figures B3.1.b and B3.1.c, the sum of the volume of the red patches is exactly equal to that of the green patches, even if their size and shapes vary. Theoretically, the application of the patch (characterized by the same mechanical properties and by the same volume) on the MIN potential energy areas should lead to a reduction of the potential energy amplitude level, but with a less impact to that caused by the placement of the patch on the MAX potential energy areas.

Said this, in Figure B5.23 is presented the comparisons between the different trends obtained by studying the base configuration (red line), the patch application on the MAX potential energy areas (blue line) and the patch application on the MIN potential energy areas (green line). As expected, the potential energy amplitude values are reduced compared to the case without a patch, this due to the presence of a high damping material applied on the surface of the component, but its impact is lower than that of patch application in the MAX potential energy areas. Figure B5.24 shows the patch location for the evaluation of the green line plotted in Figure B5.23.

Obviously, the potential energy and velocity trends evaluated with the patch applied on the MIN potential energy areas will provide “poor quality” results compared to that evaluated with the patch applied in the MAX potential energy areas.

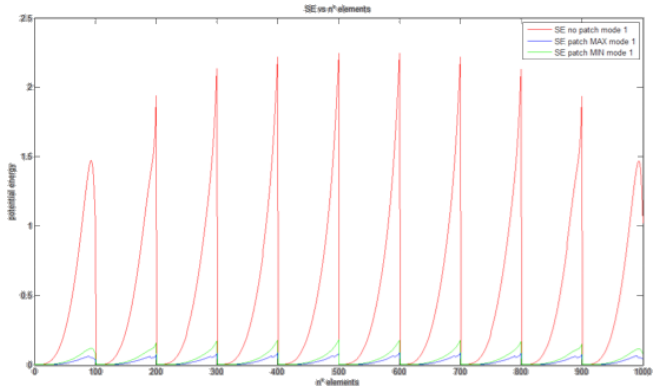

Figure B5.23 – Comparison between the potential energy density trend for the base (red), first MAX (blue) and first MIN configurations (green).

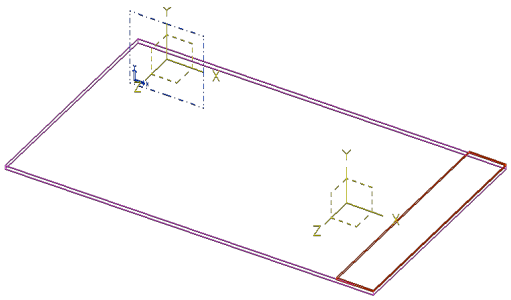

Figure B5.24 – Coupled system configuration for the first plate natural frequency study with patch on MIN area.

The numerical simulations related to the case of patch application on the MIN potential energy density areas have been made for all the following studies and in any case these studies have led to poor results (if compared with those in which the patch are applied on max potential energy areas). For these reasons, in the following will be left out this kind of numerical simulations.

Theoretically, although here it will not be treated, this study could be brought forward because the application of the patch on the surface of the plate will change its natural frequency values. It is then possible to repeat the same process taking into account this new natural frequency as the frequency on which the patch location will be based.

B5.3.3 Second patch configuration

In this third section the study of the second patch configuration will be introduced. For this second configuration, it is the evaluation of the potential energy assessed at the second natural frequency of the plate that defines and direct the location of the patches. This, in turns, will lead to an amplitude vibration reduction with an impact different by that obtained in the previous case.

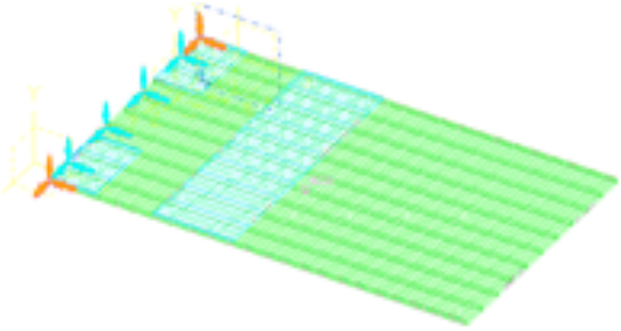

Figure B5.25 – Coupled system configuration for the study of the second natural frequency of the plate.

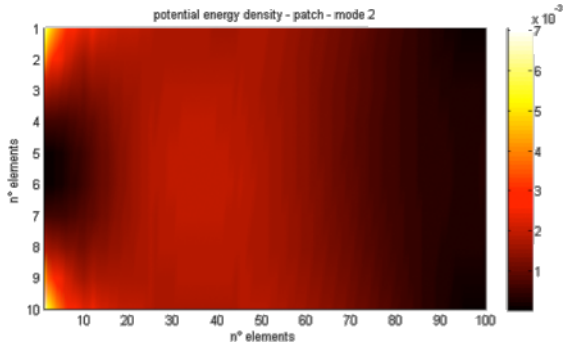

Figure B5.26 – Potential energy density map for the second natural frequency study (31.21 Hz) applying the patches.

The position of the patches and their size is defined by the graphical representations provided by Figures B5.13.b and B5.14.b referred to the base plate study (see *Section B5.3.1*).

Figure B5.25 shows the plate fem model (green mesh) including the patches (blue mesh) realized in I-DEAS environment.

Figure B5.26 shows the potential energy intensity map obtained by the application of the patches on the surface of the plate. From a quick comparison between Figure B5.14.b and Figure B5.26, can be clearly noted that the areas corresponding to the highest potential energy density areas has been reduced and therefore has been also reduced the amplitude levels of potential energy density (see the scale value on the right side of the intensity maps). Following the same path adopted in the previous section, the potential energy trend (Figure B5.27) and the normal velocity trend (Figure B5.28), obtained for this second configuration, are presented below.

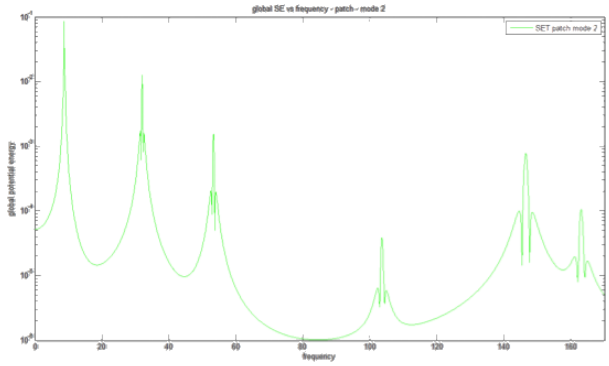

Figure B5.27 – Potential energy trend obtained for the second configuration of the coupled system.

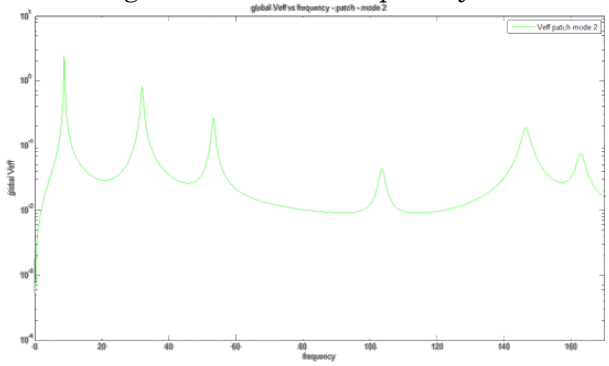

Figure B5.28 – Velocity trend obtained for the second configuration of the coupled system.

B5.3.4 Third patch configuration

In this fourth section will be introduced the study of the third patch configuration. For this third configuration, it is the evaluation of the potential energy assessed at the third natural frequency of the plate that defines and direct the location of the patches. This, in turns, will lead to an amplitude vibration reduction with an impact different by that obtained in the previous cases.

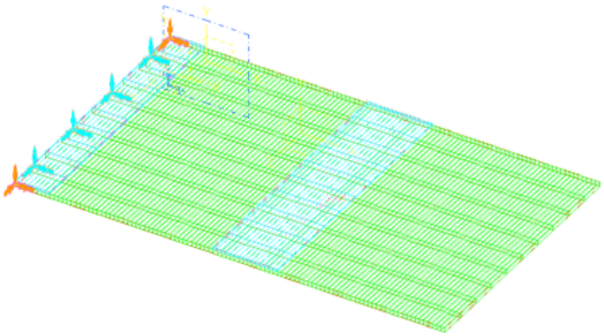

Figure B5.29 – Coupled system configuration for the study of the third natural frequency of the plate.

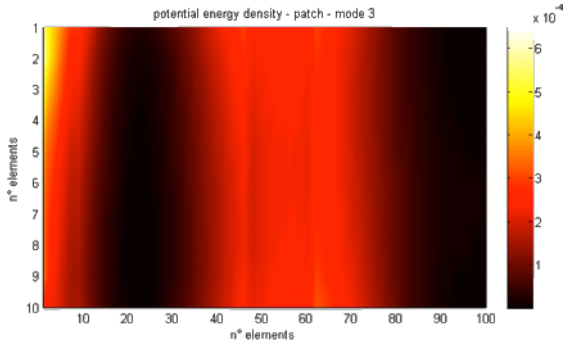

Figure B5.30 – Potential energy density map for the third natural frequency study (53.03 Hz) applying the patches.

The position of the patches and their size is defined by the graphical representations provided by Figures B5.13.c and B5.14.c referred to the base plate study (see *Section B5.3.1*).

Figure B5.29 shows the plate fem model (green mesh) including the patches (blue mesh) realized in I-DEAS environment.

Figure B5.30 shows the potential energy intensity map obtained by the application of the patches on the surface of the plate. From a quick comparison between Figure B5.14.c and Figure B5.30, can be clearly noted that the areas corresponding to the highest potential energy density areas has been reduced and therefore has been also reduced the amplitude levels of potential energy density (see the scale value on the right side of the intensity maps). Following the same path adopted in the previous section, the potential energy trend (Figure B5.31) and the normal velocity trend (Figure B5.32), obtained for this third configuration, are presented below.

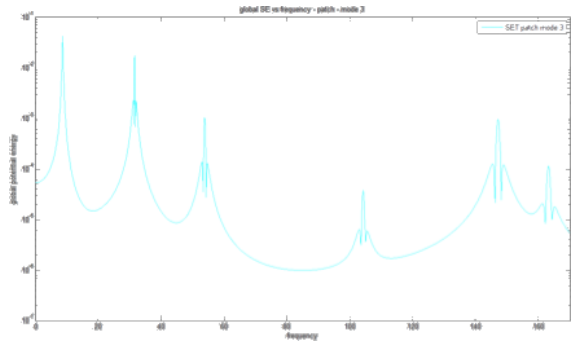

Figure B5.31 – Potential energy trend obtained for the third configuration of the coupled system.

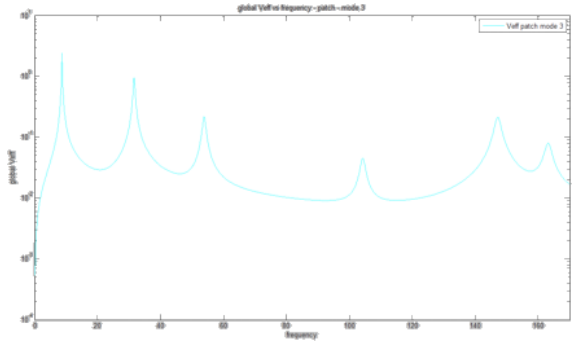

Figure B5.32 – Velocity trend obtained for the third configuration of the coupled system.

B5.3.5 Fourth patch configuration

In this fifth section will be introduced the study of the fourth patch configuration. For this fourth configuration, it is the evaluation of the potential energy assessed at the fourth natural frequency of the plate that defines and direct the location of the patches. This, in turns, will lead to an amplitude vibration reduction with an impact different by that obtained in the previous cases.

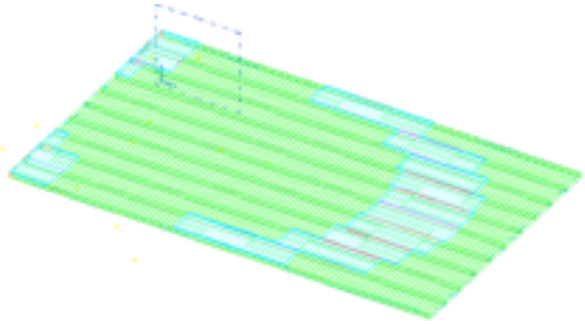

Figure B5.33 – Coupled system configuration for the study of the fourth natural frequency of the plate.

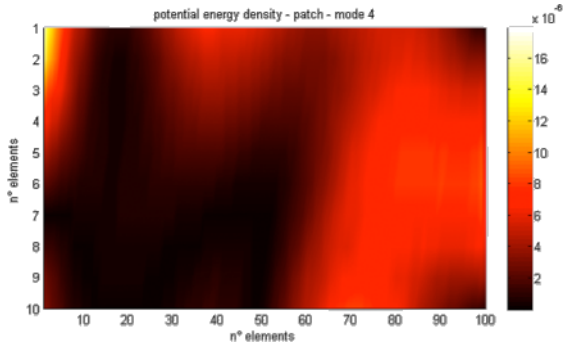

Figure B5.34 – Potential energy density map for the fourth natural frequency study (103.75 Hz) applying the patches.

The position of the patches and their size is defined by the graphical representations provided by Figures B5.13.d and B5.14.d referred to the base plate study (see *Section B5.3.1*).

Figure B5.33 shows the plate fem model (green mesh) including the patches (blue mesh) realized in I-DEAS environment.

Figure B5.34 shows the potential energy intensity map obtained by the application of the patches on the surface of the plate. From a quick comparison between Figure B5.14.d and Figure B5.34, can be clearly noted that the areas corresponding to the highest potential energy density areas has been reduced and therefore has been also reduced the amplitude levels of potential energy density (see the scale value on the right side of the intensity maps). Following the same path adopted in the previous section, the potential energy trend (Figure B5.35) and the normal velocity trend (Figure B5.36), obtained for this fourth configuration, are presented below.

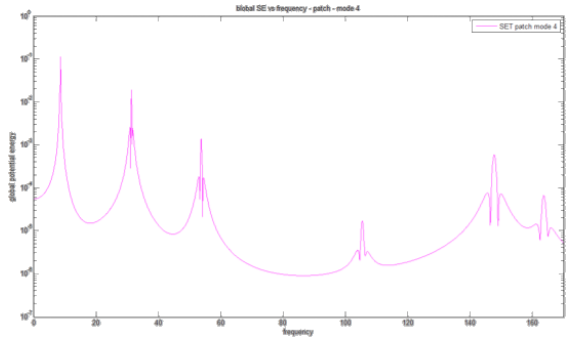

Figure B5.35 – Potential energy trend obtained for the fourth configuration of the coupled system.

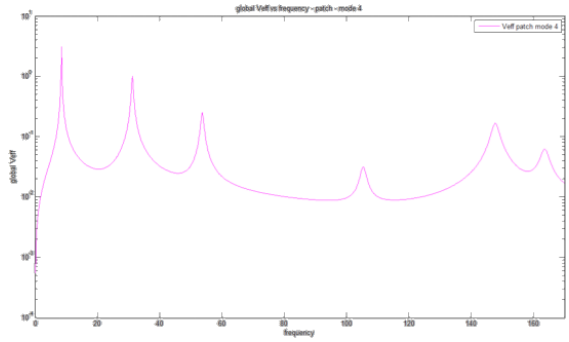

Figure B5.36 – Velocity trend obtained for the fourth configuration of the coupled system.

B5.3.6 Fifth patch configuration

In this sixth section will be introduced the study of the fifth patch configuration. For this fifth configuration, it is the evaluation of the potential energy assessed at the fifth natural frequency of the plate that defines and direct the location of the patches. This, in turns, will lead to an amplitude vibration reduction with an impact different by that obtained in the previous cases.

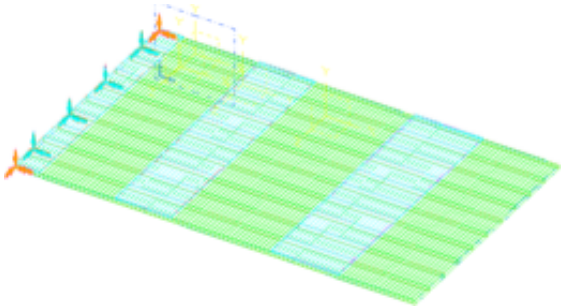

Figure B5.37 – Coupled system configuration for the study of the fifth natural frequency of the plate.

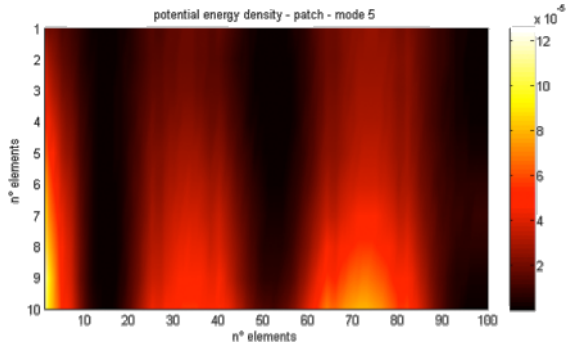

Figure B5.38 – Potential energy density map for the fifth natural frequency study (145.87 Hz) applying the patches.

The position of the patches and their size is defined by the graphical representations provided by Figures B5.13.e and B5.14.e referred to the base plate study (see *Section B5.3.1*). Figure B5.37 shows the plate fem model (green mesh) including

the patches (blue mesh) realized in I-DEAS environment.

Figure B5.38 shows the potential energy intensity map obtained by the application of the patches on the surface of the plate. From a quick comparison between Figure B5.14.e and Figure B5.38, can be clearly noted that the areas corresponding to the highest potential energy density areas has been reduced and therefore has been also reduced the amplitude levels of potential energy density (see the scale value on the right side of the intensity maps). Following the same path adopted in the previous section, the potential energy trend (Figure B5.39) and the normal velocity trend (Figure B5.40), obtained for this fifth configuration, are presented below.

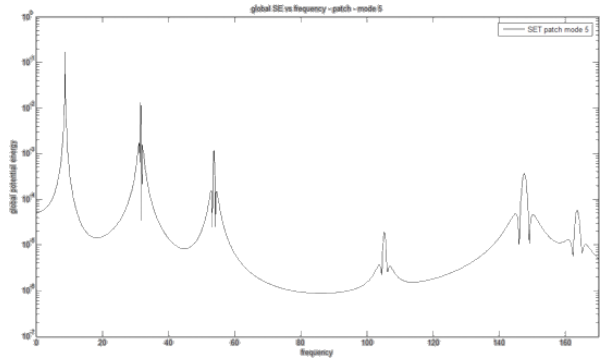

Figure B5.39 – Potential energy trend obtained for the fifth configuration of the coupled system.

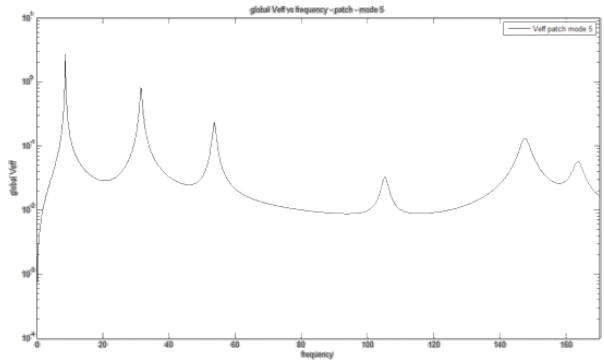

Figure B5.40 – Velocity trend obtained for the fifth configuration of the coupled system.

B5.3.7 Sixth patch configuration

In this seventh section will be introduced the study of the sixth patch configuration. For this sixth configuration, it is the evaluation of the potential energy assessed at the sixth natural frequency of the plate that defines and direct the location of the patches. This, in turns, will lead to an amplitude vibration reduction with an impact different by that obtained in the previous cases.

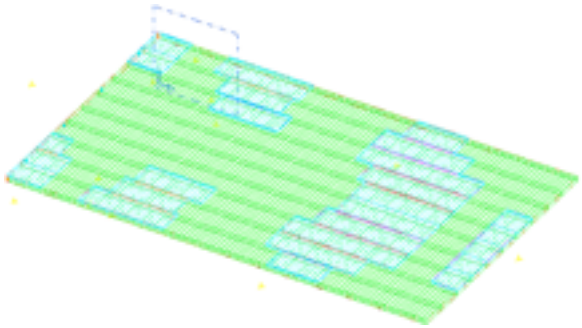

Figure B5.41 – Coupled system configuration for the study of the sixth natural frequency of the plate.

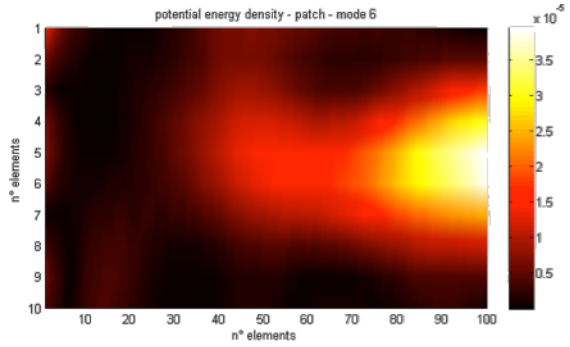

Figure B5.42 – Potential energy density map for the sixth natural frequency study (162.49 Hz) applying the patches.

The position of the patches and their size is defined by the graphical representations provided by Figures B5.13.f and B5.14.f referred to the base plate study (see *Section B5.3.1*). Figure B5.41

shows the plate fem model (green mesh) including the patches (blue mesh) realized in I-DEAS environment.

Figure B5.42 shows the potential energy intensity map obtained by the application of the patches on the surface of the plate. From a quick comparison between Figure B5.14.f and Figure B5.42, can be clearly noted that the areas corresponding to the highest potential energy density areas has been reduced and therefore has been also reduced the amplitude levels of potential energy density (see the scale value on the right side of the intensity maps). Following the same path adopted in the previous section, the potential energy trend (Figure B5.43) and the normal velocity trend (Figure B5.44), obtained for this sixth configuration, are presented below.

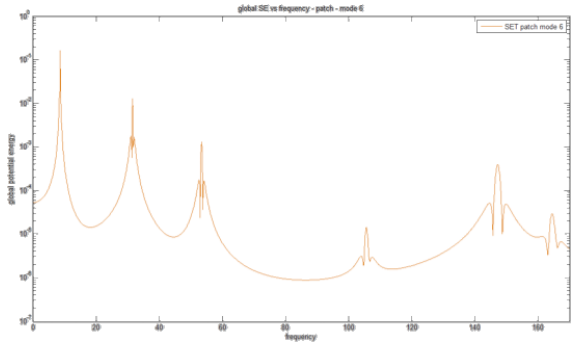

Figure B5.43 – Potential energy trend obtained for the sixth configuration of the coupled system.

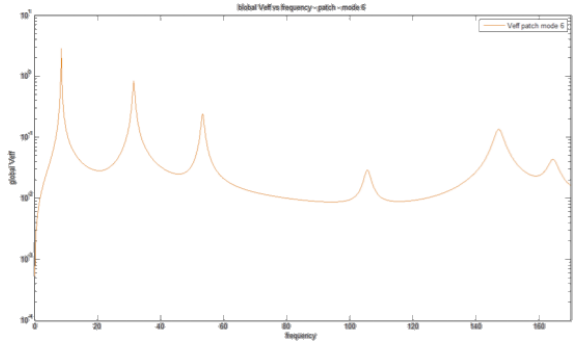

Figure B5.44 – Velocity trend obtained for the sixth configuration of the coupled system.

B5.4 Comparisons and conclusions

In this section will be judged and compared the results obtained through the study of the plate component, then including all the configurations characterized by the introduction of the patches in order to improve the vibratory behaviour of the base component. In other words, in this section will be introduced the graphs in relation to the comparisons between the results coming from the seven different configurations, the first one on the base plate and the latter six on the patch addition, in order to assess which of the above configurations can introduce the best contribution to the overall vibratory behaviour of the plate component. In Figures B5.45 and B5.46 the comparisons between the potential energy and velocity values plotted for the entire frequency range and evaluated for the seven different configurations are shown. As can be seen from both the representations, it is difficult to conduct a study, an assessment of the accuracy of the results obtained for these different numerical simulations. In other words, simply relying on these two graphs it is not possible to quickly and easily understand which configuration will allow to obtain the best results and therefore which of the seven configurations will generate the highest reduction on the overall amplitude vibration level of the plate component.

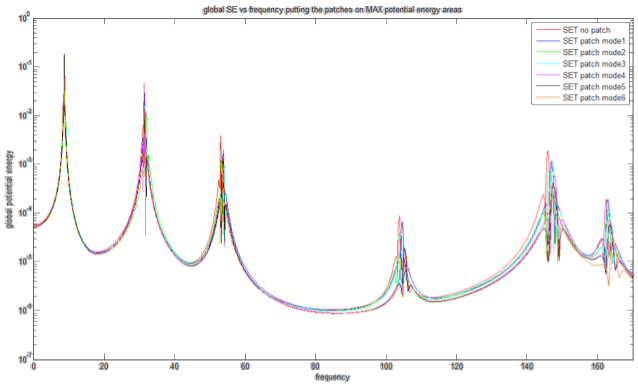

Figure B5.45 – Comparisons between the potential energy trends obtained for the seven different configurations.

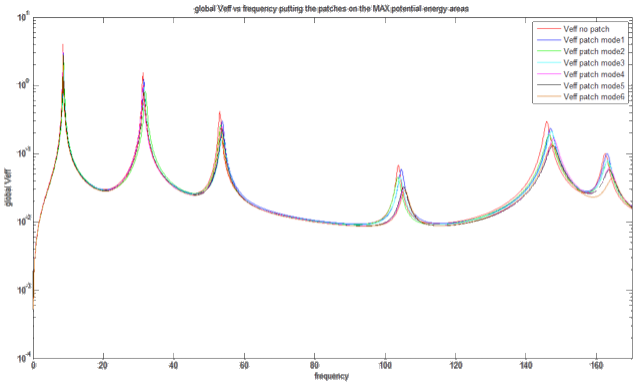

Figure B5.46 – Comparisons between the velocity trends obtained for the seven different configurations.

This problem is overcome by a series of expedient and calculations maid in Matlab environment that, taking as input all the velocity values just presented and graphed in Figure B5.46, will provide a new visualization form of these velocity results much more directly and easily than that just given.

In order to address in a more simply and quickly way the study performed to generate a clearer results visualization, it is supposed to consider a velocity trend as a function of frequency as the one presented in Figure B5.47, and included in a generic frequency range.

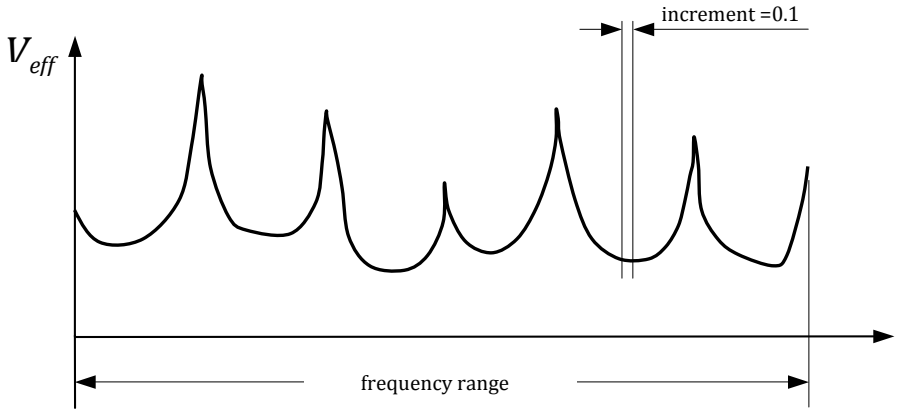

Figure B5.47 – Generic trend velocity.

In order to achieve this target two steps will follow, that are: (i) the effective velocity evaluation by taking into account the velocity trend displayed on the entire frequency range (see Figure B5.47.a), and (ii) the effective velocity assessment for each frequency band within the entire frequency range, (see Figure B5.47.b). In other words, through the knowledge of the velocity values for each configuration, will be evaluated the OVERALL and LOCAL effective velocity values respectively.

The evaluations performed in Matlab environment for both the measures will be based on the following equation (see eq. B3.1 in *Section B3.2*), in the case of $F(\omega) = cost$:

$$V_{eff} = \sqrt{\int_{\omega_1}^{\omega_2} |v(\omega)|^2 \, d\omega} \tag{B5.1}$$

where $v(\omega)$ are the velocity values and $d\omega$ is the increment value already defined in *Section B5.2* regarding the setting phase for the implementation of the velocity evaluation. In essence this value is nothing more than the value that outdistance two consecutive velocity values evaluation. This value that of course remains constant for all the numerical simulations performed is equal to 0.1 (see Figure B5.47). In relation to the study case took into account the frequency values placed on the integral sign will change. Indeed, considering the OVERALL effective velocity evaluation, the frequencies values will be $\omega_1 = 0$ and $\omega_2 = \omega_{\max}$ respectively, while considering the LOCAL effective velocity estimation, the frequencies values will be $\omega_1 = \omega_{res,n} - \Delta\omega$ and $\omega_2 = \omega_{res,n} + \Delta\omega$ respectively. The frequency values ω_1 and ω_2 related to the LOCAL effective velocity determination will be estimated through equations B5.2.a and B5.2.b, see Figure B5.47.b.

$$\omega_{res,n} - \Delta\omega = \sqrt{\omega_{n-1} \cdot \omega_n} \tag{B5.2.a}$$

$$\omega_{res,n} + \Delta\omega = \sqrt{\omega_{n+1} \cdot \omega_n} \tag{B5.2.b}$$

In summary, the effective velocity values for both the cases (OVERALL and LOCAL) are evaluated using the following relationships:

$$V_{eff,OVERALL} = \sqrt{\int_0^{\omega_{max}} |v(\omega)|^2 \cdot (0.1)} \qquad \text{(B5.3.a)}$$

$$V_{eff,LOCAL} = \sqrt{\int_{\sqrt{\omega_{n-1} \cdot \omega_n}}^{\sqrt{\omega_{n+1} \cdot \omega_n}} |v(\omega)|^2 \cdot (0.1)} \qquad \text{(B5.3.b)}$$

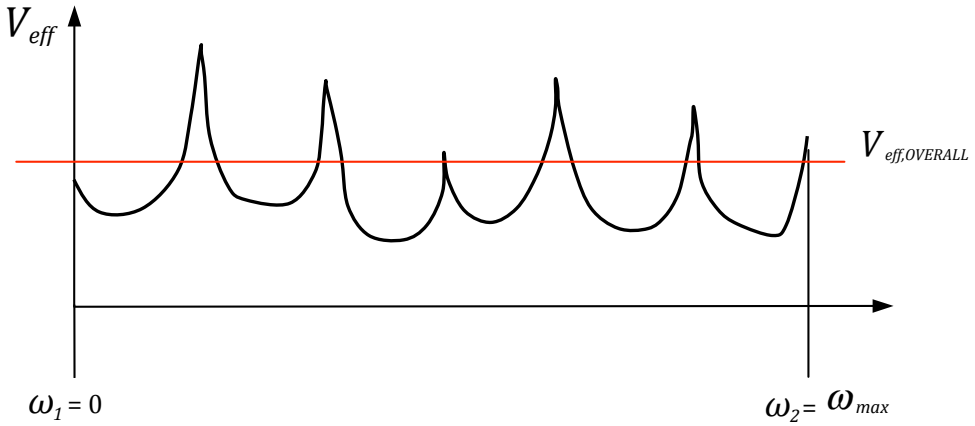

Figure B5.47.a – OVERALL effective velocity.

The velocity values previously obtained and visualized are now processed in Matlab environment, which according to the equations previously presented will provide a series of velocity values that will be used to address the assessment of the component improvement in terms of vibration amplitude reduction through a much simpler and direct way. The effective velocity values thus obtained are presented in Table B5.4 for all the configurations studied, including the base configuration. The table, and thus the velocity values, will be subdivided into two parts relating to which of the previously equations will be used for perform this study case, or more specifically, in relation to the

kind of effective velocity that is evaluated (overall or local).

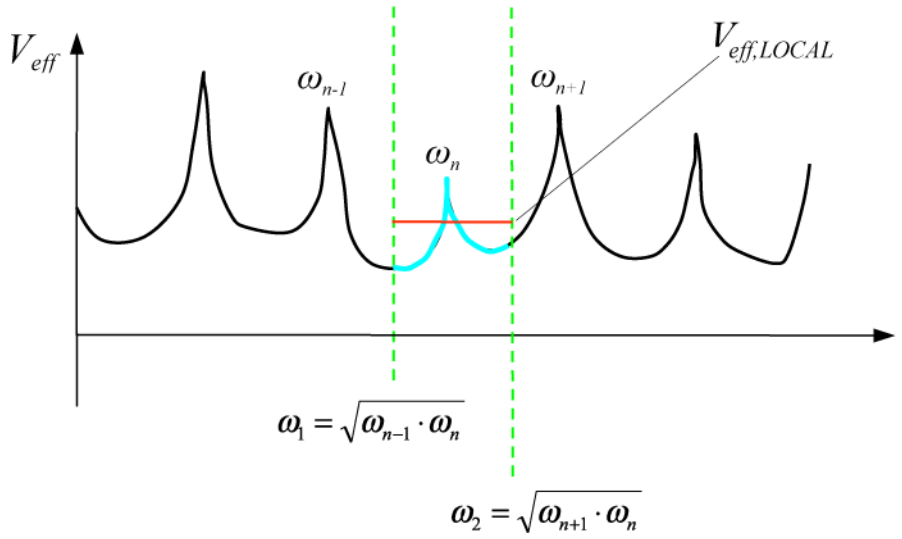

Figure B5.47.b – LOCAL effective velocity.

Simply giving a look of the values listed in Table B5.4, it is easy to comprehend that obviously the highest effective velocity values for all its assessment cases is referred to the base configuration. The patch application for all the six different configurations lead to a reduction of the velocity values compared to the case without patches, defining as the best configuration, that which locate the patches depending by the study of the vibratory behaviour of the plate at its fifth natural frequency (velocity values highlighted in red). Although the OVERALL velocity value is the lowest for the fifth case, that is the one which produces the highest amplitude velocity reduction of the plate, it does not mean that all its velocity values calculated for the different frequency band (LOCAL values) are for each case the lowest compared to that of the other configurations. Indeed, as shown on the "right side" of the table, only three of the six local velocity values for the fifth configuration are the lowest. In other

words, the fifth configuration produces the highest reduction of the velocity values for the 50 % of the cases, while the second, third and sixth cases each lead to an amplitude velocity reduction equal to 17 % of the total number of considered cases. Therefore, the fifth configuration is the best one, both in relation to the GLOBAL both to the LOCAL effective velocity study case.

	OVERALL	**LOCAL**					
Configuration number	Entire band	Band 1	Band 2	Band 3	Band 4	Band 5	Band 6
Base	2.1134	1.7038	1.0837	0.3936	0.1072	0.4402	0.1703
First (max)	1.7797	1.3855	0.9682	0.3408	0.1052	0.3902	0.1761
Second (max)	1.5814	1.2750	0.7909	0.3128	0.0923	0.3474	0.1502
Third (max)	1.6641	1.3430	0.8469	0.2833	0.0925	0.3682	0.1558
Fourth (max)	1.7513	1.4513	0.8627	0.3017	0.0808	0.3177	0.1350
Fifth (max)	1.5787	1.3061	0.7761	0.2888	0.0821	0.2773	0.1308
Sixth (max)	1.6128	1.3413	0.7845	0.2970	0.0794	0.2835	0.1481

Table B5.4 – GLOBAL and LOCAL effective velocity values for the seventh plate configurations studied.

It is important to note that all the values listed in Table B5.4

are related to the numerical simulations carried out by applying the patches only on the areas of highest potential energy density (MAX). This is due to the knowledge of the results already obtained in the previous work, which showed that the application of the patches in the areas of MIN potential energy density leads to a reduction of the potential energy levels, but with less intensity (see *Section B5.3.2*). Anyway, in order to increase the reliability of the methodology created and used to develop the results exhibited in this thesis part, in the following the results obtained studying the best configuration (the fifth configuration) applying the patches on the MIN potential energy areas will be presented. The position of the patches and their size are defined by the graphical representations provided by Figures B5.13.e and B5.14.e referred to the base plate study (see *Section B5.3.1*) in addition to that of the fifth configuration already presented in *Section B5.3.6* (see Figure B5.37). Figure B5.48 shows the plate fem model (green mesh) including the patches (blue mesh) applied on the MIN potential energy areas. Figure B5.49 shows the potential energy density map obtained for this case. From a quick comparison between the potential energy density map related to the patches applied on the MAX (Figure B5.38) and MIN (Figure B5.49) areas, can be clearly seen as the potential energy amplitude values for the latter case are reduced compared to the base configuration (Figure B5.14.e), but increased compared to the MAX configuration case. This then is in accordance with what explained above.

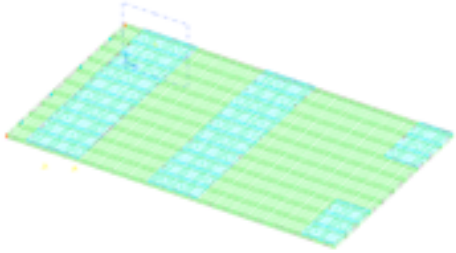

Figure B5.48 – Coupled system fem model applying the patches on the MIN potential energy areas.

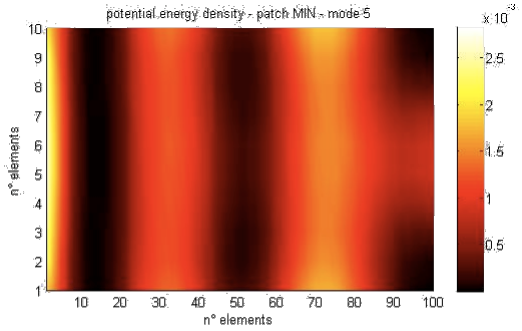

Figure B5.49 – Potential energy density map for the fifth natural frequency study applying the patches on the MIN areas.

	OVERALL	**LOCAL**					
Configuration number	Entire band	Band 1	Band 2	Band 3	Band 4	Band 5	Band 6
Fifth (MAX)	1.5787	1.3061	0.7761	0.2888	0.0821	0.2773	0.1308
Fifth (MIN)	1.6032	1.3271	0.7801	0.3009	0.0986	0.3984	0.1358

Table B5.5 – GLOBAL and LOCAL effective velocity values for the fifth plate configurations.

The effective velocity values achieved by the considerations presented in this section are listed in Table B5.5, showing only the comparisons between the results obtained for the fifth configuration evaluated by applying the patches on the MAX and MIN potential energy density areas respectively. Again, the best value is achieved by the case of patch application on the MAX potential energy density areas. In the case of patch application on MIN potential energy density areas, any effective velocity values produce on the plate a lower reduction compared to the MAX case.

In order to better comprehend the importance of these results and thus the correctness of the path followed in the study, the percentage values of the effective velocity reduction for the six

different configurations of the plate in comparisons to the base case are listed in Table B5.6. For example, taking into account the second configuration, it can be noted that the application of the patches on the surface of the plate, defined by the study of its second natural frequency leads to a reduction of the overall velocity value equal to the 25.2% compared to the case without any patch applied on it. This means that the application of the patches on the base structure causes the velocity reduction, i.e. improvement of the vibratory behaviour, compared to the basic case, with different impacts depending by the positions on which the patches are applied and then depending by the configuration studied. In red is highlighted the best reduction percentage value determined for the entire band whereas, in green are listed the highest reduction percentage value determined for each frequency band.

	OVERALL	**LOCAL**					
Configuration number	Entire band	Band 1	Band 2	Band 3	Band 4	Band 5	Band 6
First	15.8	18.7	10.7	13.4	1.9	11.4	-3.4
Second	25.0	25.2	27.0	20.5	13.9	21.1	11.8
Third	21.3	21.2	21.9	28.0	13.7	16.4	8.5
Fourth	17.1	14.8	20.4	23.3	24.6	27.8	20.7
Fifth (MAX)	25.3	23.3	28.4	26.6	23.4	37.0	23.2
Sixth	23.7	21.3	27.6	24.5	25.9	35.6	13.0
Fifth (MIN)	24.1	22.1	28.0	23.6	8.0	9.5	20.3

Table B5.6 – Percentage velocity reduction for the six configurations compared to the base plate.

Taking a look of Table B5.6, it is possible to see that all the configurations leads to a reduction of the amplitude vibrations levels of the base component, i.e. only the plate. Obviously, certain configurations produce higher reduction levels compared to other. The best one is defined by the fifth configuration that produces the highest velocity reduction, i.e. reduction of the 25% of the vibration amplitude level of the plate. In one particular case (value highlighted in blue in Table B5.6), the application of the patches on the surface of the plate for a specific frequency band, although slightly, leads to increased values of local effective velocity, and thus to worsening vibration level of the plate component (see sixth band of the first configuration). This implies that the application of the patches on the surface of the unrefined component must be done in an appropriately and intelligent manner, that is clear from the results here obtained. Obviously this does not involve negative considerations on the correctness of the methodology adopted and created during this thesis work because this results is only generated by the first configuration, the worst configuration, and because this "strange" behaviour occurs on the sixth frequency band (sixth natural frequency of the plate), which as already mentioned does not reflect the threshold frequency normally studied. Still looking Table B5.6, it is possible to see that all the percentage related to the application of the patches on the MIN potential energy areas are lower compared to the respective values obtained through the application of the patches on the MAX potential energy areas. This last point confirms all the considerations and evaluations previously exposed, consciously bringing to light the certainty of a reliable and repeatable methodology.

In Figure B5.50 is presented a column chart that shows the comparison between the percentages of the effective velocity reduction for the base case (red column) with respect to the better case, which is represented by the fifth configuration (blue column). The figure can clearly and quickly represent the improvement of the structure from the vibratory point of view

caused by the application of the patches.

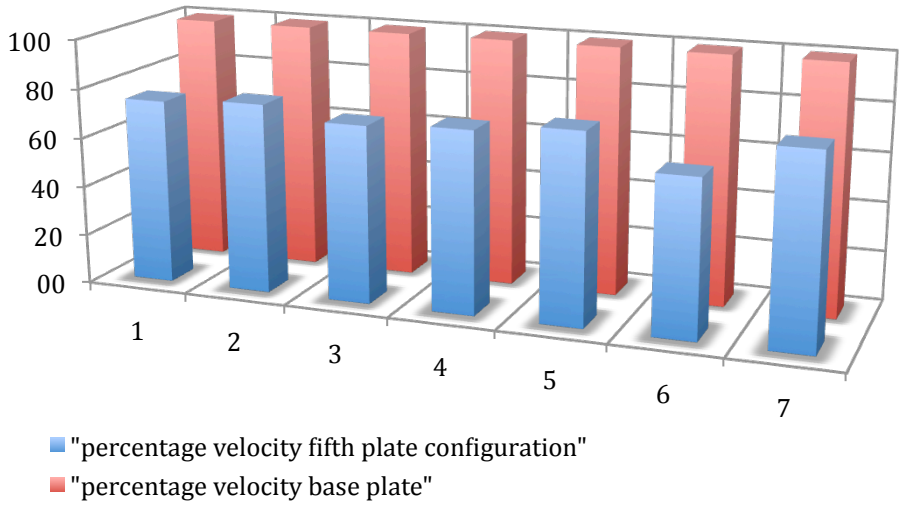

Figure B5.50 – Percentage velocity reduction for the fifth configuration (blue column) compared to the base plate (red column).

In this figure, as in the tables above, on the abscissa are listed the frequency range on which the effective velocity evaluations are performed. The number "1" corresponds to the OVERALL effective velocity study case, while the numbers from "2" to "7" obviously represents the six frequency bands that corresponds to the LOCAL effective velocity study case. Simply looking the column chart in Figure B5.50 it is easy to understand that the difference between the columns obtained for the two different configurations (blue and red) represents the amount in percentage of the effective velocity reduction achieved through the application of the patches (of course for the fifth configuration case); thus giving an idea of the amount of the vibratory improvement of the plate component. Obviously, for this specific case, the difference between these peaks velocity values will give exactly the same values of that listed in the fifth row of Table

B5.6.

All the considerations made throughout the work explanation and all the results obtained throughout the methodology created leads to the following considerations:

- Generally, the study leads to the creation of a methodology that overcomes all the problems that may arise during the creation of the coupled system and during the implementation of the analysis that has to be carried out. Besides, using these steps, it is possible and feasible to quickly and correctly see all the results that have been calculated through the accurate numerical simulations allowing to define for which conditions is provided the best component behaviour in terms of amplitude vibration reduction.
- Specifically, in relation to the plate study performed in this chapter, can be concluded that the application of the high damping material for the study of the fifth natural frequency of the plate leads to the best configuration. In fact this configuration produce the best velocity results which are labeled in a clear and unambiguous as the best candidate to reduce the velocity values of the plate component and consequently to improve its overall vibratory behaviour by reducing its overall amplitude vibration level. In other words, through this fifth configuration the amplitude vibration level of the plate component has been reduced by about the 25%, sign of a significant contribution in the improvement of the vibratory behaviour of the mechanical component.

CHAPTER B6

Vibration reduction in a bracket through patch applications

This chapter defines the attainment of the goal, labeled as the determination of the damping placement on a structure in order to ensure its noise reduction and obviously the improvement of its vibrational behaviour. In the following will be shown, through numerical simulations and data elaborations, how potential energy distribution can define the placement of constrained layer damping patches on the surface of a bracket in order to produce changes (reduction) in the velocity pattern of the structure and thus in the overall vibrational behaviour of the unrefined component.

As explained in the previous chapter, the confirmative

numerical simulations carried out in *Chapter B4* provides the foundation for obtaining results with high accuracy and reliability in relation to the determination of the best patches locations on the surface of the unrefined component in order to reduce unwanted vibrations.

In this chapter all the informations introduced in the bracket FEM model has been presented, and therefore all the results obtained for this study case will be shown. In other words, through this approach, several numerical simulations will be performed on the bracket by measuring the potential energy distribution and normal velocity values. The first will be essential in order to precisely define the location of the patches, while the second can be used to identify which patches arrangement produce the highest improvement.

As introduced in *Chapter B5*, in this chapter only the typical informations that have to be introduced in the FEM model of the bracket will be presented in addition to the exposition and explanation of the results achieved.

B6.1 Bracket study overview

During the discussion treated in this section will be considered and explained the following points regarding the study of a single bracket, that are obviously the same as that defined for the plate component.

(i). Definition of the methodology followed for develop the FEM model;
(ii). Definition of the informations directly related to the component study and subsequently introduced in its FEM model;

(iii). Introduction of some figures, illustrative of the steps made in I-DEAS environment in order to clarify certain concepts;
(iv). Data processing of the results obtained through the software, using Matlab;
(v). Considerations about the methodology validity and the results accuracy.

B6.2 FE model definition

The methodology used to develop the bracket fem model, the analysis setting and the procedures followed for estimate the final results will retrace exactly the same path already followed by the plate component, see *Section B5.2*. In addition, in this study part will be left out all the introductory phase regarding the procedure by which the informations that characterize the bracket component will be introduced in I-DEAS software, because already explained in *Section B5.2* referred to the plate study case.

Due to small variations on the data entered in the bracket fem model, in the following will be represented the procedure used to obtain the velocity and potential energy values in the entire frequency range of the component; obviously without going into detail. These variations are essentially made at the sixth and seventh steps of the afore-mentioned methodology. Specifically the following changes will be performed:

(i). Increase in the maximum number of points regarding the creation of the frequency function (1800 instead of 1700), due to variation of the frequency range extension for this component (0-180 Hz, instead of 0-170 Hz for the plate);
(ii). Change in the direction of the force that has to be applied on the upper surface of the bracket compared to

that applied on the plate (Z instead of Y), due to variation in the reference system adopted for its realization;

(iii). Increase in the maximum frequency value identified as the upper frequency limit of the frequency range in the results evaluation (180 instead of 170), see point "i".

For the bracket, as for the plate, the methodology is made up of nine macro-steps, eight of which performed in I-DEAS environment while the last carried out in Matlab environment.

1. Geometry creation
2. Material definition

Steel (bracket)	→	$E_Y = 2.1e11\ Pa$
		$\upsilon = 0.3$
		$\rho = 7800\ \ kg/m^3$
		$\eta_{h,bracket} = 1\%$
Asphalt (patch)	→	$E_Y = 1.2e10\ Pa$
		$\upsilon = 0.21$
		$\rho = 2100\ \ kg/m^3$
		$\eta_{h,pacth} = 17\%$

3. Boundary conditions definition
4. Mesh definition
5. Model solution definition

Type of solution	→	Normal mode dynamic-Lanczos
Options	→	Chose modal damping
		Define number of modes
Output selection	→	Mode shapes
		Displacements

Potential energy

Kinetic energy

6. Response analysis definition

Frequency function → Force

Translational

Real

Equation:

- Abscissa min = 0
- Abscissa increment = 0.1
- Max number data points = 1801
- Force value = 100 N

Filename:

- “value_force”

Create event → Event type:

- Frequency

Element data recovery

- Element formulation

Add force:

- Define node application
- Define direction (Z)
- Insert the function created

ω_n :

- Insert viscous damping

7. Results evaluation

Response domain → Start/end point:

Output start frequency = 0

Output end frequency = 180

Decimation order = 1

Velocity (nodes)

Potential energy (elements)

8. Post-processing with I-DEAS®

Potential energy for each mode

Displacement for each mode

9. Post-processing with Matlab®

Potential energy on the entire frequency range

Velocity on the entire frequency range

In order to simplify all the concepts so far listed, in the following the figures related to the real passage performed in I-DEAS environment, and all the results evaluated in Matlab environment will be presented for the bracket component.

First point of this process is defined by the creation of the bracket geometry, followed by the definition of the force location on the surface of the component, both shown in Figure B6.1, and by the introduction in the fem model of the information related to the mechanical characteristics of the bracket; the latter reported in the second point of the above listed methodology.

Figure B6.2 shows the bracket component generated in I-DEAS environment, including mesh and boundary conditions; the latter applied on two different surfaces. The component is thus clamped in the left and lower side of the bracket component.

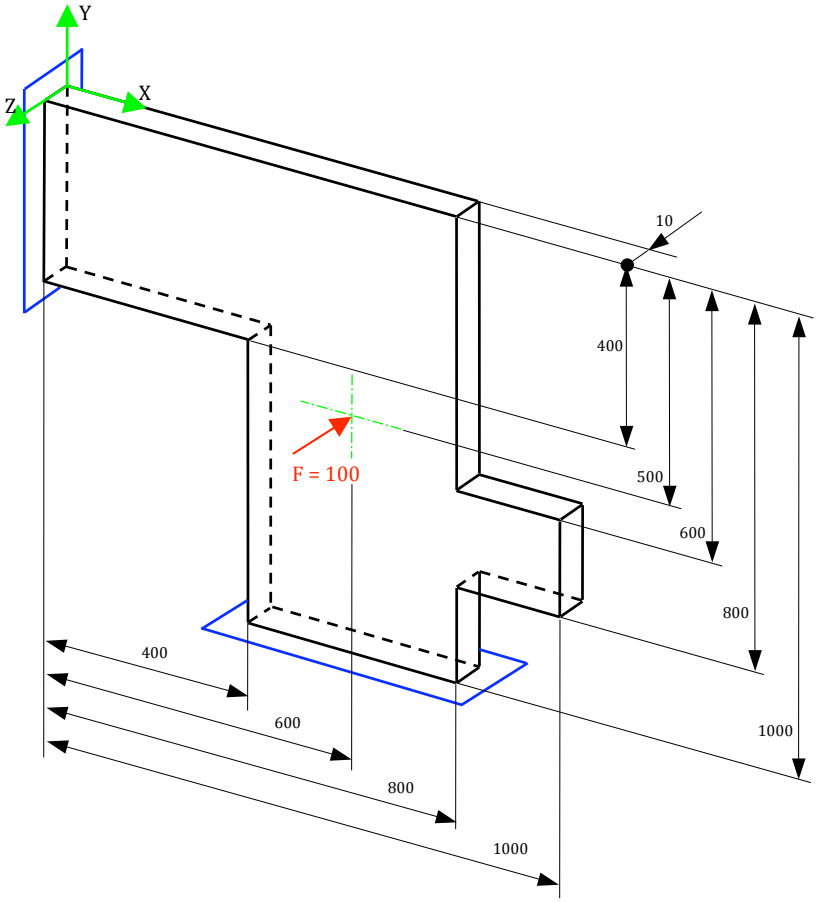

Figure B6.1 – Force location on the surface of the bracket and its characteristic dimensions.

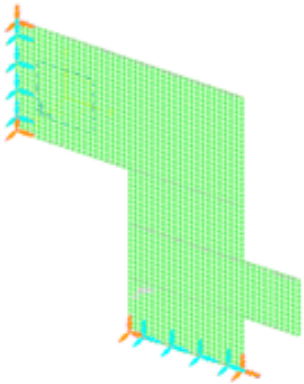

Figure B6.2 – Mesh creation on the bracket component.

As is shown in Figure B6.3, the component is virtually subdivided into a number of sub-components (six in this case). This expedient will generate a precise mesh element numeration, which will remain for all the numerical simulations performed and then for all the different configurations that will be studied. This will greatly simplify (i) the research step of the mesh elements on which the material damping has to be placed and (ii) the implementation of the Matlab code allowing the potential energy intensity maps generation over the entire component.

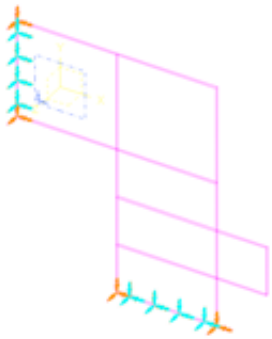

Figure B6.3 – Bracket component virtually subdivided into six sub-components.

Figures B6.4.a – B6.4.f shows the first six mode shapes of the bracket component.

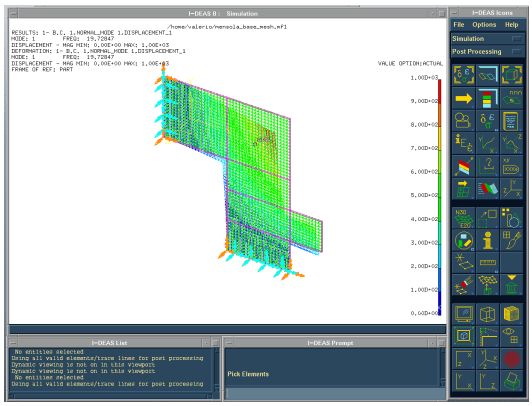

Figure B6.4.a – First mode shape of the steel bracket.

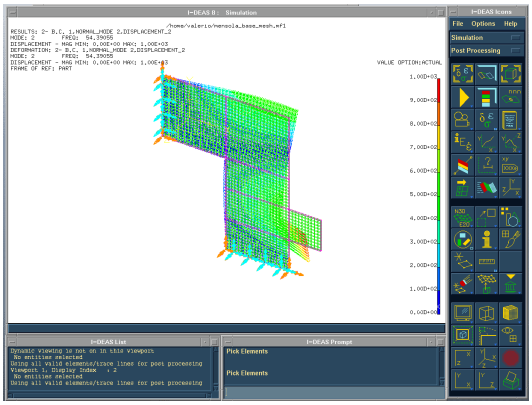

Figure B6.4.b – Second mode shape of the steel bracket.

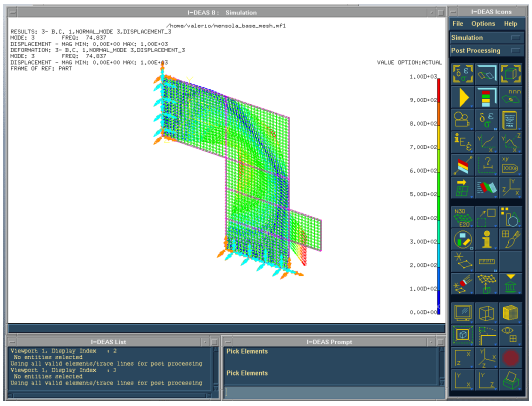

Figure B6.4.c – Third mode shape of the steel bracket.

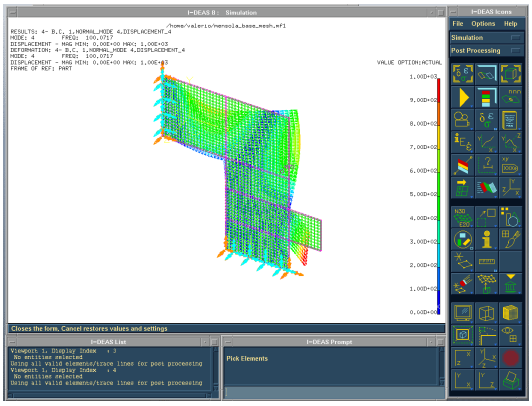

Figure B6.4.d – Fourth mode shape of the steel bracket.

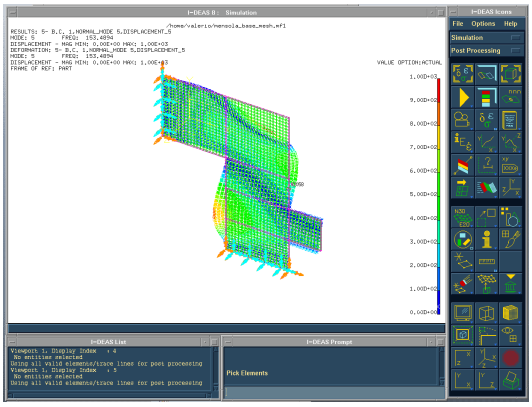

Figure B6.4.e – Fifth mode shape of the steel bracket.

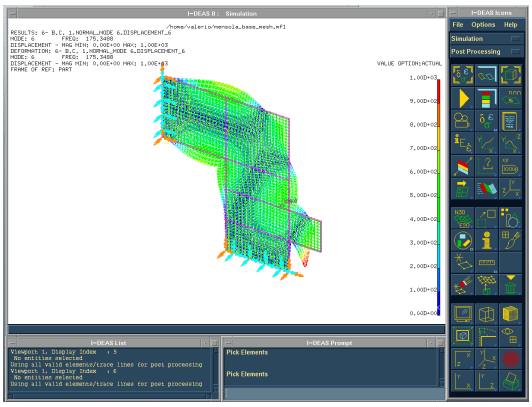

Figure B6.4.f – Sixth mode shape of the steel bracket.

As for the plate, also for this component, the kind of numerical simulations performed are three:

- ✓ Potential energy evaluation at a single characteristic frequency;
- ✓ Potential energy evaluation for all the frequency range of the component;
- ✓ Velocity evaluation for all the frequency range of the component.

Let's consider the first numerical simulation case, which is the analysis performed on the bracket for reach the potential energy values corresponding to the component behaviour at a

precise natural frequency. In turn, this quantity will be fundamental in order to clarify and identify the location of the patches that has to be applied on the surface of the bracket. In order to perform a study on a precise characteristic frequency (the first in this case) and on the entire frequency range of the bracket component, the values listed in Table B6.1 will be introduced in one of the I-DEAS form. Then, through the numerical simulations, the potential energy trend and the potential energy distribution regarding the study of the component behaviour at a single natural frequency and on the entire frequency range, respectively, will be obtained. The first will be essential in order to precisely define the location of the patches, while the second can be used to identify which patches arrangement produce the highest improvement. In reality, this latter task will be entrusted by the velocity evaluation, obviously studying the component behaviour in the entire frequency range.

	Potential energy *first frequency*	Potential energy *frequency range*	Velocity *frequency range*
Abscissa min	0	0	0
Abscissa increment	19.728	0.1	0.1
Max. number of data points	100	1801	1801

Table B6.1 – Values introduced in the bracket fem model for the characterization of the frequency function for different cases.

In order to perform the study on a precise natural frequency (first bracket natural frequency in this case) and on the entire

frequency range of the bracket component, the values listed in Table B6.2 will be introduced in one of the I-DEAS form. Through these values, directly introduced in the seventh step of the aforementioned methodology, the potential energy values for the bracket component will be evaluated

	Potential energy *first frequency*	Potential energy *frequency range*	Velocity *frequency range*
Output start frequency	19.728	0	0
Output end frequency	19.728	180	180
Decimation order	1	1	1

Table B6.2 – Values introduced in the bracket fem model for the evaluation of different quantities.

This point conclude the creation and the establishment stage of the bracket fem model realized in I-DEAS environment related to the study of the base bracket or to the study of its unrefined configuration, i.e. only the bracket without any patch applied on it with the aim to improve its vibratory behaviour.

From this point, all the results thus obtained will be developed in Matlab environment in order to make them more readable and understandable for perform practical considerations. In essence, the results concerning the estimation of potential energy values regarding the specific natural frequency of the bracket component will be useful to understand in which location the patches has to be applied; the results concerning the

estimation of potential energy values in addition to those concerning the velocity values, both relating to the entire frequency range, will be useful to clearly define the impact that each natural frequency of the bracket has on its overall amplitude vibratory behaviour. This in turns will provide in addition to the knowledge of the net input power to the component important information about the loss factor estimation (aspect not treated here). It is important to remember that the specific numerical simulations carried out in *Sections B4.1* and *B4.2* help to give certainty on the accuracy and reliability of the methodology created.

B6.3 Result presentation

Following the methodology outlined in the previous section of this chapter will be obtained through the numerical simulations performed in I-DEAS environment a series of files relating to (i) the study of the unrefined configuration of the bracket component, that in other words is nothing else the bracket without any patch applied on it and, (ii) the study of all the configurations that coming from the study of the first six natural frequencies of the bracket, each one characterized by a precise location of the patches on its surface.

Essentially, the configurations that will be explained and presented below will be the following:

(i). Base configuration (only the bracket);
(ii). First patch configuration (in relation to the study of the bracket behaviour at its first natural frequency);
(iii). Second patch configuration (in relation to the study of the bracket behaviour at its second natural frequency);
(iv). Third patch configuration (in relation to the study of the bracket behaviour at its third natural frequency);

(v). Fourth patch configuration (in relation to the study of the bracket behaviour at its fourth natural frequency);
(vi). Fifth patch configuration (in relation to the study of the bracket behaviour at its fifth natural frequency);
(vii). Sixth patch configuration (in relation to the study of the bracket behaviour at its sixth natural frequency);

B6.3.1 Base configuration

The files that are generated through the aforementioned methodology according to the information given in *Section B6.2* and therefore introduced in the bracket fem model are the following:

- Potential energy evaluation in relation to the study of the bracket behaviour at its first natural frequency;
- Potential energy evaluation in relation to the study of the bracket behaviour at its second natural frequency;
- Potential energy evaluation in relation to the study of the bracket behaviour at its third natural frequency;
- Potential energy evaluation in relation to the study of the bracket behaviour at its fourth natural frequency;
- Potential energy evaluation in relation to the study of the bracket behaviour at its fifth natural frequency;
- Potential energy evaluation in relation to the study of the bracket behaviour at its sixth natural frequency;
- Potential energy evaluation in relation to the study of the bracket behaviour on the entire frequency range (0-180 Hz);
- Velocity evaluation in relation to the study of the bracket behaviour on the entire frequency range (0-180 Hz);

Essentially, two files will be generated in relation to the

evaluation of the potential energy and velocity values, both estimated in all the frequency range; in addition to a series of files (six in this case) containing the potential energy values evaluated for certain natural frequencies of the bracket. These eight files will contain all the information needed to perform a comprehensive study on the overall vibratory behaviour of the bracket component. In this study case will be directly presented the potential energy density maps for the first six natural frequencies of the bracket, avoiding to present their trends (see the considerations already exposed and treated for the plate case, Figures from B6.5.a to B6.5.f).

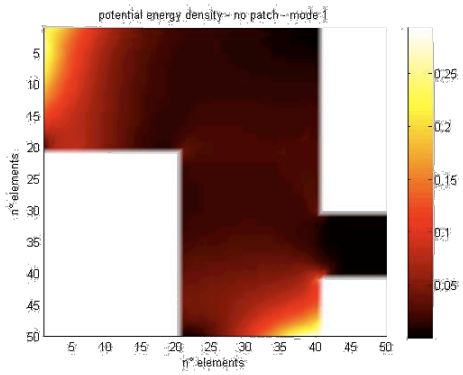

Figure B6.5.a – Potential energy density map for the first natural frequency study equal to 19.728 Hz.

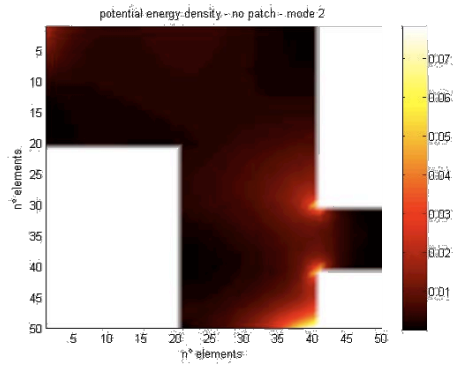

Figure B6.5.b – Potential energy density map for the second natural frequency study equal to 54.390 Hz.

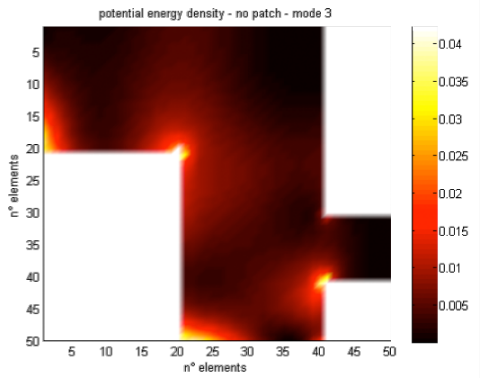

Figure B6.5.c – Potential energy density map for the third natural frequency study equal to 74.837 Hz.

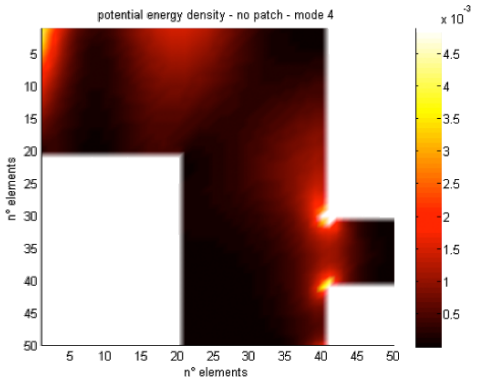

Figure B6.5.d – Potential energy density map for the fourth natural frequency study equal to 100.071 Hz.

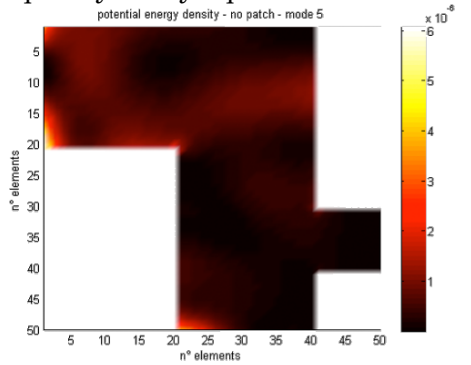

Figure B6.5.e – Potential energy density map for the fifth natural frequency study equal to 153.489 Hz.

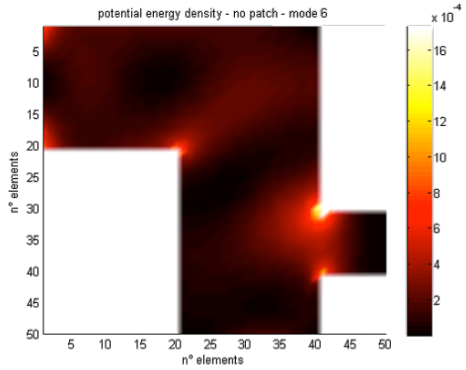

Figure B6.5.f – Potential energy density map for the sixth natural frequency study equal to 175.348 Hz.

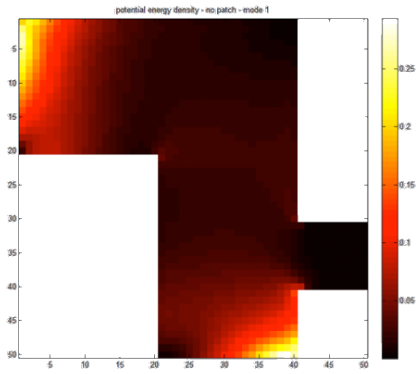

Figure B6.5.g – Gross potential energy density map for the first natural frequency study equal to 19.728 Hz.

Giving a quick look at the six figures presented above, the basis on which the potential energy density is presented is exactly the bracket, thus making very simple the definition of the mesh elements of the bracket that corresponds to the highest level of potential energy (hot colors). The mesh elements that show the potential energy values above this level will require the presence of the patches. In reality, the figures presented here shows the potential energy density perfectly slapped on the bracket surface, while in Figure B6.5.g, is also presented the same potential energy density map characterized by a raw visualization of the potential energy density giving the presence of each mesh

elements in a clear manner. This then leads to the display of stair-step (due to the difference in color) between two consecutive mesh elements. In this manner a "grid" is created on the surface of the bracket exactly equal to the bracket mesh grid. This kind of visualization is less beautiful but much more important because it already provides the exact and rapid identification of the mesh element that should be covered by the patches.

Returning to introductory phase, two are the files that still remain, that are the potential energy and velocity evaluation on the entire frequency range of the bracket. Figures B6.6 and B6.7 shows the potential energy trend and the velocity trend respectively, both depending by the entire frequency range of the bracket component. The velocity trend reported in Figure B6.7 is obtained by manipulating the velocity values that comes from the numerical simulations performed in I-DEAS environment through eq. B3.2 treated in *Section B3.2*.

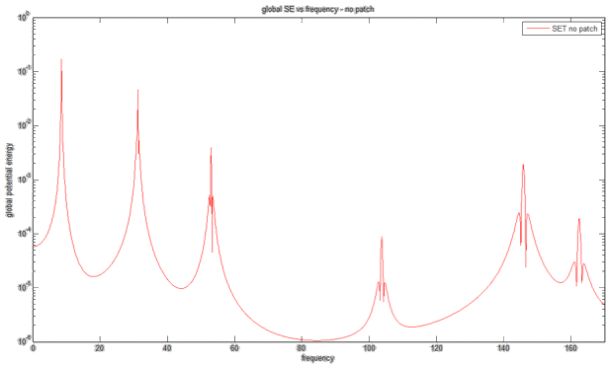

Figure B6.6 – Potential energy trend obtained for the entire frequency range.

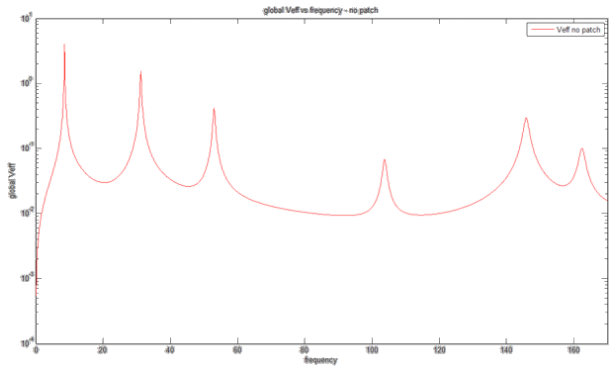

Figure B6.7 – Velocity trend obtained for the entire frequency range.

With this last considerations ends the study phase of the base bracket component (unrefined configuration). In the following sections the results obtained for the study of the coupled system, i.e. the bracket with the patches applied on it, will be presented.

B6.3.2 First patch configuration

The files that are generated through the aforementioned methodology according to the information given in the *Section B6.2* and therefore introduced in the bracket fem model are the following:

- Potential energy evaluation in relation to the study of the component behaviour on its entire frequency range;
- Velocity evaluation in relation to the study of the component behaviour on its entire frequency range;

Essentially two files in relation to the potential energy and velocity evaluations for the coupled system will be generated. The values contained in this files, in turns, will provide important information about the bracket vibratory behaviour improvement by reducing its amplitude vibration level. For this first case, the

patches are applied on the surface of the component by studying the behaviour of the bracket in correspondence of its first natural frequency (see Figure B6.5.a). Figure B6.8 shows the bracket fem model (green mesh) in addition to the patch (blue mesh) realized in I-DEAS environment. Again, as in the plate case, it is possible to represent the mode shape configuration for the coupled system. For simplicity, is only shown one representation of the above-mentioned mode shape configuration, see Figure B6.9, with the aim of making visible as the deformed configuration of the patch exactly follows that of the bracket. This latter consideration, in addition to the numerical simulations presented in the *Chapter B4* gives an idea of the correctness of the procedure established and followed in the study of generic component such as the plate and the bracket.

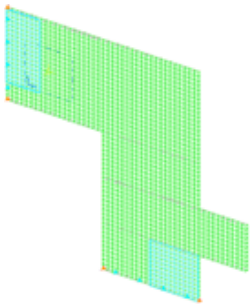

Figure B6.8 – Coupled system configuration for the study of the first natural frequency of the bracket.

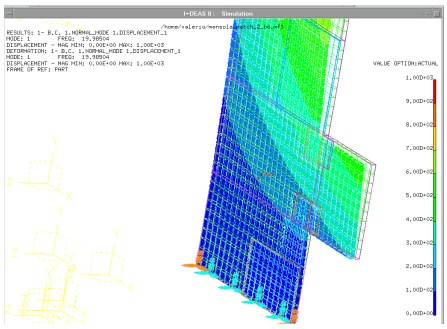

Figure B6.9 – Fifth mode shape zoom of the coupled system configuration.

Due to changes in the system, because of the presence of the patch, the potential energy distribution at the first natural frequency changes. Therefore, it is possible to study this variation, and to define a new potential energy distribution that takes into account the presence of the patch. Figure B6.10 takes into account this change.

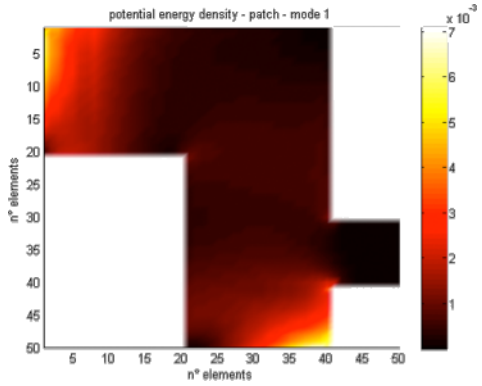

Figure B6.10 – Potential energy density map for the first natural frequency study (19.728 Hz) applying the patch.

From a quick comparison between Figure B6.5.a relative to the potential energy density map obtained without the application of any patches and Figure B6.10 characterized by the application of the patches on the surface of the bracket, can be clearly noted that the areas corresponding to the greatest potential energy density areas has been reduced. In addition, the amplitude levels of potential energy values for the second case (maximum value equal to 7x10^-3) are decreased compared to the first case (maximum value equal to 0.3). It is easy to understand how the patch application, if appropriately located, causes a significant decrease on the potential energy level.

Following the same path adopted in the previous section, potential energy (Figure B6.11) and velocity trend (Figure B6.12) obtained for this first configuration are represented below.

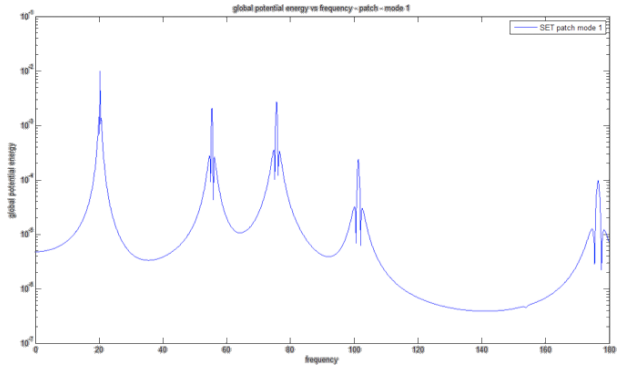

Figure B6.11 – Potential energy trend obtained for the first configuration of the coupled system.

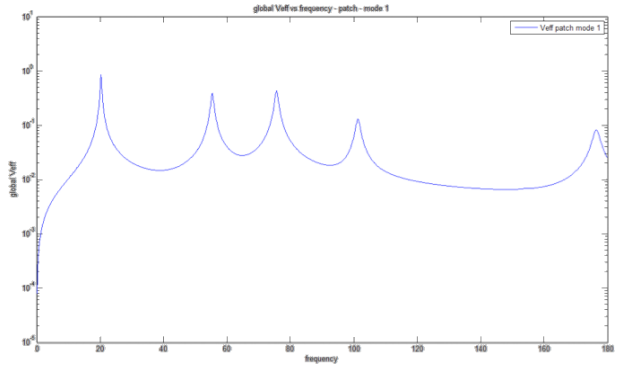

Figure B6.12 – Velocity trend obtained for the first configuration of the coupled system.

These results are obtained through the generation of numerical simulation in which the patches has been applied on the MAX potential energy density areas (see Figure B3.1.b, *Section B3.2*). The application of the patches, characterized by the same mechanical properties and the same global volume, on the areas of MIN potential energy density will lead as in the plate case, to a reduction of the potential energy amplitude level but with less impact that caused by positioning the patches in the areas of MAX potential energy density. Then for this second component, this point will be omitted.

B6.3.3 Second patch configuration

In this third section the study of the second patch configuration will be introduced. For this second configuration, it is the evaluation of the potential energy assessed at the second natural frequency of the bracket that defines and direct the location of the patches. This, in turns, will lead to an amplitude vibration reduction with an impact different by that obtained in the previous case.

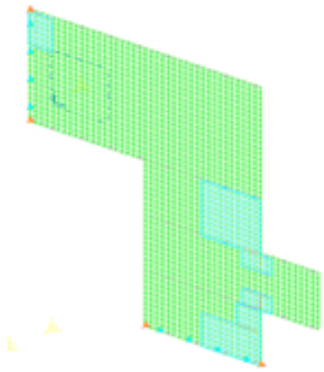

Figure B6.13 – Coupled system configuration for the study of the second natural frequency of the bracket.

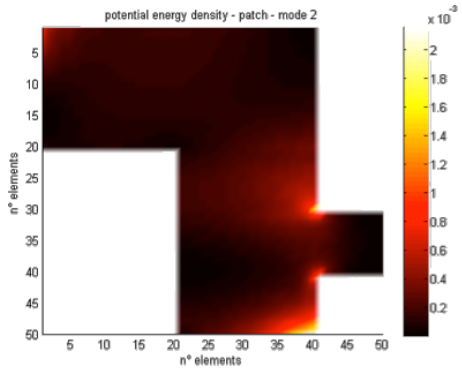

Figure B6.14 – Potential energy density map for the second natural frequency study (54.390 Hz) applying the patches.

The position of the patches and their size is defined by the graphical representations provided by Figure B6.5.b referred to the base bracket study (see *Section B6.3.1*). Figure B6.13 shows

the bracket fem model (green mesh) including the patches (blue mesh) realized in I-DEAS environment.

Figure B6.14 shows the potential energy intensity map obtained by the application of the patches on the surface of the bracket. From a quick comparison between the Figure B6.5.b and Figure B6.14, can be clearly noted that the areas corresponding to the highest potential energy density areas has been reduced and therefore has been also reduced the amplitude levels of potential energy density (see the scale value on the right side of the intensity maps). Following the same path adopted in the previous section, the potential energy trend (Figure B6.15) and the velocity trend (Figure B6.16) obtained for this second configuration are presented below.

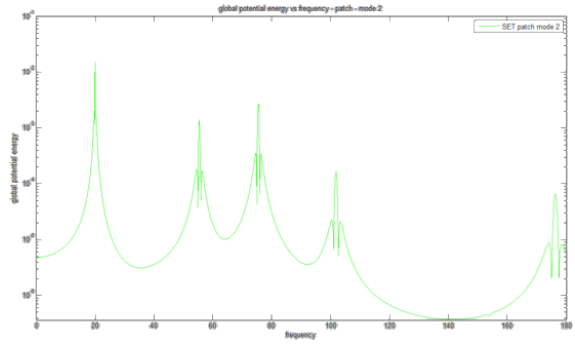

Figure B6.15 – Potential energy trend obtained for the second configuration of the coupled system.

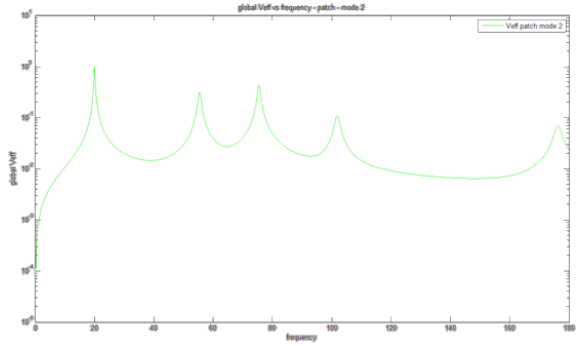

Figure B6.16 – Velocity trend obtained for the second configuration of the coupled system.

B6.3.4 Third patch configuration

In this fourth section will be introduced the study of the third patch configuration. For this third configuration, it is the evaluation of the potential energy assessed at the third natural frequency of the bracket that defines and direct the location of the patches. This, in turns, will lead to an amplitude vibration reduction with an impact different by that obtained in the previous cases.

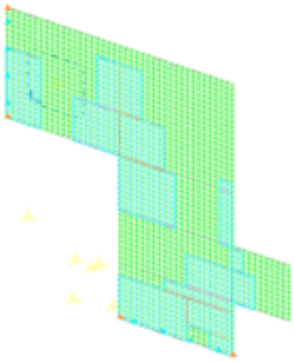

Figure B6.17 – Coupled system configuration for the study of the third natural frequency of the bracket.

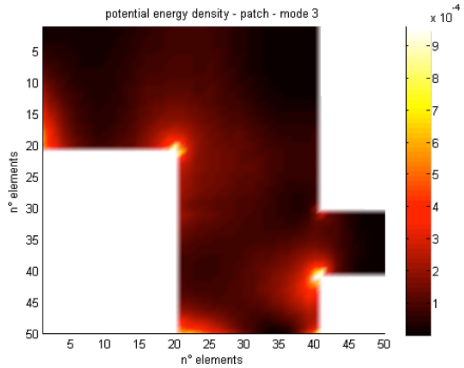

Figure B6.18 – Potential energy density map for the third natural frequency study (74.837 Hz) applying the patches.

The position of the patches and their size is defined by the graphical representations provided by Figure B6.5.c referred to the base bracket study (see *Section B6.3.1*). Figure B6.17 shows

the bracket fem model (green mesh) including the patches (blue mesh) realized in I-DEAS environment.

Figure B6.18 shows the potential energy intensity map obtained by the application of the patches on the surface of the bracket. From a quick comparison between Figure B6.5.c and Figure B6.18, can be clearly noted that the areas corresponding to the highest potential energy density areas has been reduced and therefore has been also reduced the amplitude levels of potential energy density (see the scale value on the right side of the intensity maps). Following the same path adopted in the previous section, the potential energy trend (Figure B6.19) and the normal velocity trend (Figure B6.20), obtained for this third configuration, are presented below.

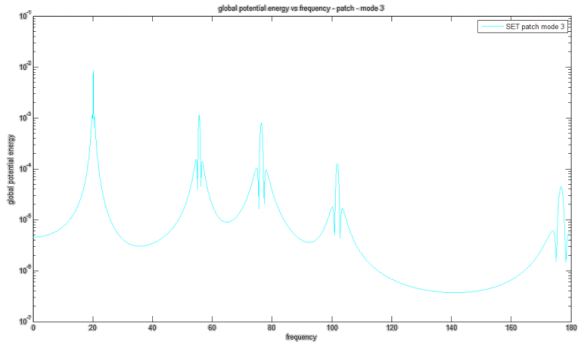

Figure B6.19 – Potential energy trend obtained for the third configuration of the coupled system.

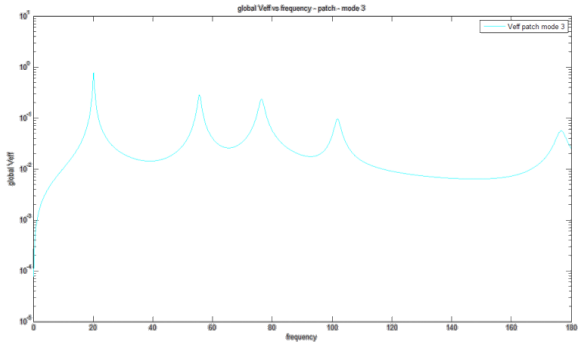

Figure B6.20 – Velocity trend obtained for the third configuration of the coupled system.

B6.3.5 Fourth patch configuration

In this fifth section will be introduced the study of the fourth patch configuration. For this fourth configuration, it is the evaluation of the potential energy assessed at the fourth natural frequency of the bracket that defines and direct the location of the patches. This, in turns, will lead to an amplitude vibration reduction with an impact different by that obtained in the previous cases.

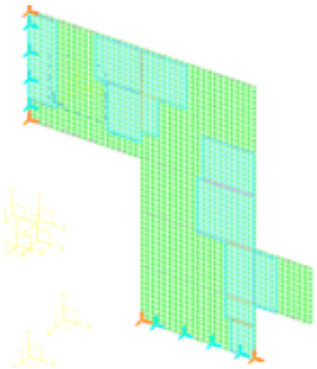

Figure B6.21 – Coupled system configuration for the study of the fourth natural frequency of the bracket.

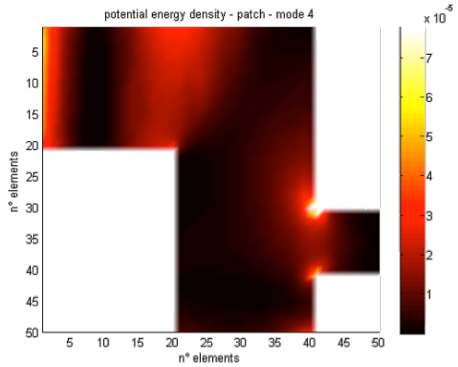

Figure B6.22 – Potential energy density map for the fourth natural frequency study (100.071 Hz) applying the patches.

The position of the patches and their size is defined by the graphical representations provided by Figure B6.5.d referred to the base plate study (see *Section B6.3.1*). Figure B6.21 shows the

bracket fem model (green mesh) including the patches (blue mesh) realized in I-DEAS environment.

Figure B6.22 shows the potential energy intensity map obtained by the application of the patches on the surface of the bracket. From a quick comparison between Figure B6.5.d and Figure B6.22, can be clearly noted that the areas corresponding to the highest potential energy density areas has been reduced and therefore has been also reduced the amplitude levels of potential energy density (see the scale value on the right side of the intensity maps). Following the same path adopted in the previous section, the potential energy trend (Figure B6.23) and the normal velocity trend (Figure B6.24), obtained for this fourth configuration, are presented below.

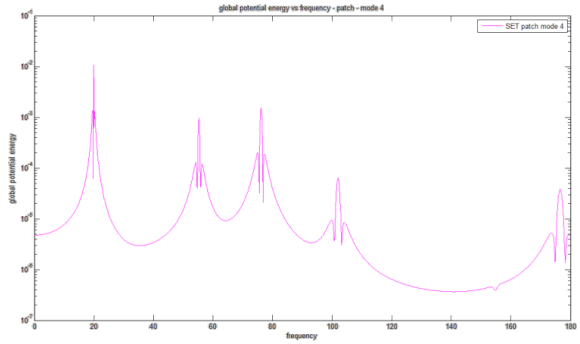

Figure B6.23 – Potential energy trend obtained for the fourth configuration of the coupled system.

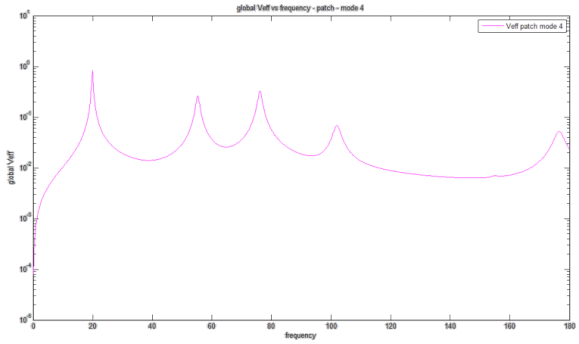

Figure B6.24 – Velocity trend obtained for the fourth configuration of the coupled system.

B6.3.6 Fifth patch configuration

In this sixth section will be introduced the study of the fifth patch configuration. For this fifth configuration, it is the evaluation of the potential energy assessed at the fifth natural frequency of the bracket that defines and direct the location of the patches. This, in turns, will lead to an amplitude vibration reduction with an impact different by that obtained in the previous cases.

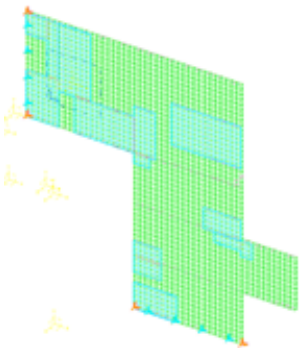

Figure B6.25 – Coupled system configuration for the study of the fifth natural frequency of the bracket.

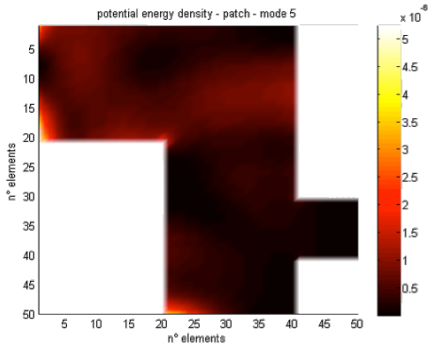

Figure B6.26 – Potential energy density map for the fifth natural frequency study (153.489 Hz) applying the patches.

The position of the patches and their size is defined by the graphical representations provided by Figure B6.5.e referred to the base bracket study (see *Section B6.3.1*). Figure B6.25 shows

the bracket fem model (green mesh) including the patches (blue mesh) realized in I-DEAS environment.

Figure B6.26 shows the potential energy intensity map obtained by the application of the patches on the surface of the bracket. From a quick comparison between Figure B6.5.e and Figure B6.26, can be clearly noted that the areas corresponding to the highest potential energy density areas has been reduced and therefore has been also reduced the amplitude levels of potential energy density (see the scale value on the right side of the intensity maps). Following the same path adopted in the previous section, the potential energy trend (Figure B6.27) and the normal velocity trend (Figure B6.28), obtained for this fifth configuration, are presented below.

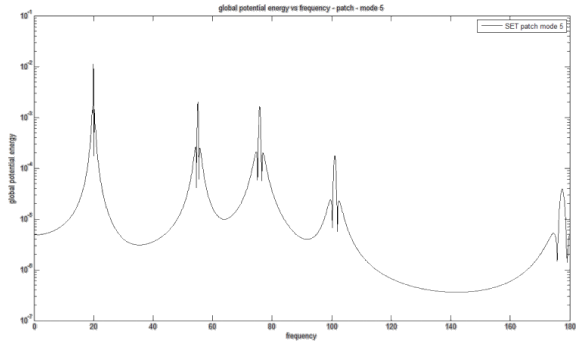

Figure B6.27 – Potential energy trend obtained for the fifth configuration of the coupled system.

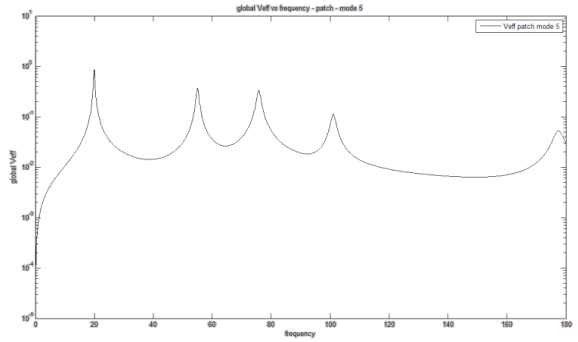

Figure B6.28 – Velocity trend obtained for the fifth configuration of the coupled system.

B6.3.7 Sixth patch configuration

In this seventh section will be introduced the study of the sixth patch configuration. For this sixth configuration, it is the evaluation of the potential energy assessed at the sixth natural frequency of the bracket that defines and direct the location of the patches. This, in turns, will lead to an amplitude vibration reduction with an impact different by that obtained in the previous cases.

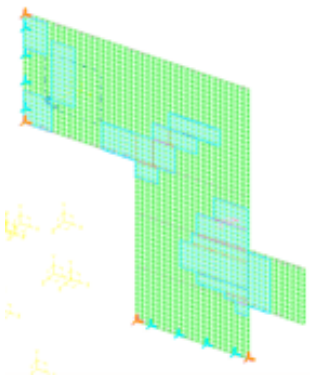

Figure B6.29 – Coupled system configuration for the study of the sixth natural frequency of the bracket.

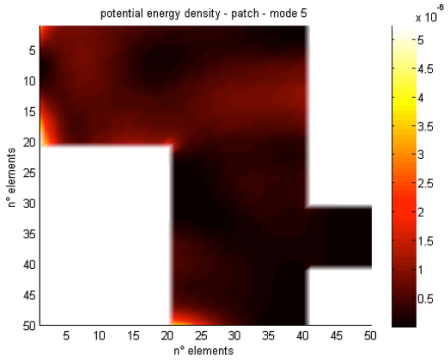

Figure B6.30 – Potential energy density map for the sixth natural frequency study (175.348 Hz) applying the patches.

The position of the patches and their size is defined by the graphical representations provided by Figure B6.5.f referred to the base bracket study (see *Section B6.3.1*). Figure B6.29 shows

the bracket fem model (green mesh) including the patches (blue mesh) realized in I-DEAS environment.

Figure B6.30 shows the potential energy intensity map obtained by the application of the patches on the surface of the bracket. From a quick comparison between Figure B6.5.f and Figure B6.30, can be clearly noted that the areas corresponding to the highest potential energy density areas has been reduced and therefore has been also reduced the amplitude levels of potential energy density (see the scale value on the right side of the intensity maps). Following the same path adopted in the previous section, the potential energy trend (Figure B6.31) and the normal velocity trend (Figure B6.32), obtained for this sixth configuration, are presented below.

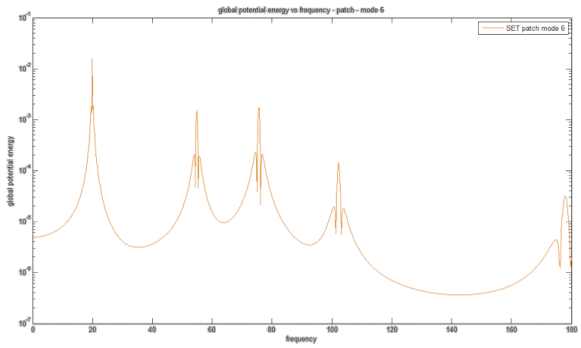

Figure B6.31 – Potential energy trend obtained for the sixth configuration of the coupled system.

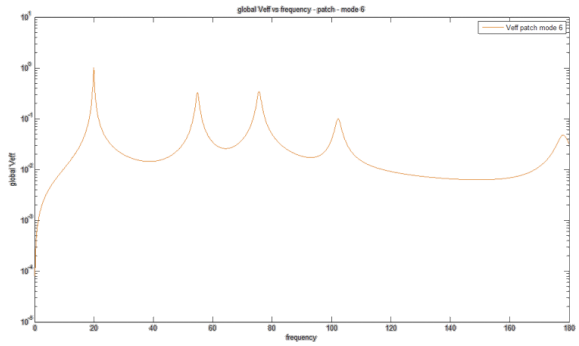

Figure B6.32 – Velocity trend obtained for the sixth configuration of the coupled system.

B6.4 Comparisons and conclusions

In this section will be judged and compared the results obtained through the study of the bracket component, then including all the configurations characterized by the introduction of the patches in order to improve the vibratory behaviour of the base component. In other words, in this section will be introduced the graphs in relation to the comparisons between the results coming from the seven different configurations, the first one on the base bracket and the latter six on the patch addition, in order to assess which of the above configurations can introduce the best contribution to the overall vibratory behaviour of the bracket component. In Figures B6.33 and B6.34 the comparisons between the potential energy and velocity values plotted for the entire frequency range and evaluated for the seven different configurations are shown. As for the plate study case, also for this case it is difficult to conduct a study, an assessment of the accuracy of the results obtained for these different numerical simulations simply relying on these two graphs. This problem is overcome by a series of expedient and calculations maid in Matlab environment that, taking as input all the velocity values just presented and graphed in Figure B6.34, will provide a new visualization form of these velocity results much more directly and easily than that just given.

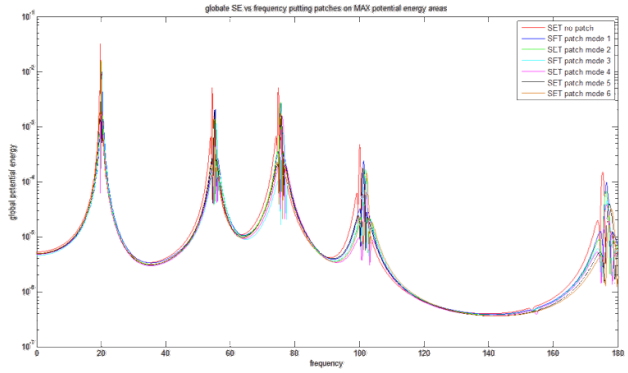

Figure B6.33 – Comparisons between the potential energy trends obtained for the seven different configurations.

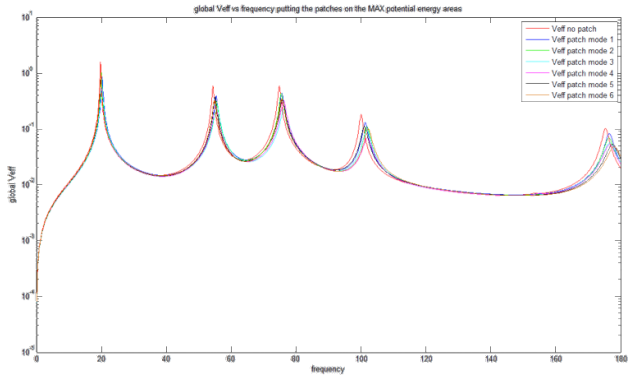

Figure B6.34 – Comparisons between the velocity trends obtained for the seven different configurations.

The velocity values obtained and visualized are now processed in Matlab environment, which according to the equations (B5.3.a) and (B5.3.b) will provide a series of velocity values that will be used to address the assessment of the component improvement in terms of vibration amplitude reduction through a much simpler and direct way. The effective velocity values thus obtained for this component are presented in Table B6.3 for all the configurations studied, including the base configuration. The table, and thus the velocity values, will be subdivided into two parts relating to which of the previously equations will be used for perform this study case, or more specifically, in relation to the kind of effective velocity that is evaluated (OVERALL or LOCAL).

Simply giving a look of the values listed in Table B6.3, it is easy to comprehend that obviously the highest effective velocity values for all its assessment cases is referred to the base configuration. The patch application for all the six different configurations lead to a reduction of the velocity values compared to the case without patches, defining as the best configuration, that which locate the patches depending by the study of the vibratory behaviour of the bracket at its third natural frequency (velocity values highlighted in red). Although the OVERALL velocity value is the lowest for the third case, it does not mean

that all its velocity values calculated for the different frequency band (LOCAL values) are for each case the lowest compared to that of the other configurations.

	OVERALL	**LOCAL**					
Configuration number	Entire band	Band 1	Band 2	Band 3	Band 4	Band 5	Band 6
Base	1.2652	0.9025	0.5452	0.6365	0.2350	0.0456	0.1631
First (max)	0.9975	0.6624	0.4480	0.5409	0.2011	0.0452	0.1427
Second (max)	1.0005	0.7094	0.3977	0.5360	0.1854	0.0441	0.1270
Third (max)	0.8506	0.6221	0.3794	0.3834	0.1748	0.0441	0.1145
Fourth (max)	0.8843	0.6360	0.3579	0.4633	0.1454	0.0437	0.1182
Fifth (max)	0.9455	0.6601	0.4286	0.4747	0.1894	0.0445	0.1170
Sixth (max)	0.9682	0.7114	0.4021	0.4754	0.1799	0.0436	0.1179

Table B6.3 – GLOBAL and LOCAL effective velocity values for the seventh bracket configurations studied.

Indeed, as shown on the “right side” of the table, only three

of the six local velocity values for the third configuration are the lowest. In other words, the third configuration produces the highest reduction of the velocity values for the 50% of the cases, and the fourth case leads to the remaining 50% reduction of the velocity values. Independently by the amplitude of the LOCAL effective velocity values for all the frequency band, that however are very close to each other (third and fourth case), the third configuration is the best one (see the difference in the amplitude values for all the configurations relating to the overall velocity evaluation).

It is important to note that all the values listed in Table B6.3 are related to numerical simulations carried out by applying the patches only on the areas of greatest potential energy density (MAX). This is due to the knowledge of the results already obtained in the previous work, which showed that the application of the patches in the areas of MIN potential energy density leads to a reduction of potential energy levels but not of the same amplitude that instead is produced by applying the patches in the MAX potential energy areas. Anyway, in order to increase the reliability of the methodology generated, in the following the results obtained studying the best configuration (the third bracket configuration) applying the patches on the MIN potential energy areas will be presented. The position of the patches and their size are defined by the graphical representations provided by Figure B6.5.c referred to the base bracket (see *Section B6.3.1*) in addition to that of the third configuration already presented in *Section B6.3.4* (see Figure B6.18). Figure B6.35 shows the bracket fem model with the patches applied on its MIN potential energy areas. Figure B6.36 shows the potential energy density map obtained for this new case. From a quick comparison between the potential energy density map related to the patch applied on the MAX (Figure B6.18) and MIN (Figure B6.36) areas of the bracket surface, can be clearly seen as the potential energy amplitude values for the latter case are reduced compared to the base configuration (Figure B6.5.e), while increased compared to the

MAX configuration case. This in turns is in accordance with what introduced in *Chapter B4* and demonstrated in the previous chapter.

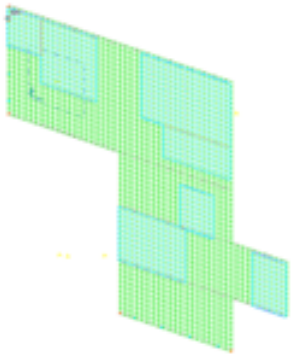

Figure B6.35 – Coupled system fem model applying the patches on the MIN potential energy areas.

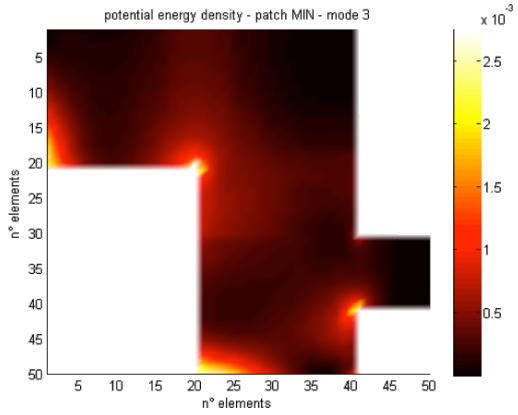

Figure B6.36 – Potential energy density map for the third natural frequency study applying the patches on the MIN areas.

Table B6.4 lists all the effective velocity values achieved by the considerations presented in this section, showing only the comparisons between the results obtained for the third configuration (MAX and MIN cases). Again, the best value is achieved by the case of patch application on the MAX potential energy density areas. In the case of patch application on the MIN

potential energy density areas any effective velocity values produce on the bracket a lower reduction compared to the MAX case.

Configuration number	OVERALL Entire band	LOCAL Band 1	Band 2	Band 3	Band 4	Band 5	Band 6
Third (MAX)	0.8506	0.6221	0.3794	0.3834	0.1748	0.0441	0.1145
Third (MIN)	0.9530	0.6485	0.4029	0.5312	0.1751	0.0448	0.1161

Table B6.4 – GLOBAL and LOCAL effective velocity values for the third bracket configuration.

In order to better comprehend the importance of these results and thus the correctness of the path followed in the study, the percentage values of the effective velocity reduction for the six different configurations of the bracket in comparisons to the base case are listed in Table B6.5. For example, taking into account the second configuration, it can be noted that the application of the patches on the surface of the bracket studying its vibratory behaviour at its second natural frequency leads to a reduction of the overall velocity value equal to the 20.9% compared to the case without any patch applied on it. This means that the application of the patches on the base structure causes the velocity reduction, i.e. improvement of the vibratory behaviour, compared to the basic case. Obviously, each patches configuration will affect the vibratory behaviour of the component generating different amplitude vibration levels reduction. In red the best reduction percentage value determined on the entire frequency range (the

entire band) is highlighted whereas, in green the highest reduction percentage value determined for each frequency band are listed.

	OVERALL	**LOCAL**					
Configuration number	Entire band	Band 1	Band 2	Band 3	Band 4	Band 5	Band 6
First	21.2	26.6	17.8	15.0	14.4	0.9	12.5
Second	20.9	21.4	27.1	15.8	21.1	3.3	22.1
Third (MAX)	32.8	31.1	30.4	39.8	25.6	3.3	29.8
Fourth	30.1	29.5	34.4	27.2	38.1	4.2	27.5
Fifth	25.3	26.9	21.4	25.4	19.4	2.4	28.3
Sixth	23.5	21.2	26.2	25.3	23.4	4.4	27.7
Third (MIN)	24.7	28.1	26.1	16.5	25.5	1.8	28.8

Table B6.5 – Percentage velocity reduction for the six configurations compared to the base plate.

Observing Table B6.5, it is possible to see that all the configurations lead to a reduction of the amplitude vibrations levels of the base component, i.e. only the bracket. Obviously, certain configurations produce higher reduction levels compared to the other. The best one is defined by the third configuration that produces the highest velocity reduction, i.e. reduction of about 33% of the vibration amplitude level of the bracket. Differently from the plate case, no patch application produces an increase in the LOCAL velocity values compared to the base case and therefore an increase in the vibration amplitude (see value highlighted in blue in Table B5.6 of the previous chapter).

Although all the percentage values listed in the fifth band column are positive, thus leading to an amplitude vibration reduction compared to the base case, the values remain still close to the limit (0% equal to no improvement); in fact the values defining the percentage of vibratory improvement of the structure (the bracket) are about the 3% for this particular frequency band. Despite this, all the percentage values listed in the other frequency bands column are very high, and also higher compared to the plate case. Obviously, a comparison between the results obtained by the two models (plate and bracket) cannot be made; whatever, there is the opportunity to note that the best results come from the more complex component (the bracket), thus increasing the reliability of the methodology created and the hope of the usefulness of this approach to component of much more complex geometry and constraining conditions. In fact, in this case is produced a velocity reduction of about 33% instead of the 25% for the plate case. This implies that the application of the patches on the surface of the unrefined component is done in an appropriately and intelligent manner. Still looking the values listed in Table B6.5, it is possible to see that all the percentage related to the application of the patches on MIN potential energy areas are lower compared to that obtained through the application of the patches on MAX potential energy areas. This last point confirms all the considerations and evaluations previously exposed, consciously bringing to light the certainty of a reliable and repeatable methodology.

Figure B6.37 shows a column chart that attempts to compare the effective velocity reduction percentage of the base case (red column) with those obtained for the better case that is represented by the third configuration (blue column). The figure can clearly and quickly represent the improvement of the structure from the vibratory point of view caused by the application of the patches on the surface of the bracket component. In this figure, as in the tables above, on the abscissa exes are listed the frequency range on which the effective velocity

evaluations are made. The number "1" corresponds to the OVERALL effective velocity study case, while the numbers from "2" to "7" obviously represents the six frequency bands that corresponds to the LOCAL effective velocity study case. Simply looking the column chart in Figure B6.37 it is easy to understand that the difference between the columns obtained for the two different configurations (blue and red) represents the amount in percentage of the effective velocity reduction achieved through the bright application of the patches on the surface of the bracket; thus giving an idea of the amount of the vibratory improvement of the bracket component. Obviously, the difference between these peak velocity values will give exactly the same values of that listed in the third row of Table B6.5.

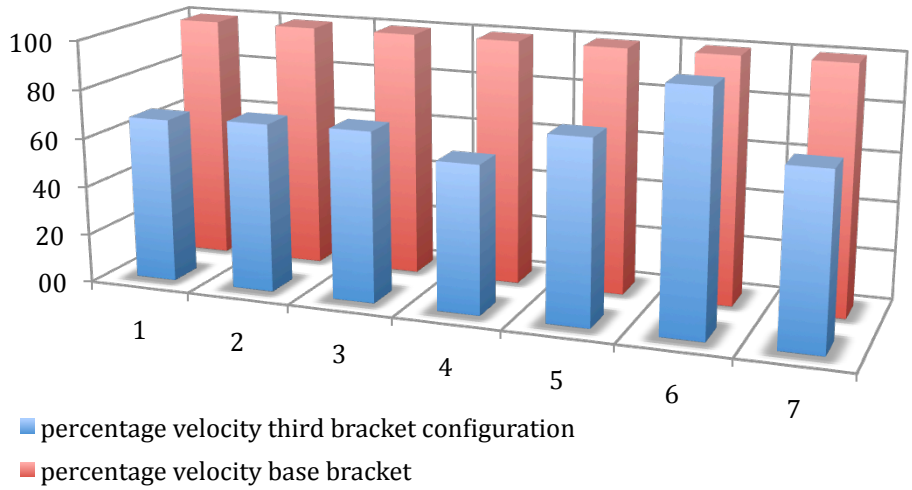

Figure B6.37 – Percentage velocity reduction for the third configuration (blue column) compared to the base bracket (red column).

All the considerations made throughout the work explanation and all the results obtained using the methodology created leads to the following considerations:

- Generally, also for this second case that is characterized by different boundary conditions and more complex geometries compared to the plate case, the study leads to the creation of a methodology that overcomes all the problems that may arise during the creation of the coupled system and during the implementation of the analysis that has to be carried out. Besides, using these steps, it is possible and feasible to quickly and correctly see all the results that have been calculated through the accurate numerical simulations allowing defining for which conditions is provided the best component behaviour in terms of amplitude vibration reduction.
- Specifically, in relation to the bracket study performed in this chapter, can be concluded that the application of the high damping material for the study of the third natural frequency of the bracket leads to the best configuration. In fact this configuration produce the best velocity results which are labeled in a clear and unambiguous as the best candidate to reduce the velocity values of the bracket component and consequently to improve its overall vibratory behaviour by reducing its overall amplitude vibration level. In other words, through this third configuration the amplitude vibration level of the bracket component has been reduced by about the 33%, sign of a significant contribution in the improvement of the vibratory behaviour of the mechanical component.

PART C

Conclusions

The first part (*PART A*) of this thesis addressed the development of a hybrid FE/LP model for the dynamic analysis of gear pumps with automotive applications. The FE model regards the external parts of the pump (case and end plates) while the LP model regards the interior parts (bushes and gears). Specifically, the lumped-parameter part of the model aimed at obtaining figures for gear acceleration and the forces acting between the

moving parts and the case, while the FE part estimated the external case accelerations using the results from the LP part; both the models were experimentally assessed. In particular, the non-linear lumped-parameter model (*Chapter A2*) took into account pressure distribution variability on gears, hydrodynamic bearing behaviour, parametric excitations due to time-varying meshing stiffness and tooth profile errors, backlash effects between meshing teeth, and the possibility of tooth contact on both lines of action. This non-linear model included all these important dynamic effects in order to consider and analyse their interactions. The motion equations were numerically integrated, using Simulink software. In order to reduce integration time, the average positions of the journal axes in the bearings were previously estimated. For this calculation, the periodically variable model parameters were set to constant values – which are equal to their mean values – and the stationary axis positions were computed as the solution of a non-linear system of algebraic equations. Thus, the variable pressure forces on the gears were approximately estimated from this average axis positions, before starting numerical integration, obtaining an important reduction in integration time. Subsequently, experimental apparatus (*Chapter A3*) were set up to measure the accelerations and force components applied to the pump case in operational conditions. The validation procedure was based on a comparison between simulation and experimental results concerning forces and moments: it dealt with the external and inertia components acting on the gears, which were estimated using the model, and the reactions and inertia components on the test plate and case, which were obtained by measurements. These components could excite case vibrations and produce noise; consequently, such estimates have a practical application in noise reduction. The validation of the results in the frequency domain was carried out by comparing the resonances region, as exhibited by the experimental waterfall maps, with the natural frequency of the linearised model and the simulation waterfall maps. The initial

natural frequencies of the linearised model were found in the experimental maps, while the correspondence between the experimental and simulation maps was quite good. Considering the validation results overall, the correspondence between simulations and tests could be considered satisfactory overall, taking into account the complexity of a model which included several non-linear dynamic phenomena.

Subsequently, (*Chapter A4*) a hybrid FE/LP model of the gear pump was built with the aim of evaluating the acceleration on the exterior part of the gear pump (the external surface of the case, flange and cover) during operational conditions. In this dynamic analysis the damping was estimated using data from an experimental modal analysis (EMA) while the excitation forces, acting on the internal surface of the case due to bearing reactions and pressure forces, were obtained from the LP model. In particular, FRFs (accelerations divided by the forces) obtained using the FE model were multiplied by the spectra of the dynamic forces on the case, as calculated by the LP model described in *Chapter A2*, in order to evaluate case acceleration. In this sense, the model is globally a hybrid LP/FE model. The combined FE/LP model was validated by comparing the experimental accelerations measured during a run-up test with the simulated accelerations estimated using the model. The validation results showed that the hybrid model was able to foresee system resonances and estimate the accelerations amplitude on the external surfaces of the pump as a function of working conditions. It should be noted that this validation not only assesses its effectiveness but could also be considered a global validation procedure for the FE/LP model, since the exciting dynamic forces in the combined model are evaluated in the LP part of the model. In addition, the assessed hybrid FE/LP model could be used for the estimation of pump dynamic behaviour in the presence of design modifications, such as the evaluation of the external case accelerations in case of design modification such as length of the relief grooves milled into the bush. Due to these considerations, other design modification

could be taken into account and thus assessed by the hybrid model. Vibration evaluations of external surfaces are very important for manufacturing industry and customers since these vibrations produce noise directly and transfer vibrations to neighbouring structures (e.g. the car chassis).

Furthermore, the FE model overcomes the difficulties relating to component connections in creating an assembled FE model to simulate and model real contact between adjacent surfaces in different components and to prevent their penetration. In addition, relating to appropriate considerations and using advanced techniques the hard problem concerning the coupling stage of the FE model with the LP model is also overcome.

The main original contribution regarding this first part of the thesis concerns the development of a non-linear model for a gear pump integrating formulations on pressure distribution, hydrodynamic bearing forces and meshing stiffness; in particular, the innovative inclusion of all these important dynamic effects in one model, in order to take their interactions into account. This could be important in order to (i) foresee the actual dynamic behaviour (real position of the gears, separations or impacts between meshing teeth, etc.), (ii) foresee the influence of working conditions and design modifications on vibration and noise generation and (iii) optimise the design of the mechanism as a function of its dynamics. In addition, it is worth noting that the main operational problem in gear pumps is generally their high level of vibration and noise. As a consequence, the development of an FE/LP model for estimating the case vibration due to the dynamic behaviour of the pump rotating components is important. Thus, the model could be a very useful tool in prototype design and in design optimisation in order to identify the origin of unwanted dynamic effects.

Although the use of this hybrid model is an excellent tool for improving the dynamic behaviour of gear pumps and for optimising the early stages of prototype design, some problems could still remain related to unwanted vibrations in precise

ranges of frequency or physical problems due to design constraints that cannot be bypassed. In other words, it is possible that the optimisation stage of the project in terms of its modelling cannot be arrived at, both due to the time that is needed for redesign and further implementation and due to costs; issues that industry rarely wants to take on board. This problem is considered in the second part of this thesis (*PART B*) which addresses the optimisation of mechanical components and systems via the application of high damping material components known as patches; thus allowing the reduction of vibration amplitude at precise frequency ranges without the need to redesign the component. Patch damping design is an efficient and cost effective concept for solving noise and vibration problems.

In particular, a new methodology providing for surface damping treatment was created and adopted. Such treatment could be applied to existing structures and provides high damping capability over wide temperature and frequency ranges. Due to the fact that in many practical plate and machinery casing structures, such as the gear pump described in *PART A*, it is difficult to treat the whole surface with constrained layer viscoelastic material, because of there being small or inaccessible parts, this second part addresses partial coverage treatment in an effective and efficient manner. Indeed, it may be desirable to selectively apply one or more damping patches to control certain resonances.

As a result, the work described in *PART B* attempts to define a new methodology, based on a purely energetic approach, to reduce unwanted vibration levels in mechanical components via the appropriate application of elements characterised by a high damping properties. In fact, formulations related to an energetic approach which enable energy flow to be estimated within a structure could be used for improving numerical vibration analysis by identifying “hot spots” within an elastic structure which, if locally damped, could be best suited to global vibration reduction. This kind of aim can be reached by estimating

potential energy distribution within a structure. It is worth noting that, while various techniques have been developed on the topic of energy flow, energy estimation in structures has been fairly neglected. In particular, an evaluation of potential energy has never been considered an issue. This research aims at being a step towards the goal of determining damping placement on a structure in order to ensure noise reduction and therefore, to improve structural vibrational behaviour. All the informations introduced in PART B shown how potential energy distribution estimation can clearly define the placing of constrained layer damping patches onto a structure in order to reduce its amplitude vibration level. All the considerations and results are based on numerical data obtained by evaluating potential energy distribution and normal velocity trend on a steel plate (see *Chapter B5*) and a steel bracket (see *Chapter B6*), characterised by different loading and boundary conditions. Through the numerical simulations performed on both these components, the potential energy trend and the potential energy distribution regarding the study of the component at a single natural frequency and on the entire frequency range, respectively, will be evaluated. The first was essential in order to precisely define the location of the patches, while the second was used to identify which patches arrangement produced the highest improvement (the highest amplitude vibration reduction level). In reality, this latter task was entrusted by the velocity estimation, obviously assessed on the entire frequency range. In essence, the results concerning the estimation of potential energy values in addition to those concerning the velocity values, both relating to the entire frequency range, are useful to clearly define the impact that each patch arrangement has on the overall amplitude vibration reduction of the component studied.

The numerical simulations carried out in *Chapter B4* provide important information about all the problems and mistakes to be avoided when drawing up an FE model, applying patches, and elaborating results, thus providing a foundation for obtaining

results with high accuracy and reliability. Moreover, this chapter assesses a methodology for reducing the locally acting amplitude vibration level. In other words, two different vitally important aspects for the proper development of this study were correctly addressed using the numerical simulations presented in *Chapter B4*. These crucial points are, as follows, the potential energy evaluation and the definition of how to apply the patches to the surface of the component. In essence, the methodology created was approved and validated by the results obtained in *Chapter B4* and by the result comparisons and considerations that were carried out for the plate and bracket study cases in *Chapter B5* and *Chapter B6*, respectively. In other words, the following questions found precise answers: can we be fully confident that the potential energy evaluation procedure is correct? Can we be fully confident that the simulations performed provide "true" potential energy values for the component? In the light of the fact that we are working on an FE model and not with experimental tests, can we be sure that the patches were applied to the surface of the host structure properly? Can we be sure that the base component is altered/affected by the presence of the patches on it and that the latter are not only resting on its surface?

Generally, the study led to the creation of a methodology to overcome all the problems which may arise during the creation of a coupled system and during any analytical implementation. Furthermore, it is possible and feasible to quickly and correctly display all the results calculated by accurate numerical simulations, allowing the definition of which conditions provide the best component behaviour in terms of amplitude vibration reduction. In other words, through the knowledge of the velocity values for each patch configuration (arrangement), the OVERALL and LOCAL effective velocity values, respectively, was evaluated. The first gives information about the amplitude vibration reduction level arising by each patch configuration studying the component in its entire frequency range, while the second providing the same kind of information but relating to each

frequency band comprised into the entire frequency range of the component studied. Through this expedient the velocity trend will be replaced by a series of values which will be used to address the assessment of the component amplitude vibration reduction through a much simpler and direct way. In addition, through this procedure is also simple to direct the study in order to reduce only a precise frequency of the component, which in practice is often required.

Specifically, in relation to the plate study performed in *Chapter B5*, it could be concluded that the application of the damping material in relation to the study of the component behaviour at its fifth natural frequency led to the best configuration. In fact, this configuration produced the lowest velocity results, which are clearly and unambiguously labelled as the best candidates in reducing the velocity values of the plate component and consequently, in improving its overall vibratory behaviour, by reducing its overall amplitude vibration level. In other words, using this fifth configuration (this particular patch arrangement), the amplitude vibration level of the plate component was reduced by about the 25% providing a significant contribution to the improvement of the mechanical component vibratory behaviour. In relation to the bracket study, performed in *Chapter B6*, it could be concluded that the application of the damping material, relating to the study of the component behaviour at its third natural frequency (particular patch arrangement), led to the best configuration. As found for the plate component, improvements in its vibratory behaviour were produced. Indeed, in this second case, the third configuration reduced the amplitude vibration level of the bracket component by about 33%, providing a significant contribution to the improvement in mechanical components vibratory behaviour.

Obviously, a comparison between the results obtained by the two models (plate and bracket) cannot be made; whatever, there is the opportunity to note that the best results come from the more complex component (the bracket), thus increasing the

reliability of the methodology created and the hope of the usefulness of this approach to component of much more complex geometry and constraining. Indeed, knowing the quality of the results generated by numerical simulations carried out on these two different components, this methodology gives hope to properly work to components of more complex forms and characterised by different boundary conditions while maintaining the same values of reliability and accuracy.

The main original contribution in this second part of the thesis concerns the development of a methodology which makes it possible to address mechanical system modelling in terms of energy distribution within a structure. The explicit formulations referred to the energy-based approach, that shows a clear correlation between the input power to a structure, its potential energy and its loss factor (that is unknown), can guide the identification of the positions on a generic mechanical structure which, if locally damped, can be best suited to vibration reduction in the entire frequency range. This kind of target can be reached by estimating potential energy distribution within a structure. The knowledge of potential energy, in addition to the knowledge of the input power to a structure could lead to the loss factor determination; unknown value of considerable importance in the study of vibrations of any mechanical component. Although this aspect is not dealt in this thesis, will provide suggestions for future studies.

Summarizing, advanced methodologies were developed to reduce vibrational amplitude in components such as plates and brackets by applying patches by using potential energy evaluations. The methodology allowed the reduction of vibrational amplitude, referring both to a single component or a complex system. This methodology made it possible to improve component vibratory behaviour in certain frequency ranges, contemporarily reducing dangerous resonance effects, while acting on the location, extent and quantity of the patches to be applied on the base component surface.

REFERENCES

The thesis has relied on many publications, directly and indirectly, in its evolution and development. During the writing of this work I have tried to provide a wealth of knowledge regarding my doctoral studies. Although it is not possible or useful to list all such material, some selected publications are listed below.

PART A

[1] R. Dearne; *The fine art of gear pump selection and operation*, World pumps, 38-40, June 2001.

[2] MSC, *MSC.Nastran*, Version 2006, (2006).

[3] The Mathworks, Matlab, Version 6.1, Release 12.1, May (2001).

[4] H. N. Ozguven, D. R. Houser; *Mathematical Models Used in Gear Dynamics* – A review, Journal of Sound and Vibration 121(3), 383-411, (1988).

[5] J. D. Smith, M. Dekker; *Gear noise and vibration*, Marcel, Inc. (1999).

[6] H. N. Ozguven, D. R. Houser; *Dynamic analysis of high speed gears by using loaded static transmission error*, Journal of Sound and Vibration, 125(1), 71-83, (1988).

[7] G. Dalpiaz, A. Rivola, R. Rubini; *Dynamic modelling of gear systems for condition monitoring and diagnostics*, Congress on Technical Diagnostics, Proceedings of the Congress of Technical Diagnostics, Gdansk, Poland, 185-192, (1996).

[8] M. Amabili, A. Rivola; *Dynamic analysis of spur gear pairs: steady-state response and stability of the sdof model with time-varying meshing damping*, Mechanical Systems and Signal Processing 11 (3), 375-390.

[9] M. Amabili, A. Fregolent; *A method to identify modal parameters and gear errors by vibrations of a spur gear pair*, Journal of Sound and Vibration, 214(2), 1998, 339-357.

[10] O. S. Sener, H. N. Ozguven; *Dynamic analysis of geared shaft systems by using a continuous system model*, Journal of Sound and Vibration, 166 (3), 539-556, (1993).

[11] G. Dalpiaz, A. Rivola, R. Rubini; *A Kineto-elastodynamic model of a gear testing machine*, International Conference on Mechanical Transmissions and Mechanisms (MTM '97). 1-4/7/1997. (pp. 549-553). Tianjin (China).

[12] H. N. Ozguven, D. R. Houser, J. Zakrajsek; *Dynamic analysis of geared rotors by finite elements*, Journal of Sound and Vibration.

[13] S. H. Choi, J. Glienicke, D. C. Han, K. Urlichs; *Dynamic gear loads due to coupled lateral, torsional and axial vibrations in a helical geared system*, Journal of Vibration and Acoustics, Vol 121/141, ASME, April 1999.

[14] R. Li Yang, T. Lin, X. Chen, L. Wang; *Finite element simulation of the dynamic behavior of a speed-increase gearbox*, Journal of materials processing technology 150, 170-174, (2004).

[15] H-H. Lin, R. L. Huston, J. J. Coy; *On dynamic loads in parallel shaft transmissions*: *Part I- Modeling and Analysis*, Journal of Mechanisms, Transmissions, and Automation in Design, Vol 110/221, June 1988.

[16] H-H. Lin, R. L. Huston, J. J. Coy; *On dynamic loads in parallel shaft transmissions: Part II- Parameter study*, Journal of Mechanisms, Transmissions, and Automation in Design, Vol 110/226, June 1988.

[17] J. H. Kuang, Y. T. Yang; *An estimate of mesh stiffness and load sharing ration of a spur gear pair*, International Power Transmission and Gearing Conference, Vol 1, DE-vol 43-1, ASME, (1992).

[18] J. H. Kuang, A. D. Lin; *The effect of tooth wear on the vibration spectrum of a spur gear pair*, Proceedings of DETC99, Design Engineering Technical Conference, September 12-15, ASME, (1999).

[19] R. Muthukumar, M. R. Raghavan; *Estimation of gear tooth deflection by the finite element method*, Mechanisms and Machinery Theory, Vol 22, N°2, 177-181, (1987).

[20] M. Velex, P. Maatar; *A mathematical model for analyzing the influence of shape deviations and mounting errors on gear dynamics behaviour*, Journal of Sound and Vibration, 191(5), 629-660.

[21] G. W. Blankenship, R. Singh; *A new gear mesh interface dynamic model to predict multi-dimensional force coupling and excitation*, Mechanisms and Machinery Theory, Vol 30 No 1, 1995, 43-57.

[22] K. Umezawa, T. Suzuki, T. Sato; *Vibration of power transmission helical gears (approximate equation of tooth stiffness)*, Bulletin of JSME, Vol. 29, N° 251, May 1986.

[23] F. K. Choy, Y. K. Tu, J. J. Zakrajsek, D. P. Townsend; *Effect of gear box vibration and mass imbalance on the dynamics of multistage gear transmission*, Journal of Vibration and Acoustics, Vol 113/333, July 1991.

[24] Y. Cai; *Simulation on the rotational vibration of helical*

gears in consideration of the tooth separation phenomenon (A new stiffness function of helical involute tooth pair), Transactions of the ASME, Vol. 177/460, Sep. 1995.

[25] S. Theodossiades, S. Natsiavas; *Non-linear dynamics of gear-pairs systems with periodic stiffness and backlash*, Journal of sound and vibration, 229(2), 287-310, (2000).

[26] C. Bonacini, M. Borghi; *Calcolo delle pressioni nei vani fra i denti di una macchina oleodinamica ad ingranaggi esterni,* Oleodinamica-pneumatica, (1991).

[27] A. Fernández del Rincón, G. Dalpiaz; *A model for the Elastodynamic Analysis of External Gear Pumps*, Proceedings of International Conference on Noise and Vibration Engineering (ISMA 2002), 2002 September 16-18, Leuven, Belgium, 1387-1396.

[28] G. Dalpiaz, A. Fernández del Rincón, M. E. Poppi; *Simulazione del comportamento dinamico di pompe ad ingranaggi per servosterzo,* Proceedings of XVI AIMETA Congress of Theoretical and applied Mechanics, 2003 September 9-12, Ferrara, Italy, 2003.

[29] G. Dalpiaz, A. Fernández del Rincón, E. Mucchi; *Modelling meshing phenomena in gear pumps*, Proceedings of International Conference on Noise and Vibration Engineering (ISMA 2004), 2004 September 16-18, Leuven, Belgium, 949-963.

[30] E. Mucchi, G. Dalpiaz, V. Venturi; *A hybrid LP/FE model for the dynamic analysis of external gear pumps*, Proceeding of the International Mechanical Engineering Congress & Exposition (IMECE 2007), November 11-16, 2007, Seattle, Washington, USA.

[31] A. Seireg; *Friction and lubrication in mechanical design*, Marcel Dekker, Inc., (1998).

[32] S. Theodossiades, S. Natsiavas; *On geared rotor dynamic systems with oil journal bearings,* Journal of Sound and Vibration, Vol. 243 No.4, Academic Press (2001), pp 721-745.

[33] D. Childs, H. Moes, H. Van Leeuwen; *Journal bearing impedance descriptions for rotordynamic application*, Transactions of the *ASME*, April (1977).

[34] E. Mucchi; *Dynamic analysis of external gear pumps by means of non linear models and experimental techniques*, Thesis for the degree of Doctor of Philosophy, Engineering Department in Ferrara, Ferrara, March 2007.

[35] G. Miccoli, P. Vagnoni; *Determinazione per via sperimentale dei carichi sul corpo di una pompa ad ingranaggi esterni*, Oleodinamica-pneumatica, 145-155, Novembre 1988.

[36] S. Mancò, N. Nervegna; *Pressure transient in an external gear hydraulic pump*, Fluid power, Edited by T. Maeda, (1993).

[37] CATIA V5 R14 On-line Help.

[38] LMS Virtual.Lab On-line Help Rev 6A; www.lmsvirtuallab.com.

PART B

[1] D. J. Ewins; *Modal Testing: Theory and practice*; Somerset: Research Studies Press (1984).

[2] W. Heylen, S. Lammens, P. Sas; *Modal Analysis Theory and Testing*; Katholieke Universiteit Leuven - Departement Werktuigkunde - Celestijnenlaa Heverlee (Belgium): 300B, B-3001.

[3] J. He; *Structural Modification*; Faculty of Engineering and Science, Victoria University of Technology, Footscray Park: 359, 187–204 (2001).

[4] A. Sestieri; *Structural Dynamic Modification*;

Dipartimento di Meccanica e Aeronautica, Università "La Sapienza", Rome, Italy; Sadhana, Vol. 25, Part 3, pp. 247-259 (2000).

[5] T. K. Kundra; *Structural Dynamic Modifications via Models*; Mechanical Engineering Dipartment, Indian Institute of Technology, New Delhi; Sadhana; Vol. 25, Part 3, pp. 26-276 (2000).

[6] A. D. Nashif, D. I. Jones, J. P. Henderson; *Vibration Damping*; A Wiley-Interscience publication (1984).

[7] B. C. Nakra; *Structural Dynamic Modification Using Additive Damping*; Mechanical Engineering Department, Indian Institute of Technology, New Delhi; Sadhana, Vol. 25, Part 3, pp. 277–289 (2000).

[8] A. Sestieri; *SDM applications to machine tools and engines*; Dipartimento di Meccanica e Aeronautica, Università "La Sapienza", Rome, Italy; Sadhana, Vol. 25, Part 3, pp. 305–317 (2000).

[9] F. Aryana, H. Bahai; *Sensitivity analysis and modification of structural dynamic characteristics using second order approximation*; Engineering Structures 25 (2003) 1279-1287.

[10] S. G. Braun, Y. M. Ram; *Modal modification of vibrating systems: some problems and their solutions*; Mechanical Systems and Signal Processing 15(1) (2001) 101-119.

[11] R. M. Lin, M. K. Lim; *Structural sensitivity analysis via reduced-order analytical model*; Comput. Methods Appl. Mech. Engrg. 121 (1995) 345-359.

[12] H. Bahai, K. Farahani, M. S. Djoudi; *Eigenvalue inverse formulation for optimising vibratory behaviour of truss and continuous structures*; Computers and Structures 80 (2002) 2397-2403.

[13] J. E. Mottershead, M. Ram Yitshak; *Inverse eigenvalue problems in vibration absorption: Passive modification and active control*; Mechanical Systems and Signal Processing 20

(2006) 5-44.

[14] Valder Steffen Jr; *Model-Based Inverse Problems in Structural Dynamics - Part II*; School of Mechanical Engineering, Universidade Federal de Uberlandia (Brazil); Pan American Advance Study Institute on Demage Prognosis (2003).

[15] L. Tao, H. Jimin; *Local structural modification using mass and stiffness changes*; Department of Mechanical Engineering, Victoria University of Technology, Melbourne (Australia); Engineering Structures 21 (1999) 1028-1037.

[16] T. Lauwagie, H. Sol, E. Dascotte; *Damage identification in beams using inverse methods*; Katholieke Universiteit Leuven, Department of Mechanical Engineering (PMA), Heverlee (Belgium); Celestijnenlaan 300b, 3001.

[17] E. Dascotte, J. Strobbe; *Identification of pressure forces in a cavity using an inverse solution method*; Dynamic Design Solutions (DDS), Leuven (Belgium); 23th International Seminar on Modal Analysis (ISMA) (1998).

[18] J. Eui-Il, P. Youn-Sik, K.C. Park; *Structural dynamics modification via reorientation of modification elements*; Finite Elements in Analysis and Design 42 (2005) 50-70.

[19] W. Baisheng, L. Zhengguang; *Approximate reanalysis for modifications of structural layout*; Engineering Structures 23 (2001) 1590-1596.

[20] W. D'Ambrogio, A. Sestieri; *Coupling theoretical data and translational FRFs to perform distributed structural modification*; Mechanical Systems and Signal Processing 15 (1) (2001) 157-172.

[21] S. Benfratello, G. Muscolino; *A perturbation approach for the response of dynamically modified structural systems*; Computers and Structure 68 (1998) 101-112.

[22] C.J. Hoff, M.M. Bernitsas, R.E. Sandstrm, W.J. Anderson; *Inverse perturbation method for structural redesign with frequency and mode shapes constraints*; AIAA J. 22 (9) (1984) 1304-1309.

[23] M.J. Smith, S.G. Hutton; *A perturbation method for inverse frequency modification of discrete, undamped systems*; J. Appl. Mech. 61 (7) (1994) 887-892.

[24] Lord Rayleigh; *Theory of sound*; 2nd edn. (1945) New York: Dover.

[25] J. T. Weissenburger; *Effects of local modification on the vibration characteristics of linear systems*; J. Appl. Mech. 35 (1968) 327-332.

[26] R. J. Pomazal, V. W. Snyder; *Local modifications of damped linear systems*; Am. Inst. Aeronaut. Astronaut. J. 9 (1971) 2216-2221.

[27] Y. M. Ram, J. J. Blech; *The dynamic behaviour of a vibratory system after modification*; J. Sound Vib. 1 (50) (1991) 357-370.

[28] B. P. Wang; *Structural dynamic optimisation using re-analysis techniques*; Int. J. Modal Analysis 2 (1987) 50-58.

[29] Y. G. Tsuei, E. K. L. Yee; *A method to modify dynamic properties of undamped mechanical systems*; Trans. ASME Dynamic Systems, Measurement and Control 111 (1987) 403-408.

[30] I. Bucher, S. Braun; *The structural modification inverse problem: an exact solution*; Mech. Syst. Signal Process. 7 (1993) 217-238.

[31] J. He, Y. Li; *Relocation of anti-resonances of a vibratory system by local structural changes*. Int. J. Anal yt. Experimental Modal Analysis 10 (1995) 224.

[32] J. P. Den Hartog; *Mechanical vibrations*; McGraw-Hill (1956).

[33] S. Timoshenko; *Vibration problems in engineering*; Van Nostrand (1995).

[34] J. B. Hunt; *Dynamic vibration absorbers*; London: Mechanical Engineering Publications (1979).

[35] J. E. Mottershead; *On the zeros of structural frequency response functions and their application to model assessment and updating*; In Proc. 16th Int. Modal Analysis Conf., Santa

Barbara, CA, USA, pp. (1998) 500-503.

[36] N. Maia, J. Silva, J. He, N. Lieven, R. Lin, G. Skingle, W. To, A. Urgueira; *Theoretical and experimental modal analysis*; ch. 6. Wiley (1997).

[37] J. F. Baldwin, S. G. Hutton; *Natural modes of modified structures*; AIAA J. 23 (1985) 1737-1743.

[38] V. W. Snyder; *Structural modification and modal analysis*; Exp. Tech. 9 (1985) 245-315.

[39] J. A. Brandon; *Strategies for structural dynamic modification*; New York: John Wiley (1990).

[40] S. S. Rao; *Optimum design of structures under shock and vibration environment*; Shock Vibr. Dig. 21 (7) (1989).

[41] A. Berman; *Determining structural parameters from dynamic testing*; Shock Vibr. Dig. 7 (1975) 10-17.

[42] H. G. Natke; *Identification of vibrating structures*; New York: Springer Verlag, Wein (1982).

[43] M. Imergun, W. J. Visser; *A review of model updating techniques*; Shock Vibr. Dig. 23 (1991) 9-20.

[44] T. Li, J. He; *Optimisation of dynamic characteristics of a MDOF system by mass and stiffness modification*; In Proc. 15th Int. Modal Analysis Conf., pp. (1997) 1270-1276.

[45] S. V. Modak, T. K. Kundra, B. C. Nakra; *Use of un updated finite element model for dynamic design*; Mechanical Systems and Signal Processing 16(2-3) (2002) 303-322.

[46] J. Brian Schwarz, H. Mark Richardson; *Structural Modifications Using Higher Order Elements*; Vibrant Technology, Inc. 18141 Main Street Jamestown, California 95327; 15th IMAC Conference (1997).

[47] B. P. Wang, C. M. Lu; *Topology optimization using MSC Nastran*; Department of Mechanical and Aerospace Engineering, University of Texas Arlington, Texas 76019.

[48] M. P. Bendsoe, O. Sigmund; *Topology optimization: Theory, Methods and Applications*; Springer, Berlin (2003).

[49] C. Barcelos; *CAD Based Optimization*; Director of Development, MacNeal-Schwendler Corporation.

[50] W. Clarence de Silva; *Vibration: Fundamentals and Practice*; CRC Press LLC, (2000) N. W. Corporate Blvd., Roca Raton, Florida 33431.

[51] L. Meirovitch; *Analytical methods in vibrations*; College of Engineering, Virginia Polytechnic Institute and State University, Macmillan Publishing Co., New York (1967), 67-15548.

[52] L. Cremer, M. Heckl, E. E. Ungar; *Structure-Borne Sound*; Springer, Berlin (1988).

[53] D. J. Nefske, S. H. Sung; *Power flow finite element analysis of dynamic systems: theory and application to beams*; Journal of Vibration, Acoustics, Stress and Reliability in Design 111 (1989) 94-100.

[54] J. C. Wohlever, R. J. Bernhard; *Mechanical energy flow models of rods and beams*; Journal of Sound and Vibration 153 (1992) 1-19.

[55] V. D. Belov, S. A. Rybak, B. D. Tartakovskii; *Propagation of vibrational energy in absorbing structures*; Physics Acoustics 23 (1977) 115-119.

[56] W. Maysenhölder; *Energy of Structure-Borne Sound*; S. Hirzel Verlag, Stuttgart (1994).

[57] B. A. Auld; *Acoustic Fields and Waves in Solids*; Second ed., Vol. 1, Krieger Publishing, Malabar (1990).

[58] K. S. Alfredsson; *Active and reactive structural energy flow*; Journal of Vibration and Acoustics 119 (1997) 70-79.

[59] G. Pavic; *The role of damping on energy and power in vibrating systems*; Journal of Sound and Vibration 281 (2005) 45-71.

[60] R. H. Lyon, R. G. de Jong; *Theory and Application of Statistical Energy analysis*; Second ed., Butterworth-Heinemann, Boston (1995).

[61] R. S. Langley; *A general derivation of the statistical energy analysis equations for coupled dynamic systems*; Journal of Sound and Vibration 135 (1989) 499-508.

[62] B. Jaishi, W.-X. Ren; *Finite element model updating*

based on eigenvalue and strain energy residuals using multiobjective optimisation technique; Mechanical Systems and Signal Processing 21 (2007) 2295-2317.

[63] C. Saravanan, N. Ganesan, V. Ramamurti; *Study on energy dissipation pattern in vibrating fluid filled cylindrical shells with a constrained viscoelastic layer*; Computers and Structures 75 (2000) 575-591.

[64] C. Saravanan, N. Ganesan, V. Ramamurti; *Vibration and damping analysis of multilayered fluid filled cylindrical shells with constrained viscoelastic damping using modal strain energy method*; Computers and Structures 75 (2000) 395-417.

[65] S. W. Kung, R. Singh; *Complex eigensolutions of rectangular plates with damping patches*; Journal of Sound and Vibration 216 (1) (1998) 1-28.

[66] S. W. Kung, R. Singh; *Development of approximate methods for the analysis of patch damping design concept*; Journal of Sound and Vibration 219 (5) (1999) 785-812.

[67] J. A. Zapfe, G. A. Lesieutre; *A discrete layer beam finite element for the dynamic analysis of composite sandwich beams with integral damping layers*; Computers and Structures 70 (1999) 647-666.

[68] H. Zheng, X. M. Tan, C. Cai; *Damping analysis of beams covered with multiple PCLD patches*; International Journal of Mechanical Sciences 48 (2006) 1371-1383.

[69] H. Zheng, G. S. H. Pau, Y. Y. Wang; *A comparative study on optimization of constrained layer damping treatment for structural vibration control*; Thin-Walled Structures 44 (2006) 886-896.

[70] H. Zheng, C. Cai, X. M. Tan; *Optimization of partial constrained layer damping treatment for vibrational energy minimization of vibrating beams*; Computers and Structures 82 (2004) 2493-2507.

[71] H. Illaire, W. Kropp, B. Mace; *A phenomenological model of active constrained layers*; Journal of Sound and

Vibration 285 (2005) 281-302.

[72] S. W. Kung, R. Singh; *Vibration analysis of beams with multiple constrained layer damping patches*; Journal of Sound and Vibration 212 (5) (1998) 781-805.

[73] D. M. Rao, R. Echempati, S. Nadella; *Dynamic analysis and damping of composite structures embedded with viscoelastic layers*; Elsevier Science Limited, Composites Part B 28B (1997) 547-554.

[74] S. Yi, S. F. Ling, M. Ying; *Finite element analysis of composite structures with smart constrained layer damping*; Elsevier Science, Advances in Engineering Software Vol. 29, 3-6 (1998) 265-271.

[75] S. S. A. Ravi, T. K. Kundra, B. C. Nakra; *Reanalysis of plates modified by free damping layer treatment*; Computers and Structures, Vol. 58, 3 (1996) 535-541.

[76] M.G. Sainsbury, Q.J. Zhang; *The Galerkin element method applied to the vibration of damped sandwich beams*; Computers and Structures 71 (1999) 239-256.

[77] A. K. Lall, N. T. Asnani, B. C. Nakra; *Vibration and damping analysis of rectangular plate with partially covered constrained viscoelastic layer*; Journal of Sound and Vibration, 109 (1987) 241-247.

[78] D. S. Nokes, F. C. Nelson; *Constrained layer damping with partial coverage*; Journal of Sound and Vibration, 38 3 (1968) 5-10.

[79] A. B. Spalding, J. A. Mann III; *Placing small constrained layer damping patches on a plate to attain global or local velocity changes*; Journal of the Acoustical Society of America 97 (1995) 3617–3624.

[80] C.H. Park, A. Baz; *Vibration control of bending modes of plates using active constrained layer damping*; Journal of Sound and Vibration 227 (4) (1999) 711–734.